Controlling the Properties of a-ZTO and a-IGZO via Low Temperature Annealing and Novel Layered Structures

A dissertation submitted to the University of Dublin
for the degree of Doctor of Philosophy

Aitkazy Kaisha

February 2023

School of Physics
Trinity College Dublin
The University of Dublin

Declaration

I declare that this thesis has not been submitted as an exercise for a degree at this or any other university and it is entirely my own work.

I agree to deposit this thesis in the University's open access institutional repository or allow the library to do so on my behalf, subject to Irish Copyright Legislation and Trinity College Library conditions of use and acknowledgement.

Name: Aitkazy Kaisha

Signature: **Date:** February 2023

Summary

This thesis deals with the broader implications of amorphous ZnSnO (a-ZTO) growth via two synthesis methods, examining the in-situ resistivity monitoring approach to optimising a low-annealing temperature <300 °C and exploring oxide-oxide lamination system is to control the properties of TCOs.

Chapter 4 describes the effects of reactive and nonreactive sputtering methods on the growth of a-ZTO. Two techniques broadly correspond to an oxygen-poor and rich atmosphere. Both approaches lead to identical conductivities of a-ZTO films. The best properties are found in two distinct compositions. The elemental ratio shifts were found to be due to shifts in local bond arrangements. These local bond arrangements were confirmed by Raman spectroscopy. This demonstrates the complex relationship between growth conditions and oxygen structure in a-ZTO.

I will then discuss in-situ post-deposition annealing to improve the conductivity of a-ZTO films at lower annealing temperature <300 °C. The optimal conditions for annealing were examined via a specialist system that allowed in-situ monitoring of the resistivity in the annealing process. The system also allows for control of the annealing atmosphere. This setup examined the impacts of different annealing parameters on final film properties. The parameters examined include the gas composition of the annealing atmosphere, the relationship between annealing time and temperatures, and the thickness of the films. A lower annealing point of 220 °C temperature was identified that produced similar conductivities to those attained at a higher temperature of 300 °C. The successful post-deposition treatment with

a highly conductive film on a Kapton substrate demonstrated the benefits of a well-controlled annealing approach.

Chapter 5 explored a layered structure to achieve a low carrier density of TCOs. This method involved inserting an ultra-thin layer of an alternative oxide between two TCO material layers. Two common ultra-thin TCOs and insulators were used to examine the layered structures. SiO_x used as one of the layers in the trilayer that showed a marked decrease in carrier density in the insertion of SiO_x in the laminated films. The free carrier density of a-ZTO/SiO_x/a-ZTO declined by a factor of three compared to a similar thickness a-ZTO, but just 40% of reduction in carrier mobility was found. The insertion of TiO_x layers into the laminated oxides was also investigated in a similar tri-layer arrangement. Although the TiO_x layer suppressed the density of current carriers less effectively compared to the layer of SiO_x, in a-ZTO/TiO_x/a-ZTO trilayers, a significantly reduced influence on carrier mobility was observed. The lowest density of free carriers in the trilayer of a-ZTO/Insulator/a-ZTO structures was established by a small thickness 2 nm thick SiO_x and TiO_x insulators. By utilising a broader range of characterisation techniques, the carrier concentration drop in a-IGZO/SiO_x/a-IGZO was assessed (a-IGZO is amorphous InGaZnO). a-IGZO was selected for this study as the effect is markedly similar to a-ZTO while significantly enhancing in magnitude. The film growth was established to be continuous regardless of thickness by SEM due to discontinuous leads to increase resistivity. No variation in oxygen structures in trilayer structures was confirmed via in-situ XPS studies. The effect of oxygen flow on the SiO_x layer in trilayers was studied, and the oxygen flow eliminated a reduction in charge carrier in trilayers.

This thesis is dedicated to the memory of my father,
Kaisa Bolaiuly (1923-2022).
I miss him every day.

Acknowledgements

The doctoral thesis is finally over! After four years of hard work, it is finished. This PhD thesis would not have been completed without the support of many people around me during this period of my life. In the following few paragraphs, I will make my best effort to express my gratitude to the people involved, either directly or indirectly.

First, I would like to thank my supervisor Prof. Igor Shvets. Without his support, this PhD study would not have been presented. I would secondly like to thank Dr. David Caffrey, whose expertise has been indispensable since I first met him, in mapping out research questions and methodologies. His valuable insights into research topics encouraged me a tremendous effort to sharpen my thinking and led to great improvements in my work at a higher level. Thanks also to Dr. Daragh Mullarkey and Dr. Brian Walls for their help throughout the course of my PhD.

Without the sterling support of a couple of other people from Trinity College Dublin, I would have had many problems with documentation and study procedures; current Programme Development and Global Officer Dr. Niamh McGoldrick, former Global Relations Officer Bridget Gavin and Executive Officer School of Physics Helen O'Halloran, School Manager School of Physics Dr. Colm Stephens, Senior Technical Officer (CRANN) Michael Finneran. I would also like to acknowledge past and current colleagues from my research group for their outstanding collaboration and support and all members inside and outside the School of Physics and CRANN, Trinity College Dublin.

I would also like to thank my sponsor, the Government of the Republic of Kazakhstan, under its ”*Bolashak*” programme, along with

past and current Bolashak staff members. Thanks especially to Elvira Myrzaliyeva, manager of the UK and Europe department in the Centre for International Programmes (CIP). I am very grateful for her immense support.

In addition, I would like to thank my friends Oral, Ozhet, Ehsan, Olzat, Askar, and Yerlan for supporting me during my PhD and maintaining support and advice throughout this tough time. In addition, thanks to the Academic English Programme team (AEP - 2017) at the University of Reading, UK, as well as Mark Saxby and Cristina Palmer from the British Council / Bolashak project in Kazakhstan.

> **"The strength of a family, like the strength of an army, lies in its loyalty to each other." – Mario Puzo**

Unfortunately, it is now impossible to express my gratitude personally to my cousin and her son, Ryskhan and Meirambek, because they have passed away. In addition, it is also impossible to express my thanks to our dear departed Dumber. Losing her was unbelievable both for me and her husband Mubarak. Thankfully Mubarak is still a great support for me. It is a great pity that these people will not be able to see me graduate. Thanks to all, especially for helping me with the contract between myself and Bolashak.

Of course, I would like to thank my father Kaisa and mother Zhagys, sister and brothers, nieces and nephews and sisters-in-law for their insights and enthusiastic support. Then my father-in-law Shaimerden and mother-in-law Nurkul. They have looked after my son at times during this PhD study which has been a tremendous support.

Furthermore, to the one who lightens the dark side of my heart and brightens my path to the future just by being you and giving birth to a cute and healthy baby boy; my wife, Aigerim. Having both you and our son Farabi has made me stronger than other people. Thank you for everything. You are always with me!

List of Publications

Publications

Published

1. **Aitkazy Kaisha, Ainur Zhussupbekova**, Karsten Fleischer, Rajani K. Vijayaraghavan, Igor V. Shvets, and David Caffrey.
   "The Importance of Local Bond Order to Conduction in Amorphous, Transparent, Conducting Oxides: The Case of Amorphous $ZnSnO_y$",
   ACS Appl. Mater. Interfaces 11, (47), 44399-44405, 2019

2. Ozhet Mauit, David Caffrey, Ardak Ainabayev, **Aitkazy Kaisha**, Olzat Toktarbaiuly, Yerzhigit Sugurbekov, Gulnar Sugurbekova, Igor V Shvets, Karsten Fleischer.
   "Growth of ZnO:Al by atomic layer deposition:Deconvoluting the contribution of hydrogen interstitials and crystallographic texture on the conductivity",
   Thin Solid Films 690, 137533, 2019

3. David Caffrey, Ainur Zhussupbekova, Rajani K. Vijayaraghavan, Ardak Ainabayev, **Aitkazy Kaisha**, Gulnar Sugurbekova, Igor V Shvets, Karsten Fleischer.
   " Crystallographic characterisation of ultra-thin, or amorphous transparent conducting oxides-the case for Raman spectroscopy",
   MDPI, Materials, 13, (2), 67, 2020

4. Pranab Biswas, Ardak Ainabayev, Ainur Zhussupbekova, feljin Jose, Robert O'Connor, **Aitkazy Kaisha**, Brian Walls & Igor V Shvets.
   "Tuning of oxygen vacancy-induced electrical conductivity in Ti-doped

hematite films and its impact on photoelectrochemical water splitting", Scientific Reports 10:7463, 2020

In Preparation

1. **Aitkazy Kaisha**, Fionnuala McGrath, Daragh Mullarkey, Qian Jing, Ardak Ainabayev, Pranab Biswas, Brian Walls, Karsten Fleischer, Louise Bradley, Igor V. Shvets, and David Caffrey.
"The Importance of In-Situ Monitoring of Resistivity Improvements by Annealing: The Demonstration for Amorphous $ZnSnO_y$",
To be submitted-ACS Appl. Mater. Interfaces

2. **Aitkazy Kaisha**, Daragh Mullarkey, Brian Walls, Igor V. Shvets, and David Caffrey.
"The examining the Annealing Parameters by In-Situ Monitoring of Resistivity of Amorphous $ZnSnO_y$",
To be submitted-ACS Nano Letter

3. **Aitkazy Kaisha**, Daragh Mullarkey, Ainur Zhussupbekova, Kuanysh Zhussupbekov, Brian Walls, Karsten Fleischer, Ardak Ainabayev, Igor V. Shvets, and David Caffrey.
"The Investigations on An Anomalous Carrier Concentration Drop in a-IGZO/SiO_x/a-IGZO Three Layered Structured Films,
To be submitted-Physical Review B

4. **Aitkazy Kaisha**, Daragh Mullarkey, Brian Walls, Karsten Fleischer, Ardak Ainabayev, Igor V. Shvets, and David Caffrey.
" Tuning The Electrical Properties of Amorphous $ZnSnO_y$ By Ultra-Thin Insulators: The Case of SiO_2",
To be submitted-Applied Physics Letter

5. **Aitkazy Kaisha**, Daragh Mullarkey, Brian Walls, Karsten Fleischer, Ardak Ainabayev, Igor V. Shvets, and David Caffrey.
" Altering The Electrical And Optical Properties of Amorphous $ZnSnO_y$ By Ultra-Thin Insulators: The Case of TiO_2",
To be submitted-Journal of Materials Science

6. Ardak Ainabayev, Daragh Mullarkey, Brian Walls, David Caffrey, Kuanysh Zhussupbekov, Ainur Zhussupbekova, Cansu Ilhan, **Aitkazy Kaisha**, Pranab Biswas, Alexander Tikhonov, Oisin Murtagh, and Igor V. Shvets. " Suppressed Hysteresis and Low-Resistivity Facile Grown Epitaxial VO_2 with high Temperature Coefficient of Resistance for high-performance Thermal Sensor Application",
   To be submitted-ACS Applied Nano Materials

Contents

List of Publications vii

Glossary of Terms xv

List of Figures xix

List of Tables xxiii

1 Introduction 1

2 Theoretical Background of Transparent Conducting Oxides 11

2.1 Transparent Conducting Oxides . . . 11

2.1.1 Figure of Merit . . . 15

2.1.2 Fundamental Properties of Transparent Conductive Oxides and Insulators . . . 20

2.2 Why Amorphous Transparent Conducting Oxides . . . 27

2.3 The Role of Defects in Amorphous TCO Materials . . . 28

2.4 Properties of Ultra-Thin Films . . . 39

3 Thin-Film Synthesis and Characterisation Techniques 43

3.1 Thin Film Fabrication . . . 43

3.1.1 Magnetron Sputtering . . . 43

3.1.2 Magnetron Sputtering is Equipped with a Static Sample Stage . . . 46

3.1.3 Magnetron Sputtering is Equipped with a Rotating Sample Stage . . . 47

3.2 Morphological and Crystallographic Characterisation . . . 52

3.2.1 X-Ray Diffraction . . . 52

3.2.2 X-Ray Reflectivity 54
3.3 Optical Properties of Amorphous TCOs 62
3.3.1 Ultraviolet-Visible Spectroscopy 62
3.4 Electrical Measurements 65
3.4.1 Four Point Probe Measurements 65
3.4.2 The Hall Effect System 66

4 Optimisation Studies and Annealing with In-Situ Observation of Resistivity of a-ZTO 71

4.1 Optimisation Studies on a-ZTO Films 71
4.2 Introduction for Optimisation Studies on a-ZTO 71
4.3 Methods for optimisation of a-ZTO 72
4.4 Results for optimisation of a-ZTO 74
4.5 Conclusion and Further Benefits of Optimisation of a-ZTO 76
4.6 Annealing with In-Situ Monitoring of Resistivity of a-ZTO 78
4.7 Introduction of Annealing with In-Situ Monitoring of Resistivity of a-ZTO 78
4.8 Experimental Methods 79
4.9 Results and Discussion 81
4.9.1 Optical Properties of a-ZTO Films 81
4.9.2 SEM image of a-ZTO Film 82
4.9.3 XRD and XRR data of a-ZTO Films 83
4.9.4 Annealing Studies on a-ZTO with In-Situ Monitoring of the Resistivity in Nitrogen Atmosphere 84
4.9.5 Annealing with In-Situ Observation of Resistivity of a-ZTO in Oxygen-Rich Atmosphere 92
4.9.6 a-ZTO Deposited on Boron Nitride Substrates 98
4.9.7 Annealing Studies on Room Temperature Grown a-ZTO with Different Thickness 100
4.9.8 Role of In-Situ Annealing 109
4.9.9 Annealing Studies on a-ZTO Deposited on Bendable Substrate 111
4.10 Conclusions 115

5 Tuning the Electrical Properties of Amorphous TCOs Including Ultra-Thin Alternative Semiconductor Layers 117

5.1 Controlling the Electrical Properties of the a-ZTO by Applying Ultra-Thin SiO_x Layers 117
5.2 Introduction of a-ZTO/SiO_x/a-ZTO Films 117
5.3 Fabrication and Experimental Details of a-ZTO/SiO_x/a-ZTO Films 119
5.4 Results and Discussion 120
5.4.1 Optical Properties of a-ZTO/SiO_x/a-ZTO Films 120
5.4.2 SEM Studies of a-ZTO and SiO_x Layers 122
5.4.3 XRD and XRR data of a-ZTO, and a-ZTO/SiO_x/a-ZTO Films 123
5.4.4 Results and Analysis of a-ZTO/SiO_x/a-ZTO Three-Layer Films 125
5.5 Conclusions and Further Investigations 128
5.6 Altering the Electrical Properties of a-ZTO Including Ultra-Thin TiO_x Layers 129
5.7 Introduction of a-ZTO/TiO_x/a-ZTO Structures 129
5.8 Experimental Methods of a-ZTO/TiO_x/a-ZTO Films 129
5.9 Results and Discussion 131
5.9.1 Optical Properties of a-ZTO/TiO_x/a-ZTO Films 131
5.9.2 SEM Studies of a-ZTO and TiO_x Layers 132
5.9.3 XRD and XRR of a-ZTO, and a-ZTO/TiO_x/a-ZTO Films 133
5.9.4 Results and Discussion of a-ZTO/TiO_x/a-ZTO Trilayers . 134
5.10 Conclusions and Further Investigations 137
5.11 Altering the Electrical Properties of the a-IGZO with Including Ultra-Thin SiO_x Layers 139
5.12 Introduction of a-IGZO/SiO_x/a-IGZO Films 139
5.13 Experimental Methods of a-IGZO/SiO_x/a-IGZO Films 139
5.14 Results and Discussion 141
5.14.1 Optical Properties of a-IGZO/SiO_x/a-IGZO Multilayers . 141
5.14.2 AFM and SEM Studies of a-IGZO and SiO_x Layers 143
5.14.3 XRD and XRR data of a-IGZO and Trilayer Films 145

5.14.4 Hall Effect data of a-IGZO/SiO$_x$/a-IGZO Films 147
5.14.5 Results and Findings of a-IGZO/SiO$_x$/a-IGZOs 149
5.14.6 In-Situ Transfer Process of Multilayers from Magnetron to XPS 152
5.14.7 XPS Studies of a-IGZO/SiO$_x$/a-IGZO Multilayers 154
5.14.8 Alteration in Electrical Properties of In-Situ Transferred Trilayers 158
5.14.9 The Role of Oxygen in a-IGZO/SiO$_x$/a-IGZO and SiO$_x$ Films 160
5.14.10 Figure of Merit of layered structures 163
5.15 Conclusions 164

6 Conclusions 167

References 173

Glossary of Terms

Abbreviations

TCO	Transparent Conducting Oxide
CdO	Cadmium Oxide
IO	Indium Oxide (InO)
GaAs	Gallium Arsenide (GaAs)
ZnO	Zinc Oxide (ZnO)
ITO	Indium Tin Oxide (In_2O_3:Sn)
FTO	Fluorine doped Tin Oxide (SnO_2:F)
a-IGZO	Amorphous Indium Gallium Zinc Oxide (a-$InGaZnO_4$)
FOM	Figure of Merit
SiO_2	Silicon Dioxide (SiO_2)
TiO_2	Titanium Dioxide (TiO_2)
AOS	Amorphous Oxide Semiconductor
a-ZTO	Amorphous Zinc Tin Oxide
TFT	Thin Film Transistor
OLED	Organic Light-Emitting Diode
c-IGZO	Crystalline Indium Gallium Zinc Oxide (a-$InGaZnO_4$)
LED	Light Emitting Diode
RF	Radio Frequency
DC	Direct Current
SEM	Scanning Electron Microscopy
XRR	X-Ray Reflectivity
XRD	X-Ray Diffraction

DOS	Density of States
XPS	X-ray Photoelectron Spectroscopy
UV-Vis	Ultraviolet-Visible
CBM	Conduction Band Minimum
VBM	Valence Band Maximum
GIXRD	Grazing Incidence X-Ray Diffraction
FWHM	Full Width Half Maximum
PL	Photoluminescence

Symbols

σ	Conductivity
E_g	Bandgap
A	Absorption
R	Reflectance
T	Transparency
α	Absorption Coefficient
ρ	Resistivity
t	Thickness
μ	Carrier Mobility
e	Charge of the electron
n_c	Carrier Concentration
R_{sh}	Sheet Resistance
$\mathbf{E}$	Electric Field
$\hbar$	Reduced Planck Constant
h	Planck's Constant
m^*	Effective Mass
κ	Relative Permittivity
ϵ_0	Vacuum Permittivity
N_i	Concentration of Ionized Impurities
N(E)	Density of States
f(E)	Fermi–Dirac Distribution

E_f	Fermi Level
E_c	Conduction Band Minimum (CBM)
k	Complex Refractive Index (extinction coefficient)
λ	Wavelength
n	Real Refractive Index
F_L	Lorentz Force
I	Current
B	Magnetic Field
N	Complex Refractive Index (n+ik)
μ	Hall Mobility
r_s	Polarisation of Light Component Perpendicular to the Surface
r_p	Polarisation of Light Component Parallel to the Surface
n_1	Refractive Index of Medium 1
n_2	Refractive Index of Medium 2
Z	Atomic Number
ω	Photon Frequency
d	Interatomic Spacing
θ	Angle of Diffraction
θ_C	Reflection Critical Angle
Ω	Electrical Resistance
s	Second

List of Figures

2.1 Band structure of metal, insulator, semiconductor and TCO . . . 14
2.2 Comparison of figure of merit of materials 18
2.3 A diagram of IGZO and ZTO based TTFs 29
2.4 Density of states of amorphous oxide semiconductors and bonding structures 31
2.5 The atomic structures of USC and UCP defects 34
2.6 A diagram of conduction path and bandgap of amorphous materials 38

3.1 Magnetron sputtering system with different magnetic array arrangements 44
3.2 Magnetron sputtering system with a static sample stage 46
3.3 A comparison of XRR data of two different sample stages 48
3.4 A diagram of Magnetron sputtering and a rotating sample stage . 48
3.5 A reactive Magnetron sputtering deposition rate 50
3.6 XRD systems 52
3.7 XRD pattern of amorphous Zinc Tin Oxide 53
3.8 XRR system 54
3.9 XRR incidence angle and critical angle 55
3.10 X-ray reflectivity curve 57
3.11 Schematic diagram of UV-Vis spectroscopy 62
3.12 A Tauc plot of a-ZTO film on glass substrate 63
3.13 Schematic diagram of a linear four-point probe method 65
3.14 Schematic diagram of Van der Pauw contact arrangements 67
3.15 Sketch of Hall effect 69

4.1 Reactive magnetron sputtering method 73
4.2 Nonreactive magnetron sputtering method 74
4.3 Optimisation study on a-ZTO via reactive and nonreactive sputtering methods 75
4.4 A reactive magnetron sputtering and its deposition rate 76
4.5 An image of a-ZTO film deposited at 300 °C 79
4.6 XPS data of a-ZTO film deposited at 300 °C 80
4.7 Optical properties of a-ZTO films 82
4.8 SEM image of 38 nm thick a-ZTO films on Glass substrate 83
4.9 XRR and XRD pattern of a-ZTO 84
4.10 An in-situ annealing method with a linear four-point probe 84
4.11 A method of calculation activation energy 85
4.12 a-ZTO films annealed in nitrogen atmosphere 87
4.13 a-ZTO films annealed in nitrogen atmosphere 88
4.14 Annealing slope for a-ZTO films prior to achieving the lowest resistivity 89
4.15 Degenerated behaviour of annealed films 90
4.16 Annealing studies on a-ZTO in oxygen-rich atmosphere 92
4.17 a-ZTO films annealed in an oxygen-rich atmosphere 94
4.18 Sheet resistance improvements of a-ZTO annealed at 190 °C . . . 96
4.19 Degenerated behaviour of annealed a-ZTO 97
4.20 SEM images of a-ZTO on Boron Nitride substrate 99
4.21 XPS data of a-ZTO film grown at RT 102
4.22 Images of a-ZTO films with different thicknesses 102
4.23 Optical properties of different thickness of a-ZTO films 103
4.24 SEM images of a-ZTO films with different thickness 104
4.25 Sheet resistance improvements in a-ZTO films with different thickness annealed in nitrogen 105
4.26 a-ZTO films with different thickness annealed in nitrogen 106
4.27 Sheet resistance improvements in a-ZTO films with different thickness annealed in oxygen-rich atmosphere 107
4.28 a-ZTO films with different thickness annealed in the oxygen-rich atmosphere 108

4.29 An image of 38 nm thick a-ZTO films on Kapton 111
4.30 Optical properties of a-ZTO on Kapton 112
4.31 SEM image of 38 nm thick a-ZTO films on Kapton 113
4.32 38 nm thick a-ZTO films on Kapton substrates 114

5.1 Trilayer structure of a-ZTO/SiO_x/a-ZTO films 119
5.2 Bandgaps of a-ZTO/SiO_x/a-ZTO multi-layers 120
5.3 Optical properties of a-ZTO/SiO_x/a-ZTO multi-layers 121
5.4 SEM images of a-ZTO and SiO_x 122
5.5 XRR and XRD data of a-ZTO/SiO_x/a-ZTO 123
5.6 Electrical properties of a-ZTO/SiO_x/a-ZTO layered structure multi-layers 125
5.7 Trilayer structure of a-ZTO/TiO_x/a-ZTO films 130
5.8 Optical properties of a-ZTO/TiO_x/a-ZTO films 131
5.9 Bandgaps of a-ZTO/TiO_x/a-ZTO multi-layers 132
5.10 SEM images of a-ZTO and TiO_x 133
5.11 XRR and XRD curves of a-ZTO/TiO_x/a-ZTO 134
5.12 Electrical properties of a-ZTO/TiO_x/a-ZTO films 135
5.13 Trilayer structure of a-IGZO/SiO_x/a-IGZO films 140
5.14 Optical properties of a-IGZO/SiO_x/a-IGZO multi-layers 141
5.15 Bandgaps of a-IGZO/SiO_x/a-IGZO multi-layers 142
5.16 AFM images of a-IGZO and SiO_x 143
5.17 SEM images of a-IGZO and SiO_x 144
5.18 XRR and XRD patterns of a-IGZO/SiO_x/a-IGZO 146
5.19 Hall measurements of samples for multilayers 148
5.20 Electrical properties of a-IGZO/SiO_x/a-IGZO layered structure multi-layers 150
5.21 Carrier concentration versus carrier mobility 151
5.22 Illustration of a transfer arm 152
5.23 The first in-situ transfer of a-$IGZO_{(20nm)}$/$SiO_{x(2nm)}$/a-$IGZO_{(20nm)}$ 153
5.24 The second in-situ transfer of a-$IGZO_{(20nm)}$/$SiO_{x(2nm)}$/a-$IGZO_{(7.5nm)}$ 154
5.25 The third in-situ transfer of a-$IGZO_{(20nm)}$/$SiO_{x(2nm)}$/a-$IGZO_{(10nm)}$ 154
5.26 Oxygen structure in a-IGZO/SiO_x/a-IGZO multi-layers 155

5.27 XPS scans of oxygen in a-IGZO and SiO_x 156
5.28 The effect of oxygen on a-$IGZO_{20\,nm}$/$SiO_{x(2\,nm)}$/a-$IGZO_{10\,nm}$ multilayers 161

List of Tables

2.1 Comparison of figure of merit of materials 17
2.2 Comparison of figure of merit of a-ZTO with different thickness . 18
2.3 Comparison of figure of merit of calculations 18
2.4 Electronegativity of elements in this work 37

3.1 Tauc plot coefficients 64

4.1 Activation energy of films prior to and after achieving the lowest resistivity of a-ZTO 89
4.2 Electrical properties of a-ZTO cooled down up to 50 °C with oxygen atmosphere 93
4.3 Electrical properties a-ZTO annealed at 190 °C 95
4.4 Activation energy of degenerately doped behavior in an oxygen-rich atmosphere 97
4.5 Elemental ratios of a-ZTO grown at RT and 300 °C 101
4.6 Comparison of electrical properties a-ZTO deposited at RT and 300 °C 109
4.7 Comparison of electrical properties of 38 nm thick a-ZTO deposited on Glass and Kapton 113

5.1 1st ionization energy of elements 128
5.2 The roughness values of each layer in a-IGZO/SiO_x/a-IGZO multilayers 145
5.3 Three layer films for hall measurement 149
5.4 The elemental composition of in-situ transferred multilayers . . . 155

5.5 Comparison of the electrical properties of samples transferred in-situ and under air 158
5.6 Comparison of the electrical properties of samples were kept in transfer arm and in air transferred sample 159
5.7 The effect of oxygen on a-IGZO$_{20\,nm}$/SiO$_{x(2\,nm)}$/a-IGZO$_{10\,nm}$ multi-layers 162
5.8 Comparison of Figure of Merit of trilayers and TCOs 164

1 Introduction

Semiconductor materials for electronic applications have attracted significant scientific attention since the beginning of the last century. Crystalline Si has become one of the dominant materials with unique and remarkable features for optoelectronic applications since used in the radio wave detector in 1906 [1]. It is suitable for a wide variety of fabrication methods, can be grown on a great diversity of substrates, well suited to integrate into technology, and is cost-effective due to its abundance in the Earth's crust and low-temperature deposition. Also, a-Si- based solar cells, thin film transistors (TFTs), light-emitting diode (LED) and many electronic applications have achieved considerable commercial success. Over the past 50 years, the performance of optoelectronic appellations has massively improved. However, this progress is slow due to a lack of alternatives to a-Si. Meanwhile, the mobility of electrons in a-Si is not high ($<1\,\mathrm{cm^2/Vs}$) [2]. Also, studies have found that crystalline Si is not ideal for use in optoelectronic and high-speed electronic applications due to its indirect bandgap, where the amount of the emitted light potential can be sorely restricted. In addition to that, metals are excellent conductors but opaque, and insulators are poor electrically conductive but transparent. An opaque property for metal and poor electrical conductivity for insulators result in withdrawing them as promising candidates

for developing certain optoelectronic applications. There are known key materials for optoelectronics, such as Si, a - Si etc and development of them will remain with a key priority in the future. In addition, TCOs are also one of the key players in optoelectronics. As a result, a certain number of optoelectronic applications require a material that combines transparency optically and electrically conductivity concurrently in one material, called Transparent Conducting Oxides (TCOs) [3]. The primary use of a-TCOs is that a-TCO materials are not only conductive or semiconducting but also transparent at the same time. There is a sizable number of examples of this. Conductive TCO materials use as transparent contacts (electrodes), such as in OLEDs or thin film solar cells. They are also used in heterojunction solar cells, where a highly transmissive charge extractor is needed at every cell interface. Heterojunction solar cells are also typically required of a material that has a high transmission from the IR to the UV light, too, for the reason that they are used in a common set of highly-specialised solar cells for Loon balloons. These loon balloons provide a network to a specific geographical area [4], where a feather-light (highly-specialised) solar panel serves energy to onboard equipment, which absorbs the light spectrum in different ranges. TCOs are particularly interesting in this regard. They can also be easily deposited in a homogeneous manner film with the standard industrial technologies over a wide area, which is a key aspect for applications. a-TCOs have a different application that has little to do with their transparency and more to do with them being high-quality semiconductors. The two most common amorphous TCOs, a-IGZO and a-ZTO are also popular because their electron mobility is not linked to a specific crystallographic order. This makes their deposition temperature is desirable to deposit at low temperature as you are then more compatible with other steps of the industrial process for manufacturing thin film cells. They also have high carrier mobility and controllable carrier densities, but carrier density in a-IGZO is more controllable than a-ZTO due to G acting as carrier suppressor in a-IGZO. This makes them highly desirable for high-density TFTs used in applications, such as high-resolution displays. In addition, they are also crucial for some industrial applications, such as TCOs for coating in order to reduce electromagnetic radiation interference (EMI), where they maintain visual access and reduce the amount of EMI simultaneously. This means that, leakage of radiation must be

reduced by the coating of transparent TCOs, and this prevents exposure to the users. Finally, transparent heating elements rely heavily on TCOs as defrosters in aircrafts [5].

TCOs are semiconductors that simultaneously possess a wide bandgap, exhibiting high conductivity and visible-range transparency (E_g >3 eV). Well-known TCO of Indium Tin Oxide (ITO) has showed its impressive properties, such as the lowest resistivity 10^{-3} ohm-cm and transmittance of T>90% in the visible range light spectrum at the same time. However, concern over the shortage of In in the earth's crust has prompted a search for ITO to fulfil the optoelectronic application's requirements. Here, a few alternative materials have been extensively studied for that reason, such as silver nanowires (AgNWs) and graphene as a transparent electrodes in optoelectronic devices and organic solar cells [6]. These alternatives have made great progress with a high priority on ultra-thin films and a mesh of nanowires. These ultra-thin materials facilitate excellent transparency as well. Furthermore, recently, increased attention has been given to oxide TCO materials, which benefit from low synthesis temperatures and higher mechanical flexibility while maintaining low electrical resistivity by the arrival of novel amorphous oxide semiconductors. Also, the ability to control carrier concentration is noticeably absent from crystalline TCOs, making them unviable for some electronic applications. All the above properties are possessed by amorphous Indium Gallium Zinc Oxide (a-IGZO) and Zinc Tin Oxide (a-ZTO). In 2004, an a-IGZO-based TFT was developed by Japanese scientists Nomura Kenji et al. and a-ZTO based TFT was fabricated by Chiang and et al. in 2005 [7, 8]. They present excellent electrical properties (high conductivity and carrier mobility) and are optically transparent simultaneously. In addition, they are an excellent candidate for electronic devices with flexible substrates due to low synthesis temperature as low as room-temperature [9]. The advantages of above materials have made them as a predominant part of thin-film transistors (TFTs), solar cells, an organic light-emitting diode (OLED or organic LED), and flat-panel displays [7–9]. In recent decades, a-IGZO and a-ZTO have been extensively studied; as a result, both have been achieved with resistivity around 10^{-3} ohm-cm while exhibiting lower than 10% absorption in the visible range of the light spectrum concurrently [10, 11]. Moreover, the durability of amorphous

materials needs be taken into account as the material bending radius is essential for flexible electronics. Moreover, a-IGZO and a-ZTO showed a good performance in terms of inducing stresses, due to which bending thin films of them and the ability to withstand the strain without fracture by flexible substrates and thickness of films themselves. A number of bending tests on both materials showed that at a certain radius range, they do not show any cracks and degradation in performance, where the bending radius of 3 mm for 14 nm thick a-ZTO and 2 mm for 50 nm thick a-IGZO, respectively [12, 13]. 40 nm thick a-ZTO was tested by bending radius 15 mm, which came out with excellent performance previously published elsewhere [14].

Furthermore, the challenges of inadequate optimisation prevent them from implementation in optoelectronic devices, so that understanding the nature of the defects with alteration by post-deposition treatment and tuning the electrical properties without introducing undesirable side effects, like dephasing or ionised impurity scattering. In this thesis, I focus on a promising candidate amorphous Zinc Tin Oxide (a-ZTO) with low-cost, abundant compound constituent elements [8] and one of the best performers is an amorphous Indium Gallium Zinc Oxide (a-IGZO) [7]. This work focuses on optimisation study, annealing process for a-ZTO, and tuning electrical properties of a-ZTO and a-IGZO films. Both materials have less In content compared to the most commercialised Indium Tin Oxide (ITO), which has impressive electrical properties, such as 200 nm thick ITO with 2×10^{-4} ohm-cm resistivity while exhibits 30 cm^2/Vs carrier mobility, simultaneously [15]. Nevertheless, there is a shortage of In, and a replacement of ITO with less In content candidates would only sort out a problem, which including several alternatives as stated above. The candidates are a-ZTO and a-IGZO, but a-IGZO is not the best replacement for ITO due to there is also concern over potential occupational exposures during the manufacture of gallium compounds. However, a-ZTO is a good replacement for a-IGZO. The films a-ZTO and a-IGZO were fabricated and contain ultra-thin (below 10 nm) insulator layers between two TCO layers. This work aims to tune the electrical properties of a-ZTO and a-IGZO films. Here, the insulating layer was either SiO_2 or TiO_2.

Indium and Gallium are high-cost elements due to the depth of mining. Also, a substantial increase in manufacturing these elements for the semiconductor in-

dustry results in alteration in environmental concentrations of these elements, which may lead to exposure to humans but practical research has not been hesitated to investigate these elements for a wide variety of purposes. It is clear to researchers that amorphous transparent conducting oxides are exciting and complicated materials. Complex a-IGZO and a-ZTO are intrinsic oxide semiconductors, where the optical and electrical properties depend on a stack of crucial factors, such as deposition conditions and post-deposition treatments, etc. The former is strongly connected with the optimisation process of the thin films by different fabrication methods applied. This influences the stoichiometry of a-ZTO films that implies how each synthesis method plays a key role in creating defect levels within the materials. That is why the production of amorphous networks is rigorously controlled. It is a well-understood fact that free carriers of these materials originated from oxygen and metal cluster defect centres [16]. Here, deposition conditions alter the composition of the films and can tune the electrical and optical properties, where different synthesis methods can vary the ratios of elements. This implies that the amorphous phase is highly susceptible to material properties, and it needs to be optimised with a precise selection of the growth parameters, such as choosing the target materials, precursors, deposition conditions, etc. [16–19]. As previously stated, a-ZTO can be deposited by performing various fabrication methods, which include atomic layer deposition, sol-gel, chemical vapour deposition and magnetron sputtering. Recent research has focused on optimising annealing temperatures, thickness, oxygen vacancies, and Zn:Sn ratios correlated to the films' electrical properties of the films [20–23]. Based on the analysis of these results, I have aimed at optimising the reactive and nonreactive sputtering methods with different content of the oxygen in the same magnetron sputtering chamber to show this can be advantageous to optimise each sputtering chamber for obtaining the best possible properties of oxide materials. Reactive sputtering provides an oxygen-rich environment (oxygen partial pressure being varied from 0 to 4×10^{-1} mbar during sputtering), while nonreactive sputtering is an oxygen-poor (No external oxygen added during the synthesis process). The two sputtering methods created two different bonding arrangements due to forming different defect levels by varying the Zn:Sn ratios, where the highest conductivity is in line for samples by two sputtering methods. It is possible the

different oxygen content alters the oxidation of tin between the two sputtering modes and result in differing electronic structures. Conclusion for every fabrication method requires its optimisation parameters and creates a variety of defect levels [24].

In amorphous semiconductor materials, defects have existed ubiquitously and unavoidably and govern materials' properties. These defects are particularly prevalent for low temperature, or room temperature deposited films [14, 25]. Therefore, annealing of a-ZTO and other TCO materials is often required to maximise the attainable properties of the material for applications. In contrast, certain defects of these sorts of materials have highly undesirable consequences for a critical performance of devices [26]. In this work, I have developed annealing processes to control the defect profile of the films. In the case of a-ZTO, the TFT performance was enhanced by the annealing process [27]. The exact defect chemistry of a-ZTO is still under extensive investigation [9]. There is a strong connection between defects and post-growth annealing. Thus, the annealing subject has been studied extensively. However, most studies have been focused on before (as deposited) and after (annealed) measurements of the properties a-ZTO [11, 28–31]. There is no understanding of what is happening during annealing due to the lack of in-situ observation of resistivity. The lack of dynamic tracking of the annealing process means the most desirable characteristics cannot be obtained. In this work, we reveal that monitoring the annealing in real-time by observing the resistance and deciding when the annealing needs to be terminated, and aim to determine ideal annealing procedures for the films by examining the resistivity of the films during the annealing process. To ensure compatibility with cost-effective synthesis temperature for commercialisation, it is allowed that the annealing temperatures are kept below 300 °C.

The studies on a-TCO/Insulator/a-TCO three-layers films have shown that there is considerable attention should be directed towards improving the efficiencies of ultra-thin TCO films to make them a promising candidate for flexible electronics for device design, where high performance of devices requires ultra-thin, low carrier concentration TCOs for TFTs. The main criterion is a low-dimensional property (one dimension is in the nanoscale), and low intrinsic defects must be achieved. As a result of the requirements of devices, tuning

the electrical properties of amorphous Transparent Conducting Oxide (a-TCO) is crucial in particular for low carrier concentration based TFTs with decreasing the thickness of TCOs in order to develop an excellent switching operation [32–36]. Controlling the electrical properties of ultra-thin a-TCO for applying as thin top contacts on plasmonic-enhanced photovoltaic (PV) devices, which can be done by doping elements. However, doping can reduce the material quality and even create free carriers with ionised impurity scattering centres [37, 38]. The layering method can potentially maintain the lateral carrier mobility at ultra-thin films that can be achieved by introducing the ultra-thin insulator layers with a few nm thickness, which minimises the amount of ionised impurity scattering and intrinsic defects. This approach also offers a promising method to tune the properties of TCOs.

Altering the electrical proprieties of the amorphous oxide semiconductors has been investigated by involving a-ZTO and ultra-thin insulators SiO_x, TiO_x. There are studies on a-ZTO/SiO_x/a-ZTO and a-ZTO/TiO_x/a-ZTO multi-layers. In these investigations, room temperature (RT) was used as a deposition temperature. Here, the carrier concentration dropped almost three times for an a-ZTO/SiO_x/a-ZTO multilayer compared to pure a-ZTO. While carrier mobility did not drop too much. At the same time, ultra-thin TiO_x with different film thicknesses were less effective than SiO_x films in reducing the carrier concentration. However, carrier mobility was maintained at $\approx 6.5\,cm^2/Vs$, which is in line with the a-ZTO film.

In this work, a-IGZO/Insulator/a-IGZO threelayers were also studied as well. Much of the work was carried out on thick superlattices of a-IGZO/SiO_x/a-IGZO for tuning the refractive index of the materials, where a carrier concentration drop was a side effect, and the carrier concentration drop in these superlattices was not investigated. These multilayered films were deposited at a high-temperature (300 °C) [39]. In this work, I will address the carrier concentration decrease in a-IGZO/SiO_x/a-IGZO three-layer films, which has been investigated by undertaking theoretical and experimental work. To reveal the peculiar drop in carrier concentration in a-IGZO/SiO_x/a-IGZO films, the synthesis temperature was maintained at room temperature due to the three-layer film deposited at a high temperature (180 °C) has got rid of charge carrier drop. This can be understood

by in-situ annealing of trilayers during the deposition. Here, 2 nm thick SiO_x decreased the carrier concentration of a-IGZO/SiO_x/a-IGZO film by one order of magnitude compared to pure a-IGZO.

In this thesis, three things have been discussed, and the motivation behind three things are; understanding the optimisation of a-ZTO films and annealing with an in-situ monitoring of resistivity of a-ZTO films and altering the electrical properties of two amorphous TCOs, where this was done via ultra-thin insulator films. Firstly, I will present challenges in deposition methods for a-ZTO, where a-ZTO is an intrinsic semiconductor, meaning that in an intrinsic semiconductor, its electrical properties and optimisation are directly linked to its own electronic structure. This electronic structure is essential for optimisation to understanding in detail of optimisation condition effects. Optimisation study implies that prescriptions of fabrication of a-ZTO are crucial to controlling the properties of materials, and highly-accessible fabrication techniques must be tuned for growing the desirable properties of a-ZTO, where the magnetron sputtering method was used in order to show impacts of the different deposition environments of magnetron sputtering on the properties of a-ZTO. Deposition environments can vary across the film synthesis and understanding of the consequences of sputtering atmosphere variations in the film's synthesis process. Furthermore, post-deposition annealing is often a key element of the performance of a-TCO for various applications. Defects in amorphous materials define the performance of a-TCOs. The nature/type of the defects in a-TCOs is essential, not just their number. The nature of the defects is defined by the growth conditions and the post-growth anneal. That is why I focus on these aspects in my thesis. It is a proven fact that altering the nature/type of the defects can enhance the electrical properties of a-ZTO films, which can fulfil the requirements of TFTs or other applications. One of the best examples is that device requirements for highly conductive and transparent films with high electron mobility to enhance the refresh rate of oxide-based displays. By doing post-growth annealing, an annealing method can improve electrical properties, such as enhancing conductivity and carrier mobility. However, most studies deal with high-temperature annealing (>300 °C) that results in loosing the appropriateness for the low temperature based plastic

substrates and device manufacturers. This implies that understanding the importance of low-temperature annealing with monitoring of resistivity is crucial. Also, high-temperature annealing can lead to high-cost TCO-based electronics due to the fact that, maintaining high-temperature annealing requires a challenging procedure. In-situ monitoring of the annealing process can reduce the annealing temperature and this annealing method showed its efficiency in examining the different annealing gas atmospheres and film parameters. Furthermore, certain amorphous Transparent Conducting Oxides (a-TCOs) based TFT applications need the low-carrier density of TCOs ($<10^{18}\,cm^{-3}$), while maintaining the mobile carrier high. The benefits of achieving a low carrier density of TCOs via novel layered structures are to minimise the intrinsic defect levels, where low-cost, environmentally friendly, and more abundant elements can be used. As I have investigated multilayered structures, where a-IGZO and a-ZTO are used as TCO layers, and SiO_x and TiO_x are selected for insulator layers in trilayer structure. All materials have been extensively studied for developing optoelectronic devices, although they can be used as research materials for developing and understanding the layered structures in this thesis. Also, these materials' impressive optical and electrical properties could benefit this layering oxide investigation. Based on the above discussion, a short description of each chapters is given below:

In Chapter 2: I will start with identifying the properties of the TCOs, which can be compared with other well-known solid materials (metals and insulators). Then the basic physics of the TCO materials will be discussed. I will outline the concept of defects in two main a-ZTO and a-IGZO materials that have been studied theoretically and experimentally. The thickness of these materials, it is a function of the electrical and optical properties will be stated.

In Chapter 3: I will reveal the details of thin-film synthesis and characterisation techniques that was used in this work. Will also show the fundamental Physics concealed in these techniques for obtaining films' electrical, optical and structural properties.

In Chapter 4: I will outline the use of annealing on a-ZTO with in-situ monitoring of the sheet resistance in order to show effective ways to prevent missing the best point during the annealing process (fixed time annealing could skip the best gains). Observed peculiar curve of resistivity and a high activation

energy of the reaction was found a sharp decrease in the resistivity slope. These are used to determine the conditions of the greatest rate of change with time. These studies allow us to select the lowest temperatures where the most significant changes occur with estimating a lower temperature. In doing so, I have found a range of values where little improvement is gained with increases in annealing temperature. In this range, it was observed that an increase in total annealing time served as a substitute for increasing the temperature. While samples were annealed in oxygen-rich atmosphere by in-situ monitoring of the resistivity with altering metal clusters and oxygen vacancy defect centres, where changes result in improving the electrical properties of films. At the same time, a-ZTO films with different thickness were annealed to indicate that a-ZTO is a suitable material for scalable production. While different thickness of a-ZTO films were annealed to examine its bulk sensitive and suitability for variety of gas Sensors, I shall address developing a high conductive a-ZTO films on Kapton substrate by this the annealing method.

In Chapter 5: I shall outline the obtained results of a-ZTO/SiO_x/a-ZTO three-layer films, where interpretation of observed results can be discussed. I will also give the results of a-ZTO/TiO_x/a-ZTO thin films related to their electrical properties and a short review of experiments to analyse the optical properties of a-ZTO/TiO_x/a-ZTO by ellipsometry. I shall describe work performed in the investigation of reduction in the carrier density in a-IGZO/SiO_x/a-IGZO three-layers films. The investigations have been done by in-situ transfer of the samples from the magnetron to the XPS instrument. XPS data is analysed, and several samples were fabricated with an oxygen-rich atmosphere to eliminate charge carrier drop in three-layer structure films. I will describe the results of a number of characterisation techniques used for explaining the charge carrier drops. I will give the conclusions for the carrier decreases in the trilayer.

In Chapter 6: Finally, I will outline the conclusion of the investigations that have been given. I will provide plans for future work that can be extended to enhance the scientific strength of obtaining results previously, which includes annealing studies on a-ZTO and three structure multi-layers.

2

Theoretical Background of Transparent Conducting Oxides

This chapter begins by presenting the general concepts of Transparent Conducting Oxides (TCOs), while describing their unique advantages, including the properties that distinguish them from other materials. Also, the fundamental physics of semiconductor materials are discussed as relevant to transparent conductive oxides. Besides this, it introduces the defects of TCOs that help explain the optical, electrical and structural characteristics of several important types of TCOs, namely amorphous Indium Gallium Zinc Oxide (a-IGZO) and Zinc Tin Oxide (a-ZTO). Lastly, crucial role of thickness in the properties of TCO materials will be discussed.

2.1 Transparent Conducting Oxides

Material science has inevitably engaged in the invention of competitive materials for optoelectronic technologies. Progress in this area is strongly dependent on the optical and electrical properties of common solid semiconductor materials, which are widely used in modern electronic products that incorporate a variety of development features. The natural behaviour of these solid materials has been

investigated by solid-state physics to understand the fundamentals of these solid materials. These studies examine not only the main classes of metals and semiconductors but also establish the insulators. The three materials stated above can be found in electronic applications in combination or individual form. So, one of the key tasks is to create a new material which demonstrates high optical transparency in the visible range of the electromagnetic spectrum and high electrical conductivity (σ). The conductivity of certain materials is an intrinsic property. In other words, it is bulk property. The transmittance of such materials is also an intrinsic property because a film's base level of absorption is entirely linked to its band structure. However, the band structure is influenced by extrinsic properties, depending on the thickness of films and transmission properties of various substrates under the films. In addition, transmission is also influenced by the film's reflectivity, but that is a function of the total device as the refractive index miss-match dictates it at each interface. High transmission and high conductivity of films are defined by the band structure origins of materials, which could be the origins of carrier mobility and carrier density within the bandgap. Also, a lack of subgap state transition leads to low absorption. So, it is worth discussing the band structures of a few widely used, essential materials in order to show the importance of the band structure. In general, the band structure of materials is crucial for the conduction property of materials and band structure is described by band theory. First of all, the band structure of materials consists of two basic types of energy band gaps. One is an overlap in valence and conduction bands as a result of missing the forbidden energy gap between them, which belongs to the metals. The metals are composed of a unique type of metallic bonding that allows the free electrons to move smoothly through the lattice so that metals show a high electrical conductivity (σ), but metallic bonding provides more free electrons, which means all of the metal atoms are surrounded by free electrons. Free electrons in metals lead to the absorption of photons. In other words, these free electrons do not let the photon pass through the metals, and this indicates opaque property [40]. The other one is a bandgap with several eV gaps that has a large number of free carriers and possesses a large number of empty energy states, which are called semiconductors. However, there is a large forbidden gap between the valence and conduction band that is called insulators. One of the

characteristic properties of insulators is high transparency. The wide bandgap gives optical transparency because these insulators do not conduct. Also, because of a large forbidden gap, they do not absorb photons as readily as metals. This means that the valence band is entirely full (no more free electrons), and the high-energy unoccupied states are at far higher energy (the band gap). Silicon dioxide is classified as a widely recognised insulator whose bandgap energy is approximately 9 eV [41]. That is why the best alternative approach is semiconductors, which simultaneously satisfy smart devices' electrical conductivity and high transparency requirements. Figure 2.1 shows the band structure of different classes of materials. This figure depicts the band structure of the common metal [42], insulator [43], semiconductor [44], and Transparent Conducting Oxide (TCO) [45].

Transparent conducting oxides are identified as a unique semiconductor material group and have a long history. In the first half of the 20th century, semiconductor physics and technology developed and introduced a new road map to the electronic industries [46]. In 1907, Baedeker discovered the first transparent conducting oxide Nanofilm, which was a CdO thin film [47]. However, CdO has not been used in optoelectronic applications due to the exposure concerns for human health and the environment [48]. Subsequently, various TCO materials were investigated, and in 1954, transparent conducting (approximately 10 S/cm) indium oxide (IO) produced by the post-oxidation of thin metal films was reported [49]. Furthermore, the physics and properties of semiconductors - silicon (Si) and Gallium Arsenide (GaAs) - were intensively investigated, and silicon has been widely used in electronic devices. It is the most widely used semiconductor in thin film transistors (TFTs), and these are being used in the bulk of electronic applications. However, Si is an indirect band gap material; therefore, it is not optimal for optoelectronic applications that rely on the transfer of an electron from the valence band to the conduction band and vice versa, which requires a change in momentum of electrons that can not be supplied from a photon as a photon does not carry momentum. This can restrict the amount of the emitted light energy [50]. The main drawbacks of Si can be resolved by doping the oxide semiconductor materials with oxide semiconductor materials that can offer benefits for optoelectronics and can replace and complement silicon for specific

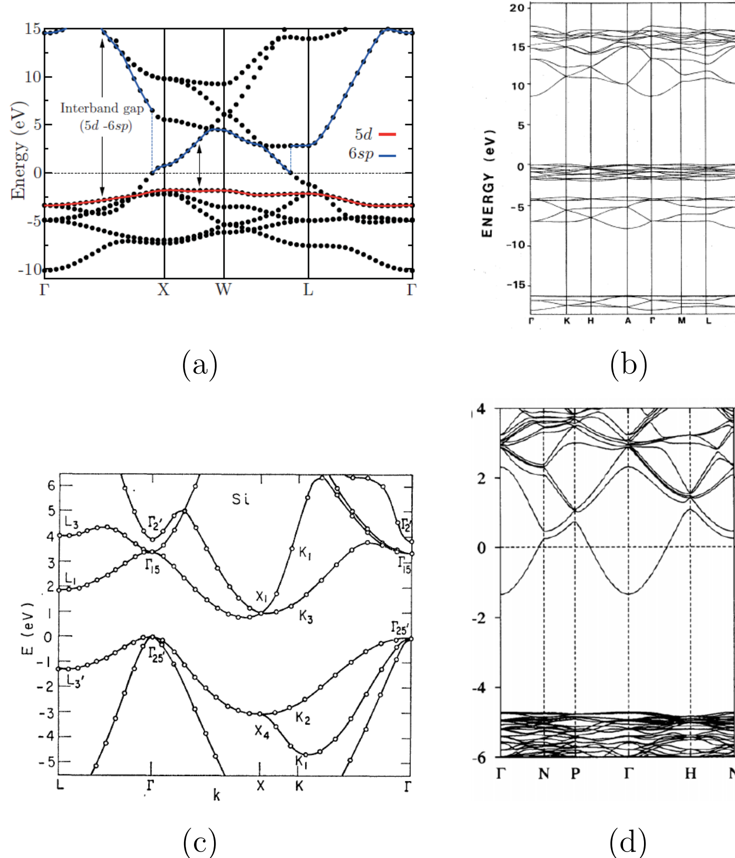

Figure 2.1: Comparison of band structure of metal, insulator, semiconductor and TCO, where (a) - Gold, (b) - SiO_2, (c) - Silicon, (d) - Indium Tin Oxide (TCO). All figures edited from cited papers [42–45].

applications. There is an urgent need to focus on alloy systems that can be used as powerful alternatives to Si. Compound semiconductors are composed of several elements, where the composition of alloy materials controls their optical and electrical properties. It is known that binary and ternary compounds (TCO materials) have been obtained using various deposition techniques. These include binary Zinc Oxide (ZnO), Indium Oxide (IO), as well as impurity-doped ternary compounds Indium Tin Oxides (ITO), Aluminum doped Zinc Oxides (AlZnO) and Fluorine doped Tin Oxides (FTO). It is clearly seen that these oxide materials do not contain Si due to as Si acts as a carrier suppressor in oxide films [51]. This means that Si reduces the current carrier concentration and, therefore, it is an interesting dopant element for oxides that are used in TCO-based TFTs that

often require low current carrier concentration. In the last few decades, transparent conducting oxides (TCOs), have become one of the most significant parts of thin, fast and flexible flat-screen displays, organic light-emitting diodes, thin-film solar cells, and electrochromic devices [52, 53]. The remarkable domination of TCO semiconductor materials has been attracting the attention of scientists, and the TCO industry has developed along several different pathways. As a result, TCO materials have been created with conductivity around 10^4 S/cm in order to create low resistivity electrodes in the TFT of optoelectronic applications [9], while exhibiting lower than 10% absorption in the visible range for transparency [54]. Today, well-known n-type TCO semiconductors Indium Gallium Zinc Oxide (IGZO) and Zinc Tin oxide have been extensively studied. They demonstrate a larger bandgap that is higher than 3 eV and optical transparency $> 92\%$ within the visible range of wavelength. However, optical transparency is influenced by the extensive properties, where an extensive property is a physical property of matter that changes as the quantity of matter changes, such as the size of the system, etc. So, optical transparency is defined by the amount of light absorbed by the material. This means that optical transparency is linked to surface texture, the thickness of films and absorption of substrates, where these factors must be considered in order to obtain desirable low absorption films, such as thicker films with higher absorption of light. Having both high electrical conductivity and transparency properties allows for the production of fully transparent TCO-based logic circuits [9]. From the above discussion, it is apparent that the properties of TCOs are different from other materials, where understanding the basic nature of TCOs is crucial to overcoming the complexity of practical research and commercialisation. Moreover, in the following several paragraphs, I will outline a few paragraphs on qualitative performance (Figure of Merit) and the basic physics of TCOs.

2.1.1 Figure of Merit

Although much research has been done towards finding and developing n-type TCOs, there is still a particular concern that needs to be addressed concerning the performance of TCOs in terms of transparency and the electrical properties of n-type TCOs. All n-type TCOs mentioned above exhibit high performance

in commercial industries. One way of quantifying the performance of the n-type TCOs is by involving a Figure of Merit (FoM), which combines both their optical and electrical properties, and allows comparison with other TCOs. The figure of merit has units of Ω^{-1}. The figure of merit (FoM) was introduced by Fraser & Cook in 1972, where they determined the FoM of ITO grown by sputtering [55]. Here, they used $F = \frac{T}{R_{sh}}$ as a quantifying method (T is the transmittance and R_{sh} is the sheet resistance). After that, new forms of the FoM were suggested by Haacke in 1976 [56]. Half a century later, it is still showing its importance for TCOs.

$$\sigma = \frac{1}{\rho} \Rightarrow \rho = R_{sh} \times t \Rightarrow \sigma = \frac{1}{R_{sh} \times t} \tag{2.1}$$

$$\alpha = \frac{-\ln(T+R)}{t} \tag{2.2}$$

where R is the reflectance, and the best performing TCOs should have a combination of high electrical conductivity and low absorption of visible range light. From the equations (2.1) and (2.2), an equation of Figure of Merit (FoM) is defined:

$$FOM \quad is \quad the \quad ratio \quad of \quad \sigma \quad to \quad \alpha$$
$$F_{TCO} = \frac{\sigma}{\alpha} \quad or \quad F_{TCO} = -\frac{1}{R_{sh}\ln(T+R)} \tag{2.3}$$

where σ is the conductivity of TCOs, R_{sh} is the sheet resistance, α is the absorption coefficient, t is the thickness of the materials.

Table 2.1 shows the figures of merit for a few TCOs and alternative materials for transparent electrodes. They possess different values of FoM due to the specific needs for different applications in transparent electrodes. In general, it is desirable for the electrodes to have absorption below 10% and sheet resistance better than 100 Ω/□ [6]. This is a powerful tool to precisely assess a promising candidate for a variety of applications, but the FoM has to be used in comparing similar films since a few properties of films have an impact on it. Firstly, its sheet resistance and dependence on the film thickness must be born in mind. Also, FoM uses a single wavelength value of transmission and reflection of films (for example representative transmission value for films is usually selected for a 550 nm wavelength and it is defined by the highly sensitive wavelength value of human eyes [62]). However, those transmission and reflection values often vary across the

Material	Growth technique	R_{sh} $\Omega/\square$	T(%)	Thickness (nm)	FoM (Ω^{-1})	Ref
n-type a-IGZO	Sputtering	95.4	77.2	100	0.7×10^{-3}	[57]
n-type a-ZTO	Sputtering	600	80	300	1.3×10^{-3}	[16]
p-type a-Cr_2O_3:Mg	Sputtering	20000	60	50	5.9×10^{-8}	[58]
ITO	Spin-coated	730	90.5	115	4.8×10^{-4}	[59]
AgNWs	Solution-processed	23	90.4		1.5×10^{-4}	[60]
Graphene	CVD	860	91.6	bi-layers	4.836×10^{-4}	[61]
As deposited a-ZTO	Sputtering	1952	79	38 nm	4.9×10^{-5}	here
Annealed a-ZTO	Sputtering	796	79.7	38 nm	1.4×10^{-4}	here
SWNTs	N/A	N/A	N/A	N/A		

Table 2.1: Comparison of figure of merit of materials for the average transmission of films in the visible spectral range, where R_{sh} is the sheet resistance and T(%) is the optical transmittance.

entire spectrum. An additional consequence is that FoM gives no indication of the material's bandgap and, therefore, on the spectral range where the material is transparent. This means that FoM can be useful, but its limitations must be considered. As FoM is very dependent on the sheet resistance of materials, it can put emphasis on materials which are very conductive at the expense of materials that are more transparent (ultra-thin). This can be seen from Table 2.1, where two a-ZTO films with the same thickness in this work but different sheet resistance are included. Lower sheet resistance film (annealed) has a better value of FoM. This means that it becomes very difficult to compare FoM between samples that have different thicknesses. For example, for two a-ZTO films in this work as shown in Table 2.2, the first film has a sheet resistance of 5865 ohm, but an a-ZTO film that is three times thicker has a sheet resistance of approximately 1456 ohm, and they have different FoM values as shown in Table 2.2. Note that two a-ZTO films were deposited in a similar fashion at room temperature to a different

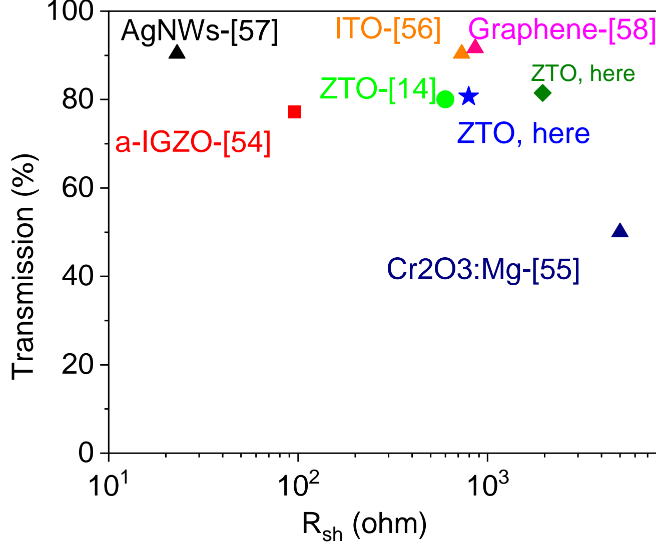

Figure 2.2: Comparison of figure of merit of materials.

thickness. Also, a particular matter for concern is using only the transmission

Material	R_{sh} $\Omega/\square$	T(%)	R(%)	FoM$_T$ (Ω^{-1}) $\frac{T}{R_{sh}}$	FoM$_{TR}$ (Ω^{-1}) $\frac{1}{R_{sh} ln(T+R)}$
a-ZTO (38 nm)	5865	80	18.8	1.9×10^{-5}	1.4×10^{-2}
a-ZTO (117 nm)	1456	79.5	18	7×10^{-5}	3.4×10^{-2}

Table 2.2: Comparison of figure of merit of calculations of a-ZTO with different thickness in this work, where R(%) and T(%) are the optical reflectance and transmittance of films at 550 nm.

data of films, which might not precisely assess the FoM of materials. Furthermore,

Material	R_{sh} $\Omega/\square$	T(%)	R(%)	FoM$_T$ (Ω^{-1}) $\frac{T}{R_{sh}}$	FoM$_{TR}$ (Ω^{-1}) $\frac{1}{R_{sh} ln(T+R)}$
a-ZTO (38 nm)	796	79	19.4	1.4×10^{-4}	6.2×10^{-2}

Table 2.3: Comparison of figure of merit of calculations of a-ZTO in this work, where R(%) and T(%) are the optical reflectance and transmittance of films at 550 nm.

both the transmittance (T%) and reflectance (R%) data of thin films must be considered because a variation in the thickness of films can cause reflectivity

changes. Reflectivity changes can shift the reflectivity spectra in energy while they affect the interference of thin films. Alteration in reflectivity can make differences in the transmission values between the films seem larger than they actually are. This is clearly seen from the FoM values for T and T+R as shown in Table 2.3, where the FoM of the a-ZTO film is different due to including a consideration of reflectance (R%) data. All of this highlights that the figure of merit can be a valuable metric for identifying promising TCOs for applications requiring highly conductive TCO layers, but its limitations must be understood when selecting materials for specific applications.

2.1.2 Fundamental Properties of Transparent Conductive Oxides and Insulators

Conductivity: Semiconductor physics theories can be applied to understand the electrical and optical properties of metals and TCOs. In general, free electrons are only one type of current carrier in metals, and electrons and holes are charge carriers in semiconductors. The electrical conductivity (σ, units of Siemens per centimetre) of a TCO is described by the number of electrons and holes under the current flow. This can be written as [63, 64]:

$$\sigma = e \times (n_n \mu_n + n_p \mu_p) \tag{2.4}$$

where e is the electron's charge, μ_n and μ_p are the electron and hole mobility, respectively (units is cm^2/Vs), and n_n and n_p are the free-carrier concentration of electrons and holes (units of cm^{-3}), respectively. TCOs can be doped in two ways: n-type and p-type doping. In general, transparent conducting oxides are mostly n-type transparent oxide semiconductors, so the conductivity of n-type oxide semiconductors is defined by the equation (2.5), and the main carrier type is electrons.

$$\sigma = e n_e \mu_e \tag{2.5}$$

$$\sigma = \frac{1}{\rho} = \frac{1}{R_{sh} t} \tag{2.6}$$

It can be seen from the equation (2.5) that the conductivity of the semiconductor TCOs strongly depends on carrier density and electron mobility. Resistivity (ρ, unit is Ohm-cm) of the transparent oxide semiconductors is determined by the conductivity of films as shown in equation (2.6), which is defined by the sheet resistance (R_{sh}) and thickness (t) of the films. Sheet resistance is determined by a square sheet with a sheet resistance and that is why the unit of sheet resistance is ohms per square ($\Omega/\Box$).

Carrier Mobility: as stated in the above equation (2.5), μ_e can be articulated by how fast the electrons move when an electric field is applied [64–66]. This can lead to a drift of the electrons in the oxide semiconductors, and an electron can be subjected to a drift velocity as shown (2.7):

$$\vartheta_d = -\mu_e E \tag{2.7}$$

now we can describe the drift velocity of the electrons using Newton's Law, which can be written as:

$$\vartheta_d = a\tau \tag{2.8}$$

where τ is the mean free time. If the force on an electron is described by F=eE, the acceleration of the electron is shown below:

$$a = \frac{eE}{m_e} \tag{2.9}$$

by combining equation (2.8) and (2.9), we can get:

$$\vartheta_d = \frac{eE\tau}{m_e^*} \tag{2.10}$$

therefore, from the equations (2.7) and (2.10), the mobility of the semiconductor can be expressed as:

$$\mu_e = \frac{e\tau}{m_e^*} \tag{2.11}$$

where τ is the mean free time (also called average relaxation time, see equation 2.20) and m^* is the effective mass of the electrons of the TCOs. In general, effective mass in the conduction band of the TCOs can be defined by energy-momentum curves (E versus k), shown by the equation:

$$m_e^* = \frac{\hbar^2}{\frac{\partial^2 E}{\partial k^2}} \tag{2.12}$$

Ionized impurity scattering: Ionized impurity scattering in doped semiconductors plays a key role in charge transport, as the electrons travelling in the lattice can be scattered by each other and by an electrostatic. This phenomenon is described by the Brooks-Herring-Dingle (BHD) approach. Based on this model, carrier mobility in films is limited by ionized impurities (μ_{ii}). Here, the mobility

limiting mechanism of electrons can be written in the equation (2.13) [67–69]:

$$\mu_{ii} = \frac{3\pi\hbar^3(4\pi\epsilon_0\kappa)^2}{2Z^2e^3m^{*2}}\left(\frac{N_e}{N_i}\right)\left(\frac{1}{F(\xi)}\right)$$
$$F(\xi) = \ln(\xi+1) - \frac{\xi}{1+\xi} \tag{2.13}$$
$$F(\xi) = 4\pi^3\left(\frac{3}{\pi}\right)^{\frac{1}{3}}\frac{\epsilon_0\kappa\hbar^3N_e^{\frac{1}{2}}}{e^3m^*}$$

where the concentration of ionized impurities is N_i, the effective mass m*, the screening function *F(ξ)*, the elementary electron charge e, the relative permittivity κ , the reduced Planck constant $\hbar$, the vacuum permittivity ϵ_0, the charge of the impurity Z, free carrier density N_e, and the distribution function ξ.

Carrier Concentration: In n-type TCOs, the density of electrons in the conduction band (n) is defined as follows [64–66, 70]:

$$n = \int_{E_{CB}}^{\infty} N(E)f(E)dE \tag{2.14}$$

where N(E) is the density of states, E_{CB} is the bottom of the conduction band (minimum), and f(E) the Fermi–Dirac distribution given by:

$$f(E) = \frac{1}{1+exp^{\frac{E-E_F}{kT}}} \tag{2.15}$$

for n-type TCOs's the density of states in the conduction band can be expressed as:

$$N(E) = \frac{(2m_e^*)^{\frac{3}{2}}}{2\pi^2\hbar^3}\sqrt{E-E_c} \tag{2.16}$$

where the number of energy states is equal to E_c, and where $E_c<E_{CB}$. By combining equations 2.15 and 2.16, we get n as shown in 2.17:

$$n = N_c\left[-\frac{E_c-E_F}{kT}\right] \tag{2.17}$$

where N_c is the effective density of states in the conduction band and E_F is the

Fermi level. N_c is given as:

$$N_c = 2\left(\frac{2\pi m_e^* kT}{h^2}\right)^{\frac{3}{2}} \tag{2.18}$$

the density of free carrier electrons in amorphous oxide semiconductor networks is very complicated. The amount of the free carrier is defined by the defect levels within random networks. They are also related to the preparation methods (PVD and CVD methods), synthesis temperature, post-deposition treatment under various gas atmospheres and composition of targets. The defect centres in amorphous materials have been discovered by theoretical and experimental works. In this work, these defect centres will be described as their results by the in-situ annealing method, which will be outlined in the following sections.

Electrical properties of semiconductor oxide ultra-thin films:

The properties of ultra-thin films play a key role in their performance in electronic applications. The mechanical, electrical and magnetic properties of thin films have to be studied to determine their performance. Instead of investigating the mechanical and magnetic properties of thin films, I focus on the electrical properties of TCO films in this chapter. The properties of thin films are defined by the dimensions of the thin film materials. The properties of thin film semiconductor materials are defined by thickness. When such cases occur in thin films, where the penetration depth of the field needs to be considered, it is called the Debye length (known as screening length) and can be written as [71, 72]:

$$L(D) = \sqrt{\frac{4\pi\epsilon kT}{e^2(n_0 + p_0)}} \tag{2.19}$$

where ϵ is the static dielectric constant, e is the electron charge, T is the temperature, k is the Boltzmann constant, and n_0 and p_0 are the concentrations of electrons and holes in the semiconductors, respectively. Here, the Debye length depends on the concentrations of electrons n_0 , holes p_0, dielectric constant ϵ and temperature. To understand effects of thin films' thickness on electrical properties more precisely, it is crucial to identify the scattering time (τ) because the two surfaces of the film come close to each other. It consists of both the surface and the bulk scattering. Total relaxation time for the two of them is given as [72]:

$$\frac{1}{\tau_f} = \frac{1}{\tau_s} + \frac{1}{\tau_0} \Rightarrow \tau_f = \frac{\tau_s \tau_0}{\tau_s + \tau_0} \tag{2.20}$$

$$\tau_s = \frac{t}{\upsilon_s} = \frac{t}{\lambda}\tau_0 \tag{2.21}$$

where λ is the mean free path of the electron, (τ_s) is the surface scattering time, (τ_0) is the bulk scattering time, (τ_f) is resultant relaxation time, and υ_s is the mean velocity By recalling the equation (2.11) from the previous section:

$$\mu_f = \frac{e}{m^*}\tau_f \tag{2.22}$$

$$\mu_f = \frac{e}{m^*}\left(\frac{\frac{t}{\lambda}\tau_0^2}{\frac{t}{\lambda}\tau_0 + \tau_0}\right) = \frac{e}{m^*}\tau_0\left(\frac{\gamma}{\gamma+1}\right) = \frac{\mu_0}{1+\frac{1}{\gamma}} \tag{2.23}$$

where $\gamma = \frac{t}{\lambda}$. The mean free path of the electron is defined by equation with relation to other film parameters (2.24):

$$\lambda = \mu_0 \frac{h}{e} \sqrt[3]{\frac{3n_0}{8\pi}} \tag{2.24}$$

where μ_0 is bulk mobility, and n_0 is the carrier concentration of thin films. From the equation (2.21), $\gamma = \frac{t}{\lambda}$, which means increasing carrier mobility as thickness increases. This can be explained by the surface carrier depletion layer, where the free carriers appear superfluous near both surfaces of the film, even if it occurs in the middle of the films due to more ionised impurity scattering near the surface [73].

General concept of conduction mechanisms of the insulator films:

Thin oxide dielectric films have been applied in bulk electronic devices, where they exhibit a semiconductor and insulating behaviour. In this work, a few of them were used for investigations. Namely, Silicon dioxides (SiO_2) and Titanium dioxides (TiO_2). These are well-known dielectric materials. Although they are dielectric, they show different electrical properties. In general, these dielectric thin films have a tiny number of free charge carriers at room temperature while having a broad forbidden band (>several eV). As a result, there is a small excitation from the valence to the conduction band at room temperature [74]. Such solid materials are known as insulators. However, the conduction mechanism of these insulators is complicated since it is defined by themselves and the contact properties of electrodes. So, the conduction of dielectrics can be classified into two major types [75]: electrode-limited conduction and bulk-limited conduction mechanisms. The former links to contact material properties with dielectrics. The latter is not related to contacts but to the properties of the dielectric itself. Here, a few conduction mechanisms can be taken into account. Firstly, excited electrons can be trapped by trapping centres due to Coulomb interaction in the conduction band, where the applied electric field can thermally activate these electrons. This is called Poole-Frenkel emission and is also known as a Schottky emission [76].

In the conduction and valence bands, the mobile electrons and holes dominate conduction because they move freely, which is known as ohmic conduction [77]. Furthermore, trapped electrons in the tunnelling barriers can hop from site to site in dielectric films, which is called Hopping conduction [78]. Moreover, some ions originating from the lattice defects can move freely due to the applied electric field that facilitates ionic conduction in the dielectric materials [79]. These are very crucial properties of dielectrics that need to be examined in-depth. This is just a short description of the conduction mechanism of insulators.

The general concepts, the fundamental physics of transparent conducting oxides, and the conduction mechanism of several insulators have been discussed. However, the importance of the amorphous phase and the existence of defects in these thin film networks plays a crucial role in studying the TCOs, which will be outlined in the following few sections.

2.2 Why Amorphous Transparent Conducting Oxides

Numerous transparent conducting oxide (TCO) semiconductor investigations have shown the great importance of amorphous transparent conducting oxides. Typically, crystalline semiconductors require a very high synthesis temperature in order to produce a high-quality crystalline structure, which results in high-cost optoelectronic devices [80]. An essential benefit of amorphous TCOs is their low synthesis temperature. This is a vital aspect of cost-effective manufacturing devices and achieving flexible electronic applications. Over the past 20 years, many amorphous TCOs have been synthesized at low temperatures ($<300\,^{\circ}$C) or room temperature (RT). Amorphous Zinc Oxides and other amorphous films have been grown at room temperature for different purposes [81–83].

A key task is to achieve a carrier mobility for transparent conducting oxide that is as high as possible. Crystalline and amorphous Si are widely used in solar cells due to their abundance and environmentally friendly nature. Although amorphous Si shows an excellent performance, it exhibits very low electron mobility ($\mu_e<1\,\mathrm{cm^2\,V^{-1}\,s^{-1}}$) for facilitating the requirements of specific optoelectronic applications [84, 85]. Apart from that, certain crystalline TCO materials have low carrier mobility.

Low resistivity, controllable carrier-concentration, surface flatness and low operation voltage properties are essential in Amorphous Oxide Semiconductor (AOS) based TFTs to upscale the characteristics of profitable technology [86, 87]. As a result, amorphous transparent conducting oxides have become viable candidates for replacing the traditional silicon and other oxides in electronic devices.

There are many amorphous transparent conducting oxide candidates that can be suggested by researchers, of which amorphous Indium gallium Zinc Oxide and Zinc Tin Oxide are two of the best performing and promising materials, respectively (amorphous $IGZO_4$ and $ZnSnO_y$ are simplified as “a-IGZO and a-ZTO” for short in the following). Both amorphous materials show high conductivity and high carrier mobility. This is because of amorphous oxides consist of heavy-metal cations with $(n-1)d^{10}ns^0(n \geq 4))$ electronic configurations. This presents high electron mobility because the conduction band is operated by spherically

symmetric heavy-metal cation with *ns* orbitals; these orbitals possess a large radius. As a result of this large radius, such *ns* orbitals result in a large degree of overlap between adjacent orbitals, and a substantial amount of band dispersion occurs. a-ZTO and a-IGZO consist of In, Ga, Zn, and Sn elements, which are heavy-metal cations [8, 88, 89]. Nowadays, both a-ZTO and a-IGZO have been studied extensively.

Amorphous materials are of potential interest for technologies. Nevertheless, defects in these AOS materials have a significant effect on the performance of contemporary semiconductor-based devices. Defects of AOSs are crucial and prominent characteristics of AOS thin films. Understanding these defects, which will be described in the next section,is essential.

2.3 The Role of Defects in Amorphous TCO Materials

The performance of semiconductor-based devices is defined by the nature of the defects in the semiconductor. These defects play a vital role in the opto-electronic devices' bias stability. The bias stability of transparent oxide TFTs is identified by no effects of light illumination/other things on it under a real operating conditions, where a shift in operating voltage through the trapping of electrons due to the defect centres. That is why understanding and investigating AOS defects is a complicated and important process. Amorphous semiconductor oxide defects have attracted far more attention as the electrical and optical properties of AOSs are linked to defects [25]. Here, I have focused on studying the two primary materials: amorphous-Indium Gallium Zinc oxide (a-IGZO) and Zinc Tin oxide (a-ZTO).

I will give a short history of ternary Zinc Tin Oxide (ZTO) and multi-component Indium Gallium Zinc Oxide (IGZO). The first oxide semiconductor-based thin-film transistors were invented in 2003; a large number of amorphous transparent conducting oxides were extensively studied for a semiconductor layer and employed in thin-films transistors as transparent electrodes. These AOS materials were binary oxides (ZnO and SnO_2), ternary Zinc Tin Oxide (ZTO), and multi-component Indium Gallium Zinc Oxide (IGZO). In 2004, thin-film transistors based on amorphous-Indium Gallium Zinc Oxide were fabricated by

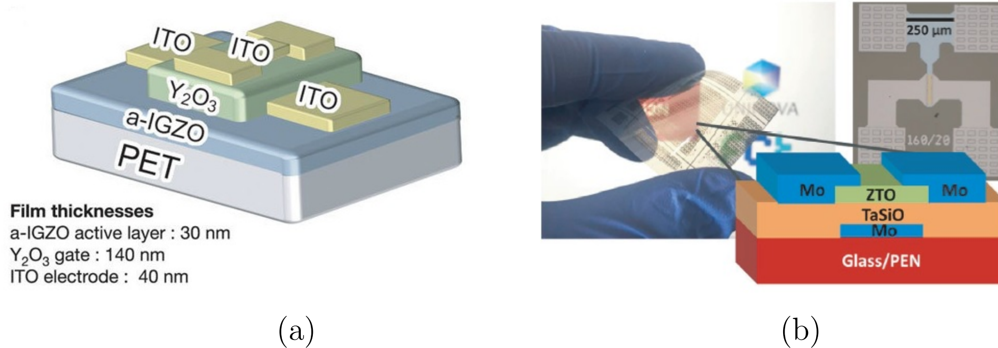

(a) (b)

Figure 2.3: TCOs based TFTs, where (a) - a diagram of IGZO based TTFs, (b) - a schematic of the flexible ZTO TFTs, also PET is the polyethylene terephthalate and PEN is the polyethylene naphthalene substrate. All figures are edited from cited works [7, 14].

Japanese scientists Nomura Kenji *et al.* This TFT achieved a higher hall mobility ($>10\,cm^2\,V^{-1}\,s^{-1}$) and lower absorption compared to IGZO. These top-gate, flexible, transparent thin-film transistors (TFTs) applied a-IGZO film as an active channel layer, as shown in Figure 2.3 (a). In this report, the a-IGZO film was synthesised at room temperature [7]. Beyond that, Japanese scientists H.Hosono and co-workers developed a high mobility a-IGZO, and in 2006, Samsung Ltd used a-IGZO based TFT LCD displays in the iPad 3 [90]. Furthermore, a dramatic increase in research into the a-IGZO has taken place recently, and IGZO has become one of the best performers among the amorphous TCOs. In recent decades, due to a-IGZO being extensively studied, the resistivity of a-IGZO has been achieved around 10^{-4} ohm-cm while exhibiting lower than 10% absorption in the visible range of the light spectrum concurrently [8, 54, 91–94].

The composition of the a-IGZO plays a prominent role in the material's electrical and optical properties, so that some elements play the dominant role and others play a secondary role in a-IGZO properties. Based on many research reports, in quaternary compound a-IGZO, the resistivity of thin films is a function of the variation of the atomic ratio of In:Ga:Zn elements. Namely, increasing the In content enhances the carrier concentration and Hall mobility due to the metal-oxygen bonds in the amorphous structure in the majority of the conduction band minimum [19, 87]. Furthermore, Zn possesses a smaller s-orbital than In, which leads to an increase in the possibility of direct overlap of s-orbital of neigh-

bouring In, and it enhances carrier mobility. Also, the number of free carriers can be enhanced by increasing the zinc content in the films, but it also creates more scattering centres due to changes in oxygen defect states. This is due to Zn and O having strong bonding arrangements. It is a fact that increasing carrier concentration increases conductivity [30, 95]. Lower content of Ga in the films results in increased oxygen vacancy concentration with an increase in electron concentrations. Ga element dominates as a carrier suppressor due to a high oxide bond strength compared to the other elements, where Ga effectively mediates the oxygen vacancy density within the amorphous structure [30, 96].

As stated in the previous paragraph, amorphous Zinc Tin Oxide (a-ZTO) is a solid amorphous state ternary compound compared with a-IGZO. a-IGZO has one more Ga element than a-ZTO. a-ZTO is a wide bandgap, n-type semiconductor without high-cost elements (In and Ga) [20, 97, 98]. It was developed by Chiang and et al. in 2004 and applied in thin-film transistors. Research activities have shown that a-ZTO has achieved remarkable properties in the past two decades. Low resistivity was found to be around 10^{-3} ohm-cm, while it exhibits lower than 20% absorption in the visible range of the light spectrum for the films grown by both sputtering and PLD methods [23, 99, 100]. a-ZTO has been synthesised at both room and high (<350 °C) temperatures with a high carrier mobility ($>15\,cm^2\,V^{-1}\,s^{-1}$). Even at a deposition temperature of <350 °C, a-ZTO films still present an amorphous phase [99, 101]. Like a-IGZO, the properties of a-ZTO are also highly correlated to chemical composition. There are two main Zn:Sn elements ratio governing the electrical and optical properties of the materials [102, 103]. To understand the exact role of the content of the elements, I will discuss several studies. A high Sn concentration was observed in many of the a-ZTO films that showed the highest conductivity. Here, Sn is the main free carrier generator [103]. The carrier mobility of films is strongly dependent on Zinc content in the samples, whose mobility can vary by Zn content. This implies that Zn is a main carrier mobility driver [11, 16, 104, 105]. It is worth mentioning that the Sn/[Zn+Sn] ratios varied from 0.28 to 0.77 in solution-processed Zinc Tin Oxide (ZTO) films that showed an amorphous phase between 0.28 and 0.48 Zn: Sn ratios. Furthermore, ZTO's carrier density increases with increasing Sn concentration [18]. The solution-processed method implies that a

precursor solution was obtained via mixing zinc acetate (Zn(CH_3COO) and tin (II) chloride dihydrate ($SnCl_2$)2H_2O in 2-methoxy ethanol solvent and solutions were spin-coated on a substrate. Finally, the ZTO precursor was dried at 150 °C temperature while obtaining ZTO films. Moreover, ZTO films within this ratio region were amorphous films with good electrical properties when grown using sputtering and spray techniques. For reactive sputtering 0.32 and nonreactive sputtering 0.27 and for spray samples 0.38 [104, 106].

These studies have revealed that both a-IGZO and a-ZTO are suitable for many electronic devices. It can be seen in Figure 2.3 the film is employed as an active channel of the TFTs for optoelectronic devices [107]. While a-ZTO-based TFTs as shown in Figure 2.3 (b), which showed high performance with a high Field-effect mobility of 20∼50 $cm^2 V^{-1} s^{-1}$, and is much better than other crystalline oxides [8]. Again, amorphous-ZTO has performed well in a thin-film TFT fabricated by Cristina Fernandes *et al*, which is depicted in Figure 2.3 (b) [14].

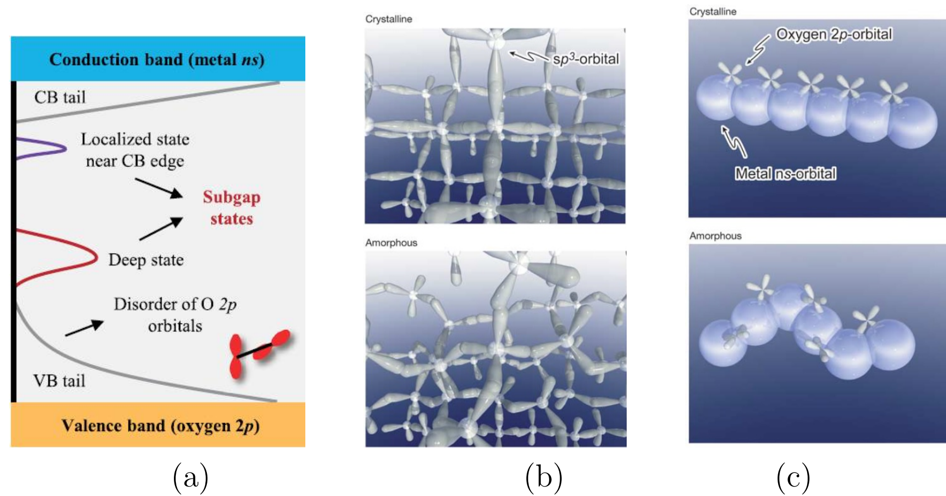

(a) (b) (c)

Figure 2.4: Density of states and bonding structures of oxide semiconductors, where (a) - an illustration of the density of states of amorphous oxide semiconductors, where the valence and conduction band tails, deep states in the band gap, and localised states near the CB edge are shown, (b) - covalent silicon, (c) - ionic semiconductors. Figures edited from cited works [107, 108].

In the following paragraphs, I will discuss the nature of free carriers for the various categories of elements in the films. Some defects are still being exten-

sively studied because they are complicated and difficult to understand precisely [109, 110]. The fundamental properties of these materials can be recalled to understand the nature of their defects, such as bandgap and density of states of materials. Certain properties of AOS materials are strongly dependent on their band gaps, which is the primary character of the materials, where the highest rate of defects has existed. In general, amorphous material's density of states consists of delocalised (the conduction referred to as CB, and valence bands referred to as VB) and localised electron states [111]. The delocalised states of amorphous networks are similar to the extended state of a crystalline solid. The disorder of the amorphous network causes the latter. Both VB and CB edges are separated by mobility edges, called the localised-delocalised transition. Furthermore, a disordered distribution of atoms creates sub-gap defect states between the conduction and valence bands induced by under-coordinated atoms or atomic vacancies. This can be found at near CB band edges and deeper states as shown in Figure (2.4) (a) [108, 112, 113]. It can be seen from Figure (2.4) (a) that sub-gap defect states originated from localised defect states near the CB edge and the deep defect states over the valence band. This can be articulated by the orientation of the materials' orbitals of metals and oxygen atoms. Due to the structural disorder, the spatially spread spherical *ns* metal orbitals are formed mainly by the CB with a small band tail. A large VB tail above the VB exists, which is governed by the sensitivity of direction-dependent oxygen 2P orbital with a disorder of the amorphous structures [107, 108, 114–116].

There is a direct correlation between these orbitals, achieving the high conductivity and mobility properties of amorphous semiconductors. This implies that understanding the nature of the bonding between cations and anions can be rigorously studied. The most striking future of the study is to invoke the covalent and ionic bonding in the materials to compare them with each other. These common semiconductors employ a covalent (silicon) and ionic (oxide) composition of the CB minimum. CBM is formed mainly of strongly directly and anisotropic sp3 orbitals (Figure 2.4 (b)) in crystalline silicon when it is converted into amorphous phase silicon, where the structure of crystalline silicon is acquired by changing the bond angles. This manifests inside the bandgap with dense, localized states with energy levels. However, in oxide semiconductors, there is a completely different

circumstance observed, where the CBM of oxide semiconductors is governed by the large spherical isotropic *ns* metallic cation orbitals, and these orbitals can overlap due to their large radius as shown in Figure 2.4 (c). These properties cannot be the best reason for understanding fully the electrical conductivity, and carrier mobility of materials [7, 40]. However, the particularly complex behaviours of this bonding can form defects in a material. Bonding related to these defect complexes was discovered in a-IGZO and a-ZTO thin films. A small, deep state lower part of the CB minimum, associated with the under-coordinated cations in a-IGZO and a-ZTO films, has been investigated. This is called a shallow trap state [107]. On the other hand, anions deficiency defects over the VB maximum in a-IGZO and a-ZTO were discovered, and these defects' role in the materials' transport properties was formed as deep trap states. It is generally accepted that analysis of the origin of defect states in both amorphous semiconductors requires an in-depth study, although a-IGZO and a-ZTO have been widely studied. a-IGZO is a multi-component semiconductor; its electrical and optical properties can be controlled by varying the oxygen partial pressure during the deposition condition. These oxygen species generate the density states of the electrons in a-IGZO that can also result in certain defects [109, 117, 118].

There is a great variety of approaches to explain the behaviour of these free carrier sources of defects that include the undercoordinated cations, interstitial oxygen and the trapping of electrons by oxygen vacancies and, undercoordinated oxygen [119, 120]. The charge carrier density of a-IGZO and a-ZTO is defined by these possible mechanisms given in the above discussion.

One should start by understanding the undercoordinated cations. One computational approach (Density Functional Theory) study on the atomic structure of a-IGZO under O-poor conditions showed that the undercoordinated cations are classified into two groups, which are called undercoordinated single cations (USC) as shown in Figure 2.5 (a) and undercoordinated cation pairs (UCP) as also shown in Figure 2.5 (d) [108, 121]. In order to show the USC defects in a-IGZO as shown in Figure (2.5) (b), the bonding distribution of compound material must be discussed in the following paragraphs. The main carrier generator in the Indium-based disordered oxides has a prototypical bonding distribution of metals and oxygen vacancies, which consists of a certain configuration of distances, bond

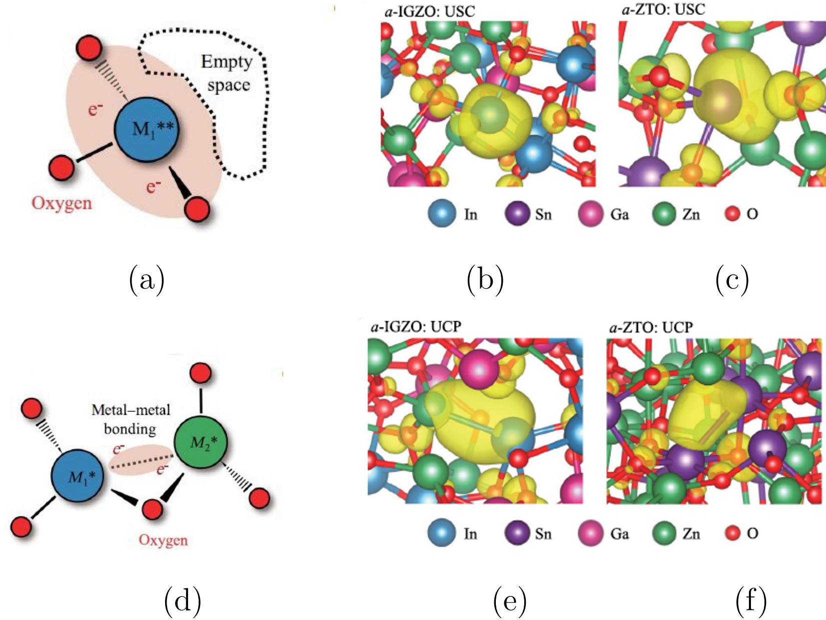

Figure 2.5: The atomic structures of USC and UCP defects, where (a) and (d) - simplistic diagram for the atomic structures of USC and UCP defects, (b) and (e) - USC and UCP defects in a-IGZO thin films, (c) and (f) - USC and UCP defects in a-ZTO films. Figures reproduced from cited work [108].

angles, and nearest-neighbour (NN) coordination numbers. As shown in Figure 2.5 (a), the metal atom is not bonded with other adjoining atoms, but the ionic bonds are boned between metal and the surrounding O atoms as shown in Figure 2.5 (b). This is called a dangling cation bond, which is a source of the charge density in these defect-induced states. The USC defects act as electron trap centres because of their low coordination with strong, attractive potential. On the other hand, UCP defects in a-IGZO as shown in Figure 2.5 (e), implies that there is a void between two metal cations due to the removed oxygen atom from the ionic bonding. This is called an oxygen deficiency in a material that causes two metal atoms to be close to each other and form a defect pair, for instance, In-Zn, or In-Ga [108–110, 122, 123]. Under-coordinated In atoms are a source of carrier concentration due to electron crowding around them; even one In atom is sufficient to cause crowded electrons [123]. On the other hand, in a-ZTO USC and UCP defects are defined by the metal ions, which show a desirable electronic property. Furthermore, it is clear that USC defects are formed by undercoordi-

nated tin atoms, as shown in Figure 2.5 (c), and two undercoordinated cations create the UCP defects, such as Sn^*-Sn^* and Zn^*-Sn^* as shown in Figure 2.5 (f). All these defects in a-IGZO and a-ZTO have a strong relationship with the coordination numbers of systems due to the amorphous phase being a complex system with disorder [16, 108].

The second-most common sources of defects that have been investigated are oxygen vacancy (V_O) defects that are related to the structure of oxygen vacancy in these amorphous networks. These defects in a-IGZO influence the atomic and electronic properties of amorphous phases. Data obtained from the first-principles density functional calculation studies indicated that V_O defects strongly depend on local environments, such as ratios of the elements in the a-IGZO. In this study, more Ga content created more O-deficiency defects in the films due to G and metal with high formation energies, where interestingly, V_O defects have been found in both shallow donors and deep defect levels because of the formation energy differences [124, 125]. Besides, this is in agreement with the experimental data that showed increasing the In content reduced these types of defect levels in a-IGZO material while resulting in enhancing the carrier concentration and mobility simultaneously [126, 127]. Here, a consideration of the formation energy of the V_O defects indicated that they were formed by Ga-Ga, Ga-M, and M-M bonds. There is a trend that sees the formation energy increase along with the increasing number of bonds with Ga atoms in order to form metal and metal and oxygen chemical bonds. The average formation energy varied from 4.06 eV to 4.87 eV for Ga- Ga to 3.88 eV to 4.38 eV for M-M bonds by the results of GGA + U and hybrid density functional calculations, respectively [124]. Another concept of oxygen-related defects that research has pointed to is that the subgap states have been categorised into two parts within the upper and lower half of the band gaps. The former is generated by oxygen vacancies (under-coordinated O atoms). The majority of the metal atoms cause the latter without bonding oxygen to each other. The formation energies for these defects range from 3.8 eV to 5 eV [114] These average formation energies are also found between 3.3 eV and 4.7 eV for defects originating from oxygen vacancies [10]. In addition, these defects can be altered by incorporating hydrogen and increasing the conductivity of the films at the same time, where hydrogen atoms ideally bond with the under-coordinated O

atoms that compensate for the deficit in electron density [128]. The compositional study found that varying Sn content altered the O_v states in the films [18]. It is worth mentioning that the interstitial oxygen defects (O_i) in a-IGZO can be explained by the fact that interstitial oxygen captures electrons because of the O- O dimer broken bond that accommodates O_i charge trap properties [129].

On the other hand, let us consider the DFT study in the local density approximation (LDA) with a self-interaction-corrected (SIC) on a-ZTO band structures (conduction and valence) [115]. This study showed that undercoordinated oxygen atoms are located over the valence band (deep subgap states) and impact the properties of a-ZTO. Here, a-ZTO's conduction band (CB) consists of metal s orbitals, and the valence band (VB) mainly originated from the oxygen 2 p orbitals and they have a direction-dependent property because the structural disorder in amorphous phase. In these local bondings, structures can be altered by the high electronegativity of oxygen. This implies that the average coordination numbers in the amorphous networks have changed depending on the tendency of tetrahedral zinc and octahedral tin coordination, where 4–5 and 5–6 neighbouring oxygen atoms are required for zinc and tin, respectively. However, the miscoordinated tin-oxygen atoms can be created at the deep part of the conduction band by differences between coordination of Oxygen and Tin. This means that in this local area, undercoordinated oxygen atoms are present due to oxygen having tetrahedral or lower cation coordination. This was also confirmed by experimental work, including a hydrogen atom joining this oxygen atom, where they create an O- H bond. While the lack of oxygen atoms at the deep levels below the CB forms undercoordinated tin atoms, the tin coordination can be increased by annealing in an oxygen-rich atmosphere [11, 128, 130]. Oxygen also plays a key role in crystalline Zn_2SnO_4 that exhibits a deep-level defect in the bandgap [30]. To conclude, the defect-related carrier generation centres (oxygen vacancies) have a crucial influence on the conductivity of a-ZTO and also dictate the carrier trapping in the films. Considerable further research is required to fully understand this.

To explore how metal and oxygen are connected to defects, XPS studying how the strong elements bonded with each other has been performed. XPS is a versatile characterisation technique for analysing the surface of the materials

Elements	Electronegativity
In	1.78
Ga	1.81
Zn	1.65
Sn	1.96
O	3.44
Si	1.9
Ti	1.48

Table 2.4: Comparison of electronegativity of elements. Data taken from cited works [135, 136].

but is limited by the penetration depth of X-Ray [131]. Here, XPS informs the binding energy values that can be used for identifying the local chemical bonding arrangements. Furthermore, XPS measurement on a-IGZO showed that the representative XPS spectra of IGZO peaks were observed in the XPS survey spectra. The main peaks are usually found In 3d, Zn 2p, Ga 2p, and O1s and these peaks have different binding energies, such as the peak at 444.4 eV for In 3d5/2 , 1116.6 eV for the Ga 2p3/2, and 1020.8 eV for the Zn 2p3/2 peak indicating these metal atoms are bonded with oxygen [132]. As I mentioned above, oxygen 1s peaks are the most fitted and analysed peaks. Through the binding energies of O1 s peak, the surrounding element can be identified. Furthermore, binding energy also presents elements charge states, such as the position of O1s peaks of the a-IGZO at 530.5 eV and 531.9 eV for metal-oxygen and local oxygen-deficiency centre respectively [133]. This means that XPS data provides information on the quantitative and qualitative chemical properties of materials, and XPS can examine the chemical and electronic structures of the a-ZTO like an a-IGZO. Moreover, the observed binding energies for a-ZTO were 1021.49 eV and 486.22 eV for Zn 2p3/2 and Sn 3d5/2 individually. Compared to a-IGZO XPS peaks, in a-ZTO only Sn related peaks are different to a-IGZO. To conclude, binding energies have been found by XPS, and these binding energies can be used to characterise the valence state, and the bonds of the elements, such as 486.22 eV for Zn^{2+} [134]. Here, one more thing for consideration is that all the elements in these two compound materials have different electronegativity values, as shown in Table 2.4 [135]. For In, this influences bonding arrangements and attracts more electrons from other

elements that could cause certain undercoordinated atoms. In previous work, it was found that undercoordinated In has a strong electron trap behaviour [123]. More detailed XPS data analysis can be taken into account for interpreting the obtained results in the following chapters.

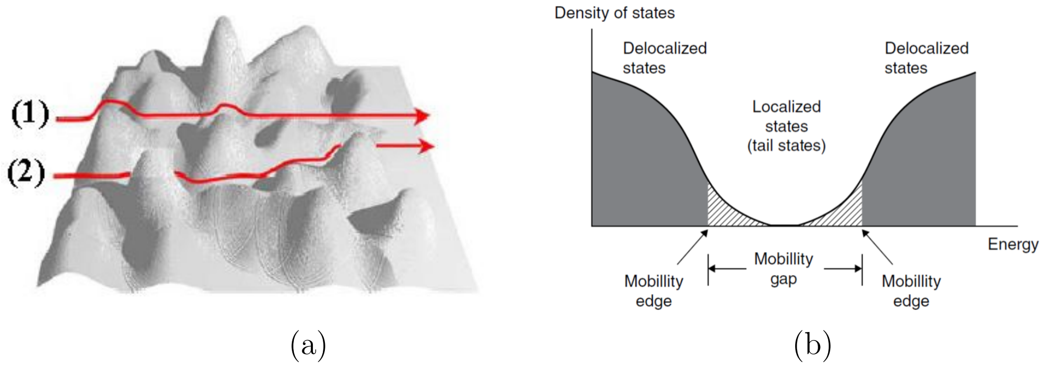

(a) (b)

Figure 2.6: Conduction path and bandgap of amorphous materials, where (a) - a diagram of percolation conduction over the distributed potential barriers with various energy heights, (1) - Electron path for high temperature with shorter travelling distance over the barriers, (2) - Electron path for low temperature with longer distance through the lower barriers. (b) - bandgap of amorphous materials. Figures edited from cited works [137, 138].

The above discussions have linked the carrier transport property of the amorphous materials, namely both a-IGZO and a-ZTO. It is a subject that has been extensively studied experimentally and theoretically for a few decades. The charge transport properties are the most remarkable characteristic of disordered networks compared to perfect crystalline networks; that is why they need to be studied to be precisely understood. As a result of complicated transport properties, the carrier transport mechanism is not well understood and is being extensively investigated. A few experimental and theoretical approaches have been suggested few carrier transport mechanisms for amorphous networks [139]. It is also found that in a-IGZO, above room temperature carrier transport mechanisms are based on the Arrhenius type thermally activated behaviour $\sigma(T) = \sigma_0 exp(\frac{-E_\sigma}{K_B T})$. However, another type of electron transport is involved below room temperature (low temperature) due to structural disorder [137]. Here, the free electron density must be taken into account when the carrier transport is examined at low temperatures, where the free carriers travel with variations in electron mobility. a-IGZO

with low carrier concentration ($<10^{19}\,cm^{-3}$) does not follow the Arrhenius law in the low-temperature region. Surprisingly, a reduction in carrier mobility was observed experimentally and interpreted by the percolation model. The concept of this model is that there is a potential fluctuation above the mobility edge as shown in Figure 2.6 (b), which is an amorphous semiconductor (as Adler and co-workers discovered) [140], where deviation in the distribution of the height of the potential barrier affects the conductance for electrons over these potential barriers. Figure 2.6 (a) shows electron paths (1) and highlights that at a low temperature, they travel shorter distances. The electrons take longer distances due to the low-barrier wide paths as shown in Figure 2.6 (a) electron path (2). The travel distances of the electron are defined by the distribution of the potential barrier height over the mobility edge, and the potential barrier height originates in levels of structural disorder. Here, mobility is limited by the Boltzman transmission factor [137]. This is not the only charge transport model for characterising the charge transport properties in AOS, but also the Variable Range Hopping (VRH) method has been applied to describe electron transport in AOS. The main message of this model is that at a low temperature, the Arrhenius equation mentioned above follows logσ versus $T^{\frac{-1}{4}}$ law, and VRH can explain this. Here, free electrons hop within the sites.

In summary, the defects of both a-IGZO and a-ZTO are altered or passivated by the post-deposition treatment method as can be observed with many compelling techniques. However, the discussions regarding the amorphous materials' defects are insufficient to finalise a conclusion which requires more experimental work to conclude them, so in the following few chapters, I will provide an in-depth discussion of annealing studies to alter these defects. I will outline the influence of defect alteration on the electrical properties of materials.

2.4 Properties of Ultra-Thin Films

Low-dimensional material properties have attracted considerable attention from scientists because of need to decrease the size of materials in optoelectronic products. Investigations have been carried out on the physical properties of ultra-thin film materials because characterising the properties of low-dimensional materials is crucial for showing their behaviour in the applications [73, 141, 142].

This paragraph considers the properties of ultra-thin films of a-IGZO, a-ZTO, SiO_2 and TiO_2. Starting with a-IGZO, decreasing the thickness of this material affects both optical and electrical properties. Carrier concentration, electron mobility, and transparency depend on the thickness of the a-IGZO. These results of bulk and surface trap states are strongly dependent on the thickness of a-IGZO [73]. In other words, changing the thickness of materials with alteration in the distribution of the density of states per unit volume of the films results in changing the electronic structures of materials. The properties of the films are defined via the electronic structures of the materials. Also, increasing thickness leads to decreasing the interaction between free electrons, and such interactions also affect the electrical properties of films because when the electrons come too close, they can interact with each other in the form of a Coulomb interaction. Thick films possess a low sheet resistance and high electron mobility due to a small number of ionised impurity centres. Thickness affects the a-IGZO film's bandgap, and electron concentration results in a change in the dielectric function of a-IGZO [143]. This can be understood in terms of an increase in the concentration of free electrons, increasing the effect of Coulomb interactions. Here, the modification of electronic states in the films occurs, leading to a bandgap change. Varying the film thickness also impacts the materials' defects (trap) densities [144, 145]. Variation in defect levels has a vast effect on the surface of the materials, where there is a strong relationship between the thickness and screening length in the case of a-IGZO. As a result, thinner a-IGZO films are very sensitive to surface adsorption from the gas phase [146]. All this implies that working with ultra-thin a-IGZO films is a challenging and complicated process that requires further dedicated investigation.

Another well-known AOS is a-ZTO. This material demonstrates a bandgap dependence on its composition. Composition studied on a-ZTO showed that Sn rich films have a high absorption for the visible range of the spectrum. However, these films have good electrical properties for making transparent electrodes. This can be explained by Sn content governing the ZTO valence band edge of a-ZTO, creating different levels of oxygen vacancies-related defects near the valence band maximum. Zn-rich films showed high transmittance due to their stable bonding arrangement with oxygen [147]. In solution-processed ultra-thin a-ZTO films,

the oxygen vacancies are controlled by varying the Sn content as well [148]. In addition, samples with a higher Sn content show a high density of charge carrier compared to Zn rich films due to Sn donating a large number of electrons. As a result, a-ZTO films with a high ratio of Sn:Zn showed a low optical transmission. This depends on what experimental methods have been used for synthesising the materials due to the different growth kinetics influencing bandgap defect states [104, 149]. In ALD-grown a-ZTO films, the bandgap varied from 3.02 eV to 2.95 eV for 21% and 34% Sn in films respectively. Generally, the overall trends in the bandgaps of a-ZTO films are located approximately between the ZnO and SnO_2 bandgap values, regardless of deposition methods, with a certain number of scatters. Furthermore, the shifts in the defect states within the bandgap can be controlled by the deposition conditions and might be the purpose of reducing the thickness of the films. This also impacts the properties of the materials [150].

The properties of well-established a-SiO_2 and a-TiO_2 are defined by their thickness. Reducing the thickness changes the electronic properties, which are linked to their physical and electrical properties. Both materials have high resistivity, a large bandgap, excellent dielectric properties, and a high melting point [151, 152]. A variation in the bonding arrangements for thin SiO_2 is caused by a reduction in thickness of the a-SiO_2. Thickness reduction results in formulating more suboxides near the surface of the thin films [153, 154]. Also, the film thickness limits the phonon mean free paths, which prevent the thermal conductivity because of incoherent boundary scattering phonons, ballistically traversing within the films [155]. The thickness of the SiO_2 can alter the materials' electronic structure, where the defects' position varies with distance from the interface and surface of films. In other words, the properties of materials are strongly affected by the part of the defect level within the band gap [156]. The presence of suboxides is also connected with the thickness of the SiO_2, where it plays a key role in the stoichiometry map of the material [111]. The density of electron traps depends on the thickness of the SiO_2 [154]. Studies have discovered that the thickness of the SiO_2 also determines how the current passes through the films. In general, Fowler-Nordheim (FN) tunnelling means the energy of the incident electrons is higher than the potential barrier in the films; the electron wave function can travel via this potential barrier when the film's thickness is lower than

10 nm [157]. In other words, Fowler-Nordheim (FN) tunnelling dominates in these films with thicknesses between 5 nm and 3.5 nm. Furthermore, direct tunnelling can be involved in films with thicknesses below 3 nm [79]. A massive amount of work has been done to understand the fundamentals of thin silicon dioxide. However, in this thesis, I have just referenced a few reports due to there being many things that can be discussed regarding silicon dioxide.

A well-known insulator I used in this study is TiO_2 films with remarkable properties. This material has various structures: rutile, anatase, brookite and srilankite [158]. It is a comprehensive bandgap material that consists of valence and conduction band tail states [159]. Moreover, a higher oxygen content affects films with fewer oxygen defects due to the energy bandgap. A number of studies on TiO_2 have found that the increased oxygen ratio results in an increase in the energy bandgap values from 3.62 eV to 3.77 eV [160, 161]. Another approach to modifying the bandgap is doping with metallic and non-metallic elements found in this publication [162]. In this material, optical and electrical properties can be altered by defects densities that are related to Ti^{+3} and oxygen vacancies [160]. The reflection and absorption increased with the increasing thickness of the films due to homogeneity changes in the film structure caused by various types of structural faults [163].

In general, thin-film synthesis and characterisation techniques are important to developing TCO materials, and these techniques define the properties of oxide films, so I will outline the importance and functions of those techniques in the next chapter.

3

Thin-Film Synthesis and Characterisation Techniques

3.1 Thin Film Fabrication

The current investigations involved growing and characterising amorphous materials, using many versatile techniques. There are many synthesis techniques that can be used to fabricate amorphous materials. The properties of the produced materials depend on the methods of preparation. In general, we classify thin film deposition techniques into the following methods: physical vapour deposition, evaporation, magnetron sputtering, and spray pyrolysis. Compared to the other thin-film growth techniques mentioned above, magnetron sputtering is a versatile technique producing superior films and the scalability to offer large area coating advantages [164, 165]. In the following discussion, the basic principles of magnetron sputtering will have to be considered.

3.1.1 Magnetron Sputtering

Magnetron sputtering is a process in which the nanoparticles of the materials are emitted from a target within the magnetic field through bombardment by energy particles produced by plasma, mostly inert gas ions. Then, these atoms

from the target are deposited on a substrate. In most magnetron sputtering processes, argon is employed as an energetic bombardment gas due to its low-cost advantage, and chemical inertness [164, 166]. Magnetron sputtering as a deposition technique has seen a significant increase in industrial and laboratory use in recent years. This is due to its ability to produce high-quality films with high throughput, making it competitive with other industrial techniques. As a result, magnetron sputtering now sees significant use in the deposition of large-area surface coatings for various functional applications, such as electronic displays and anti-corrosive or physically protective coatings.

In the sputtering targets, one pole of the magnetic field is in the centre, and the second pole is near the edge of the targets. This is designed to enhance the circular trajectory of emitted secondary electrons from the target surface and improve the chamber's plasma density under the ultimate pressure. The employed magnetic array can be divided into two categories depending on the application. These forms can be called balanced and unbalanced. If the same strength of field

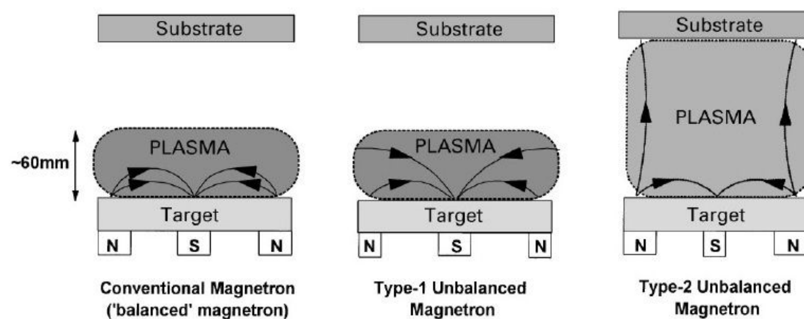

Figure 3.1: A schematic side-view of the Magnetron sputtering system with different magnetic array arrangements. This figure is edited from this work [164].

lines of a magnet are used, and all magnet lines are delivered to the centre of the magnet, this traps the plasma electrons and prevents the plasma electrons from escaping easily from the magnetic trap. This means that the plasma is confined in front of the target by a magnetic arrangement that is known as balanced magnetron sputtering as shown in Figure 3.1. On the other hand, when only weak centre magnets are applied, all the magnetic field lines do not arrive in the centre of the magnet, and some are forwarded to the surface of the substrate.

As a result, some of the electrons from plasma electrons arrive at the substrate, which generates a plasma condition for the whole space between the target and substrate. This can be called an unbalanced magnetron sputtering, and is shown in Figure 3.1. Magnetron sputtering is a highly complex process due to the design and control of the deposition conditions during the fabrication of thin films. Here, a few key parameters define properties of sputtered materials: the sputtering vacuum chamber, base pressure, substrate temperature, target powers, bombardment, and other reactive gas flows. The pumping speed, the conductance of the pumps, and the volume of the chamber play a crucial role in achieving the required pressure for a sputtering chamber [167]. The base pressure is an essential parameter for depositing thin films as it maintains the collision process between the bombarding particles and the targets to form thin films. Another critical parameter for magnetron sputtering is the substrate temperature, which is extremely important for controlling film formation and its final stoichiometry. The substrate temperature is also an essential factor in defining the properties of thin films. Moreover, it is not only the above-mentioned parameters that affect the film properties. The deposition rate of sputtering is also defined by the target power, where deposition rate increases with target power. Also, the electrical properties of materials are affected by the sputtering target power allied to the target [168]. Sputtering gas composition influences some properties of the films; an example of that is a reactive gas (oxygen) controlling the film structures and deposition rate [169]. This will be discussed in the results chapter with more details that I have obtained. All this implies that deposition parameters have a strong influence on the properties of the films of the materials. All the above aspects discussed require careful investigation. These are complicated things, all affecting the film properties, and I am going to talk about some of them in this work.

Magnetron sputtering can be powered with a DC or RF power source. RF sputtering is employed with insulator targets as the rapid switching of the bias direction allows for the easy removal of built-up charges on the target. If DC sputtering is attempted with an insulating target, then an accumulation of positive ions on the surface of the target prevents the sputtering process. Using an in-situ reactive gas allows for the alteration of the state of the material sputtered

from the target during the deposition, which is called reactive sputtering. In the next section, the magnetron sputtering used in this work will be addressed.

3.1.2 Magnetron Sputtering is Equipped with a Static Sample Stage

The thin-film synthesis in this work was achieved by magnetron sputtering. The films were deposited via DC or RF magnetron co-sputtering from two different targets. One target is vertically placed on the top of the chamber, which is

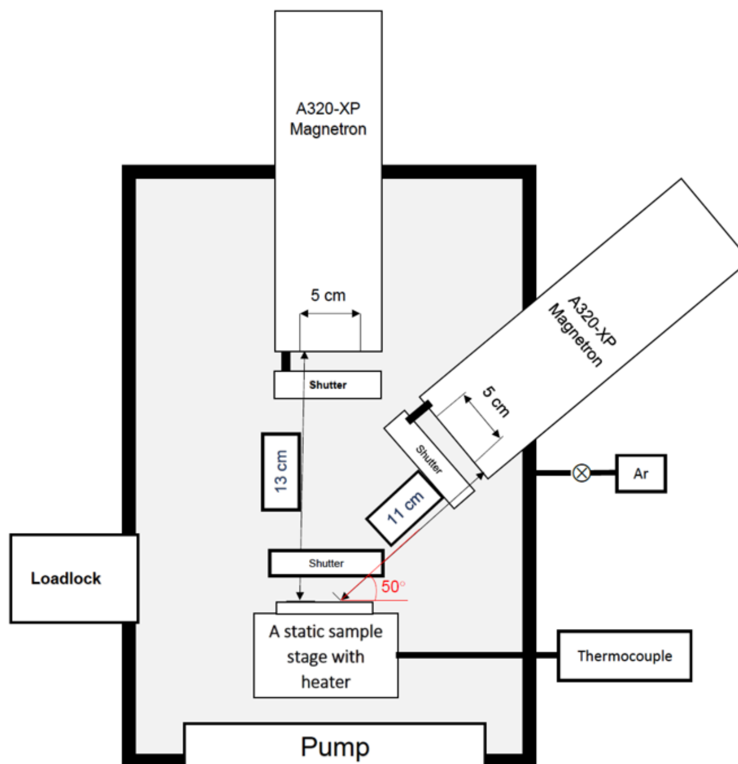

Figure 3.2: Internal schematic diagram of magnetron sputtering system with a static sample stage in this work. This schematic reproduced from the cited work [170].

far from the substrate (13cm), while the second target is attached to one of the adjacent flanges at a 50° angle to the horizontal substrate, as shown in Figure 3.2. The distance between the second target and the horizontal substrate centre is 11cm. Each sputtering target is equipped with separate shutters to isolate the

target from the magnetron chamber as a protector. Likewise, another shutter is applied between the sample stage and the sputtering chamber. These shutters facilitate the growth of multilayer thin films and keep the substrate clean before starting the deposition process (during the plasma stabilisation). The sample stage is horizontally attached to the chamber, which is made up of a Tectra Borolectric heater (boron nitride ceramic and pyrolytic graphite conductor) for the growth of thin films at up to around 700 °C. A thermocouple is attached to the surface of the Tectra Borolectric heater to control the temperature. Both, the top surfaces of the heater and thermocouple are housed in a thin tantalum foil to reduce harm. A schematic illustration of Magnetron sputtering is given in Figure 3.2.

To maintain the magnetron chamber in the appropriate clean sputtering condition, the pressure in the chamber was kept at 5×10^{-3}mbar using the rotary roughing pump and turbopump. RF sputtering power was obtained using an Alternating Current (AC) with 13.52 MHz radio-frequency.

3.1.3 Magnetron Sputtering is Equipped with a Rotating Sample Stage

The main goal of switching from a static sample stage to a rotating stage is to eliminate the resistivity gradient across the sample because one of the targets is not located vertically. An XRR comparison between the two stages shows that the intensity of the oscillations drops faster in a static sample stage due to the thickness gradient as shown in Figure 3.3. This also affects the electrical properties of the films, which is seen in the distribution of resistivity across the films. Figure 3.4 (a) shows Magnetron sputtering with a rotational sample stage, which upgraded a previous magnetron sputtering (see 3.2); the only thing hanged was the pump's position. It was repositioned from the bottom of the chamber to one of the adjacent flanges (used to attach an old sample stage) to angle a line in the sputtering chamber.

A rotational manipulator as shown in Figure 3.4 (b) is fixed in a vertical position at the bottom of the sputtering chamber. Other sources, including targets, gas lines, and a load-lock chamber, are kept the same as the sputtering chamber with a static sample stage. I will discuss the rotational sample stage

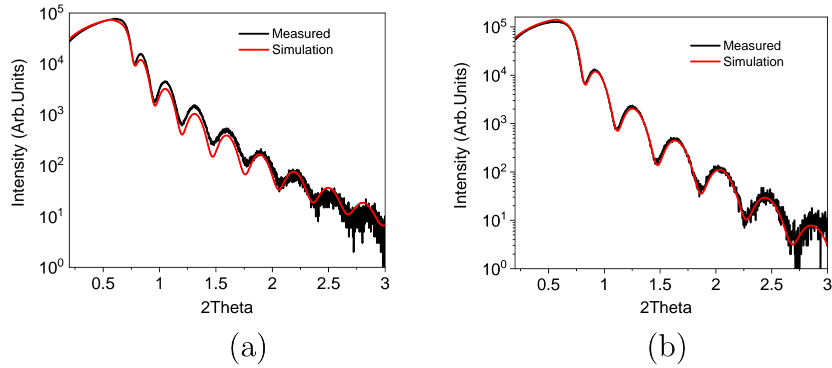

(a) (b)

Figure 3.3: A comparison of XRR data a-ZTO films grown by two different sample stages, where (a) - XRR data of a-ZTO by a static sample stage, (b) - XRR data of a-ZTO by a rotating sample stage.

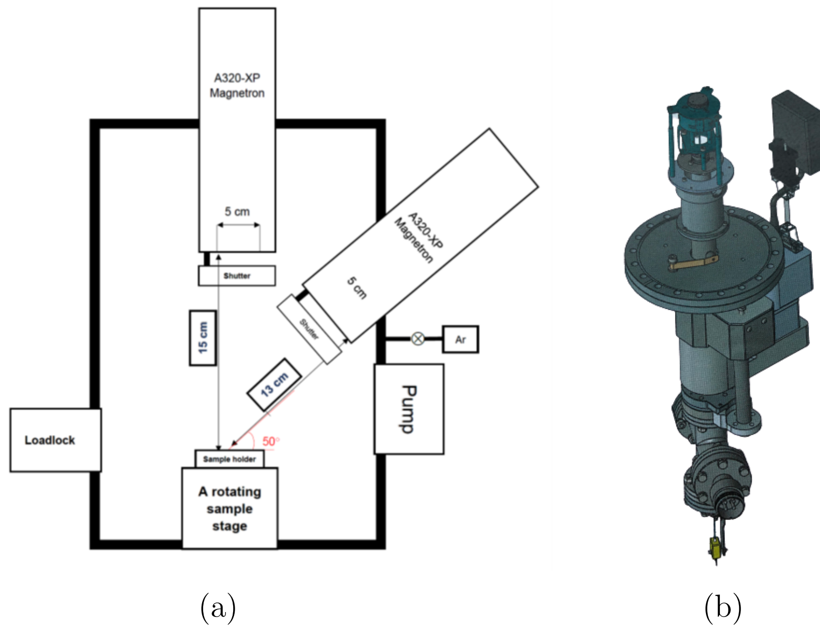

(a) (b)

Figure 3.4: A diagram of Magnetron sputtering with a rotating sample stage and rotating sample stage used in this work, where (a) - a diagram of Magnetron sputtering, (b) - sample stage equipped with a rotation function. All figures are edited from cited works [170, 171].

in detail. This stage consists of two main parts: a part for heating substrates and a part for providing the rotation, as shown in Figure 3.4 (b). The former is constructed with a heating element, and the Inconel cradle is generally called a sample cradle assembly. The Inconel cradle is designed for mounting the Moly-

block sample holders, and a Heating element is made from a solid Silicon Carbide. A thermocouple is located 1.8 mm away from the heater. The heater's maximum temperature is up to 900 °C. The latter is a Magilift part with a magnetically coupled rotary tube to transmit rotation and assists an axial motion under vacuum to the sample cradle assembly. The drive thimble supplied the rotation that connected a pitch HTD timing belt with a twenty-tooth pulley gearbox. The gearbox is equipped with a brushless DC motor. The motor speed is governed by a handheld box with a direction control function operated by a toggle switch and a power supply knob on a handheld box. The maximum speed of the rotation is 60 RPM.

Reactive sputtering-target poisoning issues:

Magnetron sputtering is a highly complex thin film synthesis process, so I have investigated the physical vapour deposition of thin films and coatings. When discussing reactive sputtering, the target poisoning issue has to be addressed, where there appears a hysteresis style behaviour in the deposition rate as shown in Figure 3.5. In reactive sputtering, the sputtering rate is an essential factor due to the influence of the oxygen partial pressure (μbar) on the properties of films. Here, oxygen partial pressure can be varied to obtain appropriate properties of samples.

Furthermore, reactive sputtering impacts material properties due to the interaction between metal targets and reactive gas. This will be discussed in the following paragraphs. At region A (along the horizontal line), the deposition from the metal target in reactive sputtering is shown in Figure 3.5. The amount of oxygen is insufficient to promote the formation of a full oxide surface on the metal target, thereby increasing the oxygen partial pressure to the maximum point B, at which time the oxygen partial pressure in the chamber is too high. Under high oxygen conditions, the formation rate of oxide layers on the target is higher than the rate at which metal atoms are removed by ordinary sputtering. At region B→C the sputtering rate is lower than the rate of formation of the oxide layer, which causes a complete oxide layer on the target. This limits the sputter rate due to the increased hardness of most oxide materials. Region C is referred to as compound mode. In order to prevent the poisoning of the targets, it is possible to reduce the oxygen partial pressure and remove the oxide layer on the target

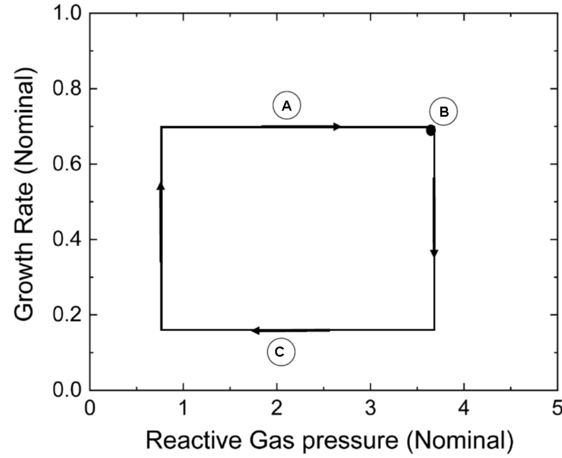

Figure 3.5: An experimental behaviour of a reactive sputtering deposition rate, where A - is the oxygen partial pressure during the deposition of the metal target, B - is the maximum oxygen partial pressure point for the formation of oxide layer on a surface of a metal target, C - is the oxygen partial pressure for the compound mode (oxide layer) of metal target and the oxygen partial pressure hits the maximum value (B), sputtering rate of target decreases sharply due to sputtering rate of oxide layer on the surface of the target is lower than a metal target, then decreasing the oxygen partial pressure with removing the oxide layer (C), at a point oxygen partial pressure, target switches from compound mode to metallic mode while the sputtering rate is recovered. Figure edited from cited work [172].

surface. Also, the removal of the oxide layers is accomplished by applying higher sputtering power on the target than optimised power for sputtering conditions [173]. Furthermore, the inert gas pressure in a reactive sputtering chamber can prevent the sputtering yield of oxide and metals due to a reduced discharge voltage [174]. As the deposition area is compacted by gas pressure due to the effects of desirable distance between target and substrate, the material redeposits on the target surface [175]. Apart from that, target power controls thin film thickness and the electrical properties of the materials to be synthesised. This means that increased power increases the sputtering capacity of the ions of the materials in the plasma [169]. In addition, the pre-sputtering process is the stabilisation time of bombarding the target with high-energy ions. It uses the stabilisation of the sputtering plasma and removes the oxide layers on the surface of targets created by the tiny amount of oxygen gas in the deposition chamber.

Although magnetron sputtering is a challenging synthesis technique, all films in this work were deposited using this method. I needed to measure the thickness of films to know the density of electrons and resistivity accurately. XRD and XRR systems are the most common methods used to examine films' morphological characteristics and thickness. These techniques will be discussed in detail in the next section.

3.2 Morphological and Crystallographic Characterisation

3.2.1 X-Ray Diffraction

X-ray Diffraction (XRD) is a versatile technique for investigating crystalline orientation. The XRD involved is an un-monochromated Bruker D8 Discover with a Cu source. However, the XRD system in this work has only been used for projects identifying whether samples are amorphous or crystalline. I will therefore discuss XRD briefly and show an example of XRD data for a-ZTO film. X-ray diffraction is now a widely used technique for understanding the structure of solid materials.

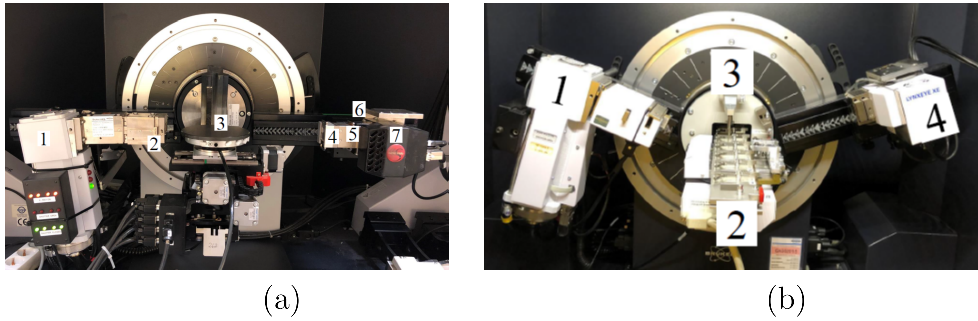

(a) (b)

Figure 3.6: The XRD systems applied in this work: (a) - high-resolution Bragg monochromated Bruker D8 Advance consisting of (1) - Cu Ka tube, (2) - entrance slit manually changeable (0.1 – 6 mm), (3) - sample stage (vacuum chuck), (4) - fixed anti-scatter slit, (5) - place for Cu absorber, (6) - exit soller slit, (7) - LynxEye detector (horizontal), and (b) - unmonochromated Bruker D8 Discover that consists of (1) - Cu Ka tube, (2) - motorised sample stage, (3) - beam knife, (4) - LynxEye detector.

$$n\lambda = d_{hkl} sin\,\theta \tag{3.1}$$

where d is the interplanar distance, θ is the incident angle, n is the positive integer (n=1,2,3,..), λ is the wavelength, and hkl are Miller indices.

The basic principle of XRD based on the Braggs Law of Diffraction is that diffraction peaks can be generated by the interference of the scattered x-ray, so X-Ray Diffraction (XRD) is a technique for determining the crystalline orientation and composition of a material. It is clear the diffraction in Equation 3.1 that the

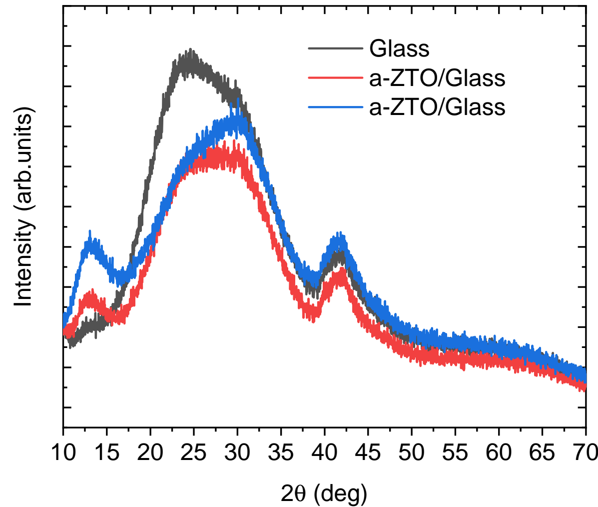

Figure 3.7: XRD pattern of amorphous Zinc Tin Oxide deposited on SiO_2 glass substrate by Magnetron sputtering.

ideal crystalline material is characterized by well-defined sharp Bragg peaks in X-ray diffraction profiles due to the crystalline material possessing a long-range order. However, amorphous materials lack this long range order, which results in their diffraction not exhibiting sharp Bragg peaks. Nevertheless, the XRD system can observe some broad halo peaks in the XRD diffraction data. These broad halo peaks might be associated with background signals due to X-ray scattering by air, and sample holder [176].

Fig 3.7 shows a typical XRD pattern of a-Zinc Tin Oxide films. Three halo peaks were observed at around 13°, 28°, and 42° due to a large variation in the length of amorphous bonds. This is usually called a halo peak and is an indicator of an amorphous nature. The first two peaks originate from the thin film or part of the glass. If one of them is the XRD peak of the film, the other is the peak of the glass substrate at the angle of 20-30°. The 40∼45° is from the XRD sample holder. These XRD patterns were observed in a previous report [177]. It can be seen from Figure 3.7 that the XRD peaks of the film were not sharp. All a-ZTO samples in this work showed an amorphous state. The main goal of my studies was to focus on the amorphous phase, and XRD is not widely used for amorphous

materials.

3.2.2 X-Ray Reflectivity

Determining the layer thickness in a single-layer oxide semiconductor:

Thickness is crucial for most properties of materials. X-ray-reflectometry (XRR) involves a non-contact, non-destructive technique to determine the thickness of the thin films of metals and semiconductors in the range of a few nm to 150 nm. The Bruker D8 Advance is also employed to identify materials' density and interface roughness.

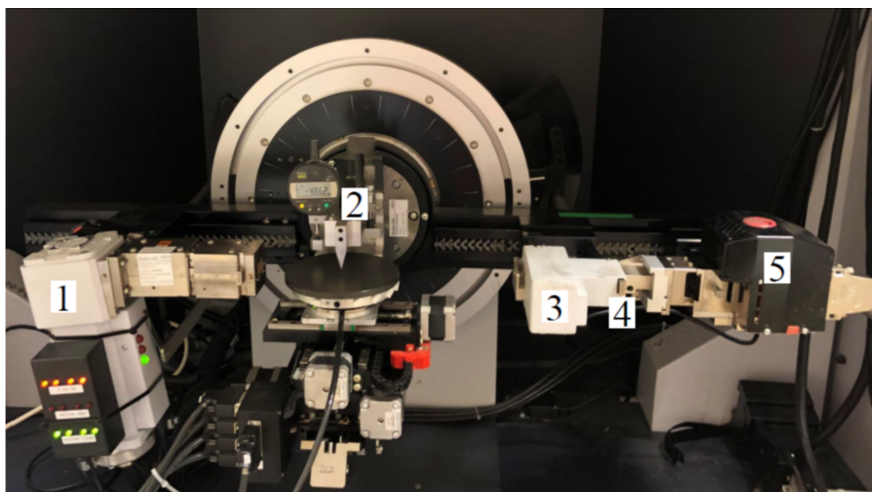

Figure 3.8: the XRR system involved in this work, where (1) - standard tube configuration, (2) - beam knife (for XRR measurements), (3) - variable anti-scatter slit, (4) - detector slit (use 0.1 mm), (5) - LynxEye in vertical mode (0D mode only).

In this work, the Bruker D8 Advance system was utilised for carrying out all XRR measurements. The apparatus is composed of an x-ray tube, a sample stage with a beam knife, and a position-sensitive detector (PSD or Lynx-Eye detector), as shown in Figure 3.8. Fundamentally, XRR probes the interference between the reflected x-ray from the material's surface and the interfaces between the material and substrate. XRR works on a thin film interference principle (X-rays). X-ray is reflected from each interface in a film and interferes, producing an interference pattern as shown in Figure 3.10. This can be used to determine the

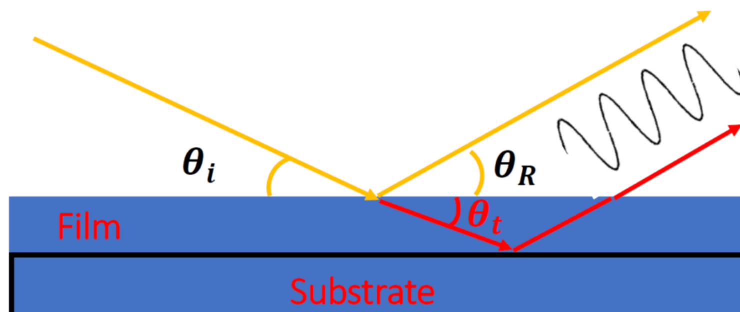

Figure 3.9: The relation between the incidence angle and critical angle of the total reflection of X-rays at different material surfaces. Figure has been reproduced from cited work [178].

thickness of the individual layers so long as they are not above 150 nm. At this point, the oscillations become too close together to be accurately distinguished by the XRD. Depending on phase difference, waves interfere constructively or destructively to produce an interference pattern. The interference fringes are referred to as Kiessing fringes after their discoverer as shown in Figure 3.10 [178]. In the case of scanning the thin films using X-rays techniques, where the XRR curve can be produced by obtaining the scattered X-ray intensity against the angle of incidence. This implies that scattered X-ray intensity is a function of the incident angle. The physics of this subject matter can be explained by the optics law of the incident and reflection beams. So wen can start with basic optics law relating to the complex refractive index $\tilde{n}$ of material for X-rays, which can be written with the following equation [179]:

$$\tilde{n} = 1 - \delta - i\beta = 1 - \frac{\lambda^2}{2\pi} r_e \rho_e - i\frac{\lambda}{4\pi}\mu \tag{3.2}$$

where β is the absorption coefficient of the material (called an imaginary deviation of the refractive index), δ is the real deviation of the refractive index, λ is x-ray wavelength, r is the radius of the electron, and ρ is the electron density of materials, while recalling the Snell's law to get the equation below:

$$n_{air} \cos\theta_i = \tilde{n} \cos\theta_t \tag{3.3}$$

where n_{air} is the air's refractive index, and θ_t and θ_i (see the Figure (3.9)) are the

angles of transmitted and incident beam. We can combine equations (3.2) and (3.3), and in (3.2) equation consider as $\tilde{n} = 1 - \delta$ due to absorption being very small (β=0). The critical angle θ_c is defined:

$$\theta_c^2 = 2\delta \tag{3.4}$$

when X-rays incident meet at a flat surface of materials at the grazing angles of incidence, the total reflection can occur at or below a certain angle, which angle is called the critical angle. If absorption is taken into account, θ_t can be written using equation 3.3 (the Snell–Descartes law):

$$n\theta_t = n\sqrt{\theta_i^2 - 2\delta - 2i\beta} \tag{3.5}$$

When n_{air} is 1:

$$\theta_t = \sqrt{\theta_i^2 - 2\delta - 2i\beta} \tag{3.6}$$

by replacing $\theta_c^2 = 2\delta$, θ_t is defined:

$$\theta_t = \sqrt{\theta_i^2 - \theta_c^2 - 2i\beta} \tag{3.7}$$

it is clear that the reflectivity curve is a function of the 2θ, which can be derived from the Fresnel coefficients. Fresnel coefficients can be described by the ratio of reflected and incident intensity of the beam as shown by the equation:

$$\frac{I_r}{I_0} = \left|r^2\right| = |r_p r_s| \tag{3.8}$$

The Fresnel coefficients r, are calculated for reflected and transmitted x-rays of the beam perpendicular (for s-polarization, equation 3.11 and 3.12) and parallel (for p-polarization, equation 3.9 and 3.10) to the scattering plane, using these equations the Fresnel reflectivity can be described as the equation (3.13):

$$r_p = \frac{n_2 cos\theta_i - n_1 cos\theta_t}{n_1 cos\theta_t + n_2 cos\theta_i} \tag{3.9}$$

$$t_p = \frac{2n_1 cos\theta_t}{n_1 cos\theta_i + n_2 cos\theta_i} \tag{3.10}$$

$$r_s = \frac{n_1 cos\theta_i - n_2 cos\theta_t}{n_1 cos\theta_i + n_2 cos\theta_t} \tag{3.11}$$

$$t_s = \frac{2n_1 cos\theta_i}{n_1 cos\theta_i + n_2 cos\theta_t} \tag{3.12}$$

$$R(\theta) = |r|^2 = \left| \frac{\theta_i - \sqrt{\theta_i^2 - \theta_c^2 - 2i\beta}}{\theta_i + \sqrt{\theta_i^2 - \theta_c^2 - 2i\beta}} \right|^2 \tag{3.13}$$

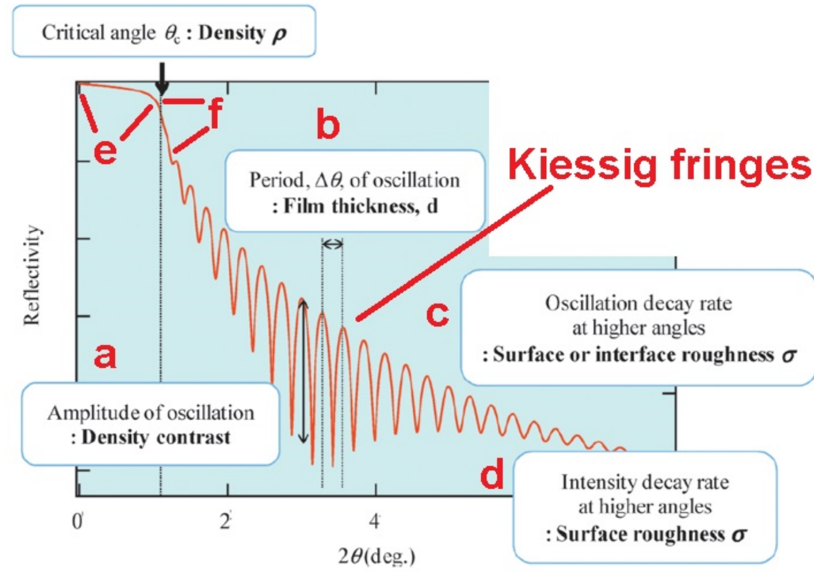

Figure 3.10: Information on thin films extracted by X-ray reflectivity curve versus theta (incident angle of X-ray), where meaning of (a) - the amplitude of the oscillations (density contrast), (b) - the thickness of films (the oscillation period), (c) - surface or interface roughness (the oscillation decay), (d) - surface roughness (intensity decay), (f) - density values (sharp decrease), (e) - plateau ($\theta_c > \theta_i$). Figure edited from cited work [180].

where it is pointed out that the transmitted intensity of X-ray is a complex mechanism, so it is not taken into account here. Also, the Fresnel coefficients require extensive study of the reflectivity of X-ray and reflection angle. The reflectivity of a single interface thin film is a function of the incidence angle θ_i, and x-ray momentum transfer vector along the surface, which is given by the equation (3.14):

$$q = \frac{4\pi}{\lambda} \sin\theta_i \tag{3.14}$$

where θ_i is the incidence angle of the X-ray, now Fresnel reflectivity can be written

in terms of the wave-vector transfer q (3.15):

$$R(q) = |r|^2 = \left| \frac{q - \sqrt{q^2 - q_c^2 - \frac{32i\pi\beta}{\lambda^2}}}{q - \sqrt{q^2 - q_c^2 - \frac{32i\pi\beta}{\lambda^2}}} \right|^2 \tag{3.15}$$

where using formula (3.14), θ_c in formula (3.13) is replaced with q_c in (3.15), the critical momentum transfer wave vector of q corresponds to θ_c. In other words, R(q) and R(θ) reflection (x-rays intensity) are functions of the incident angle θ_i, which, the way this is written, theta is the Fresnel reflectivity, whereas R is the reflectivity.

We consider the three possibilities of the relationship between θ_i and θ_c or q and q_c. First of all, if θ_c is greater than θ_i, in other words, the incident angle is below the critical angle, then the intensity of the full x-ray goes into the detector, and the Fresnel coefficient is equal to 1 as shown in Figure 3.10. This can be seen from Figure 3.10 as a plateau marked by the letter e. When the θ_i and θ_c are equal, the incident x-rays propagate along the sample surface, and the reactivity curve decreases rapidly as shown in Figure 3.10 (f). However, once the θ_i is two or three times greater than θ_c, the intensity curve is a function of the θ_i. The thickness of the film is defined by the intensity of the x-ray against incident angle oscillations. Thin films have a long oscillation period. Thick films show a short oscillation period as shown in Figure 3.10 (b). The thickness of films is calculated by the equation (3.16):

$$d = \frac{\lambda}{2(\theta_{m+1} - \theta_m)} = \frac{\lambda}{2(\triangle\theta)} \tag{3.16}$$

where the incident angle is higher than the critical angle, the x-ray penetrates the samples while the incident x-ray is reflected from the top and interface between the substrate and thin films. Furthermore, when constructive or destructive interference occurs, the thin-film density is defined by differences between the amplitude of the oscillations of the thin films and substrate. In other words, the high amplitude of the oscillations indicates the large difference in the density of film and substrate as shown in Figure 3.10 (a). Furthermore, the amplitude of the oscillations increases with the decreasing the interface roughness of the

materials. This implies that the x-ray intensity of the beam diffracted from a rough surface is less than that form a flat surface [181]. This can be observed at higher angles of the XRR curve as shown in Figure 3.10 (c) and (d), presenting an interpretation of the oscillation decay at a high angle due to the rough surface and interface while in these regions. The high degree of roughness of the surface causes intensity to decay as well. This can be described by the Debye-Waller factor as given below:

$$R_q = R_0 e^{(\frac{-4\pi \sin\theta\sigma^2}{\lambda})} \tag{3.17}$$

where σ is the surface roughness, λ is the wavelength, and R_0 is the specular Fresnel reflectivity. XRR scans for the multilayer structures will be discussed in the following paragraphs.

Multilayer structures by x-ray reflectometry:

It is clear that multilayer structures have more than two interfaces compared to the single-layer oxides semiconductors deposited on a finite substrate thickness. As a result, the X-ray scattering from all interfaces in a multilayer film should be considered along with the X-ray reflectivity of a multilayer film as a function of θ, which can be theoretically calculated via Parratt's recursion formalism based on the s- and p-component of reflected and transmitted amplitude R_j and T_j, respectively. Here recalling the equations (3.9), (3.11), (3.12) and (3.10) from previous paragraphs, that can be written as [182]:

$$r_j = \frac{r'_{j+1}E_{j+1} + r_{j+1}exp(-2i\delta_{j+1})}{1 + r'_{j+1}E_{j+1}r_{j+1}exp(-2i\delta_{j+1})} \tag{3.18}$$

$$t_j = \frac{t'_j t_j exp(-i\delta_j)}{1 + r'_j E_j r_j exp(-2i\delta_j)} \tag{3.19}$$

where δ_j is a phase factor of the jth layer, and E^j is a roughness factor of the jth interface. The roughness factor can be described by Debye-Waller factor $exp(\frac{q_j^2\sigma_j^2}{2})$, where, q is the momentum transfer vector by the equation above (3.14), and σ is the root-mean-square roughness of the surface. This implies that the atomic scale of materials, surfaces and interfaces are always rough, where obtained x-ray reflectivity is significantly lower than the Fresnel reflectivity. The Debye-Waller factor can articulate this as shown in equation 3.17 [181]. The last thing

to discuss is the penetration depth of x-rays, which is defined by the depth of a homogenous medium to which a beam can penetrate while its intensity is reduced to $\frac{1}{e}$. This depth Z_p, which is normal to the boundary of the medium, follows the equation (3.20) [183]:

$$Z_p = \frac{\sin\theta}{\mu} \tag{3.20}$$

where μ is the linear absorption coefficient, which has a strong relationship with an incident angle of θ. In general, as discussed above, for multilayer structures, the ratio of specularly reflected X-rays decreases proportionally to $1/q^4$ due to its intensity being a function of the critical angle from the equation (3.15). Furthermore, measured X-ray data must be analysed to show the thin film's properties. This is discussed in the next paragraph.

Methods for determining the thickness of thin films using the X-ray reflectivity data:

There are various XRR data analysis methods for obtaining the thickness of the thin films using measured X-ray reflectivity data. These methods are calculation using the peak separations between consecutive interference fringes, such as Fourier analysis of in reference data, determination from interference peaks using the modified Bragg equation, and the curve fitting method (also known as least-squares method). I have used a curve fitting method for studying thickness determination because of its high degree of accuracy [184]. This method identifies a thin film's thickness, density, and roughness simultaneously. In this work, Bruker Leptos software was involved in fitting the XRR spectra and determining the materials' layer thickness, interface roughness, and density. This can be done by comparing a theoretically calculated reflectivity curve with the experimentally measured curve. Here, measured data was obtained by the x-ray reflectometry technique. The fitting process includes applying the estimated values on simulated data's the density as shown in Figure 3.10 (f), oscillation period length (an estimated thickness) as shown in Figure 3.10 (b)), and surface and interface roughness (d)) as shown in Figure 3.10 (c) (d) up to overlap with the measured data. In other words, measurement and simulation data can fit and match each other perfectly.

After obtaining the film's thickness, density, and roughness, other crucial properties of thin films should be considered, such as optical properties. The transmission and reflectance spectra are measured to demonstrate the optical properties of films, which are used to show how films are transparent, as well as other qualities of films. UV-Vis Spectrophotometry can do these tasks and will be outlined in the following section.

3.3 Optical Properties of Amorphous TCOs

The investigation of the thin film's optical properties involves many experimental devices. The most common one is UV-Vis Spectrophotometry to probe a few optical properties, which will be described in the following section.

3.3.1 Ultraviolet-Visible Spectroscopy

Some properties of TCO materials are defined by optical properties, which can be identified via specific characterisation techniques. UV-Vis Spectroscopy is a widely used technique to determine the transmission, reflectance and absorption of spectra of TCO materials in the visible range. The schematic of UV-Vis is shown in Figure 3.11. The system employed in this work is a Perkin Elmer Lambda 650 UV-Vis Spectrophotometer. In general, a UV-Vis Spectrophotome-

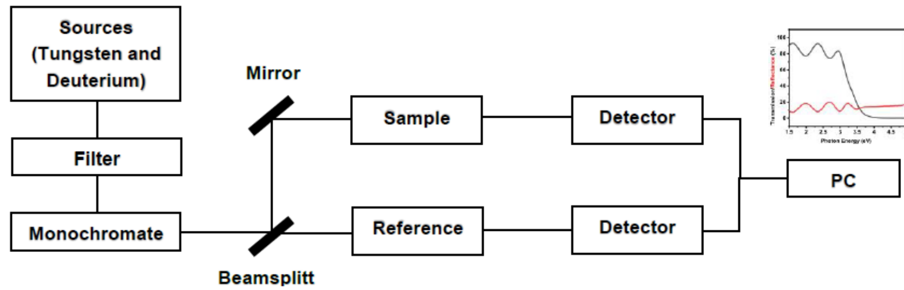

Figure 3.11: A simple schematic diagram of UV-Vis spectroscopy. Figure reproduced from cited work [185].

ter consists of a 150 mm integrating sphere, and its operating spectral range is from 1.5eV to 5.8eV. This spectral range can be achieved by independent Tungsten (TL) and Deuterium lamp (DL) sources. It also has a spherical container detector with reflective walls to provide minimum light absorption. In general, integrating the sphere ensures all light is captured, allowing for the measurement of directly (specularly) transmitted and response scattered light. In addition, the signal-to-noise ratio can prevent the process of measurements. An integrating sphere has two ports: a transmittance port and a sample reflectance port, and the beam enters through them. To control the sample beam into the sphere, we use a three-position small spot kit with a lens that includes transmission, centre

mount, and reflection. Also, there is an iris assembly that mounts the beam size, and a sample holder set with a 10x10 mm spot sample stage that supports various forms of samples.

Generally, all measurements record the intensity of the reference beam and the intensity of the beam passed through the sample to give us the transmission and reflectance spectra of the film. These are defined following equation (3.21) [186]:

$$T(\lambda) = \frac{I_{ref}}{I_{sample}} \tag{3.21}$$

now we can get a simple expression to calculate the absorption of the samples, the formula given by (3.22):

$$A = 1 - (T + R) \tag{3.22}$$

$$\alpha = \frac{-\ln(T + R)}{t} \tag{3.23}$$

where t is the thickness of the films, T is the transmission, and R is the reflectance spectra. Furthermore, the absorption and absorption coefficient can be calculated using the transmittance and reflectance spectra of thin films as shown in equations (3.22) and (3.23), respectively. Besides, the Tauc plot can be determined by

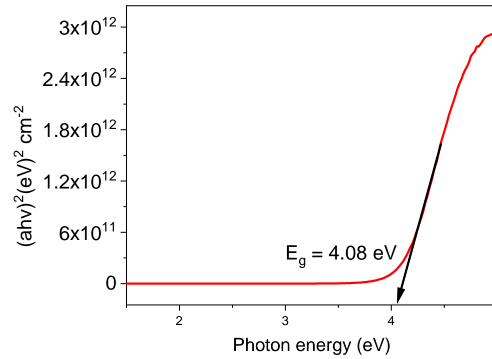

Figure 3.12: A Tauc plot of a-ZTO film on glass substrate, where bandgap of a-ZTO film (eV).

applying these spectra data, where the bandgap energy of Zinc Tin Oxide can be extracted as shown in Figure 3.12. A Tauc plot [187] of Zinc tin oxides can be obtained using the equation $(\alpha h\nu)^n$ versus $h\nu$, where α is an absorption coefficient

Transition	n
Direct Allowed	1/2
Direct Forbidden	3/2
Indirect Allowed	2
Indirect Forbidden	3

Table 3.1: Tauc plot coefficients. Data from cited works [188, 189].

of the sample and n is the nature of the optical transition, which is $\frac{1}{2}$ for ZTO. The absorption coefficients for the particular circumstance are given in Table 3.1.

As discussed above, most optical properties of films prove to be importance for research, such as determining the bandgap and other optical properties of materials. However, a UV-Vis Spectrophotometer is not the last step in characterising the films because the electrical properties of thin films are also essential for optoelectronic applications [3]. Since the electrical measurement techniques can perform more research on the electrical properties of TCOs, methods of electrical characterisation will be addressed in the next section.

3.4 Electrical Measurements

3.4.1 Four Point Probe Measurements

What follows is a more in-depth investigation of semiconductor materials, which is linked to the electrical properties of semiconductors. Many versatile electrical characterisation techniques can be used to obtain the electrical properties of materials. In this work, two main electrical measurement techniques were employed, that is to say, the Hall measurement system and Four-Point Probe Technique. The former is described in the next section. The latter has a resistive heater which calculates the thin films' activation energy using measurement data of resistivity and temperature. As shown in Figure 3.13, this system consists of four equally spaced, gold spring-loaded probe configured in a linear array to achieve the precise resistances levels of the samples and low resistance contacts. In an attempt to determine sheet resistance, four evenly spaced probes are

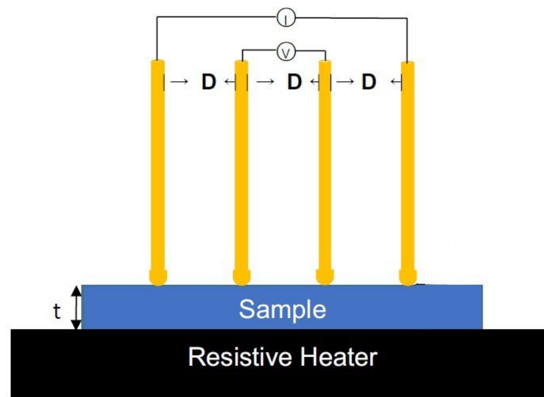

Figure 3.13: Schematic diagram of a linear four point probe method. Linear four-point probe configuration, where t is the sample thickness, D is the space of probes each other (same), I is current applied and V is voltage measured.

placed in contact with the film. A current source supplies the outer two probes to produce voltage crosswise to the sample. This voltage is then obtained by two inner probes. This is illustrated in Figure 3.13. Also, these spring-loaded probes reduce the force on the flat surface of the samples, which can eliminate the damage and penetration of films in the measurement process. Such damage

and penetration have not been observed in our films. Technically, the voltage between two inner probes can be produced when the current is applied to the two outer probes. An ohmic contact on the material defines an accurate resistivity regarding of the samples. If gold spring-loaded probes do not achieve the accuracy in resistivity measurement, they can be replaced with another metal under the circumstances to avoid the Schottky barrier. When the distance between two probes is considerably higher than the thickness of the film (D$\gg$ t), the sheet resistance of the film can be calculated using the equation below [190]:

$$R_{sh} = \frac{\pi}{\ln(2)} \frac{\triangle V}{I} = 4.53236 \frac{\triangle V}{I} \tag{3.24}$$

where R_{sh} - sheet resistance, $\triangle V$ - the potential difference between the two inner probes, I - the current is applied between two outer probes. If the thickness of the film is known, expression of the resistivity and conductivity are given:

$$\rho = R_{sh} \times t \tag{3.25}$$

the resistivity is specified as the inverse of the conductivity so that above equation (3.25) can be rearranged:

$$\sigma = \frac{1}{\rho} \tag{3.26}$$

The Four-point probe system is equipped with a separate Bell-Jar chamber in order to achieve a rough vacuum and a variety of gas atmospheres. In the results section, the priorities of this system are outlined and it is explained how to perform the Four-point probe system in regards the annealing studies of a-ZTO thin films, which are used to control the electrical properties of a-ZTO thin films. The following section will present the second important technique for obtaining film resistivity, carrier concentration and mobility.

3.4.2 The Hall Effect System

The second instrument utilised was the hall measurement system based on the van der Pauw method, which is commonly used for determining resistivity, carrier type and mobility of specimen. All of the contacts in van der Pauw were made with silver wire applying silver adhesive, which was placed on the corners of the sample. This is as shown in Figure 3.14. We ensure that the size of contacts

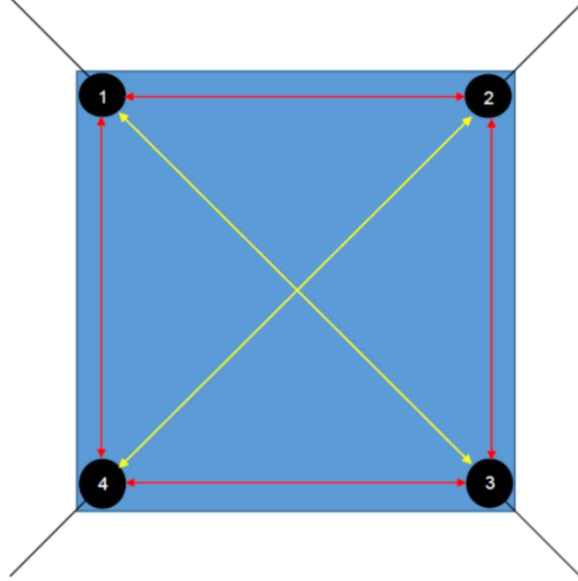

Figure 3.14: Schematic diagram of Van der Pauw contact arrangements. Figure edited from cited work [191].

must be made as small as possible. In other words, these contacts are much smaller than the sample surface area to mitigate measurement errors. Before the current-voltage measurement was carried out, all contacts on the four corners of the films were checked by applying a current to validate the contact quality on the samples. Hall measurements are performed by applying a current between two contacts and measuring the voltage between the other two contacts on the sample. In Hall mobility measurements, the field is applied perpendicular to the sample surface, and a current is applied diagonally across the film. The induced Hall field is then measured across the other diagonal contacts. A total of eight measurements are characterised by two vertical and horizontal resistance, and R_{sh} can be calculated:

$$R_{Horizontal} = \frac{(R_{12,43} + R_{21,34} + R_{34,21} + R_{43,12})}{4} \tag{3.27}$$

where $R_{12,43}$ is the resistance when a current is applied in the direction from contact 1 to 2 while measuring the voltage drop across contacts 4 and 3 on the opposite side of the sample, as shown in Figure 3.14 or vice versa. $R_{21,34}$ and

$R_{34,12}$ resistances were obtained in a similar way to the previous method for the horizontal direction of the samples. Likewise, by using equation 3.27 the same can be done for $R_{Vertical}$, which is given as 3.28:

$$R_{Vertical} = \frac{(R_{32,41} + R_{23,14} + R_{14,23} + R_{41,32})}{4} \tag{3.28}$$

using van der Pauw formula the sheet resistance equation is derived, which is given below:

$$exp(\frac{-\pi R_{Hor}}{R_{sh}}) + exp(\frac{-\pi R_{Ver}}{R_{sh}}) = 1 \tag{3.29}$$

using equation (3.29), the sheet resistance (R_{sh}) can be calculated, which is applied to determine the bulk electrical resistivity (ρ) of the samples as shown in the equation (3.25). if ρ is known, R_H (Hall coefficient) can be calculated by the following expressions:

$$R_H = \pm\frac{r}{ne} = \pm r\rho\mu \tag{3.30}$$

where the Hall coefficient (R_H) is induced voltage to the product of the current density and magnetic field, its value depends on the types of free charge carriers, such as $R_H>0$ for holes, $R_H<0$ for electrons. r is the scattering factor that corresponds to the energy dependence of the scattering rate, and usually for highly doped semiconductors is equal to 1 so that Hall coefficient (R_H) can be gained by using the Hall effect (3.31), which is described by Lorentz force (3.31) as shown in Figure 3.15 and a transverse electric field E_H [192] defined respectively as:

$$F_{Lor} = q(\upsilon \times B) \ \ and \ \ E_H = R_H B \times J \tag{3.31}$$

where q is the charge of the particle, B is the magnetic field, J is an electric current density, υ is the velocity of charged particle q. Now the expression of Hall voltage can be written:

$$V_H = \frac{R_H}{t} B \times I \tag{3.32}$$

where t is the thickness of the film, V_H is the Hall voltage, which is a measurable transverse voltage produced along the diagonal, it is a function of the current and the magnetic field. Carrier concentration and Hall mobility can be expressed by

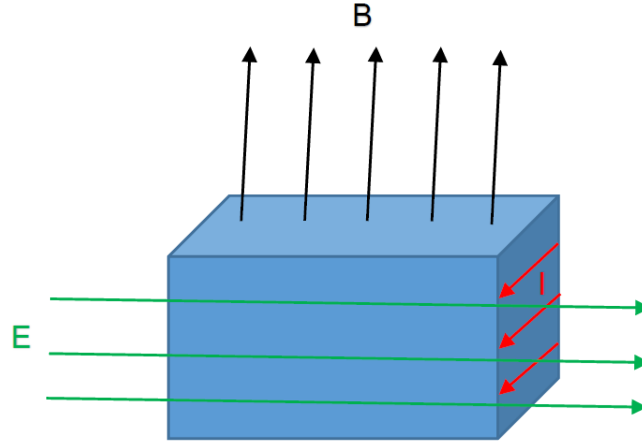

Figure 3.15: Sketch of Hall effect, where the direction of the Magnetic Field **B**, applied current **I** and the Hall induced electric field **E**.

Hall voltage [192]:

$$n_c = \frac{1}{V_H et} BI \Rightarrow \mu_H = \frac{V_H}{BIR_{sh}} \tag{3.33}$$

This work uses a Hall measurement system based on a van der Pauw configuration combined with an 800mT magnetic field. Additionally, this system also provides a vacuum pump and metal shield in order to operate a closed-loop helium cooling system, which it utilises to monitor the temperature dependence of the electrical properties of the thin films at temperature up to down 5K.

To conclude this chapter, thin-film synthesis and characterisation techniques can provide all the experimental data relating to the films. The quality of these data can be examined by analyzing and evaluating them in order to produce high-impact publication. These obtained results will be outlined in the next chapters.

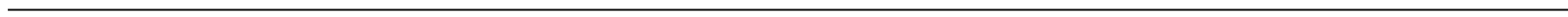

4

Optimisation Studies and Annealing with In-Situ Observation of Resistivity of a-ZTO

4.1 Optimisation Studies on a-ZTO Films

4.2 Introduction for Optimisation Studies on a-ZTO

Transparent Conducting Oxide (TCO) thin films have become essential parts of solar cells, OLEDs, flat panel displays [7, 8, 10]. TCO semiconductors exhibit high conductivity and visible-range transparency (a wide bandgap of >3 eV) at the same time. Furthermore, TCO materials can be achieved at low synthesis temperatures and substantial-high mechanical flexibility with excellent electrical properties [7, 193]. During the last two decades, resistivity $\approx 10^{-3}$ ohm-cm of a-IGZO has been achieved while demonstrating less than 10% absorption in the visible range of the light spectrum simultaneously [54, 92]. However, the high cost of Indium material and other concerns over health and environmental impacts have led to the search for a sustainable alternative material [194, 195]. As a

result of these concerns, amorphous Zinc Tin oxide (a-ZnSnO) has become one of the best candidates and is a low-cost, abundant material [8, 196], which has already been seen in solar cells and OLEDs, TFT and displays [37]. However, a key to the fabrication of a-ZnSnO is to control the properties of the films. This sets the case for the optimization of a-ZTO.

Understanding the importance of optimising the electrical properties of amorphous transparent conducting oxides is crucial for the material growth process. Also, the electrical and optical properties of amorphous semiconductors are defined by the defect chemistry of amorphous networks because they are being intrinsic oxide semiconductors, where the number of excited electrons is determined by the free electrons, not holes.

The material's properties are controlled by intrinsically occurring defects, such as metallic ion bond overlap, oxygen vacancies or hydrogen interstitials, and interlinks. All these defects can affect the electrical properties, and they are defined by the growth conditions. Therefore the situation is much more complex than in conventional semiconductors, such as the properties of Si are defined just by a single type of defect. Indeed, an examination of the literature for $ZnSnO_y$ reveals there can be variations in obtaining compositions for excellent properties of films even if they have nominally similar overall quality [16–18, 197]. Keeping this in mind, this work aims to optimise a-ZTO growth via reactive and non-reactive sputtering to demonstrate the effect of these deposition conditions and changes in composition on the electrical properties of a-ZTO. Primarily examining a common synthesis technique (magnetron sputtering) with various growth conditions in order to obtain a high quality of amorphous thin films. The study of both sputtering methods needs to be investigated to show the benefits of further developments in oxide material fabrication. Specifically, the optimisation process is crucial to designing the experimental approach. Also, finding the optimal synthesis parameters is a key to present impacts on the defect-based amorphous materials.

4.3 Methods for optimisation of a-ZTO

Amorphous-Zinc Tin Oxide (a-ZTO) films were grown via Radio Frequency (RF) magnetron co-sputtering from separate zinc and tin sources. A ZnO target

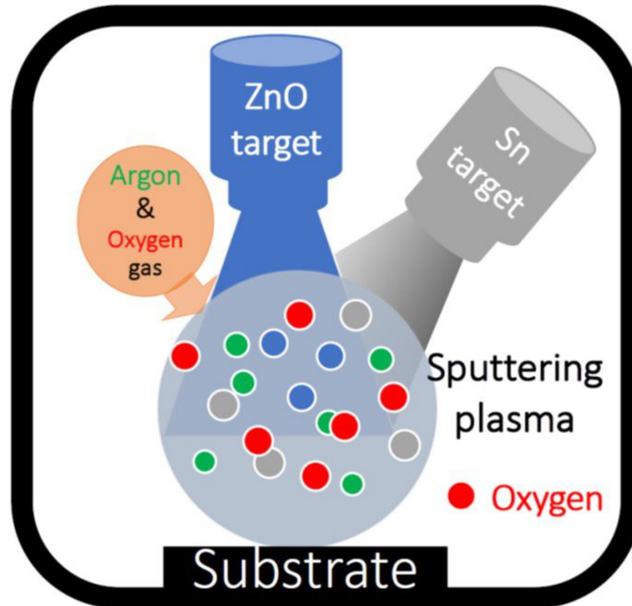

Figure 4.1: An illustration of the reactive magnetron sputtering method (referred as a-ZTO$_{Ar+O_2}$) used in this work.

was used as the zinc source for all depositions, and two separate tin sources were used. One film set was grown by reactive sputtering of a metal Sn target (99.99% purity) in Ar+O_2. Hereinafter these will be referred to as a-ZTO$_{Ar+O_2}$ as shown in Figure 4.1.

The second set of growth methods was performed using a SnO_2 target (99.99% purity) in an inert Ar atmosphere. These will be referred to as a-ZTO$_{Ar}$ as presented in Figure 4.2. The former is called the reactive magnetron sputtering method, and the latter is called the non-reactive magnetron sputtering method. During the deposition, the total gas pressure was kept constant at 5×10^{-3} mbar, with oxygen partial pressure being varied from 0 to 4×10^{-1} mbar during the reactive sputtering. All films were deposited on standard microscopy glass slides (Thermo Scientific 1x1 cm, 0.8-1mm thick). Glass substrates were sonicated in isopropanol and acetone for 5 minutes individually. The substrate temperature was 300 °C for all samples. This temperature was to produce our best performing films while still being at a low enough temperature to be comparable with the temperature acceptable for a number of common plastic substrates. However, it should be noted that this temperature (300 °C) is too high for some substrates,

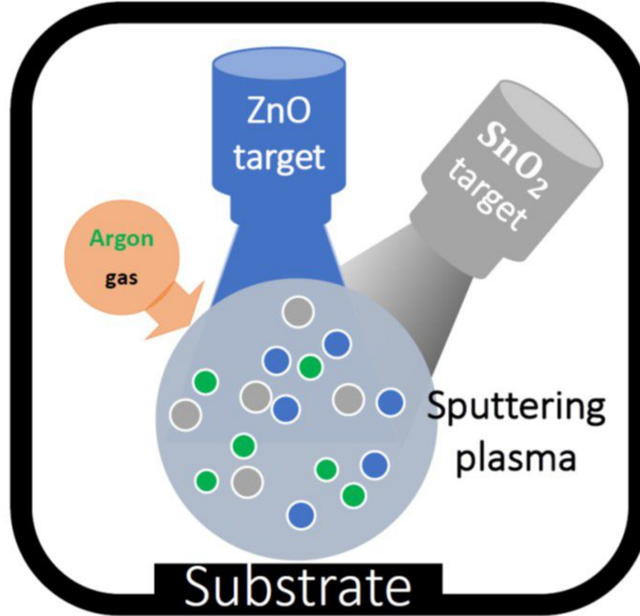

Figure 4.2: A sketch of a typical nonreactive sputtering method in this work, referred as a-ZTO$_{Ar}$.

including polyethylene terephthalate (PET).

4.4 Results for optimisation of a-ZTO

Figure 4.3 (a) shows the dependence of the conductivity of the films on the O_2 partial pressure (μbar) during reactive sputtering growth, where oxygen partial pressure can be varied in order to obtain the samples with attainable properties. One of the ideal oxygen partial pressure for the metal target case is highlighted (0.32 μbar) in Figure 4.3 (a), in which the combination of the ZnO-Sn$_{Ar+O2}$ sputtering method, where applied powers for ZnO and Sn targets were 100 and 60 W, respectively. Here, the reactive sputtering was with a constant argon gas flow, but the conductivity of films increases with oxygen partial pressure (PP) up to a maximum value as shown in Figure 4.4 (a); beyond this, it decreases rapidly. In other words, in the reactive magnetron sputtering process, the electrical and optical properties of the films show up as functions of the Ar/O_2 flow ratios, which control the conductivity of the grown samples. At the same time maintaining other deposition chamber conditions constant, such as sputtering target powers

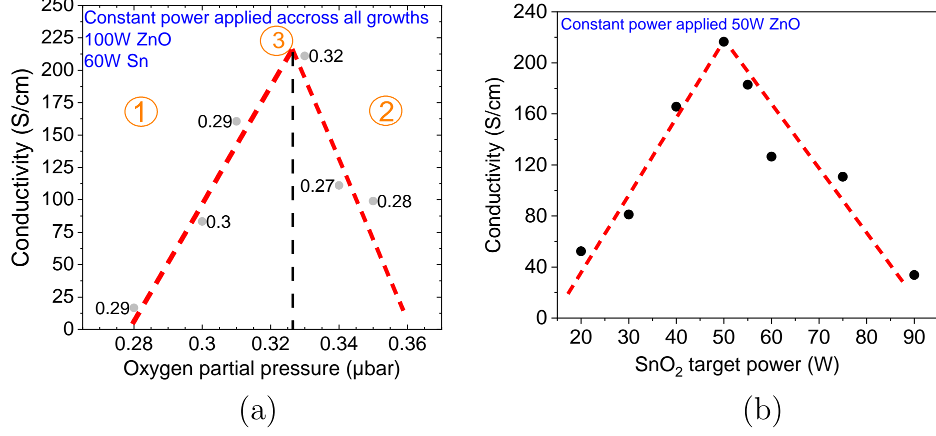

Figure 4.3: Optimisation study on a-ZTO, where (a) - reactive sputtering method (a-ZTO_{Ar+O_2}), (b) - nonreactive sputtering method (a-ZTO_{Ar}).

and chamber pressure, etc. This change in conductivity could be due to the effect of the target poisoning, where the growth rate varies with oxygen partial pressure as depicted in Figure 4.4. Regions A (the target surface is still metal due to the oxygen partial pressure is not enough to form an oxide layer on the target surface during the deposition of the metal target), B (the maximum oxygen partial pressure point for the formation of oxide layer on the surface of metal target) and C (the oxygen partial pressure for the compound mode (oxide layer on the surface) of the metal target, where the decrease in oxygen partial pressure with removing the oxide layer from target surface) in Figure 4.4 (b) could correspond to 1, 3 and 2 in Figure 4.4 (a). A variation in the target surface would result in a change in Zn/ Sn ratio, but this change is not observed as shown in Figure 4.4. In regions 1 and 2, Zn/ Sn ratio of films is almost the same. In region 3 would be expected a change in Zn/ Sn ratio due to the reduction in Sn sputter rate, where the surface of Sn metal target is in the oxide condition as shown in Figure 4.4 (a). However, changes in the elemental ratio were not observed. The conductivity change's origin is likely more subtle and related to defect formation in the $ZnSnO_y$. Here, oxygen content in the sputtering chamber plays a key role in creating the free carrier in amorphous networks. Previous work confirmed that oxygen vacancies related to the shallow donors were controlled by oxygen partial pressure during deposition [99].

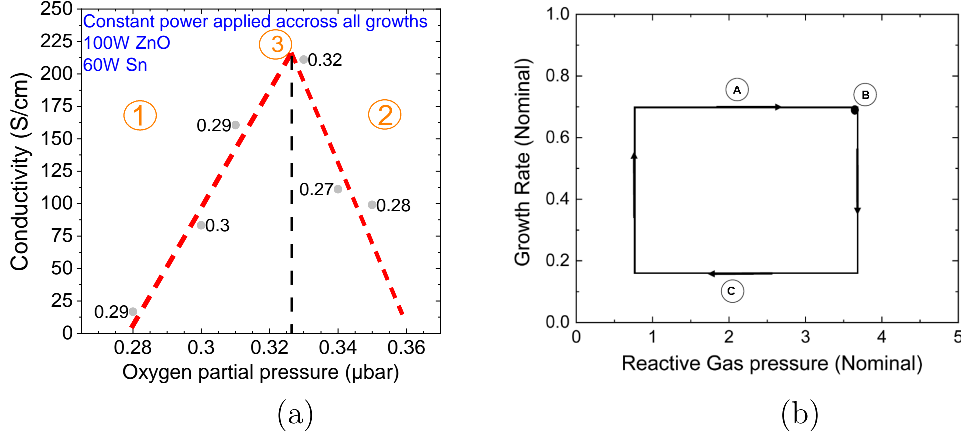

Figure 4.4: A reactive sputtering deposition rate, where (a) - reactive sputtering method (a-ZTO$_{Ar+O_2}$), (b) - reactive sputtering deposition rate. Figure (b) edited from cited work [172].

In nonreactive sputtering, as shown in Figure 4.3 (b), constant power is applied to the ZnO target, and the sputtering chamber pressure is maintained with a constant argon gas flow. Figure 4.3 (b) shows the conductivity of films as a function of the SnO_2 target power. The conductivity is seen to increase with applying until ≈ 50 W SnO_2 target power. Conductivity decreases with increasing power above ≈ 50 W. The decrease in conductivity can be explained by depositing a-ZTO films to have more tin in the composition approaching the SnO_2 structure. A previous report said that a-ZTO films with a high Sn concentration are characterised by a substantial variation in the microstructure of the films [105]. Another report highlighted that increasing the Zn content introduces a high microcrystal of ZnO [16]. It is conceivable that similar effects are observed for SnO_2 phase on a-ZTO film properties. In nonreactive sputtering, argon partial pressure during the growth is also an important parameter to govern the electrical properties of samples, where the energetic argon ions contribute to oxide material's atoms between the sputtering target and substrate surface [198].

4.5 Conclusion and Further Benefits of Optimisation of a-ZTO

To conclude, the defect formation in the films is defined by the sputtering conditions used with the two sputtering methods. This can be seen from al-

terations in Zn:Sn ratios and observed two different local bond arrangements in a-ZTO films, which is confirmed by Raman spectroscopy. This is due to the role of oxygen in the films that originated from the content of poor and rich oxygen gas during the synthesis process by the two different sputtering methods, where the oxygen structure in the film's content is a function of the oxygen content. These findings were published, and more information is in this report [104].

Furthermore, working with oxide targets (non-reactive sputtering) allows for better control of the sputtering process compared to targets with metallic surface (metal target and reactive gas). Non-reactive sputtering with an absence of oxygen gas would be advantageous to research for industrial uses because reactive gas can react with the target surface, which can prevent the sputtering process. Apart from that absence of oxygen gas in the sputtering process would benefit by reducing the cost of TCOs-based profitable product fabrication [199]. These advantages give more opportunities for further research. Therefore, we have extensively worked with non-reactive sputtering to grow a-ZTO films. Different types of defects in a-ZTO films have to be altered, and one of the common methods of increasing the desirable effects of materials is post-annealing treatment [200, 201]. In the following sections, annealing studies on a-ZTO films to alter the defects will be discussed.

4.6 Annealing with In-Situ Monitoring of Resistivity of a-ZTO

4.7 Introduction of Annealing with In-Situ Monitoring of Resistivity of a-ZTO

There is a considerable interest in Transparent Conducting Oxide (TCO) thin films for optoelectronic devices, including thin film solar cells, OLEDs, flat panel displays, and anti-frost window coatings [7, 8, 10, 36, 37, 202]. TCOs are semiconductors which possess a wide bandgap, exhibiting a high conductivity and visible-range transparency (E_g >3 eV) simultaneously. Recently increased attention has been given to amorphous oxide TCO materials, which carry the benefit of low synthesis temperatures and higher mechanical flexibility while maintaining a high electrical quality [7, 8, 193]. In recent decades, Indium Tin Oxide (ITO) and Indium Gallium Zinc Oxide (IGZO) have been extensively studied. As a result, a-IGZO has been achieved with resistivity around 10^{-3} ohm-cm, while exhibiting less than 10% absorption in the visible range of the light spectrum concurrently [8, 54, 91, 92]. However, scarcity of Indium material and concerns over health and environmental exposure has spurred a search for more sustainable alternatives [194, 195]. In this regard, one of the best alternatives is amorphous Zinc Tin oxide (a-ZnSnO), which is a low-cost and abundant compound material [196], which is already being used in solar cells and OLEDs, TFT and displays [37, 202]. However, the key to the performance of ZnSnO has been the development of annealing processes to control the defect profile of the films. This is particularly the case for low temperature, or room temperature deposited films [9, 14, 26]. The exact defect chemistry of a-ZTO is still under extensive investigation [25]. However, most studies have been focused on measurements of the properties of a-ZTO films before and after annealing [11, 28–31]. Here, we present an in-situ study of ZTO, which aims to determine ideal annealing procedures for the films by examining the resistivity of the films during the annealing process. To ensure compatibility with cost effective synthesis procedures, annealing temperatures are kept below 300 °C.

This work presents an in-situ observed annealing study on a-ZTO to highlight

the importance of the duration of annealing time. To investigate the annealing temperature significance of the activation energy of reaction that was derived from rearranged Arrhenius equation $ln(R_{sh}) = \frac{-E_a}{k}(\frac{1}{T})$, where using $ln(R_{sh})$ versus $(\frac{1}{T})$ graph slope. The highest region of activation energy of the reaction was found within a rapid decrease in the slope. This activation energy is used to determine the area of the greatest rate of change with time. These studies allow us to select the lowest temperatures where the most significant changes in resistivity of samples occur by finding a lower annealing temperature. In doing so, we have found a range of values where small improvement is gained for increases in annealing temperature. In this range, it was observed that an increase in total annealing time served as a substitute for increasing the temperature. This could have importance for device manufacture, where temperatures must be kept below certain values <300 °C, for example, in the case of substrates that are not suitable for high temperatures.

In the next section, the process of annealing with in-situ monitoring of the resistivity of a-ZTO films will be outlined.

4.8 Experimental Methods

Figure 4.5: An image of 38 nm thick a-ZTO film deposited at 300 °C on Glass substrate.

All films were deposited on standard microscopy glass slides as shown in Figure 4.5 (Thermo Scientific 1x1 cm, 0.8-1mm thick).

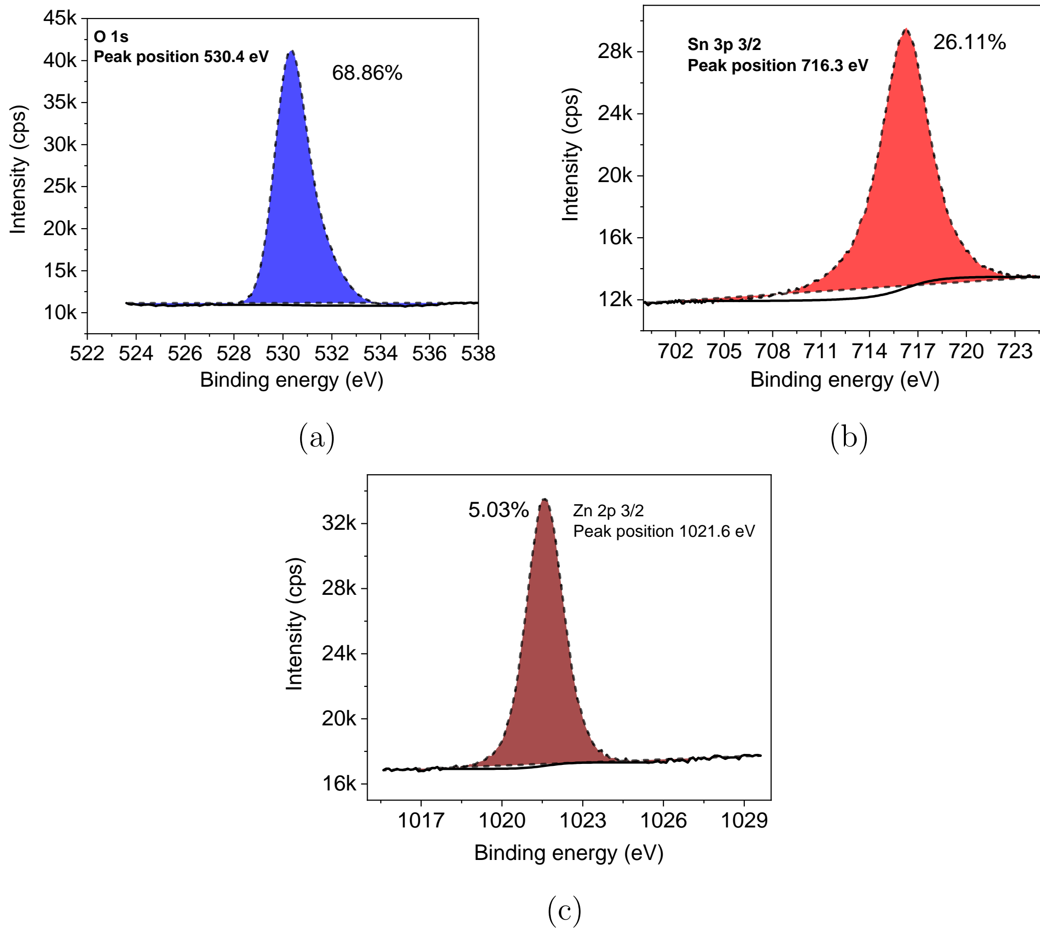

Figure 4.6: a-ZTO film deposited at 300 °C and composition study by XPS, where (a) - O XPS data, (b) - Sn XPS data, (c) - Zn XPS data.

Amorphous - Zinc Tin Oxide (a-ZTO) films were synthesized via non-reactive Radio Frequency (RF) magnetron co-sputtering (the used system is given 3.1.2). Films were sputtered from 99.99% purity ZnO and SnO_2 targets in an inert argon atmosphere. Simultaneously, the total gas pressure of the sputtering chamber was maintained constant at 1×10^{-3} mbar, with constant Argon partial pressure. The substrate temperature used was 300 °C for all thin film depositions. This temperature was found to produce our best-performing films. As deposited, and after annealing, the film's carrier concentration, electron mobility and resistivity of all films in this work were measured at room temperature by using the Hall system in the Van der Pauw method, where four contacts were contacted with

silver wire using silver adhesive. These four contacts are placed on the four corners of the sample. Transmittance and reflection spectra of the films were measured using a Perkin Elmer Lambda 650 UV-Vis Spectrometer. The thickness values of the films were measured using X-Ray Reflection (XRR) on a Bruker D8 discover with a monochromated Cu source. Meanwhile, the amorphous nature of the films was confirmed via X-ray diffraction (XRD) using a Bruker D8 Advance with an unmonochromated Cu source (XRD). These a-ZTO films were grown with a precise Zn/Sn ratio in order to indicate the consistency of the annealing studies. The elemental ratio of one of the a-ZTO films is as shown in Figure 4.6.

4.9 Results and Discussion

4.9.1 Optical Properties of a-ZTO Films

Figure 4.7 shows the transmission and reflectance spectra, absorption and absorption coefficient (linear) and absorption coefficient (log) of as-deposited and annealed a-ZTO films. It is clear that the transmission is around 80% ($\approx$ 18% of reflection) for films within the visible spectra region of light. No variation in transmission and reflectance spectra of films. However, 1-2% range noise level in our system results in a small alteration in absorption coefficients as shown in Figure 4.7 (d). All imply that a-ZTO films in this work show high optical transparency within the visible light spectrum range. Transparency is an essential factor in fulfilling the high transparency requirement of some optoelectronic devices, such as TFTs [28].

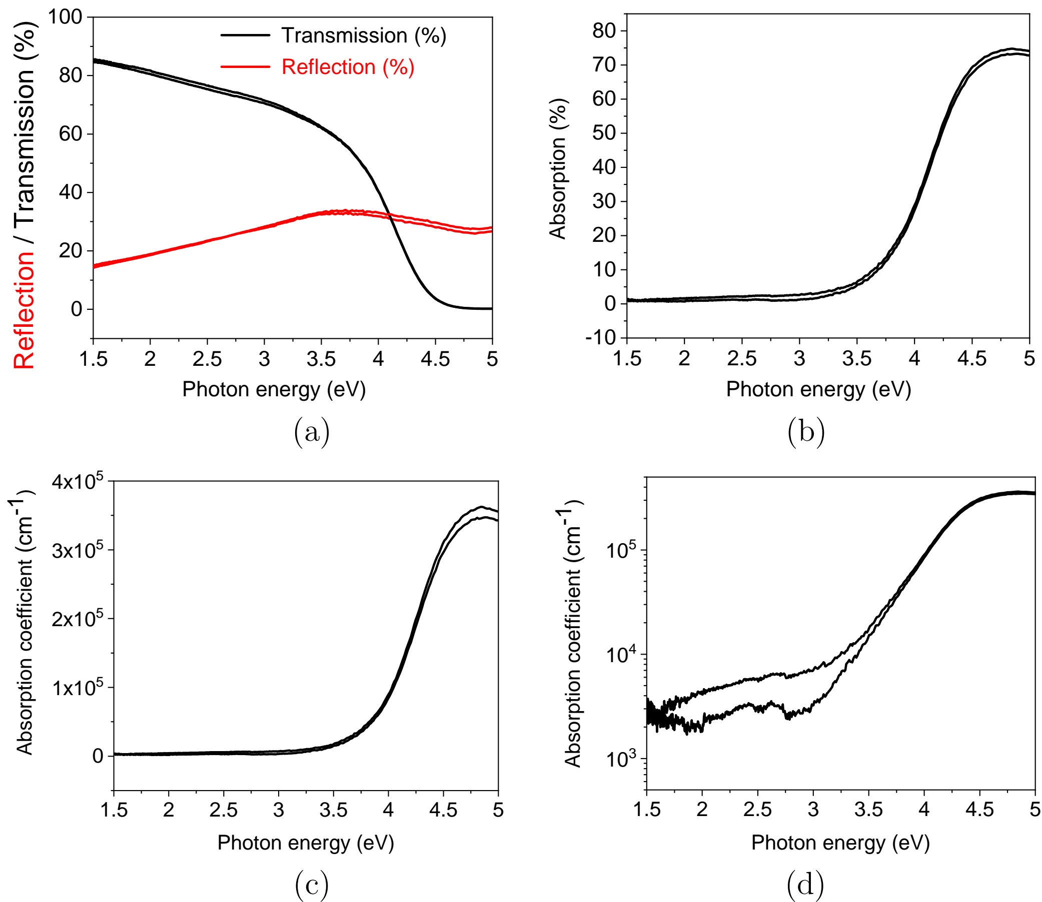

Figure 4.7: Optical properties of as deposited and annealed a-ZTO films, where (a) - transmission (black line) and reflection spectra (red line), (b) - absorption, (c) - absorption coefficient (linear), (d) - absorption coefficient (log) of a-ZTO films.

4.9.2 SEM image of a-ZTO Film

a-ZTO film deposited at 300 °C and the surface morphology of it was examined by Scanning Electron Microscopy (SEM) as shown in Figure 4.8. SEM image confirms that there are no discontinuities and deterioration on the surface of a-ZTO film. This means that smooth surface of a-ZTO film was obtained by magnetron sputtering.

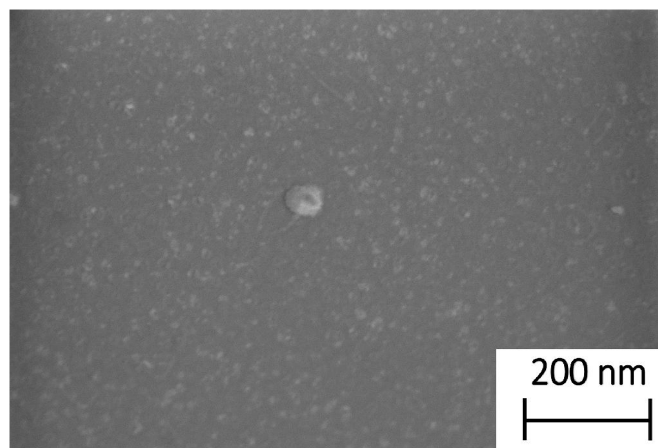

Figure 4.8: SEM image of 38 nm thick a-ZTO film deposited at 300 °C on Glass substrate.

4.9.3 XRD and XRR data of a-ZTO Films

The thickness of the films was measured by the high-resolution X-ray Diffractometer. X-ray Diffraction (XRD) confirmed the amorphous nature of a-ZTO films.

Figure 4.9 (a) shows XRR data of 38 nm thick a-ZTO film. Fittings were done via the Bruker Leptos software program, where fitting matches very well between simulation and measured data of the sample. This also highlights that XRR data give thickness, roughness and density of the materials in this work. The average density of the 6.76 g/cm^3 and roughness of $\approx$ 0.42 nm for a-ZTO was obtained.

Fig 4.9 (b) shows a typical XRD pattern of the a-ZTO films. It is clear that three halo peaks were observed at around 13°, 28°, and 42° due to the presence of amorphous bonds, which vary in length within the material. It is usually called a halo peak and is an indicator of an amorphous structure. The former two peaks originate from the thin film and part of the glass. The peak at 13° is from an amorphous structure. The glass peak is around 20-30°, and this halo peak is consistent with the previous report [177]. The peak at 40-45° is from the XRD sample holder. It can be seen from Figure 4.9 that sharp peaks were not observed by XRD. All a-ZTO samples in this work showed an amorphous structure.

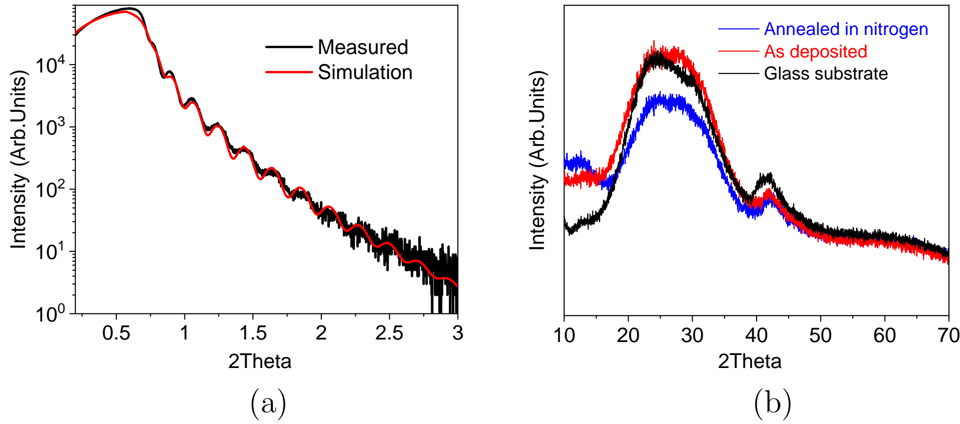

Figure 4.9: XRR and XRD pattern of a-ZTO deposited on SiO_2 glass substrate by Magnetron sputtering, where (a) - XRR pattern of 38 nm thick a-ZTO, (b) - XRD pattern of glass, a-ZTO as deposited and annealed in nitrogen atmosphere.

4.9.4 Annealing Studies on a-ZTO with In-Situ Monitoring of the Resistivity in Nitrogen Atmosphere

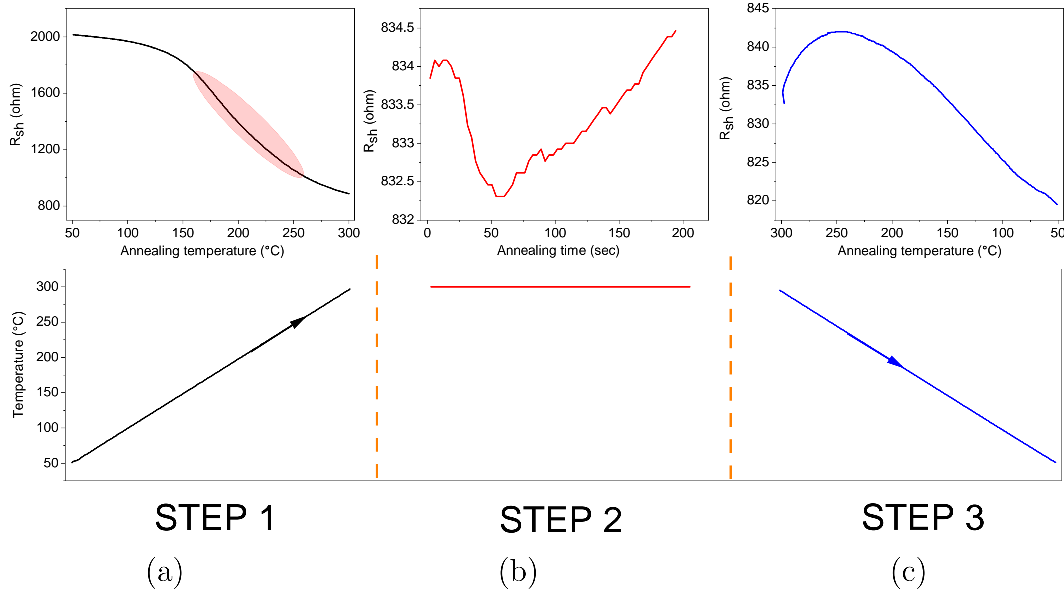

Figure 4.10: Schematic diagram of an in-situ annealing method with a linear four-point probe, where (a)- heating up from 50 °C to a target temperature, (b)- maintain at the target temperature that saturates the lowest sheet resistance, (c)- cooling down from the target temperature to 50 °C. Measurement progresses from a) to c) continuously. Below the graphs are an illustration of the temperature at each step.

The sheet resistance change of films was monitored *in-situ* during the annealing to achieve the best properties of films (a detailed description of the instrument can be found in this section 3.4.1). Annealing setup has also been utilised in our previous work [203, 204]. a-ZTO thin films were heated from 50 °C to an annealing temperature as shown in Figure 4.10 (a), step 1, and then maintained at the target annealing temperature until the lowest resistivity was reached (case for this samples at around 50 seconds) as shown in Figure 4.10 (b), step 2. Finally, samples were allowed to cool down from the target temperature down to up to 50 °C at the same rate as the heating up process as shown in Figure 4.10 (c), step 3. Figure 4.10 (a) shows a change in slope of the resistivity improvement curve, step 1 (shaded with red), which was observed, and temperature points have been selected within this region for more detailed investigations and also to find a low annealing temperature. Using these curves, the activation energy of the reaction was obtained for a red shaded region in heating up slope by plotting $ln(R_{sh})$ versus 1/T as shown in Figure 4.11 (b).

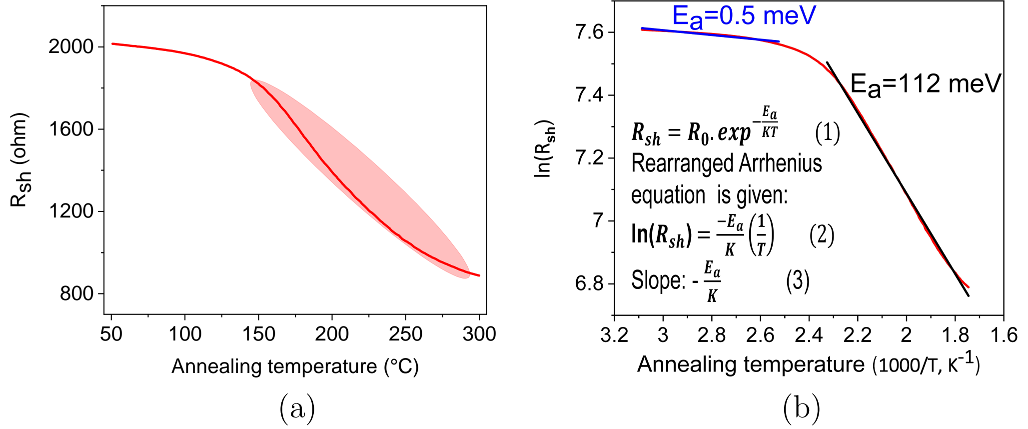

Figure 4.11: A method of calculation activation energy of reaction of a-ZTO annealed in nitrogen environment, where (a) - R_{sh} versus annealing temperature, (b) - calculation of activation energy.

For all samples, the resistivity improvement curve versus temperature and annealing time was recorded as shown in Figure 4.10. All as-deposited and annealed a-ZTO films in this work show an amorphous state, even after annealing films up to 300 °C. The amorphous phase is consistent with other reports, where a-ZTO films annealed up to 600 °C do not show a crystalline structure [205]. To

ensure the consistency of the annealing study, all samples were deposited with the same Zn/Sn ratio, as shown in Figure 4.6. These samples were annealed in 99.99% purity of nitrogen gas atmosphere.

Through the studies of R_{sh} versus temperature slope in Figure 4.11 (a), it was found that the resistivity is not changed much until temperatures at 150 °C by thermal post-growth treatment in a nitrogen atmosphere. All samples in this temperature range show a reduction of resistivity consistent with standard semiconductor thermal activation of carriers. In all cases, the activation energy of the deposited samples is around 0.5 meV, a value consistent with heavily doped a-ZTO [206]. These positive values of the activation energy showed that no films are found to be degenerately doped behaviour prior to annealing, and a discussion of this will be outlined later.

Above 150 °C there is a rapid change in the slope in Figure 4.11 (b). This area is indicated with a shaded region in Figure 4.10 (a), and the largest activation energy value was found in this region; it also can be seen in Figure 4.11 (b) as well. This indicates the onset of a secondary reaction in the film that has energy significantly above that of thermal carrier excitation, while it could be the effect of increasing the temperature on the conductivity of semiconductors. This reaction is observed to be inelastic with changes in resistance being permanent upon cooling to room temperature, indicating a more fundamental alteration of the sample. In other words, this is an irreversible change in the films.

Six temperatures were selected within a high activation region in Figure 4.11 (a) (red shaded region) in order to find the lowest temperature at which effective annealing leading to changes in the carrier concentration and mobility took place. All samples were annealed until the lowest sheet resistance achieved in the nitrogen atmosphere, as described above in Figure 4.10. This is also shown in Figure 4.12 (a) and (b) for chosen temperatures with an in-situ monitoring. Figure 4.12 shows that these two anneal times were 10 hours 30 minutes for annealing temperature 220 °C, and 1 hour 30 minutes for annealing temperature 300 °C respectively. This implies increasing the annealing time with decreasing the annealing temperature or vice versa. These cases have shown that annealing temperature 220 °C can be substituted for annealing temperature 300 °C one

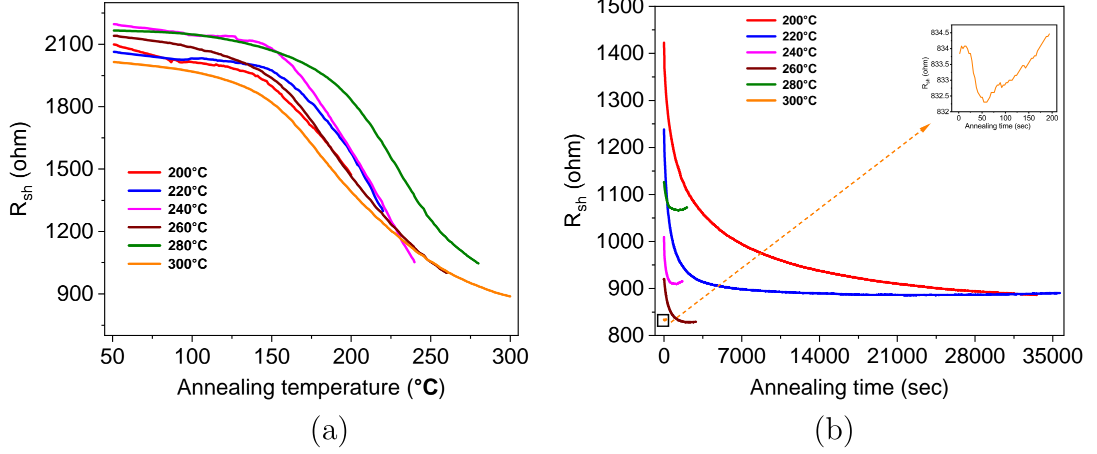

Figure 4.12: a-ZTO films annealed in nitrogen atmosphere at six different temperatures, (a) - is the sheet resistance versus annealing temperature, (b) - is the sheet resistance versus annealing time, where (-) - 200 °C, (-) - 220 °C, (-) - 240 °C, (-) - 260 °C, (-) - 280 °C, (-) - 300 °C.

can compensate for lower annealing temperatures with increasing annealing time without sacrificing the final resistivity values as shown in Figure 4.12.

For the annealed six a-ZTO films, we set a baseline of properties for as-deposited a-ZTO films in order to show consistency. For setting these baseline properties we select the 38 nm-thick a-ZTO films with average conductivity, carrier concentration and mobility 120 S/cm (see black line (-) in Figure 4.13 (a)), $6{\times}10^{19}$ cm^{-3}((-) for Figure 4.13 (b))), and 12 cm^2/Vs individually. Figure 4.13 (a) shows the conductivity and carrier concentration of these a-ZTO films as a function of the annealing temperature and time. For each sample, the temperature was maintained until the resistivity reaches a low value and saturates, and then the temperature was reduced. For annealing temperatures in a nitrogen atmosphere (referred to from now on as an oxygen-poor environment), carrier mobility is independent of the annealing temperatures and atmosphere as shown in Figure 4.13 (c) and only carrier concentration increased following the anneal. This behaviour of mobility is consistent with previous results which showed that the oxygen deficiencies and metal clusters do not only act as carrier donors, but also as scattering sites, hence limiting the carrier mobility in the films. The results in the previous works indicated that electron mobility is enhanced by high-temperature annealing (>400 °C) in a high oxygen content environment

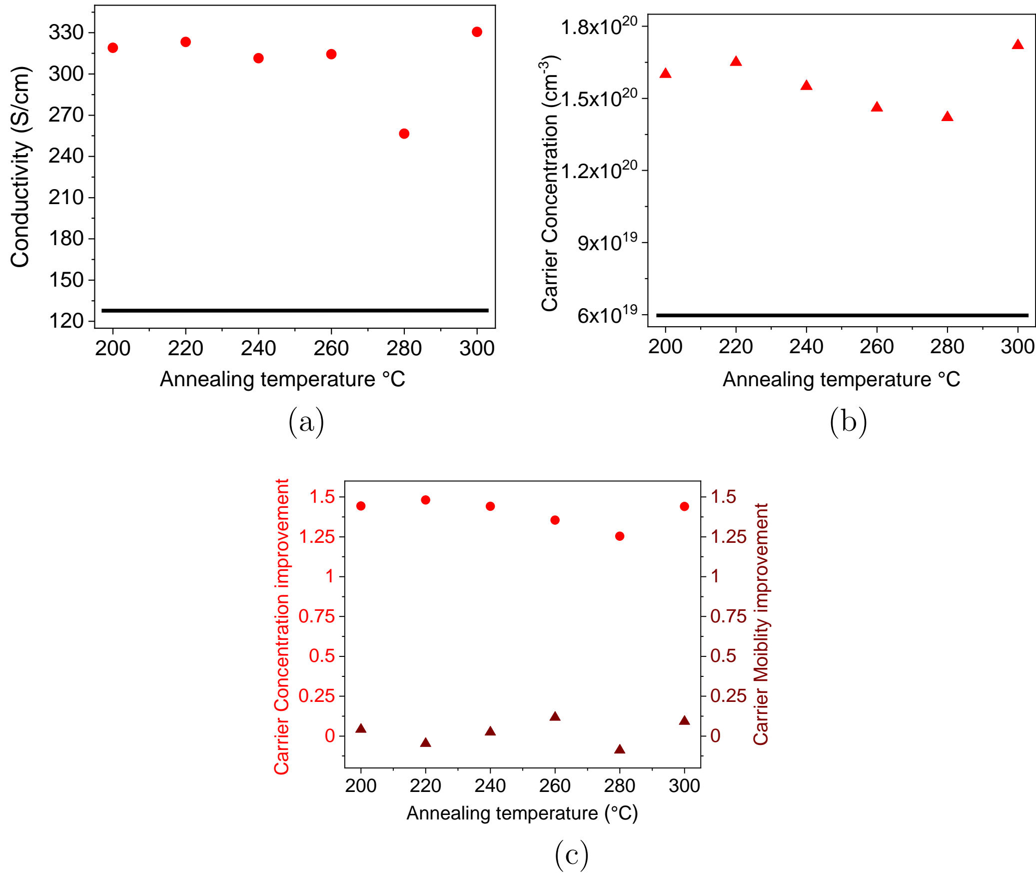

Figure 4.13: a-ZTO films annealed in a nitrogen atmosphere, (a) - conductivity, (b) - carrier concentration, (c) - improvements in carrier concentration (●) and mobility (▲). Here, (-) line shows the initial conductivity (a) and carrier concentration (b) of a-ZTO, and (●) and (▲) for samples after annealing in a nitrogen atmosphere.

[9, 11, 16]. It is worth mentioning that our annealing temperatures are lower than those in other studies, where the aim was to enhance the carrier mobility of the films [11, 31, 205].

Interestingly, it is clearly seen from Figure 4.10 (c) the resistivity of the films gradually declines with decreasing temperature. So that the activation energies of six films were investigated for between 50 °C and 100 °C annealing temperatures, which is prior to achieving the lowest resistivity as shown in Figure 4.14. The positive values of activation energies were observed as shown in Table 4.1. All positive values of activation energies imply that prior to achieving the high-

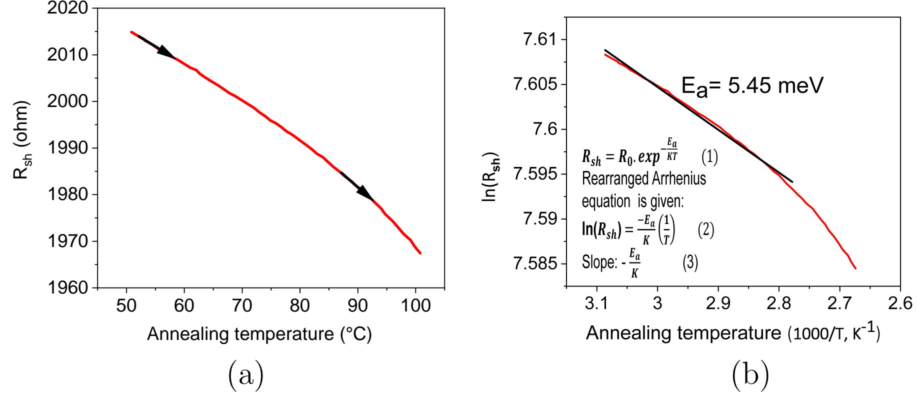

Figure 4.14: An illustration of R_{sh} versus annealing temperature for a-ZTO films prior to achieving the lowest resistivity between 50 °C and 100 °C, where (a) - sheet resistance versus annealing temperature between 50 °C and 100 °C, (b) - calculation of activation energy.

Films annealed at	200 °C	220 °C	240 °C	260 °C	280 °C	300 °C
Prior to (meV)	5.1	4.8	4.62	5.51	5.45	5.45
After (meV)	-3.12	-3.58	-3.44	-1.67	-1.25	-3.24

Table 4.1: Activation energy of films prior to and after achieving the lowest resistivity of a-ZTO.

est conductivity, a-ZTO films showed a semiconducting behaviour. This means that in semiconductors, resistance decreases with increasing temperature. The temperature range (between 50 °C and 100 °C) is a low temperature relatively. However, the temperature of the sample activates a small number of electrons. This is called a thermally activated process. The activation energies of six films after achieving the lowest resistivity were obtained as shown in Table 4.1. R_{sh} versus annealing temperature slope is also shown in Figure 4.15 (a), where the increase in the anneal temperature leads to a decrease in conductivity. This means that samples in this work present a degenerately doped behaviour that is similar to metallic conductive behaviour with a small number of energy states within the conduction band of the materials after achieving the highest conductivity. This can be understood by raising the temperature with increasing the number of free carriers to ionize, which is seen in the resistivity decreasing rapidly. As the annealing temperature is sufficiently high, a large number of the dopants are com-

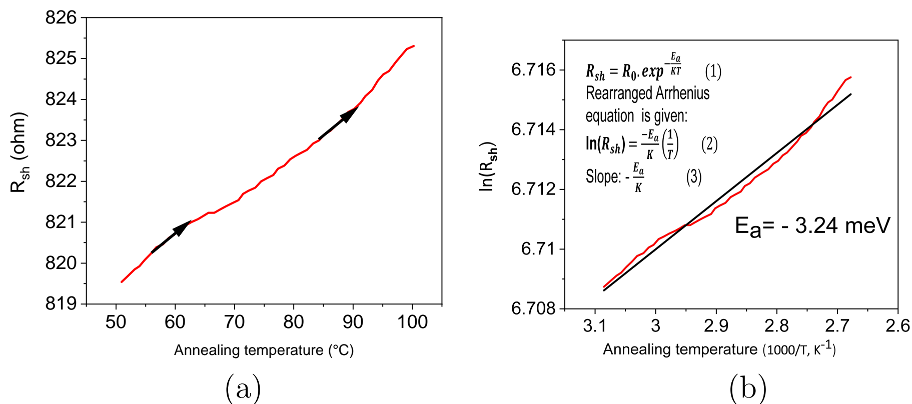

Figure 4.15: An annealing slope for a-ZTO films after achieving the lowest resistivity between 50 °C and 100 °C, where (a) - sheet resistance versus annealing temperature between 50 °C and 100 °C, (b) - calculation of activation energy.

pletely ionized. As a result of that, conductivity starts to decrease (the resistivity is increased) as is the case in metals. It is known that in metals, conductivity decreases by increasing temperature because of a high frequency of collisions of free electrons. All imply that changes in the slope of the R_{sh} versus annealing temperature indicated that the conduction mechanism of films has changed as shown in Figure 4.15 (a). As shown in Table 4.1, it also can be taken into account that the activation energies of films with different values after achieving the lowest resistivity due to samples were degenerated with different levels by six chosen temperatures. Sample annealed at 220 °C is more degenerated than sample annealed at 280 °C, and that is why the sample annealed at 280 °C shows less improvements in the final resistivity. This can be seen from the final carrier concentration of the films as shown in Figure 4.13. To understand this, an extensive investigation of anneal temperature 280 °C needs to be studied due to its close temperature to the synthesis temperature. In this report, the aim is to find a lower annealing temperature; therefore, this region was not focused on. However, a lower annealing temperature should be suitable for specific substrates and device structures. An example would be in the case of polyimides, which can exhibit degradation at temperatures above 260 °C. For flexible polyethylene terephthalate (PET) and polyethylene furanoate (PEF) substrates need to keep the process temperature below the 250 °C and therefore anneal at >220 °C is

desirable to enhance the electrical properties of films [207, 208].

To sum up, this study developed a method for observation of resistance change in situ and in real-time during the anneal. Thus, annealing studies on a-ZTO with in-situ monitoring of resistivity were performed. This aims to achieve better properties with low sample process temperatures. The largest rate of changes in the sheet resistance curve was investigated, while the activation energies were extracted and the activation energy changed most prominently by anneal in the temperature range 200 °C to 300 °C. The best properties of samples are utilised in the annealing process. The conductivity of ≈ 320 S/cm in 38 nm thick a-ZTO was achieved successfully by annealing at temperature 220 °C, which was replicated by annealing at temperature 300 °C. This means that the annealing at a lower temperature can be compensated by performing anneal over a longer period of time and results in a comparable improvement in electric properties. For all films, once the minimum in resistance was achieved resulting from the anneal, the behaviour of the material switched from a semiconducting to a metallic one. This means that annealing has changed the conduction mechanism of the films.

Furthermore, this annealing method was done in a nitrogen atmosphere, and it was achieved at a low temperature. Although the conductivity of samples was enhanced in the nitrogen atmosphere, the carrier mobility remained constant ($\approx$ 12 cm^2/Vs). In certain cases, a-ZTO films must present high conductivity and high electron mobility simultaneously, which is crucial for some optoelectronic devices [209]. The post-deposition treatment method in an oxygen-rich atmosphere was performed to enhance the carrier mobility of a-ZTO. However, most studies have shown that the carrier mobility has improved at high annealing temperature ($>$350 °C) [11, 31, 205]. Several reports have shown that annealing temperatures $\leq$300 °C in the oxygen-rich environment do not show the improvements in electrical properties [31, 205]. Taking into account all of these, the annealing process with in-situ monitoring of resistivity was done in an oxygen-rich atmosphere. The results and findings will be discussed in the next section.

4.9.5 Annealing with In-Situ Observation of Resistivity of a-ZTO in Oxygen-Rich Atmosphere

Annealing samples in oxygen-rich atmosphere method:

The investigations on resistivity changes in the process of annealing a-ZTO films in an oxygen-rich atmosphere have been carried out. In this work, the main aim of the investigation is to improve the carrier mobility of a-ZTO films in order to fulfil a high electron mobility requirement of certain optoelectronic devices [210]. Secondly, annealing temperatures were limited to be below ≤300 °C to enhance the electrical properties of a-ZTO films in the previous reports [31, 205], where the enhancement of a-ZTO carrier mobility was at high temperatures >300 °C. This can be explained by an excess of oxygen within an amorphous network, which means that the incorporation of more oxygen during the annealing (fixed time annealing) decreased the conductivity of the samples observed in these previous reports. Oxygen-rich environment affects intrinsic oxygen vacancy defects in the films as observed in this report, where oxygen vacancy defects act as charge carrier sources [31]. Another concern for this is that one can miss the best

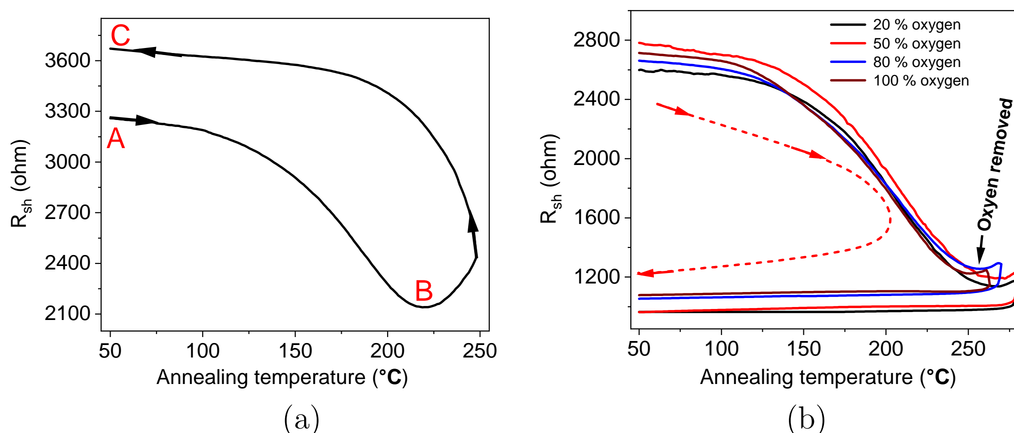

Figure 4.16: Annealing studies on a-ZTO in oxygen-rich atmosphere, where (a) - film heated up from 50 °C (A) up to 250 °C, but the lowest resistivity achieved at 230 °C (B), then a-ZTO film allowed to cool down up to 50 °C in oxygen-rich atmosphere, (b) - films heated up from 50 °C up to at a point of annealing temperature after achieving the lowest resistivity in oxygen-rich atmospheres, then allowed to cool down to 50 °C without oxygen atmosphere (oxygen removed). A red dashed line presents a direction of decrease in the resistivity of samples.

point of saturation of resistivity of samples because of the lack of an annealing

setup with in-situ resistivity monitoring. All imply that aimed to understand

a-ZTO	Thickness	ρ (ohm.cm)	n_c (cm^{-3})	μ_e (cm^2/Vs)
as deposited	38±1 nm	8.19x10^{-3}	6.7±1x10^{19}	12±1
cooling with oxygen gas	38±1 nm	1.05x10^{-2}	5.88±1x10^{19}	9±1

Table 4.2: Electrical properties of a-ZTO film (4.16 (a)) heated up from 50 °C up to 250 °C, then cooled down to 50 °C in an oxygen atmosphere, where ρ is the resistivity, n_c in the carrier concentration, μ_e is the carrier mobility.

the limitations of the annealing temperature ≤300 °C on the electrical properties of a-ZTO films. These limitations can be sorted out by in-situ observation of the resistivity method. Also, the limitations may require tight control of the annealing conditions to solve the issues. All of these can be discussed in the next few paragraphs. As shown in Figure 4.16 (a), a film of a-ZTO (the electrical properties as deposited given in Table 4.2) was heated from 50 °C (point A) to 250 °C. At the same time, resistivity improvement of it was monitored, but this film has achieved the lowest resistivity at approximately annealing temperature 230 °C (point B). When the annealing temperature hits at 250 °C, the film was allowed to cool down to 50 °C. However, during the cooling down from 250 °C to 50 °C, the resistivity begins to increase as clearly seen from Figure 4.16 (a) (B → C sheet resistance slope). Note that whole annealing process was done in the oxygen-rich atmosphere (50% oxygen). The electrical properties of as-deposited and annealed films (50% oxygen-rich atmosphere) were measured, and a comparison is given in Table 4.2. A decrease in electrical properties of film annealed in an oxygen-rich atmosphere was found. Another step to preventing the impact of high-oxygen content in the annealing atmosphere on a-ZTO film is that a film of a-ZTO was heated from 50 °C to annealing temperature ≈265 °C in the 50% oxygen content atmosphere, but when it starts to cooling down from ≈265 °C, 50% oxygen content in annealing atmosphere was removed. The removal of oxygen from the annealing atmosphere results in decreasing in the resistivity of the film is presented in Figure 4.16 (b) (red line slope). Using this method, three a-ZTO films were annealed in the same way and 20%, 80% and 100% of the oxygen-rich annealing atmospheres were examined. Three films were successfully

annealed without sacrificing the conductivity in selecting oxygen-rich annealing atmospheres. Figure 4.16 (b) shows thin films with the greatest improvement in resistivity in an oxygen-rich atmosphere. This means that this in-situ monitoring of resistivity method also assists in improving the resistivity versus temperature curve. Indeed, the films came out with excellent electrical properties as shown in Figure 4.17.

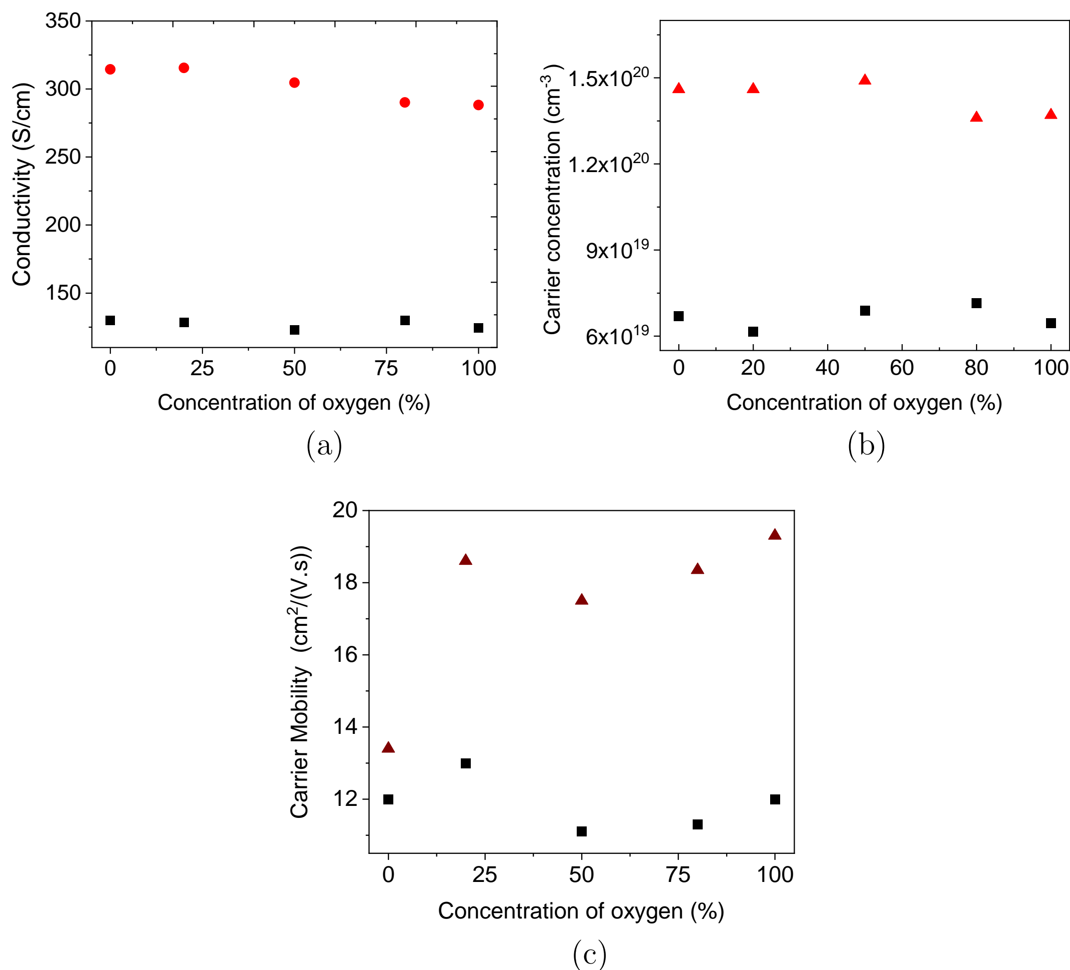

Figure 4.17: a-ZTO films annealed with in-situ monitoring in an oxygen-rich atmosphere, where (■) symbol for as-deposited film's conductivity (a), carrier concentration (b), and mobility (c); (●), (▲), and (▲) conductivity, carrier concentration and carrier mobility of a-ZTO films after annealed. Note that 0% oxygen content means a nitrogen atmosphere.

Figure 4.17 shows the conductivity (σ), carrier concentration (N_e) and mo-

bility (μ) of a-ZTO films annealed in an oxygen-rich atmosphere. The previous reports showed that free carriers were generated by changing the oxygen vacancies during the annealing in a nitrogen atmosphere (oxygen-poor environment) [27, 134]. However, both carrier concentration and mobility were enhanced simultaneously in an oxygen-rich atmosphere in this work. Improvements in carrier mobility of a-ZTO annealed in an oxygen-rich atmosphere can be understood by introducing the oxygen into the films during the annealing that can reduce the scattering centres as it passivates the defects originating from the undercoordinated Sn and Zn [11]. Comparing to the highest conductivity and carrier mobility obtained in this work with previous work showed that they obtained 150 nm thick a-ZTO with conductivity 445 S/cm and carrier mobility 35 cm^2/Vs after annealing at 500 °C in oxygen-rich atmosphere [11, 27]. In this work, a-ZTO films (38 nm) are four-times thinner than previous work that achieved average conductivity 320 S/cm and 19 cm^2/Vs carrier mobility after annealing at around 240 °C in an oxygen-rich atmosphere. This would be a great opportunity to obtain the best electrical properties without a high 500 °C post-growth annealing temperature. This implies annealing study with in-situ monitoring of the resistivity can reduce the annealing temperatures. Meanwhile, more details are needed before concluding the previous investigation on decreasing in conductivity of the sample during the cooling down as shown in Figure 4.16 (a), anneal performed at a lower temperature on a-ZTO film as shown in Figure 4.18. a-ZTO film heated up from 50 °C to 190 °C as shown in Figure 4.18 (a), then stabilised at that temperature for 2 hours as presented in Figure 4.18 (b). Even a film was annealed in an oxygen-rich atmosphere, the conductivity of a-ZTO is still getting better with increasing the annealing time. The electrical properties of the sample as-deposited and after annealing at 190 °C are given in table 4.3.

a-ZTO	Thickness	ρ (ohm.cm)	n_c (cm^{-3})	μ_e (cm^2/Vs)
as deposited	38±1 nm	7.9x10^{-3}	6.22±1x10^{19}	13±1
annealed at 190 °C	38±1 nm	4.5x10^{-3}	1.24±1x10^{20}	18.8±1

Table 4.3: Electrical properties a-ZTO annealed at 190 °C with an oxygen-rich atmosphere, where ρ is the resistivity, n_c is the carrier concentration, μ_e is the carrier mobility.

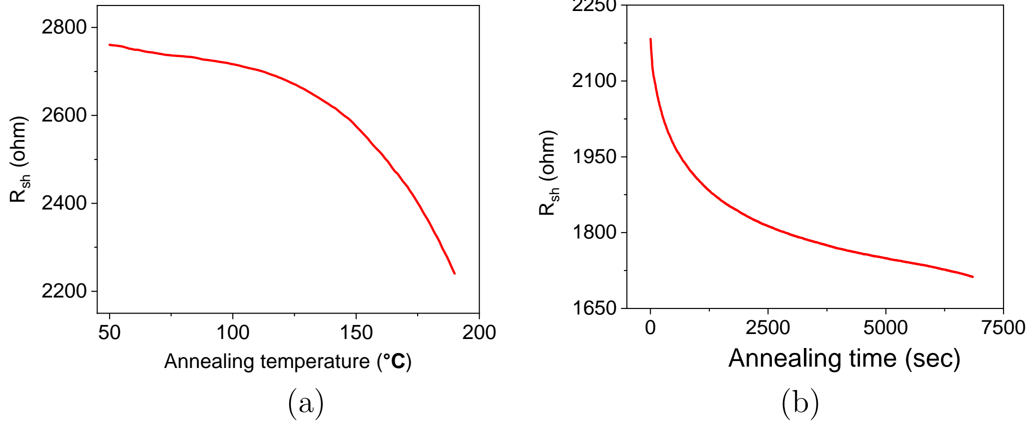

Figure 4.18: Sheet resistance improvements of a-ZTO annealed at 190 °C oxygen-rich atmosphere, where (a) - a-ZTO film heated from 50 °C to 190 °C, (b) - then maintained at 190 °C for two hours.

A lower temperature means that a higher temperature degrades the electrical properties of the samples. As a result of that, more oxygen from the annealing atmosphere interacted with oxygen vacancies in the films, which caused a decrease in carrier concentration. This can be explained as high temperature can provide more reactions in the thin films within a shorter period of time, where oxygen plays a key role as a catalyst [211]. That is why previous works confirmed that annealed a-ZTO films at up to 300 °C showed an increase in resistivity [31, 205], where there was a lack of the in-situ annealing set up or not appropriate annealing temperature for a-ZTO (>200 °C).

Interestingly, all as-deposited thin films do not show a degenerately doped semiconductor behaviour prior to achieving the highest conductivity. However, films after annealing in an oxygen-rich atmosphere, these films also showed a degenerated conductivity behaviour, where sheet resistance and annealing temperature slope between 50 °C and 100 °C was investigated after achieving the highest conductivity as shown in Figure 4.19 that is similar to the samples annealed in the nitrogen case. Studies on activation energies of films showed a negative value of the activation energies as seen in Table 4.4 for samples after annealing in an oxygen-rich-environment. This means that decreasing the resistivity of films with developing the degenerately doped semiconductor films, where more defect states are created within the conduction band and implying that the conduction

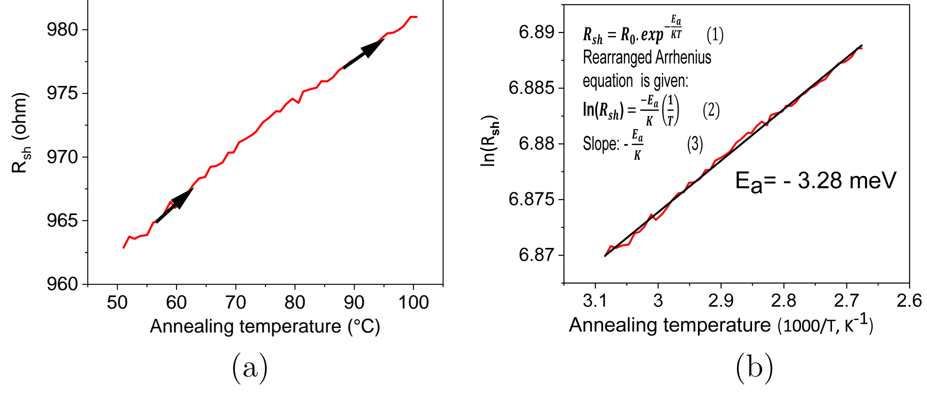

Figure 4.19: An annealing slope for a-ZTO film after achieving the lowest resistivity between 50 °C and 100 °C in an oxygen-rich atmosphere, where (a) - sheet resistance versus temperature between 50 °C and 100 °C, (b) - activation energy calculation.

Oxygen content	20 (%)	50 (%)	80 (%)	100 (%)
Activation energy (meV±0.1)	-3.23	-3.28	-1.81	-1.90

Table 4.4: Activation energies of a-ZTO films between 50 °C and 100 °C after achieving the lowest resistivity in an oxygen-rich atmosphere.

mechanism of the films was altered [212, 213]. Furthermore, the low oxygen concentration in an annealing atmosphere generates more defect levels, which can be seen from the comparison of the activation energies of the films after achieving the lowest resistivity, as shown in Table 4.4. This can be explained by the passivisation of oxygen vacancies in the films that act as the source of the current carriers. Oxygen-rich and poor annealing atmospheres can generate free carriers by altering the concentration of the oxygen vacancy defect centres during the annealing process. However, an oxygen-rich atmosphere caused to create not only free electrons but also improved film carrier mobility. This is due to passivating the undercoordinated metal clusters by introducing oxygen into materials [11].

In general, as shown in Figure 4.16 (b), higher oxygen content in the annealing atmosphere reduced the annealing temperature for a-ZTO. For example, the annealing temperature for 100% oxygen atmosphere is lower than 20% oxygen atmosphere. Also, samples annealed in a 100% oxygen atmosphere saturated the highest conductivity earlier than those in an oxygen-poor atmosphere (nitrogen

atmosphere). All imply that oxygen accelerates or facilitates whatever reaction appears to improve the electrical properties. Lower annealing temperature leads to reducing certain costs for post-deposition treatment methods and device fabrications.

In the end, a-ZTO films annealed in an oxygen-rich atmosphere revealed that samples achieved good electrical properties when the oxygen gas was removed from the annealing chamber during cooling down. Following that method, films were annealed without the degradation of the electrical properties of the samples around at $\approx$ 240 °C successfully. The best electrical properties were obtained with annealing temperature between <200 °C and <300 °C, although the whole annealing process was done in an oxygen-rich atmosphere. Conductivity and carrier mobility of samples increased by annealing in an oxygen-rich atmosphere simultaneously.

Annealing in an oxygen-rich atmosphere indicates that oxygen was introduced into thin films; following this idea, the subject of much speculation in exchanging the oxygen interface of substrate and film was taken into account. This can be understood recalling that glass substrates consist of oxide, where these oxides might impact on properties of films due to the annealing temperatures. A few samples were fabricated on oxygen-free Boron Nitride substrates to examine this. I will give the results and analysis of that study in the following section.

4.9.6 a-ZTO Deposited on Boron Nitride Substrates

In the previous section, a-ZTO films were annealed in nitrogen and oxygen-rich atmospheres, where oxygen passivated certain metal cluster defects due to interaction with samples. The passivisation in the films indicates that substrates might have impacted the electrical properties of samples during the annealing process, especially oxygen-composed glass substrates. It is worth investigating oxygen exchange between the film and the substrate during the annealing process that has been pointed out previously [214]. A number of samples were grown on the oxygen-free Boron Nitride (BN) substrate at 300 °C as shown in Figure 4.20 (d), and these thin films showed approximately $1\times10^{19}\,\mathrm{cm}^{-3}$ carrier density, but carrier mobility of samples is approximately $0.8\,\mathrm{cm}^2/\mathrm{Vs}$. Comparison with a sample on a glass substrate with $6\times10^{19}\,\mathrm{cm}^{-3}$ of carrier density and $12\,\mathrm{cm}^2/\mathrm{Vs}$ of

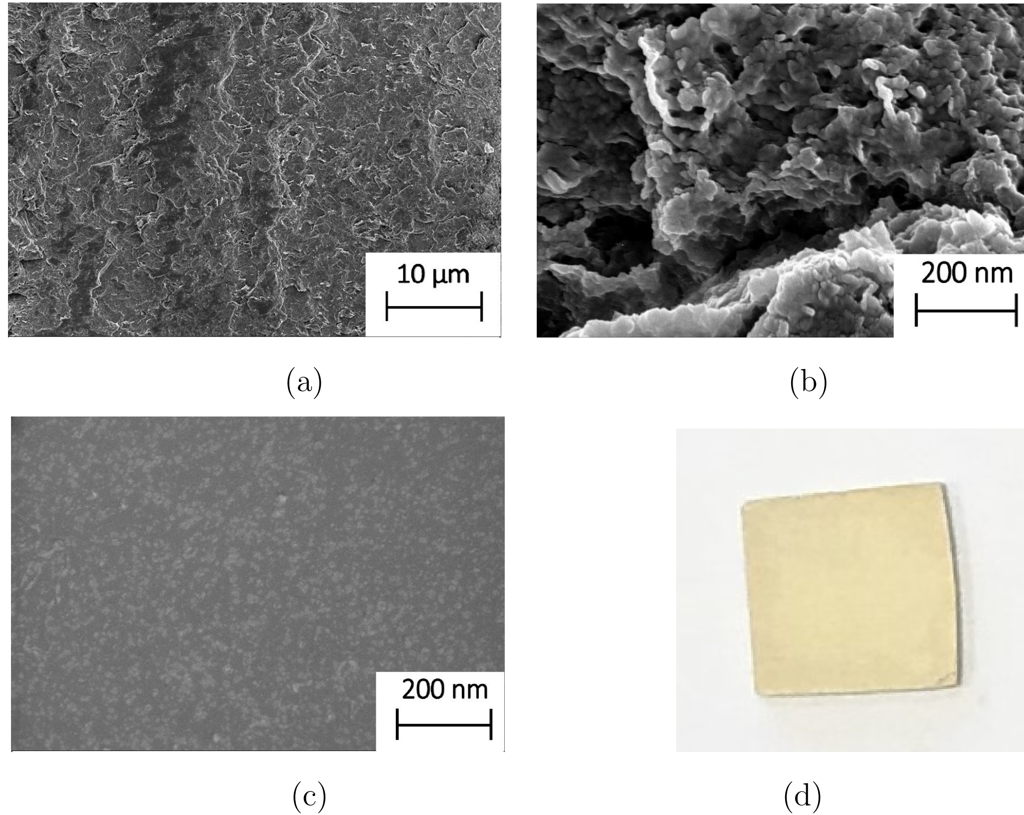

(a) (b)

(c) (d)

Figure 4.20: SEM images of a-$ZnSnO_y$ films, where (a) and (b) - a-ZTO grown on Boron Nitride substrate, (c) - a-ZTO deposited on glass substrate for comparison with (a) and (b), (d) - a-ZTO synthesised on Boron Nitride substrate.

carrier mobility, the electrical properties of the sample on BN are substantially poor. An investigation carried out on these films using SEM system, clearly revealed that boron nitride as substrate leads to structural deterioration on a-$ZnSnO_y$ samples, such as buckling or cracking as shown in Figure 4.20 (a) and (b). This is due to the thermal stress caused by the differences in the thermal expansion coefficient of boron nitride substrate ($7.2\times10^{-6}\,K^{-1}$ for boron nitride [215]) and glass ($5.5\times10^{-7}\,K^{-1}$ for glass [216]) under the a-$ZnSnO_y$ thin films. It is hard to determine the impact of oxygen-free boron nitride substrate on film properties.

While the origin of oxygen from the substrates was complicated to study due to considerable differences in the thermal expansion coefficient between glass (with oxygen) and Boron Nitride (no oxygen), we observed a deterioration of sample

structure in the case of the oxide-free substrate. In addition, Boron Nitride is a high-cost substrate. This results in increasing the cost of a large number of experiments to finalise the Boron Nitride substrate study [217]. However, annealing studies were pursued, especially for different thicknesses and plastic substrates. All imply that most modern optoelectronic devices are based on low-cost materials, so a task is being performed with reducing the fabrication costs, requiring a low cost of annealing, and others [218], such as low-temperature synthesis and post-deposition annealing method can support all these efforts. An investigation was done aiming to synthesise a-ZTO films at lower temperatures (room temperature). This means a-ZTO films will be deposited at room temperature, and we can subject them to anneal at a low temperature. Also, a-ZTO is a scalable range of materials for production. This means that a-ZTO can fulfil the downscale requirements of optoelectronic devices, such as changing the size of the samples for amorphous oxide materials based on integrated circuits [219]. However, enhancing the electrical properties of the different thicknesses of films is crucial in industrial practice in designing a high-performance small-scale apparatus [220]. In this work, applying this annealing method to different thicknesses of samples can facilitate to obtain attainable properties of films. Finally, another advantage of low-temperature annealing is that one can apply films on flexible substrates. The discussion on these issues will be outlined in the following section.

4.9.7 Annealing Studies on Room Temperature Grown a-ZTO with Different Thickness

In the previous section, low-temperature annealing was proposed. Using this method, we aim to reduce the commercial production costs of a-ZTO films. Firstly, applying the low annealing temperatures on a-ZTO films found in the previous section in order to make a chance of annealing studies on a-ZTO films on flexible substrates that are not compatible with high temperature, such as the high temperature incompatible flexible PET and PEF substrates (>220 °C) [221, 222]. In amorphous network solids, the defect levels in concentration need to be altered to enhance materials' efficiency. Certain defects still exist, even a-ZTO films synthesised at RT, where they worsen the electrical performance of the materials, reducing electron mobility by metal cluster scattering centres [25].

In addition, different thicknesses of the samples without undesirable effects can be achieved by annealing [144, 223]. For example, solar cells and OLEDs require very thick films as transparent contact, and TFTs require ultra-thin films [146]. In TFT applications, we need to control and vary the film thickness for a decrease in on/off ratio and a negative shift in threshold voltage. This shows that the electrical characteristics of AOS TFTs are governed by the semiconductor layer thickness (**d**) [144, 146, 224]. Even though the thickness is a crucial factor in these TFTs, they need to be treated in different atmospheres to enhance the electrical characteristics and gate bias instabilities. Being an essential element for these TFT structures [225, 226], a-ZTO is a promising multi-functional material system for other applications as well [224]. Most applications require very specific properties that can be developed by the post-annealing method. Thus, it is essential to know how these post-deposition treatments for thin films with different thicknesses can perform and control.

Synthesis of a-ZTO films at room temperature:

a-ZTO were deposited at room temperature in the non-reactive RF Magnetron (described here 3.1.3) chamber, which used the 99.99% purity of a Zinc Tin Oxide custom composition target (where a mixture is composed of 75% of SnO_2 and 25% of ZnO). At the same time, the total gas pressure of the sputtering chamber was maintained constant at 1.6×10^{-3} mbar with constant the 99.99% purity of argon partial pressure. The power applied on a ZTO custom target was 75 W. This is different from the previous sections' synthesis method due to using a custom target for these a-ZTO films. Firstly, ZTO custom target needs only one power source that is easy to use and control. Secondly, previously optimised a-ZTO films using two ZnO and SnO_2 targets separately in current noreactive sputtering chamber, obtained the best performing films with a range of Zn:Sn ratio [104].

a-ZTO synthesis	Zn (%)	Sn (%)	O (%)	Zn:Sn ratio
RT	4.4	26.4	69.3	0.17
300 °C	5.0	26.1	68.9	0.19

Table 4.5: Elemental ratios of a-ZTO grown at RT and 300 °C.

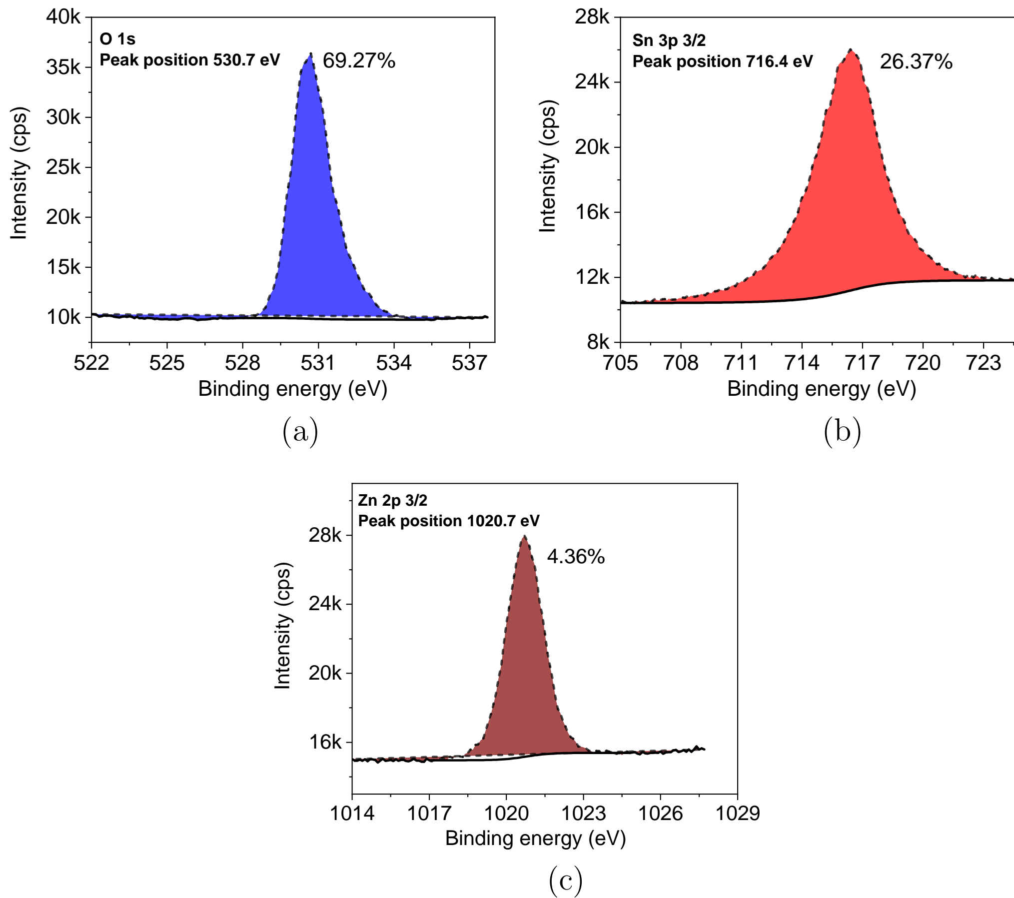

Figure 4.21: a-ZTO film grown at RT and composition study by XPS, where (a) - O XPS data, (b) - Sn XPS data, (c) - Zn XPS data.

Figure 4.22: Images of a-ZTO films with different thicknesses, where (1) - 38 nm, (2) - 77 nm and (3) - 117 nm thick a-ZTO.

For the ZTO custom target, the previous range of Zn:Sn ratio used as a reference for developing a ZTO custom target in order to deposit films is in line with the best films of previous work. The composition of the films was measured

by the XPS system as shown in Figure 4.21, which is consistent with films that were synthesised at 300 °C (previously optimised in this work [104]) as shown in a comparison Table 4.5. Figure 4.22 shows images of a-ZTO films with different thicknesses.

Optical properties of different thickness of a-ZTO films

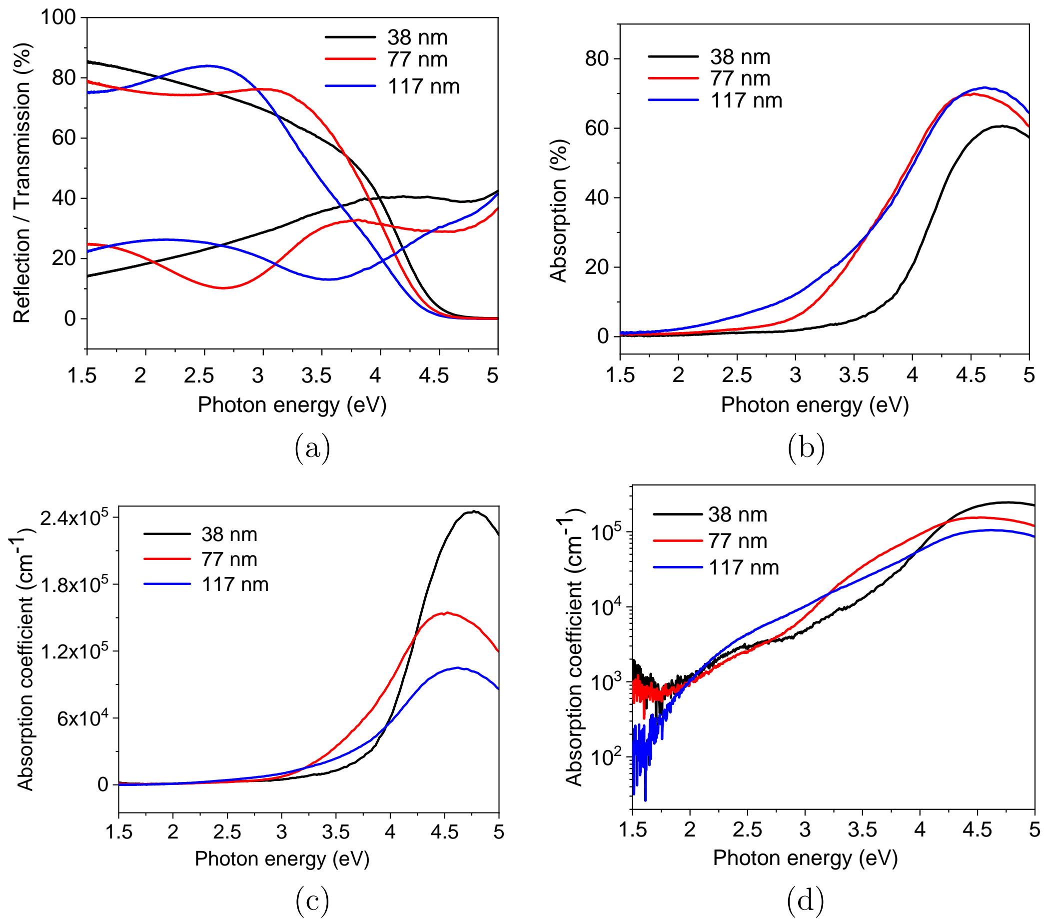

Figure 4.23: Optical properties of different thickness of a-ZTO films, where (a) - transmission (black line) and reflectance spectra (red line), (b) - absorption, (c) - absorption coefficient (linear), (d) - absorption coefficient (log) of different thickness of a-ZTO films.

Figure 4.23 shows the transmission and reflectance spectra, absorption and absorption coefficient (linear) and absorption coefficient (log) of different thicknesses of a-ZTO films. It is clear that the transmission is around 80% (≈ 18% of reflection) for films within the visible spectra region of light. However, a varia-

tion in transmission and reflectance spectra was observed because of the thickness difference in the films. Here, with increasing thickness, more oscillations are observed in the transmittance and reflectance spectrum of a-ZTO films because of the light interference in the films. The interference is due to an alteration in the amplitude of the transmitted wave of light, where scattering and absorbing the light occur. As a result, absorption of thick a-ZTO films is higher than that in thinner due to a variation in thickness results in changes in the density of these films. This results in some photon energy being absorbed by films when the light goes through the films. All imply that transmittance is inversely proportional to the absorbance of films. In addition, the thicker film showed more transparent in the long wavelength of the visible region of light, such as 117 nm thick a-ZTO showing transmittance of 84% around 470 nm (2.6 eV), but this is not true for 30 nm thick a-ZTO with a transmittance of 75% due to reflections at interfaces between a-ZTO and substrate.

SEM images of a-ZTO films with different thickness:

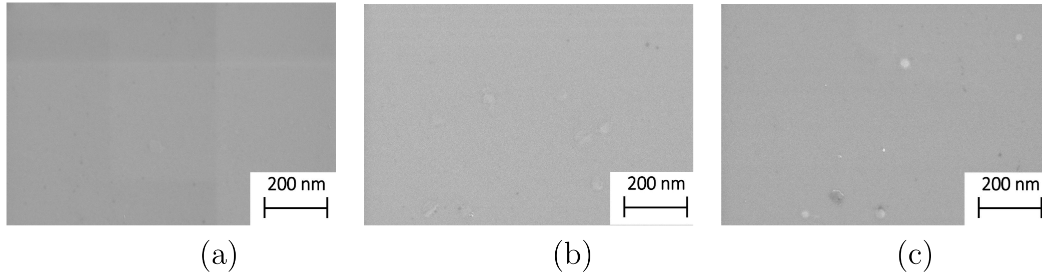

(a) (b) (c)

Figure 4.24: SEM images of 38 nm, 77 nm and 117 nm thick a-ZTO films, where (a) - 38 nm thick a-ZTO, (a) - 77 nm thick a-ZTO, (a) - 117 nm thick a-ZTO.

Figure 4.24 shows SEM images of the three a-ZTO films with the thickness of 38 nm, 77 nm and 117 nm. SEM scans confirmed that all films had a smooth surface, where no surface damages were captured. A small number of unclear particles on the surface of the films could be contaminated by air during the characterisation process.

Room temperature grown a-ZTO films with different thickness annealing in nitrogen atmosphere:

a-ZTO films of various film thicknesses were deposited using the synthesis method mentioned above, then three samples with different thicknesses were an-

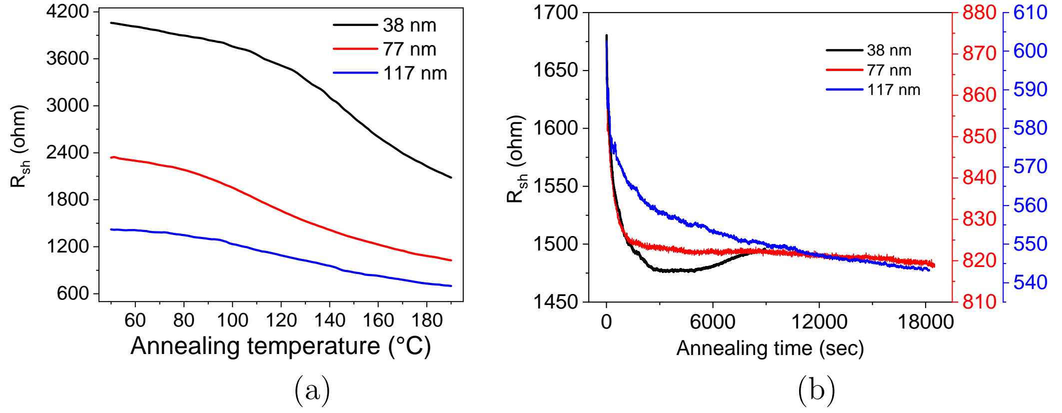

Figure 4.25: Sheet resistance improvements in 38 nm, 77 nm and 117 nm of a-ZTO films with different thickness annealed in nitrogen atmosphere.

nealed from 50 °C up to at 190 °C, then maintained at 190 °C until the resistivity decreased the most. Here, 38 nm thick a-ZTO film achieved resistivity with a short annealing time as shown in Figure 4.25. However, the other two 77 nm and 117 nm thick samples have not been saturated with the highest conductivity by the same time of 38 nm thick a-ZTO, and they need much more time to obtain the final lowest resistivity. This implies that alterations in a-ZTO films during the annealing take place in the bulk of the materials, not the surface as these films, due to these films possessing the same surface area (the consistency of substrates 1 cm×1 cm for all films). Conductivity variations have proved in Figure 4.25 and 4.26 because of sheet resistance obtained with a linear four-point probe method (More description here 3.4.1) and van der Pauw method (More description here 3.4.2). The former obtains sheet resistance using contacts placed along the diagonal of a square film surface with certain contact resistance. The latter calculates the sheet resistance using four corners of the samples with average periphery resistance.

Figure 4.26 shows conductivity, carrier concentration and carrier mobility of the a-ZTO as deposited at RT and annealed in a nitrogen atmosphere. Here, a substantial increase in carrier concentration of all three different thicknesses of the films was obtained, as shown in Figure 4.26 (b). This can be explained by generating a free carrier with altering the defect states of the samples, which originated from the band gap of the films [223]. However, there is no huge variation

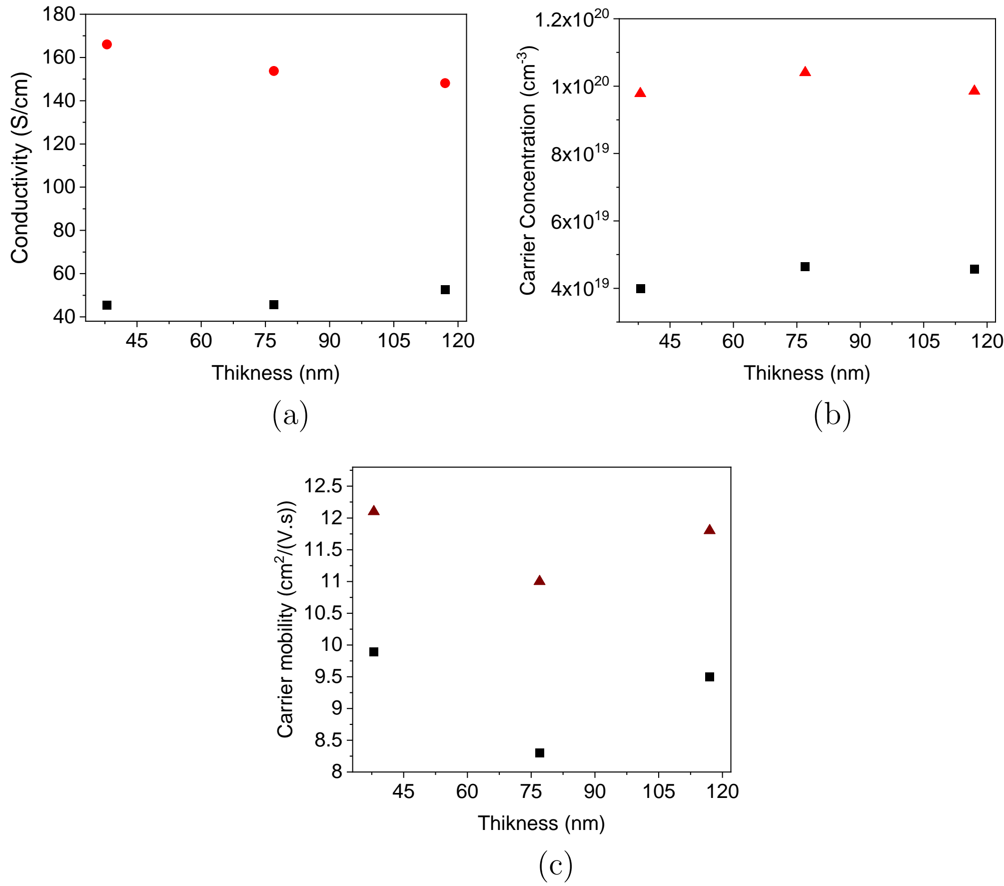

Figure 4.26: 38 nm, 77 nm and 117 nm thick a-ZTO films annealed in nitrogen atmosphere, where (■) symbol for as deposited film's conductivity (a), carrier concentration (b) and mobility (c); (●), (▲), and (▲) conductivity, carrier concentration and carrier mobility of a-ZTO films after annealed.

in carrier concentration in the films with different thicknesses. It might be the effect of the annealing time, where thick samples required a much longer time than thinner film. Here, due to the oxygen-poor atmosphere, annealing time played a key role in creating the free carriers, as shown in Figure 4.25 (a). However, the carrier mobility of different thicknesses of films was enhanced by around 20% due to annealing in the nitrogen atmosphere (oxygen-poor), which did not alter the carrier scattering centres. Prior work suggests that annealing in an oxygen-rich environment is the most effective way to alter these scattering centres [29]. In these films, a small number of scattering centres might be altered by receiving some weakly bonded oxygen atoms within the films when temperature removed

them [115].

To end, the anneal time increased with the increasing thickness of the films and improving the conductivity of films simultaneously. However, no significant change in electron mobility was expected. The difference in annealing time required to optimise films of different thicknesses indicated that changes in films occur in bulk, not on the surface of the films.

Carrier mobility of films with different thicknesses can be enhanced using annealing in an oxygen-rich atmosphere, which is discussed in the next section.

Room temperature grown a-ZTO films with different thickness annealing in an oxygen-rich atmosphere:

a-ZTO films of different thicknesses were annealed from 50 °C to 190 °C, then stabilised at the temperature of 190 °C up to the highest conductivity achieved in an oxygen-rich atmosphere. As shown in Figure 4.27 (b) 38 nm thick a-ZTO film was saturated to the best conductivity within a short annealing time. However,

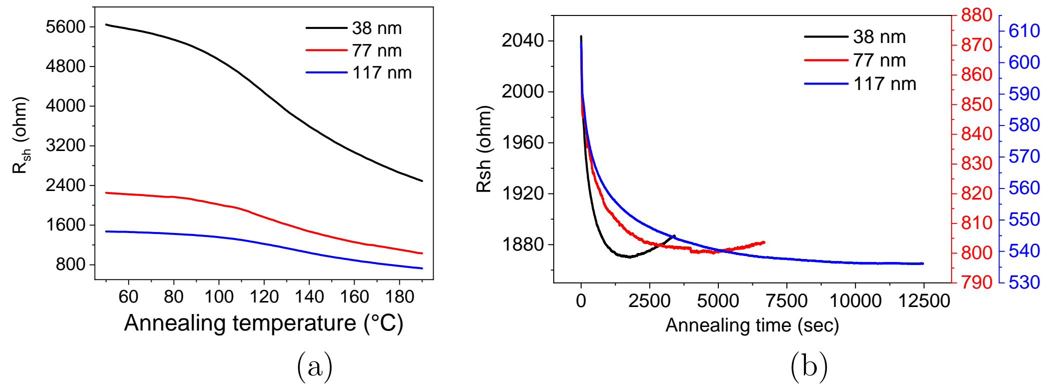

Figure 4.27: Sheet resistance improvements in 38 nm, 77 nm and 117 nm of a-ZTO films with different thickness annealed in oxygen-rich atmosphere.

77 nm and 117 nm thick samples did not attain the highest conductivity with the same annealing time as for 38 nm thick a-ZTO film, where annealing time is much longer than for 38 nm thick a-ZTO film. As shown in Figure 4.27 and 4.28 we obtained different sheet resistance values from measurements via a linear four-point probe method (More description here 3.4.1) and van der Pauw method (More description here 3.4.2). Sheet resistance is calculated by applying the contacts on along the diagonal of the sample surface using a linear four-point probe

method. The sheet resistance of films can be measured using the four corners of the samples with average periphery resistance via the van der Pauw method. As

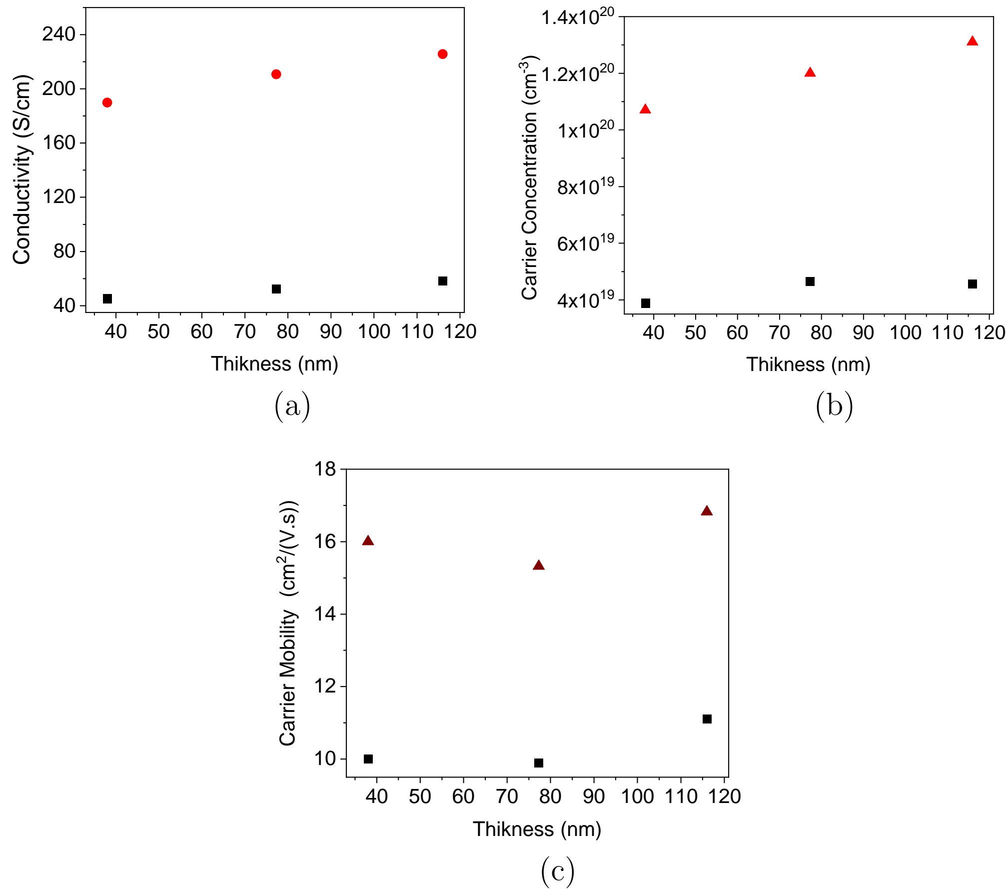

Figure 4.28: a-ZTO films with variety thickness annealed with in-situ monitoring in an oxygen-rich atmosphere, where (■) symbol as-deposited sample's conductivity (a), carrier concentration (b) and mobility (c); (●), (▲), and (▲) conductivity, carrier concentration and carrier mobility of a-ZTO films after annealed.

it was shown in the previous section, the change in carrier concentration alongside the insufficient change in mobility in an oxygen-poor atmosphere (nitrogen atmosphere) might be due to the absence of oxygen (oxygen deficiency) in the film, which reduces carrier mobility.

Figure 4.28 shows a-ZTO films with different thicknesses annealed in an oxygen-rich atmosphere. Conductivity, carrier concentration and mobility of films were enhanced concurrently. Improvement in carrier concentration originates from the sub-gap states and shallow donor-like states within the bandgap

of materials [115, 206]. The oxygen deficiencies in these films (nonreactive sputtering) create the number of under-coordinated Sn-Sn, Sn-Zn and Zn-Zn bonds, and these bonds can be altered by incorporating oxygen into the materials. Altering these undercoordinated metal atoms reduces the scattering centres. These scattering centres moderate carrier mobility increase [11, 120]. It is worth outlining that, as shown in Figure 4.28 electrical properties of the samples annealed in an oxygen-rich atmosphere were improved better than samples annealed in a nitrogen atmosphere, such as they improved their carrier concentration and mobility. For carrier concentration, which is due to the oxygen gas. It provides the alterations in the defect states with more charge carrier generation [227]. In this case, oxygen might be responsible for promoting the electron transfer in the films [228].

To end, conductivity and carrier mobility of different thickness a-ZTO films were enhanced due to an oxygen-rich atmosphere, but these values are higher than those for the films annealed in an oxygen-poor atmosphere. This is due to reactive oxygen gas. Also, two synthesis temperatures for a-ZTO films were investigated. The results of the room and high deposition temperature will be outlined in the next section.

4.9.8 Role of In-Situ Annealing

The optimisations of a-ZTO films at different growth temperatures must be taken into account to reveal the effects of these temperatures on the performance of a-ZTO. The optical and electrical properties can be controlled by one of the synthesis conditions, such as deposition environments and growth temperatures. A comparison of the electrical properties of a-ZTO synthesised at room temperature (RT) with a-ZTO grown at 300 °C will be outlined.

a-ZTO	Total thickness	ρ (ohm.cm)	n_c (cm^{-3})	μ_e (cm^2/Vs)
RT	38±1 nm	2.2x10^{-2}	4.0±0.3x10^{19}	9±1
300 °C	38±1 nm	7.6x10^{-3}	6.5±0.3x10^{19}	12±1

Table 4.6: Comparison of electrical properties of the a-ZTO deposited at RT and 300 °C, where ρ is the resistivity, n_c is the carrier concentration, μ_e is the carrier mobility.

The electrical properties of films grown at RT and 300 °C, where films substantially differ in electrical properties from each other as shown in Table 4.6. X-ray Photoelectron Spectroscopy (XPS) composition studies indicated that there is not a huge variation in elemental compositions of samples that were synthesised at room and 300 °C temperature as shown in Table 4.5. A variation in electrical properties of the room and high temperature (300 °C) is due to the films deposited at high temperatures were subjected to in-situ annealing. Both methods used a nonreactive oxygen-deficient sputtering chamber (oxygen-poor environment). An oxygen-deficient atmosphere plays a key role in generating free charge carriers in this type of amorphous material. The vacancies can be created by the synthesis temperature while altering the scattering centres related to the metal clusters. These scattering centres mitigate the carrier mobility increase. At high deposition temperatures, these scattering centres can be reduced by incorporating a tiny amount of oxygen from the sputtering chamber. In other words, samples fabricated at high temperatures possess higher carrier mobility than room temperature synthesised films, as shown in Table 4.6. This can be understood by room temperature synthesis with a low energy of creating M- O- M network formation within the material during the fabrication process, where metal trapping centres or scattering centres might be generated, hence reducing both carrier concentration and carrier mobility concurrently. Synthesis temperature is also impacting on oxidation of states of the Sn and Zn elements, which influences the presence of defects in different ways and levels in a-ZTO material [229]. All this implies that an in-depth study of film synthesis at different temperatures requires that the current magnetron chamber would have to be redesigned to measure the conductivity in-situ.

To conclude, the changes in the electrical properties of samples deposited at room and 300 °C were compared. The synthesis temperature is dominated by in-situ annealing, altering the films' properties. The studies on a-ZTO are being carried out on fabricating a-ZTO thin films on the bendable substrate.

Moreover, oxide materials are being adapted to bend and roll for applications with different geometry. Depositing a-ZTO films on bendable substrates is an essential fabrication process [230]. In the meantime, enhancing the electrical properties of a-ZTO films on a flexible substrate by annealing is challenging.

These challenges are taken into account and considered for investigations with the current in-situ annealing method. A few a-ZTO films were grown on Kapton substrates and then annealed in different atmospheres; details of annealing will be discussed in the next section.

4.9.9 Annealing Studies on a-ZTO Deposited on Bendable Substrate

The current electronic technologies aim to fabricate TCOs on transparent and light flexible plastic substrates [231]. However, a great amount of concern is raised about annealing aimed at enhancing the performance of films on flexible plastic substrates. It is also known that certain defects in amorphous a-ZTO films have a negative impact on the functionality of devices [232]. Annealing with in-situ resistivity monitoring is a promising method to anneal samples grown on flexible substrates and using the low-annealing temperature found above (<200 °C).

Figure 4.29: An image of 38 nm thick a-ZTO film deposited on Kapton substrate.

Using the same method of deposition at room temperature we previously described, 38 nm thick a-ZTO films were deposited at room temperature on plastic substrates and an image of a-ZTO on Kapton as shown in Figure 4.31.

Optical properties of a-ZTO films on Kapton

Figure 4.30 shows optical properties of a-ZTO films on Kapton® DuPont HN Polyimide film (thickness 0.08 mm), where the transmission and reflection

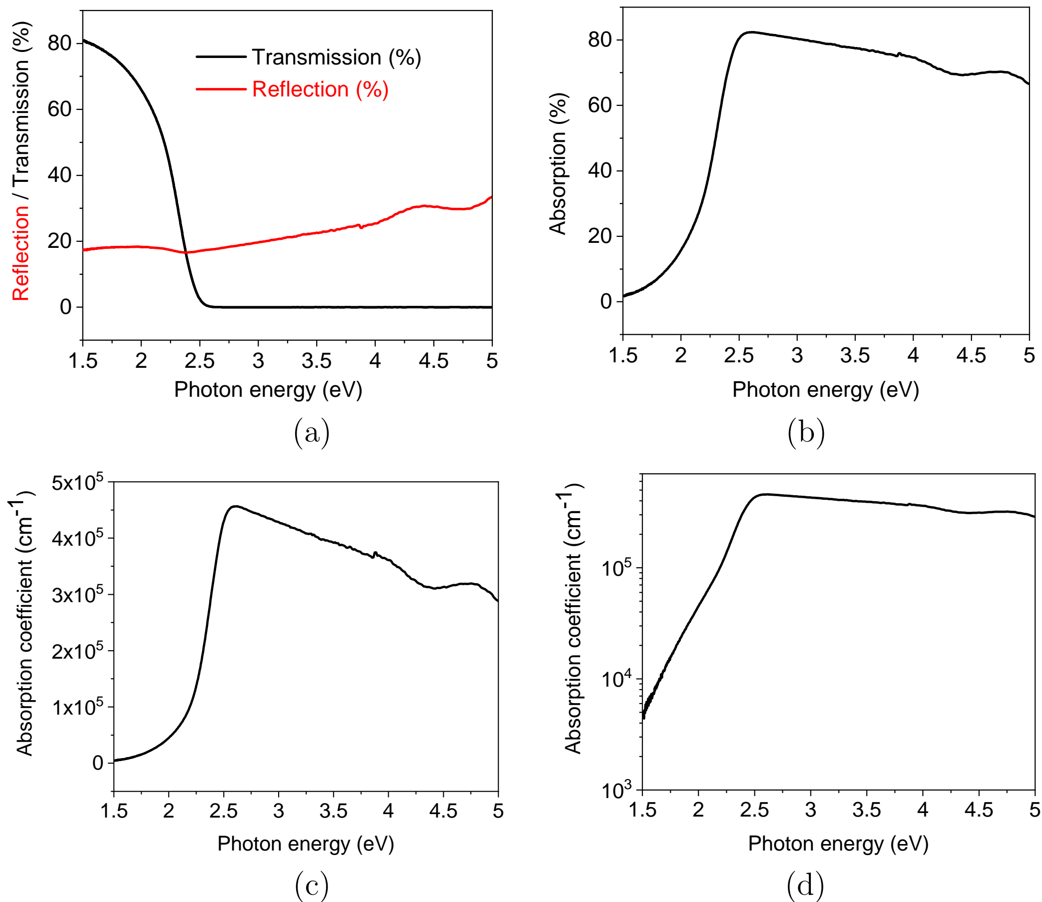

Figure 4.30: Optical properties of a-ZTO on Kapton, where (a) - transmission and reflection spectra, (b) - absorption, (c) - absorption coefficient (linear), (d) - absorption coefficient (log).

spectra were obtained by UV-Vis Spectrophotometer and data of absorption and absorption coefficient are given for a-ZTO films on Kapton substrates. In this work, the optical transmission of a-ZTO films deposited on Polyimide film is lower than films on glass substrates due to Kapton is not a highly transparent substrate. A strong absorption observed above the photon energy of 2.4 eV is due to the bare polyimide film's high absorption property.

SEM image of a-ZTO films on Kapton

Films on Kapton are prone to cracking and deterioration. SEM image of the film is shown in Figure 4.31. No cracks are seen on the film surface. The film's surface without any deterioration is a good sign for bendable substrate-

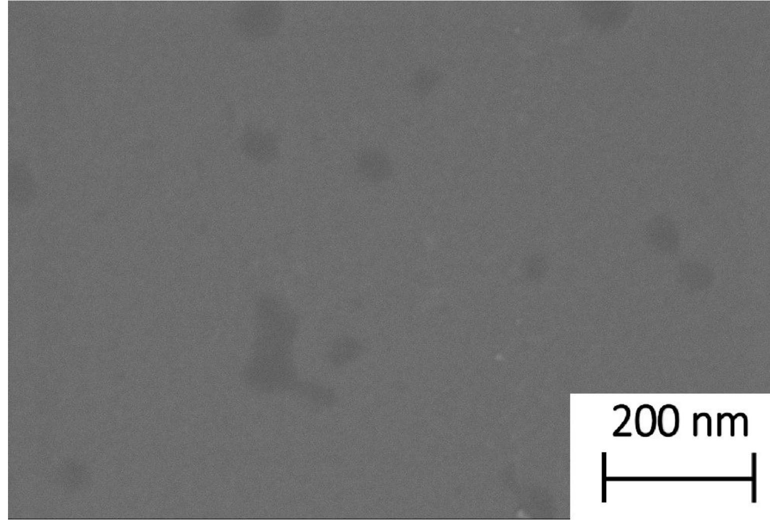

Figure 4.31: SEM image of 38 nm thick a-ZTO film deposited on Kapton substrate.

based electronic applications. One of reliable methods to examine the durability of films on flexible substrates is to perform a bending test by a bending set-up with resistance measurements. This experiment was not done due to a lack of the bending set-up, but further collaboration is desirable.

Electrical properties of a-ZTO films on Kapton

a-ZTO	ρ (ohm.cm)	n_c (cm^{-3})	μ_e (cm^2/Vs)
a-ZTO on Glass	$2.2x10^{-2}$	$4.0 \pm 0.3x10^{19}$	9 ± 1
a-ZTO on Kapton	$2.23x10^{-2}$	$3.8 \pm 0.3x10^{19}$	10 ± 1

Table 4.7: Comparison of electrical properties of 38 nm thick a-ZTO deposited on Glass and Kapton at room temperature, where ρ is the resistivity, n_c is the carrier concentration, μ_e is the carrier mobility.

Two a-ZTO films were deposited on Kapton substrates at room temperature in order to avoid damage to substrates by temperature, where the film's electrical properties are in line with 38 nm thick a-ZTO films deposited on a glass substrate as shown in Table 4.6, then annealed in two different nitrogen and oxygen-rich atmospheres. This means that consistent samples were obtained on two different substrates, as shown in Table 4.7. These film's electrical properties are in line with 38 nm thick a-ZTO films deposited on a glass substrate as shown in Table

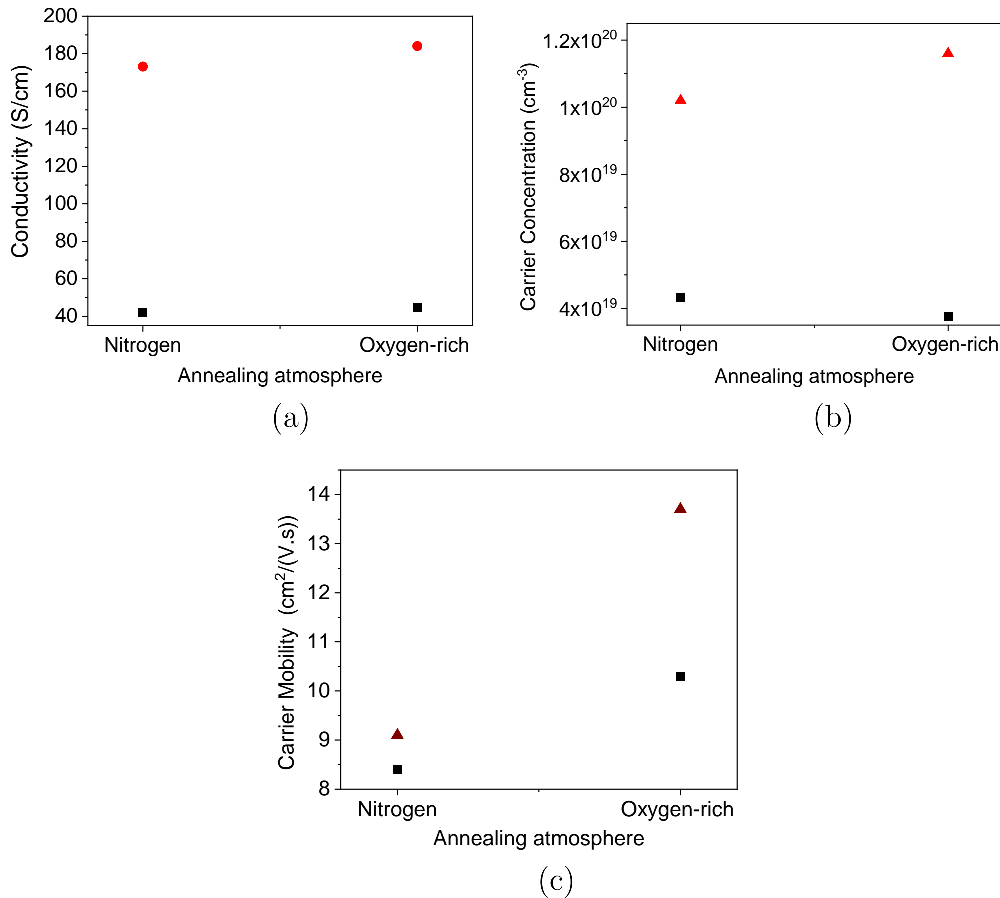

Figure 4.32: 38 nm thick a-ZTO films deposited on Kapton substrates at room temperature and annealed in different atmospheres, where as deposited film's conductivity (a), carrier concentration (b) and mobility (c) show as (■) symbol; (●), (▲), and (▲) conductivity, carrier concentration and carrier mobility of a-ZTO films after annealed.

4.6.

Figure 4.32 shows conductivity, carrier concentration, and carrier mobility as a function of the annealing environment. Specifically, carrier mobility depends on the annealing atmospheres, meaning that an oxygen-rich atmosphere has improved the carrier mobility from 10 cm^2/Vs to 14 cm^2/Vs that is approximately 40% increase. Carrier mobility of sample annealed in nitrogen atmosphere only increased by 10%. All enhancements in electrical properties are associated with altering the defect centres and creating free electrons by annealing atmospheres [233, 234]. There is only one way to improve electron mobility, which is an oxygen-

rich atmosphere due to oxygen atoms incorporated into the films to reduce the scattering centres [11].

4.10 Conclusions

In this chapter, the annealing temperature of a-ZTO films was reduced by annealing with in-situ monitoring of resistivity in the nitrogen atmosphere. Also, the highest conductivity of a-ZTO film was obtained at 220 °C instead of 300 °C by using this method. All electrical properties of a-ZTO films were enhanced in an oxygen-rich atmosphere at around 240 °C annealing temperature, although it was not successful in the previous reports. Annealing studies on a-ZTO films with different thicknesses showed that changes did not occur on the surface of films but rather in the bulk of films. a-ZTO films were deposited on Kapton and then annealed successfully. SEM image verified the appearance and condition of the surface without any damage. In other words, this annealing method successfully achieved highly conductive ZTO films on the plastic substrates.

5

Tuning the Electrical Properties of Amorphous TCOs Including Ultra-Thin Alternative Semiconductor Layers

5.1 Controlling the Electrical Properties of the a-ZTO by Applying Ultra-Thin SiO_x Layers

5.2 Introduction of a-ZTO/SiO_x/a-ZTO Films

Considerable attention needs to be paid to improving the efficiencies of ultra-thin (<10 nm) TCO films. Ultra-thin TCO films are promising candidates for novel energy applications; however, the conversion efficiency of sunlight into electricity with the films needs to be improved to be suitable for real-world applications. To be more exact, for high-performance TCOs-based TFT devices, one would need to produce thin films (<10 nm) with low concentration of defects. In particular cases, a low carrier concentration TCOs and reduced thickness of TCO films for TFTs need to be achieved [33–35]. Controlling the electrical properties of ultra-thin a-TCOs can be done by doping elements. However, doping can reduce the material quality, even if creating free carriers with ionised impurity

scattering centres [37, 38]. In the case of a-ZTO films, achieving ultra-thin a-ZTO films with a low carrier concentration is desirable for specific TFT applications in order to achieve low off-current, and large on-to-off current ratios [32]. One of the standard methods to reduce free carriers is doping, Ga is often used as a wide carrier suppressor element for oxide semiconductors that reduce the oxygen vacancy-related defect density through a strong bonding between Ga and O [235, 236]. However, there is a concern raised by cost and health and environmental issues with Ga [237]. Furthermore, theoretical and experimental works showed Si is the best carrier suppressor [51, 238]. In the previous work, current carrier reduction in Si-doped ZTO (SZTO) TFTs was obtained, where Si content can modify oxygen vacancies, which is the origin of carrier generation in this type of material [239]. However, bulk doping can introduce unwanted side effects into the films, which include dephasing or increased neutral impurity scattering. These can have significant effects on carrier properties. In this work, we explored an alternative method for suppressing the carrier density of a-ZTO films based on the insertion of ultra-thin layers of SiO_x. The goal was to investigate whether previously observed carrier drops seen in multilayers containing SiO_x [39] can be replicated with alternative materials. In other words, a-ZTO was employed in this work. A second goal is to explore the origin of carrier concentration drop in the multilayers, which are composed of a-IGZO and SiO_x [39]. In doing so, the original supposition of the paper, that carrier density differences were due to variations in the oxygen structure of the TCO layer caused by the ultra-thin SiO_x, would be tested.

Following section, ultra-thin a-ZTO films will be layered with ultra-thin SiO_x insulators to reduce the charge carrier of a-ZTO. The main goal of investigations is to tune the properties of a-ZTO with unwanted side effects as mentioned above. Moreover, a-ZTO and SiO_x are composed of low-cost, environmentally friendly, and more abundant elements [2, 196]. Secondly, they show impressive electrical properties to fulfil the requirements of particular energy conversion and TFT-based applications [35]. The results and analysis of layered films will be outlined in the following section.

5.3 Fabrication and Experimental Details of a-ZTO/SiO$_x$/a-ZTO Films

Figure 5.1 (a) shows the structure of a three-layer film consisting of a-ZTO and SiO$_x$. All three multi-layered structures of (amorphous–Zinc Tin Oxide, referred to as a-ZTO) a-ZTO/SiO$_x$/a-ZTO thin films were grown in situ by non-reactive RF Magnetron chamber (magnetron with a rotating sample stage, more info 3.1.3), which used the 99.99% purity of an a-ZTO custom composition target (the mixture of 75% of SnO$_2$ and 25% of ZnO) and SiO$_2$ target individually. At the same time, the total gas pressure of the sputtering chamber was maintained constant at 1×10^{-3} mbar for a - ZTO layers and 6×10^{-4} mbar for SiO$_x$ layer, with constant 99.99% purity of argon partial pressure for both a-ZTO and SiO$_x$ growth. The power applied on a-ZTO custom composition target was 75 W, and for SiO$_2$ target, it was 100 W. In this work, all films were synthesised on standard

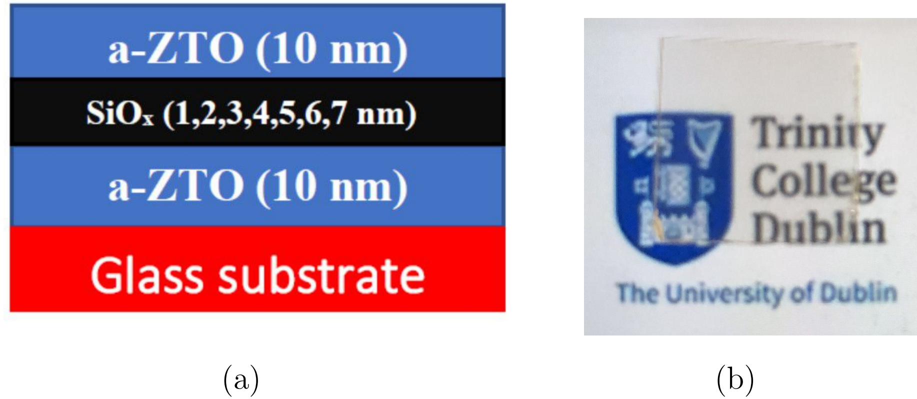

(a) (b)

Figure 5.1: Trilayer structures of a-ZTO/SiO$_x$/a-ZTO films on glass substrates, where (a) - thickness of SiO$_x$ films varied from 1 nm 7 nm between constant 10 nm thick a-ZTO films, (b) - an image of a-ZTO$_{(10nm)}$/SiO$_{x(2nm)}$/a-ZTO$_{(10nm)}$ film.

microscopy glass slides (Thermo Scientific 1x1 cm, 0.8-1 mm thick) as shown in Figure 5.1 (b). Glass Substrates were ultrasonically cleaned in Isopropanol and acetone for 5 minutes sequentially. After that, they were preserved in a load lock chamber with a high vacuum in a magnetron sputtering chamber (1×10^{-5} mbar) for an hour to avoid contamination by the environment. All trilayer film's carrier concentration, electron mobility and resistivity of all films in this work were measured at room temperature by using the Hall system in the Van der Pauw method.

The optical properties of the films were measured using a Perkin Elmer Lambda 650 UV-Vis Spectrometer. The surface morphology of all films was studied via Scanning Electron Microscopy (SEM). The thickness of the films was measured using X-Ray Reflection (XRR) on a Bruker D8 discover with a monochromated Cu source. Meanwhile, the amorphous nature of the films was confirmed via X-ray diffraction (XRD) using a Bruker D8 Advance with an unmonochromated Cu source (XRD). Each layer of trilayer films was grown with a constant sputtering power in order to provide the consistency of composition of each layer.

5.4 Results and Discussion

5.4.1 Optical Properties of a-ZTO/SiO_x/a-ZTO Films

Observed optical properties of trilayer films in this work as shown in Figure Figure 5.3.

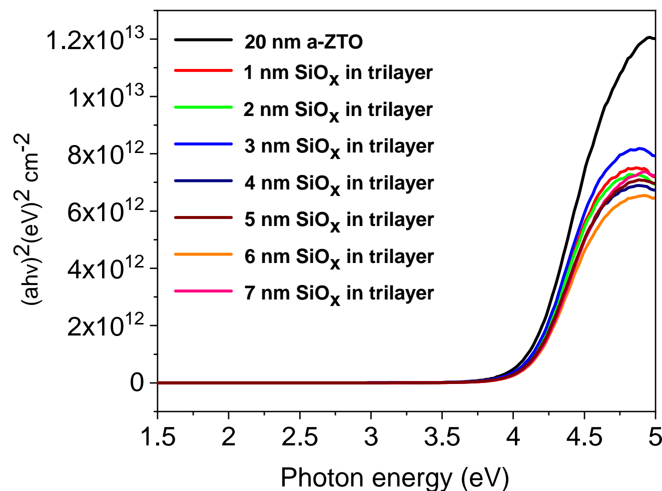

Figure 5.2: Bandgaps of a-ZTO/SiO_x/a-ZTO multi-layers, where thickness of SiO_x between 10 nm thick a-ZTO films varied from 1 nm to 7 nm, where lines are (-) - 20 thick bulk a-ZTO, (-) - 1 nm thick SiO_x, (-) - 2 nm thick SiO_x, (-) - 3 nm thick SiO_x, (-) - 4 nm thick SiO_x, (-) - 5 nm thick SiO_x, (-) - 6 nm thick SiO_x, (-) - 7 nm thick SiO_x in a-ZTO/SiO_x/a-ZTO trilayer films.

Here, the aim is to observe any electron confinement due to the bandgap difference between a-ZTO and SiO_x. Figure 5.3 indicates transmission and reflectance spectra, absorption and absorption coefficient of a-ZTO/SiO_x/a-ZTO

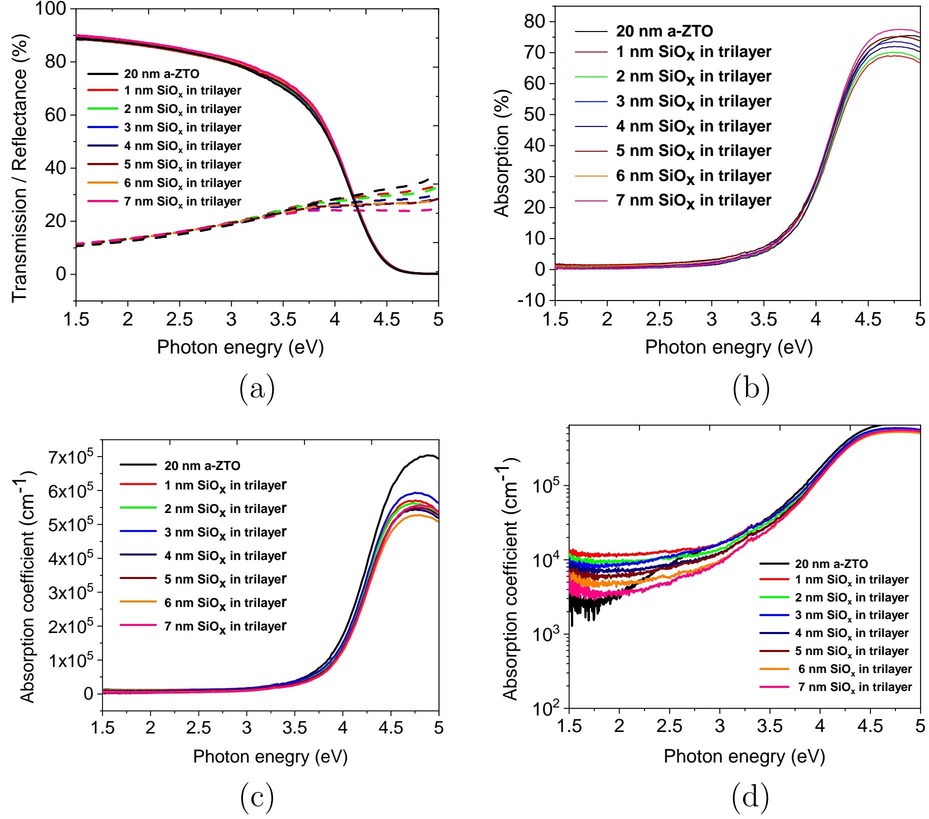

Figure 5.3: Optical properties of a-ZTO/SiO_x/a-ZTO multi-layers, where thickness of SiO_x between 10 nm thick a-ZTO films varied from 1 nm to 7 nm, where (a) - transmission and reflection spectra, (b) - absorption, (c) - absorption coefficient (linear), (d) - absorption coefficient (log) of a-ZTO/SiO_x/a-ZTO trilayer, and lines are (-) - 20 thick bulk a-ZTO, (-) - 1 nm thick SiO_x, (-) - 2 nm thick SiO_x, (-) - 3 nm thick SiO_x, (-) - 4 nm thick SiO_x, (-) - 5 nm thick SiO_x, (-) - 6 nm thick SiO_x, (-) - 7 nm thick SiO_x in a-ZTO/SiO_x/a-ZTO trilayer films.

films, Where the lack of variation in the visible range of the optical properties indicates that the optical behaviour of the a-ZTO/SiO_x/a-ZTO trilayer films without shifts average transparencies and reflections of 80% and 14%, respectively, as shown in Figure 5.3 (a) and (b).

Here, a few noticeable things can be discussed. The first is that the SiO_x does not have a negative impact on the absorption spectra of the material despite probably being quite defective, as shown in Figure 5.3 (b) and (c), and nor does there seem to be any significant bandgap shift in indicating a lack of confinement effects as shown in Figure 5.2. Only observed data with a 1∼2% shifts showed that

variations are ubiquitous and unavoidable by the measurement system. There is little sign of any changes in refractive index due to effective medium behaviour as reported previously [39]. This may be due to the lower volume fraction of the layers in these films compared to the previous nanolaminates. Thus, these data do not bear any value from a physics point of view. However, the increase in thickness of the films could have exciting things to discuss. The impact of varying the thickness on charge carriers seems a beneficial and necessary topic for further investigation.

There significant difference in optical properties of a-ZTOs in a-ZTO/SiO_x/a-ZTO three-layer structure films is not observed as shown in the previous paragraph. However, to understand carrier drop behaviour in the multi-layers, where multi-layers further investigations need to be done, which can be discussed in the following sections.

5.4.2 SEM Studies of a-ZTO and SiO_x Layers

SEM images of top layer a-$ZTO_{(10nm)}$ in trilayer structure and 2 nm thick SiO_x on a-ZTO are shown in Figure 5.4 (a) and (b) individually. Meantime, both a-ZTO and SiO_x film's surface with smooth and continuous properties are shown in Figure 5.4 (a) and (b), respectively. There is no surface deterioration and cracks during the sputtering and characterisation process. No electron trap behaviour has not been observed on the surface of films.

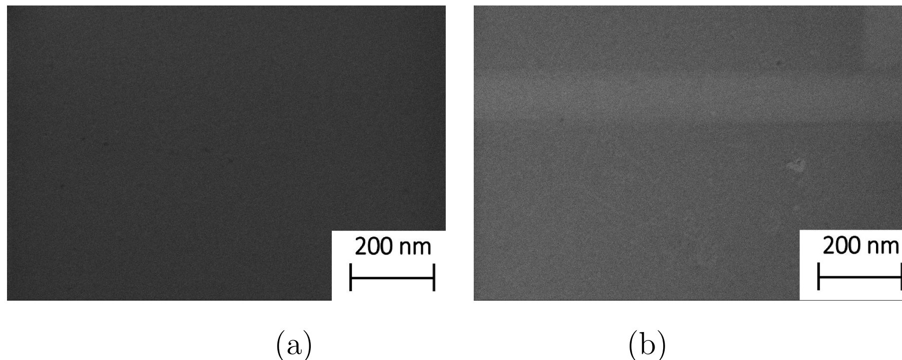

Figure 5.4: SEM images of a-ZTO and SiO_x, where (a) - a-ZTO top layer in a-$ZTO_{10\,nm}$/$SiO_{x(2\,nm)}$/a-$ZTO_{20\,nm}$, (b) - 2 nm thick SiO_x on a-ZTO.

5.4.3 XRD and XRR data of a-ZTO, and a-ZTO/SiO_x/a-ZTO Films

Figure 5.5 (a) and (b) show XRR data of as-deposited a-ZTO and three layers of a-$ZTO_{(10nm)}$/$SiO_{x(2nm)}$/a-$ZTO_{(10nm)}$ film. Data curve fittings were done with the Bruker Leptos software. Strong agreement between the fitted curve (simulation) and measured data was observed for all samples. This indicates that the

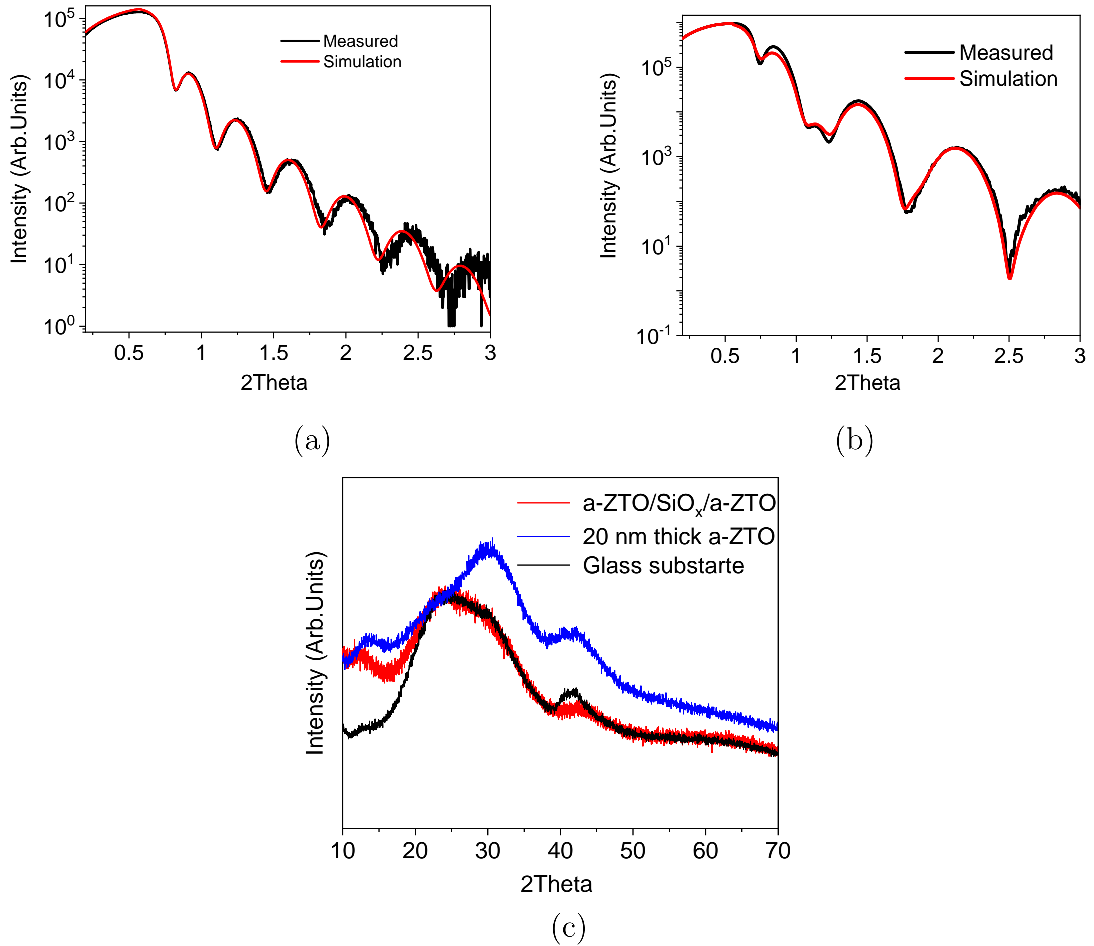

Figure 5.5: XRR and XRD data, (a) - XRR pattern of 20 nm thick a-ZTO, (b) - XRR pattern of a-$ZTO_{(10.7\,nm)}$/$SiO_{x(2.08\,nm)}$/a-$ZTO_{(10.6\,nm)}$ three layer structure, (c) - XRD patterns of glass substrate, 20 nm thick a-ZTO and a-ZTO/SiO_x/a-ZTO multilayer structure.

fitting parameters used were correct and that the samples are a simple three-layer structure, as expected. For example, no formation of interstitial regions or

significant gradients between layers was observed. This XRR data provided the thickness, roughness and density of the materials in this work. The density is 6.74 g/cm^3 for a-ZTO and 2.46 g/cm^3 for SiO_x, respectively. Note that XRR is considered an accurate measurement technique for density determination, which provides proper XRR data fitting; it gives average density across the sample. In a-ZTO/SiO_x/a-ZTO film average interface roughness of a-ZTO and SiO_x is $\approx$ 0.55 nm.

Figure 5.5 (c) shows a XRD data of a-ZTO, a-ZTO/SiO_x/a-ZTO, and Glass with no sharp crystalline peaks. Halo peaks (a wide XRD peak) were obtained at around 12°, 24°, and 32° due to variation in the length of bonding in amorphous networks. Halo peak at 12° is the sign of the amorphous nature of films that was discovered in previous work, and this work suggests that the halo peak at 24° might be originated from the glass substrates [177]. Halo peaks found at 41-44° and 32° could be originated from the XRD sample holder (See Figure 3.6 (b), 2).

5.4.4 Results and Analysis of a-ZTO/SiO_x/a-ZTO Three-Layer Films

Figure 5.6 presents the electrical properties of the a-ZTO/SiO_x/a-ZTO trilayers as a function of SiO_x thickness. It was found that upon increasing the SiO_x to 2 nm, the resistivity of three layers of a-ZTO/SiO_x/a-ZTO films increased. However, for SiO_x thicker than 2nm, the resistivity decreased.

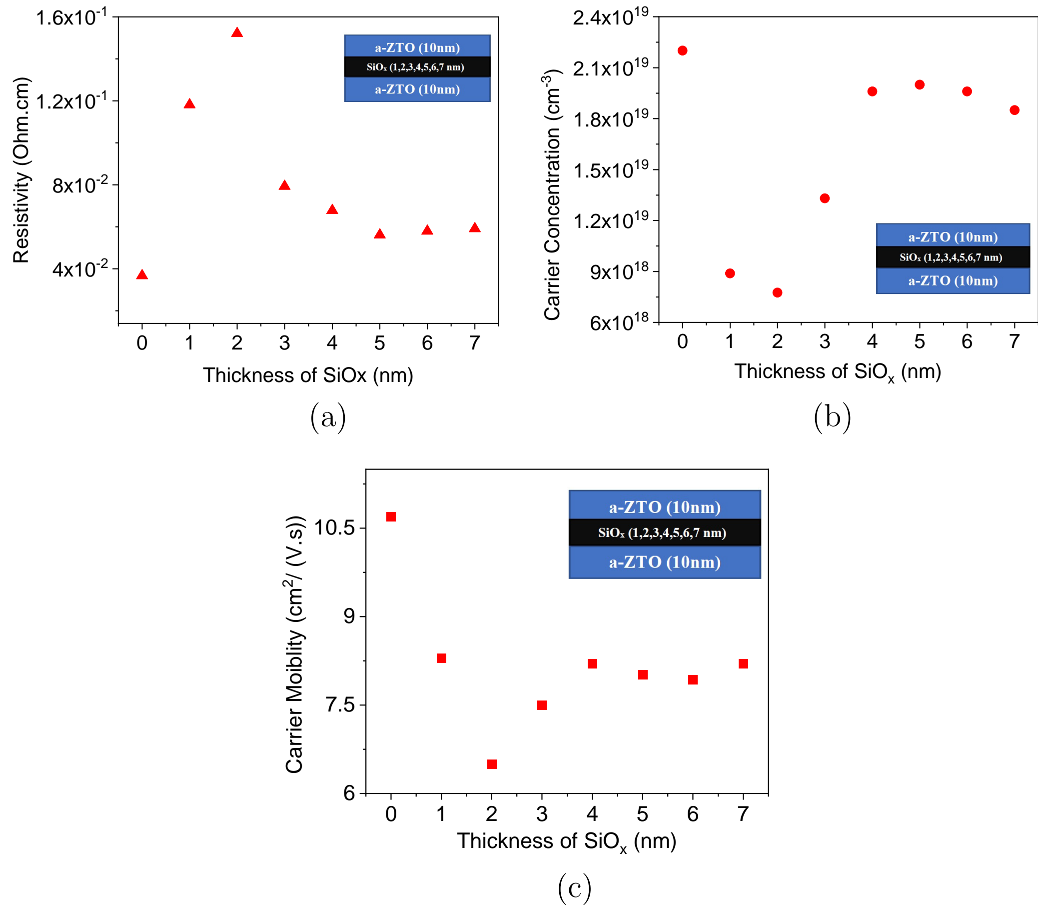

Figure 5.6: a-ZTO/SiO_x/a-ZTO layered structure of the multilayers, where (a) - resistivity, (b) - carrier concentration, (c) - carrier mobility versus thickness of the SiO_x layers maps. (▲) symbol shows resistivity, (●) indicates carrier concentration and (■) symbol for carrier mobility of the a-ZTO/SiO_x/a-ZTO films.

Carrier concentration of the a-ZTO/SiO_x/a-ZTO films dropped from $\approx 2.2 \times 10^{19}$ cm^{-3} to 7.1×10^{18} cm^{-3}, which is observed by SiO_x film with thickness of 2 nm. Furthermore, it was back to close bulk a-ZTO's carrier concentration values after

4 nm thick SiO_x in a-ZTO/SiO_x/a-ZTO films. Meanwhile, the carrier mobility of a-ZTO/SiO_x/a-ZTO films decreased from 10.7 cm^2/Vs to 6.5 cm^2/Vs as the film thickness increased to 2 nm, beyond that it increased up to 4 nm thick SiO_x and maintained at constant levels in up to 7 nm thick SiO_x. All these changes in electrical properties of a-ZTO/SiO_x/a-ZTO films indicated that, as shown in Figure 5.6 the most carrier drop in a-ZTO/SiO_x/a-ZTO films was achieved by the 2 nm thick SiO_x. This means that free carrier trap centres in ultra-thin SiO_x played a key role in charge carrier drop. Moreover, all ultra-thin SiO_x films were deposited in an oxygen-poor sputtering atmosphere that could utilise the growth of more defective SiO_x films. It has previously been presented that a variation in charge carrier concentration and mobility occurs due to the trap in the oxide semiconductor materials [240]. Here, increasing the thickness of SiO_x decreases the defect centres with fewer carrier drops from 4 nm to 7 nm thick SiO_x with fewer suboxide species. As a result, the primary defects are related to the oxygen-deficient grown ultra-thin SiO_x films with more silicon dangling bond states within the lower thickness of the material, and they act as an origin of electron trap in this material in the previous works [241, 242]. A considerable amount of awareness seems to point out that there is also a trap site by the neutral oxygen vacancy caused by strong Si-Si bonds [243, 244]. Furthermore, it is also well known that presence of the ambient oxygen in the sputtering chamber could result in the formation of defective ultra-thin oxides that act as charge carrier traps [243]. The undercoordinated silicon atoms result in electron capture in SiO_x films that are created during the growth of ultra-thin SiO_x films. This should be considered as either trapping an electron or a hole centre in the films [245, 246]. In this work, the charge carrier decrease in trilayer films could be attributed to these charge carrier trap centres.

Another interpretation of the carrier drop in a-ZTO/SiO_x/a-ZTO films is that the Sn atoms' electronegativity is higher than that of Si [135] so that there is less possibility to create the under-coordinated Sn atoms with weakly bonded oxygen atoms. A previous work discovered that undercoordinated cations act as an electron trap [34]. However, Si atoms likely interact with oxygen that is weakly bonded with Zn atoms because it has a lower electronegativity than Si. As a result, there is a greater carrier mobility drop in a-ZTO/SiO_x/a-ZTO films

upon increasing under-coordinated Zn atoms. All imply that under-coordinated metal clusters also prevent carrier mobility as they act as scattering sites [16]. Previous works have confirmed that Zn is the main electron mobility driver in a-ZTO films [16, 104]. Carrier concentration and mobility have decreased by a small proportion compared to the overall electrical properties of the a-IGZO thin films layered with SiO_x in the previous report [39]. This can be explained by both amorphous IGZO (a-IGZO), and amorphous ZTO (a-ZTO) materials having high complexity and a substantial amount of defects. Therefore, a few noticeable defect properties can be considered for comparison with both materials. In the case of a-IGZO, oxygen vacancies have been extensively studied that are associated with deep subgap states. a-IGZO's properties strongly depend on the amount and types of these subgap states, such as how these are present in materials by oxygen levels during the growth and annealing process. The free carrier source of oxygen vacancy is also controlled by Ga content because it has a strong chemical bond with oxygen that controls the concentration of oxygen vacancy in the a-IGZO films [247, 248]. However, studies of a-ZTO films by DFT point to a link of oxygen coordination to deep subgap states. However, these studies are not conclusive. Furthermore, a-ZTO films are more connected with metallic-based defect centres, and a previous study on a-ZTO films says that oxygen deficiency results in metal atom clusters. The subgap states are formed by these metal atom clusters and providing the donor electrons; at the same time, they act as the scattering centres [7, 8, 114, 120] so that both materials possess a crucial point of generating the free carriers. They show different levels of electrical properties. These trilayer structures' optical properties may also indicate a decrease in charge carriers. The results of measurements of optical properties are given in the next section.

The ionisation energies of elements in this work are compared to each other as shown in Table 5.1, which may also be the reason for a drop in carrier concentration. However, more research must be conducted to draw a comprehensive picture of the effects of ionisation energy [249]. All imply that examining the binding energies is also essential, and their impact on each other plays a vital role in a-ZTO/SiO_x/a-ZTO films. However, this must be carried out with more

Elements	Ionization energy (eV)
In	5.78
Ga	5.99
Zn	9.39
Sn	7.34
O	13.61
Si	8.15
Ti	6.82

Table 5.1: Comparison of 1st Ionization energy of elements. Data taken from cited work [249].

research to reveal changes in electrical properties. Also, the electronegativity of elements needs to be investigated to show the alteration in multilayers [135, 136].

5.5 Conclusions and Further Investigations

To conclude, we have investigated the effect of ultra-thin SiO_x interplayed with a-ZTO. I proposed a tentative reason for carrier concentration drop in these three-layers films; the oxygen and silicon atoms related to electron trap states played a role in ultra-thin SiO_x. Furthermore, measurement data of the optical properties of these multilayer films showed that defective ultra-thin SiO_x films did not cause alterations in optical properties.

The ultra-thin SiO_x films in layered structures showed that the layering method can reduce the carrier concentration, but this comes with the undesired reduction in mobility. This means it is unlikely to be a promising alternative to bulk doping materials. This could lead to searching for other materials and possibilities of working better, where several insulators are needed to see the effect on the electrical properties of a-ZTO. Here, titanium dioxide (TiO_2) is a well-studied and powerful candidate for this. This material's list of priorities will be discussed in the following sections.

5.6 Altering the Electrical Properties of a-ZTO Including Ultra-Thin TiO_x Layers

5.7 Introduction of a-ZTO/TiO_x/a-ZTO Structures

TiO_2 is an interesting and versatile material with nontoxic nature, chemical stability, a relatively low cost, and semiconducting behaviour, making it an attractive candidate for commercial uses due to this oxide semiconductor composed of transition metal. As a result of that, it has been widely studied [250]. It is used in photocatalytic applications and has potential as a TCO material (niobium doped) [251]. Apart from that, it is used as an insulating material when it is not doped with a bandgap of >3 ev [252]. The electrical properties of TCOs must be altered by the insulating material with more reliable and other properties. In certain cases, TCOs are used as a channel layer in Thin-Films Transistors (TFTs), where they are an active material for switching, but the electron concentration of TCOs must be reduced substantially to enable this application. This facilitates excellent switching. As I above stated it is difficult to reduce the concentration in ZTO ($<1\times10^{19}$cm^{-3}) [235]. We will use TiO_x for this purpose. TiO_2 presents several advantages over SiO_2 for this investigation. The primary one is that its bandgap is significantly lower than that of SiO_2, presenting the possibility of a lower tunnel barrier between the materials [253]. Other benefits include a tendency towards intrinsic n-type conductivity, a lower resistivity, and higher mobility of the films [74, 254]. TiO_2 is investigated to explore whether this reduced barrier might lead to a lower carrier mobility reduction. The results observed will be outlined in the next few sections.

5.8 Experimental Methods of a-ZTO/TiO_x/a-ZTO Films

Figure 5.7 shows multilayer structure by a-ZTO and TiO_x materials. All three layers of a-ZTO/TiO_x/a-ZTO (a-ZTO - amorphous Zinc Tin Oxide) thin films were grown in-situ by a non-reactive RF Magnetron chamber (with a rotating sample stage, details in section 3.1.3), which used a custom composition target of

ZTO with 99.99% purity (where a mixture of 75% of SnO_2 and 25% of ZnO) and TiO_2 target separately. At the same time, the total gas pressure of the deposition chamber is constantly maintained at 1×10^{-3} mbar for a-ZTO layers growth and 5.8×10^{-4} mbar for TiO_x ultra-thin layer, where the 99.99% purity of Argon flow was remained a constant for both materials synthesis process. The power applied to a ZTO custom composition target was 75 W, and the SiO_2 target was 100 W.

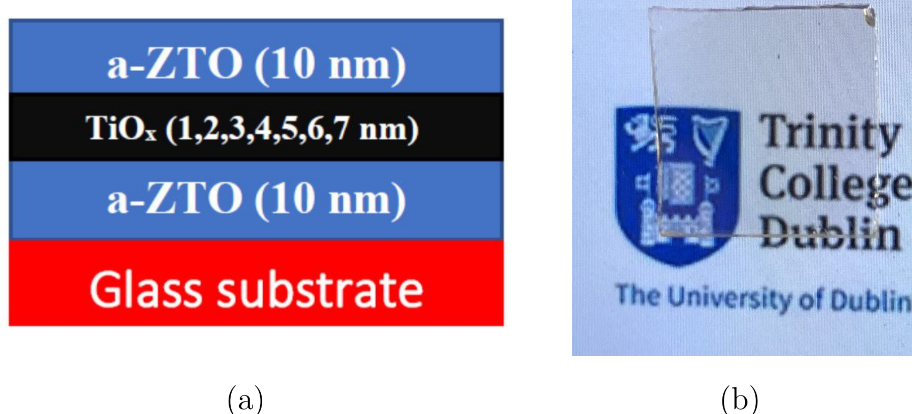

(a) (b)

Figure 5.7: Trilayer structures of a-ZTO/TiO_x/a-ZTO film on a glass substrate, where the thickness of TiO_x films varied from 1 nm to 7 nm between constant two 10 nm thick a-ZTO films, (b) - an image of a-$ZTO_{(10nm)}$/$TiO_{x(2nm)}$/a-$ZTO_{(10nm)}$ film.

All films in this work were grown on standard microscopy glass slides (Thermo Scientific 1x1 cm, 0.8-1mm thick). Glass substrates were cleaned with a sonicator in isopropanol and acetone for 5 minutes separately, then kept in magnetron load lock chamber (1×10^{-5} mbar) for an hour in order to facilitate a clean surface of substrates. The substrate temperature was maintained at room temperature for all films in this work. All films' carrier concentration, electron mobility, and resistivity were measured at room temperature using the Hall system in the Van der Pauw method. Four contacts were made of silver wire using silver adhesive. These four contacts are located on the four corners of the sample. XRR system (more details are in 3.2.2) is involved in controlling the thickness of each layer in a-ZTO/TiO_x/a-ZTO films.

5.9 Results and Discussion

5.9.1 Optical Properties of a-ZTO/TiO_x/a-ZTO Films

Figure 5.8 shows transmission and reflectance spectra, absorption and absorption coefficient of a-ZTO/TiO_x/a-ZTO films.

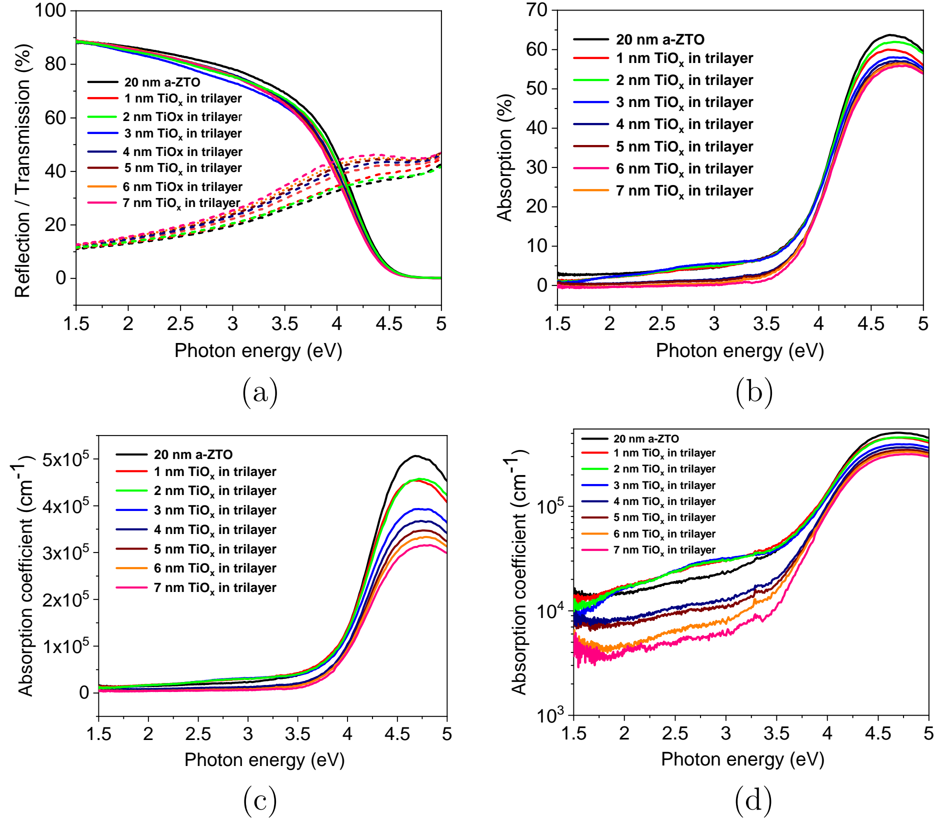

Figure 5.8: Optical properties of a-ZTO/TiO_x/a-ZTO films, where (a) - transmission and reflection spectra, (b) - absorption, (c) - absorption coefficient (linear), (d) - absorption coefficient (log) of a-ZTO/TiO_x/a-ZTO multi-layers. Also (-) - 20 thich bulk a-ZTO, (-) - 1 nm thick TiO_x, (-) - 2 nm thick TiO_x, (-) - 3 nm thick TiO_x, (-) - 4 nm thick TiO_x, (-) - 5 nm thick TiO_x, (-) - 6 nm thick TiO_x, (-) - 7 nm thick TiO_x in a-ZTO/TiO_x/a-ZTO structure films.

Figure 5.8 shows no substantial changes in transmission and reflectance of multilayers. However, all samples are with high transmission of ≈ 80% within the visible light spectrum. However, transmission spectra strongly relate to the thickness of the films and refractive index variations between the films and substrate. Thicker films have a high absorption value than thinner films. The refrac-

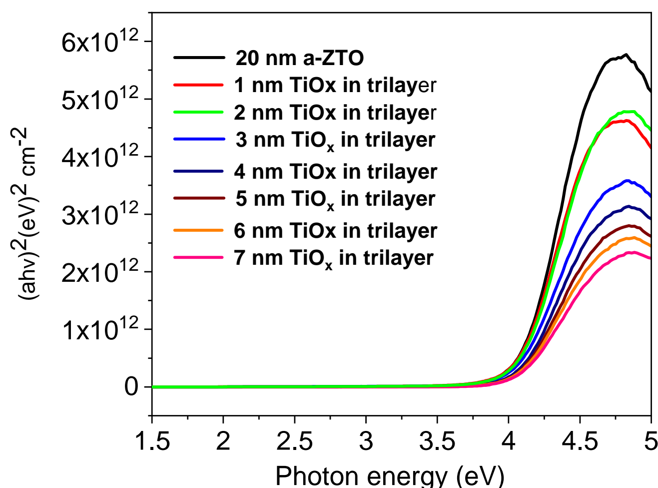

Figure 5.9: Bandgaps of a-ZTO/TiO_x/a-ZTO multi-layers, where thickness of SiO_x between 10 nm thick a-ZTO films varied from 1 nm to 7 nm, where lines are (-) - 20 thick bulk a-ZTO, (-) - 1 nm thick SiO_x, (-) - 2 nm thick SiO_x, (-) - 3 nm thick SiO_x, (-) - 4 nm thick SiO_x, (-) - 5 nm thick SiO_x, (-) - 6 nm thick SiO_x, (-) - 7 nm thick SiO_x in a-ZTO/TiO_x/a-ZTO trilayer films.

tive indexes of the substrate and TCO materials can also consider in analysing materials' optical properties. In this work, Figure 5.8 shows all optical properties of a-ZTO/TiO_x/a-ZTO films and all my films do not have changes. Shifts in optical data with the 1∼2% range are inconsistent. Shifts are originated from the noise level in our UV-Vis system. In addition, there are no bandgap shifts between a-ZTO/TiO_x/a-ZTO multi-layers and 20 nm thick a-ZTO film as shown in Figure 5.9, which means that there is no electron confinement in trilayer films.

5.9.2 SEM Studies of a-ZTO and TiO_x Layers

Figure 5.10 shows SEM images of top layer in a-$ZTO_{(10nm)}$/$TiO_{x(2nm)}$/a-$ZTO_{(10nm)}$ film and 2 nm thick TiO_x on 10 nm thick a-ZTO. It is clearly seen from Figure 5.10 (a) and (b) that there is a smooth surface for all the films of a-$ZTO_{(10nm)}$ and TiO_x. This means that the smooth surface morphology of films has been obtained by magnetron at RT, and there is no noticeable degradation of the surface of films. Also, there is no confirmation of an electron trap on the surface of the films.

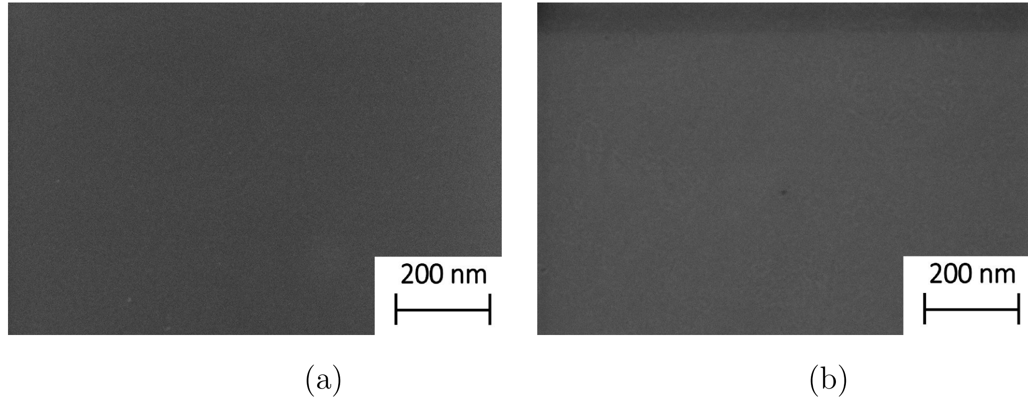

Figure 5.10: SEM images of a-ZTO and TiO_x, where (a) - top layer of **a-ZTO**$_{10\,nm}$ in a-$ZTO_{10\,nm}$/$TiO_{x(2\,nm)}$/a-$ZTO_{20\,nm}$, (b) - 2 nm thick TiO_x on a-ZTO.

5.9.3 XRD and XRR of a-ZTO, and a-ZTO/TiO_x/a-ZTO Films

XRR data of a-ZTO and trilayer structure of a-$ZTO_{(10\,nm)}$/$TiO_{x(2\,nm)}$/a-ZTO $_{(10\,nm)}$ film as shown in Figure 5.11 (a) and (b). Measured and simulation data fitted snugly, showing a uniform thickness range for each layer. The materials' thickness, roughness and density were obtained using this data. Density of a-ZTOs is 6.8 g/cm^3 and TiO_x of 4.6 g/cm^3. An average interface roughness is between a-ZTO and TiO_x $\approx$ 0.48 nm. Density of a-ZTOs is 6.8 g/cm^3 and for TiO_x, it is 4.6 g/cm^3. An average interface roughness between a-ZTO and TiO_x is $\approx$ 0.48 nm.

XRD data of a-ZTO, a-ZTO/TiO_x/a-ZTO, and Glass in Figure 5.11 (c) revealed that they do not show a crystalline phase. While several halo peaks were detected at around 14°, 23°, and 33° due to the bonding length alterations in amorphous materials. The halo peak at 14° is associated with an amorphous property, and the halo peak at 23° is from the glass substrates. The previous work confirmed these XRD peaks [177]. More XRD sample holder halo peaks at 33° and 40-44° were observed in this work (See sample holder picture in Figure 3.6 (b), 2).

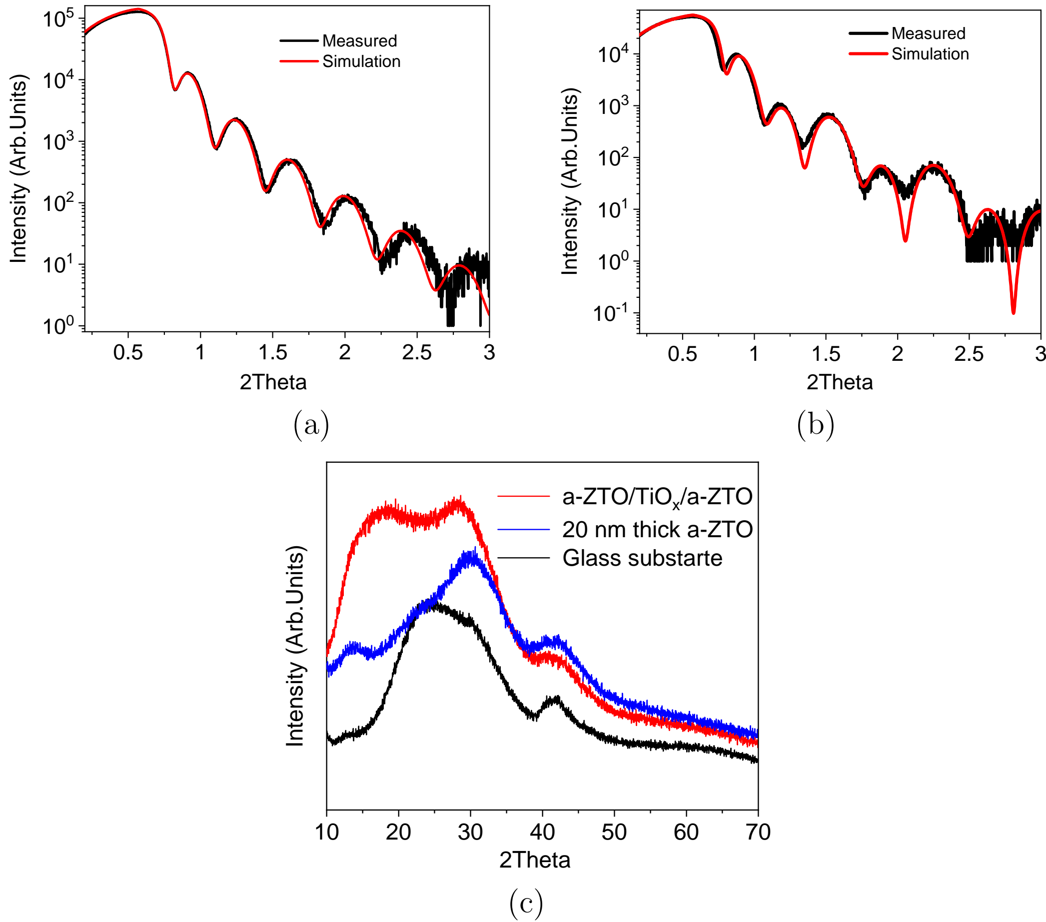

Figure 5.11: XRR and XRD curves of a-ZTO and TiO_x, where (a) - XRR pattern of 20 nm thick a-ZTO, (b) - XRR pattern of a-$ZTO_{(10.07\,nm)}$/$TiO_{x(2.05\,nm)}$/a-$ZTO_{(10.08\,nm)}$ three layer structure, (c) - XRD pattern of the glass substrate, 20 nm thick a-ZTO and a-ZTO/TiO_x/a-ZTO.

5.9.4 Results and Discussion of a-ZTO/TiO_x/a-ZTO Tri-layers

Figure 5.12 shows the electrical properties of the a-ZTO/TiO_x/a-ZTO based films altered by including ultra-thin TiO_x films, where the thickness of TiO_x films varied from 1 nm to 7 nm. Changes in the electrical properties were substantially lower in TiO_2 based three-layer structure thin films than in SiO_2 based films. This means that ultra-thin TiO_x films worked the least efficiently, decreasing 80% of carrier concentration drop in three a-ZTO/TiO_x/a-ZTO films. This was observed only in a-ZTO/TiO_x/a-ZTO film containing 2 nm thick TiO_x layer, and

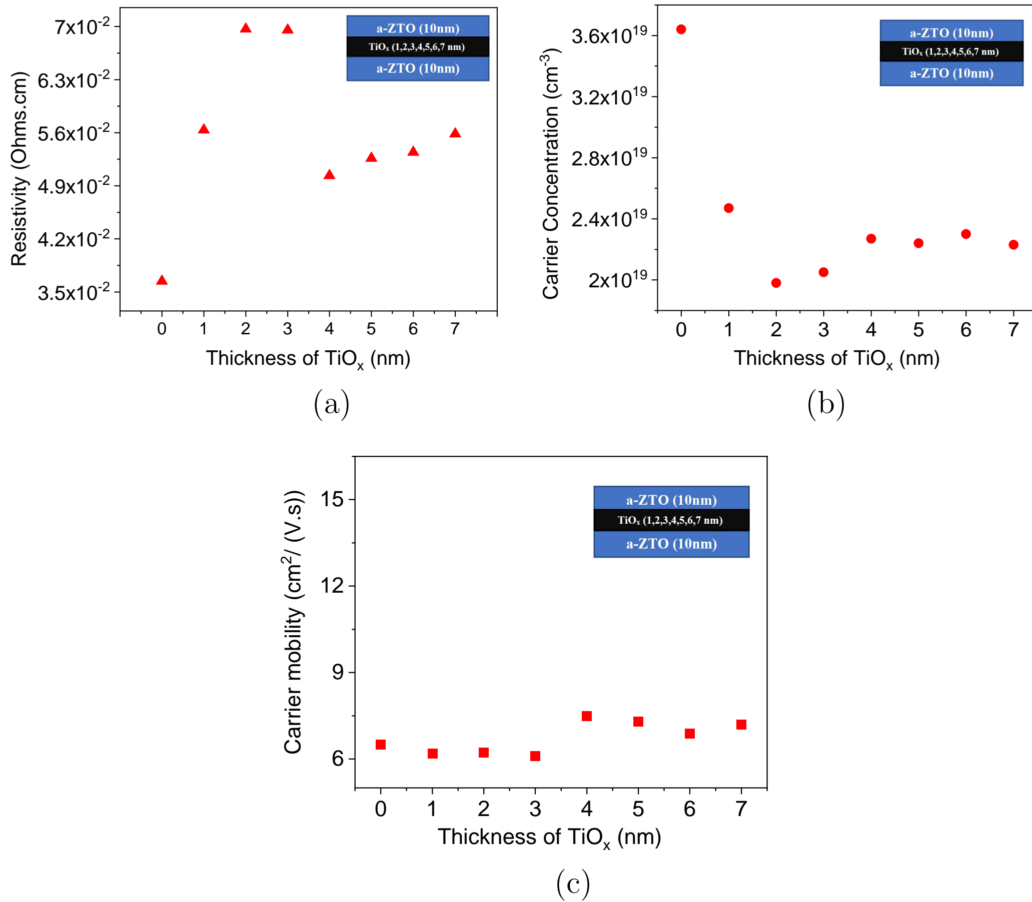

Figure 5.12: Electrical properties of a-ZTO/TiO_x/a-ZTO films, where (a) - resistivity, (b) - carrier concentration, (c) - carrier concentration versus electron mobility. (▲) symbol shows resistivity, (●) indicates carrier concentration and (■) symbol for carrier mobility of a-ZTO/TiO_x/a-ZTO films.

it increased for thicker layers. a-ZTO/TiO_x/a-ZTO films with 4 nm-7 nm thick TiO_x films showed ≈ 55% carrier drop at the same time. However, carrier mobility was maintained in line with a-ZTO film at around 6.5 cm^2/Vs. The role of defect species in TiO_x films can be taken into account for this. Also, elements' binding energy and electronegativity might be considered for understanding a constant carrier mobility behaviour. The changes in the thickness of the TiO_x films affect the surface's electronic properties. Film thickness also influences on the density of trap states' positions. These appear below the conduction band of TiO_x films because of a lack of bonding arrangements and bulk defects. This was

observed even if TiO_2 is a crystalline phase [255] as well as extended Ti–O bonding responsible for as trap states in amorphous TiO_2 [256]. These trap defect centres in TiO_2 films originate from the oxygen vacancies [257]. A variation between both $Ti_{interstitial}$ and oxygen vacancies results in a substantial structural alteration in the network, hence the presence of shallow donor trap states below the conduction band minimum [258]. This means that in this work, all a-ZTO/TiO_x/a-ZTO films were deposited under a poor oxygen atmosphere that is crucial for particularly the synthesis of TiO_2 with more defects. 2.2 nm thick titanium oxides have been deposited with more trap states in this report [259, 260], which means it might be in line with my TiO_x layers. Therefore, previously confirmed Ti^{4+} and Ti^{3+} act as electron traps in bulk TiO_2 due to the oxygen vacancy [261]. Here, one of the possible reasons is that these trapping states are responsible for carrier drops, where charge carriers might be captured by oxygen vacancies [260]. However, it is not a huge drop compared to a-ZTO/SiO_x/a-ZTO films. This may be a sign that the electronegativity of Ti is much lower than Zn and Sn and these oxygen atoms may be pulled towards to Zn and Sn, where unlikely to create more under-coordinated Zn and Sn atoms that act as the source of free carrier trap centres. Here, just TiO_2's bulk trap centres dominate as carrier drop, and it decreases with the thickness of the TiO_2. Electron mobility of a-ZTO/TiO_x/a-ZTO films remained constant at $\approx 6.5\,cm^2/Vs$ that can be explained by having the extraordinary characteristics TiO_2 itself. Certain amorphous phase TiO_2 films show that the mobility of free electrons strongly depends on the charge trap states, which they control. This means that electron mobility is governed by the trapping and de-trapping phenomenon, where electrons are travelled between shallow trap and conduction band [259, 262]. Another thing that might happen in my films is that amorphous titanium oxide films with a nonstoichiometric phase showed in the previous report excellent properties, such as metallic behaviour. These samples are in lower oxidation states of $TiO_{1.5}$ [263].

The XPS spectrum is often measured to study the composition of amorphous oxide films. The most observed XPS peak is O1s with different binding energy (BE) by in-situ XPS methods that depend on the charge states of the oxygen gained in materials. Usually, the binding energy of oxygen is $\approx 530\,eV$. The meaning of binding energy is the strength of such a chemical bond between atoms

and the maximum energy required to break or remove an electron. This highly depends on the types of bonding, including ionic and covalent bonding. Also, the electronegativity of elements identifies the strength of the bond [264]. In general, alterations in electrical properties of a-ZTO/TiO_x/a-ZTO films, where elements' binding energies need to be taken into account because they have different binding energy values. a-ZTO is composed of three main elements that are Zn, Sn and O. As a result that they form with different levels of bond strength. From the experimental data for the a-ZTO films Zn 2p3/2 is 1021.49 eV and Sn 3d5/2 is 486.22 eV binding energy values. This implies that different levels of charge states of Ti, Zn and Sn are defined amounts of binding energies with oxygen atoms. Meanwhile, charge states generate the free carriers by creating defect centres related to the variable charge states of each element. Hence, where undercoordinated metal atoms create the electron trap states [34]. That is why here, TiO_x films do not bring a dramatic change in the electrical properties of a-ZTO. A deeper understanding of these requires the in-situ transfer of the Magnetron samples to XPS, which needs further work. Also, several defect-sensitive experimental devices have to be applied to this work, such as electron paramagnetic resonance (EPR) and Photoluminescence (PL) Spectroscopy. Examining the optical properties of these multilayers may assist in finding out the charge carrier drop in the trilayer, even if the carrier concentration drop is negligible. Based on this, the optical measurements have been done on layered structures, which will be discussed in the next section.

5.10 Conclusions and Further Investigations

To sum up, two main insulators of SiO_x and TiO_x were used to alter the electrical properties of a-ZTO films. The least effective one is TiO_x, and compared to TiO_x, SiO_x worked with a greater degree. However, TiO_x films maintained carrier mobility in trilayers. The most likely explanation for carrier drop in these multilayers is that electrons get trapped by oxygen, Ti interstitial, and other trap states due to the effect of thickness reduction on the optical and electrical properties of SiO_x and TiO_x films. Also, the elements in SiO_x and TiO_x films have different electronegative values, which may change the electrical properties in these multilayers.

The electrical properties of TCOs were altered by replicating a previous report, which theorised carrier drop in a-IGZO/SiO_x superlattices due to the gettering, where charge carrier drop confirmed as a side effect of tuning the refractive index of materials. After a-ZTO films layered with SiO_x and TiO_x, a-IGZO layered with SiO_x in the same way as a-ZTO films and these three-layer films were also investigated. Before going into a-IGZO/SiO_x/a-IGZO films, the main priority is that a-ZTO and a-IGZO are intrinsic semiconductors. In other words, both a-ZTO and a-IGZO are primarily defect-based semiconductors. Oxygen plays a crucial role in two materials' electrical and optical properties. All of this implies that redoing previous a-IGZO/SiO_x superlattices by decreasing the thickness of the whole layer will be investigated, and several characterisation techniques will be used to reveal the carrier drop in a-IGZO/SiO_x/a-IGZO films. The origin of the carrier drop might be more complex and requires more research to find out the reasons. All studies on a-IGZO/SiO_x/a-IGZO films will be discussed in the upcoming sections.

5.11 Altering the Electrical Properties of the a-IGZO with Including Ultra-Thin SiO_x Layers

5.12 Introduction of a-IGZO/SiO_x/a-IGZO Films

In the case of layering materials, establishing and understanding the physics of materials is there. Also, a layering method could preserve lateral carrier mobility in ultra-thin films. A layering method can be performed by introducing the ultra-thin insulator layers with a few nm thickness, which would have the benefit of a low density of intrinsic defects. Most of the prior research was focused on thick a-IGZO/SiO_x superlattices for tuning the refractive index. A side carrier drop in a-IGZO/SiO_x superlattices was found, and this happened in all the films, including the ones deposited at elevated temperature [39]. This report allows us to identify an origin of a drop in charge carrier concentration in these multilayer structures. Also, a-IGZO possesses a complex oxygen vacancy structure, so there is an expectation of a significant carrier concentration drop in these three-layer films [265]. Carrier drop behaviour may be more complicated in these multilayers and needs more versatile experimental devices or theoretical approaches. I will focus on studies on a-IGZO/SiO_x/a-IGZO three-layered structures in the following few sections using tools, such as XPS and other characterisation techniques. In the lists of tools, the primary priority is to equip the XPS system with an in-situ transfer. The films' oxygen structure will be investigated, and the role of oxygen in these multilayers will be outlined.

5.13 Experimental Methods of a-IGZO/SiO_x/a-IGZO Films

Figure 5.13 presents a three-layer network composed of a-IGZO and SiO_x on a glass substrate. Three laminates of amorphous –InGaZnO (a-IGZO)/SiO_x/a-IGZO ultra-thin films were synthesised in-situ via non-reactive Radio Frequency (RF) magnetron sputtering (used equipped with a rotating sample stage, see in section 3.1.3). An IGZO (1:1:1:1 ratio) target with a 99.99 % purity composition

and SiO_2 target with a 99.99 % purity were used separately. Working pressure for a-IGZO growth was 1.6×10^{-3} mbar and 6.2×10^{-4} mbar for SiO_x layer, under the constant argon flow. The power applied on the IGZO custom composition target was 140 W and the power on SiO_2 target was 100 W. While sputtering, the chamber was kept for 5 minutes in the pre-sputtering process to stabilise plasma density and remove the oxide layer from the target surface built by a tiny amount of background gas.

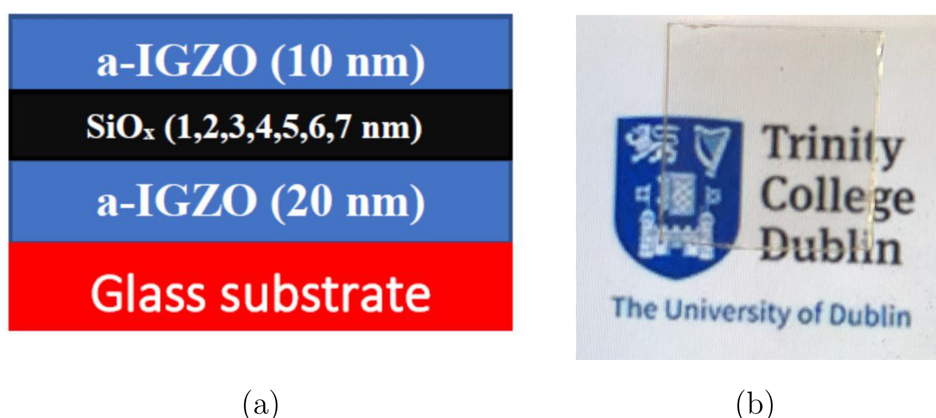

(a) (b)

Figure 5.13: Trilayer structures of a-IGZO/SiO_x/a-IGZO film on a glass substrate, where (a) - thickness of SiO_x films varied from 1 nm to 7 nm between 20 nm and 10 nmthick a-IGZO films, respectively. (b) - an image of a-$IGZO_{(20\,nm)}$/$SiO_{x(2\,nm)}$/a-$IGZO_{(10\,nm)}$ film.

The entire films in this work were deposited on standard microscopy glass slides (Thermo Scientific 1x1 cm, 0.8-1mm thick). The glass substrates were ultrasonically cleaned in isopropanol and acetone for 5 minutes individually. Then kept under a high vacuum load lock chamber in a magnetron sputtering system (1.6×10^{-5} mbar) for a minimum of an hour before deposition. The substrate temperature was room temperature without heating for all thin films in this work.

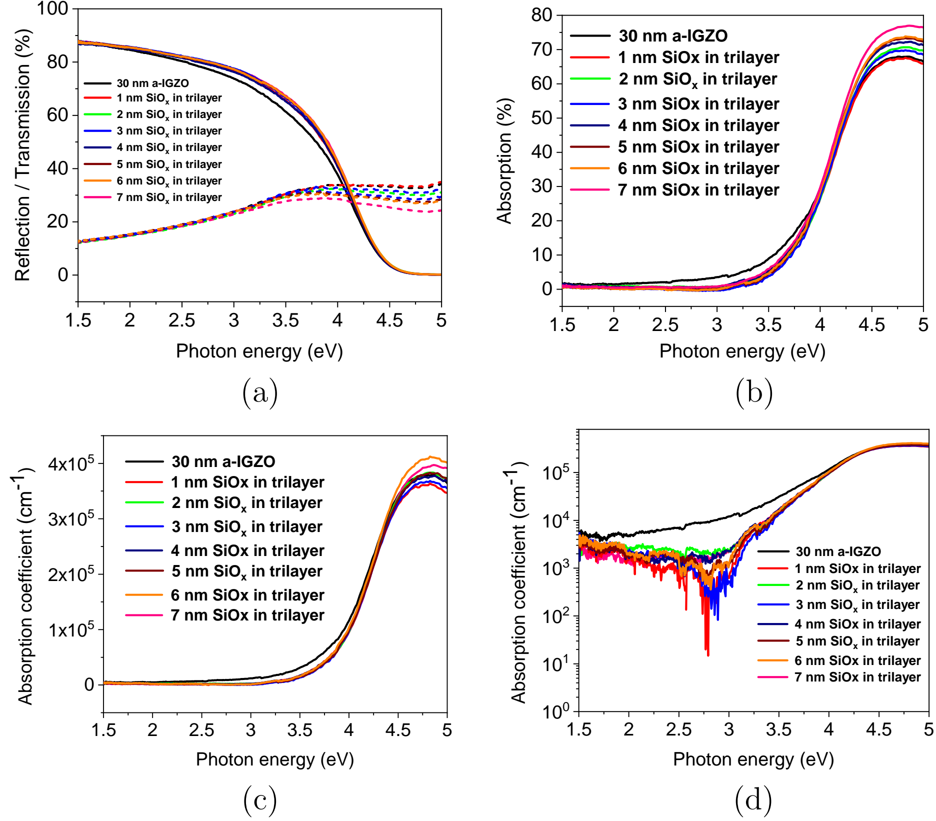

Figure 5.14: Optical properties of a-IGZO/SiO_x/a-IGZO multi-layers, where (a) - transmission and reflectance spectra, (b) - absorption, (c) - absorption coefficient (linear), (d) - absorption coefficient (log) of a-IGZO/SiO_x/a-IGZO multi-layers. Also (-) - 30 thich bulk a-IGZO, (-) - 1 nm thick SiO_x, (-) - 2 nm thick SiO_x, (-) - 3 nm thick SiO_x, (-) - 4 nm thick SiO_x, (-) - 5 nm thick SiO_x, (-) - 6 nm thick SiO_x, (-) - 7 nm thick SiO_x in a-IGZO/SiO_x/a-IGZO structure films, individually.

5.14 Results and Discussion

5.14.1 Optical Properties of a-IGZO/SiO_x/a-IGZO Multilayers

Figure 5.14 shows optical properties of a-IGZO/SiO_x/a-IGZO films, where UV-Vis Spectrophotometer measured the transmission and reflection spectra (see more detail 3.3), the data obtained was absorption and absorption coefficient for multilayers.

As you see from Figure 5.14 a total of eight samples were involved. It is clear that the transmission is around 80% within the visible spectra region for all a-

IGZO/SiO_x/a-IGZO multilayers. However, transmission spectra depend on the thickness of the films and refractive index changes between the film and substrate. The former is defined by the absorption (A) proportionality to thickness. The thickness variation from the average thickness of the films can affect this. The latter is the difference between the average refractive index of the substrate and materials. The reflectivity curves of the films strongly depend on the uniformity of the thickness due to the thin-film interference from the top and bottom interface of the sample. It shows that the thickness is not uniform, which causes different oscillations. As a result, the discussion of the absorption coefficient can be helpful in the cases of very thin films such as those discussed here. This is plotted in

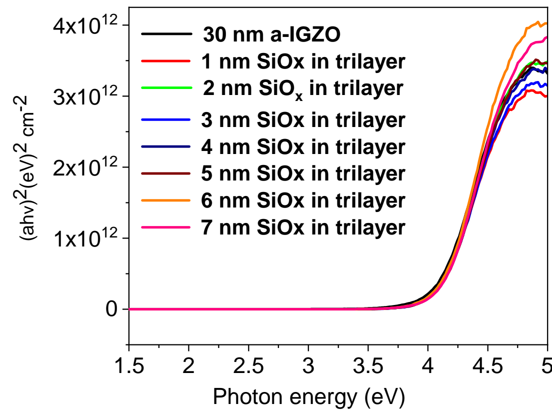

Figure 5.15: Bandgaps of a-IGZO/SiO_x/a-IGZO multi-layers and a-IGZO, where thickness of SiO_x between 20 and 10 nm thick a-IGZO films varied from 1 nm to 7 nm, where lines are (-) - 20 thick bulk a-ZTO, (-) - 1 nm thick SiO_x, (-) - 2 nm thick SiO_x, (-) - 3 nm thick SiO_x, (-) - 4 nm thick SiO_x, (-) - 5 nm thick SiO_x, (-) - 6 nm thick SiO_x, (-) - 7 nm thick SiO_x in a-ZTO/TiO_x/a-ZTO trilayer films.

Figure 5.14. Also, bandgaps of a-IGZO/SiO_x/a-IGZO multilayers and a-IGZO showed no bandgap energy difference between films as shown in Figure 5.15, which means it is hard to consider electron confinement in the trilayer structures. It can be seen that a slight shift in absorption was observed in the films. However, this shift is inconsistent and is in the 1∼2% range, which coincides with the noise level in our system, leading to much un-physical behaviour in the absorption coefficient due to T+R approaching 100%. As a result, it is difficult to identify whether a consistent shift in absorption is occurring for the thin films here. This could

be better investigated in the future by growing substantially thicker multilayer films, increasing the absorption level (α) outside that 1-2% noise level. Thick films would allow for a more accurate calculation of the absorption coefficient. This is also found in the absorption and absorption coefficient of all a-IGZO/SiO_x/a-IGZO films as shown in Figure 5.14 (d).

5.14.2 AFM and SEM Studies of a-IGZO and SiO_x Layers

Through oxygen structure study in the trilayer, these charge carrier drops in trilayer subjects require more approaches, so AFM and SEM instruments were used to perform studies of a-IGZO and SiO_x layers. Images of AFM and SEM for a-IGZO and SiO_x are shown in Figure 5.16 and 5.17 respectively.

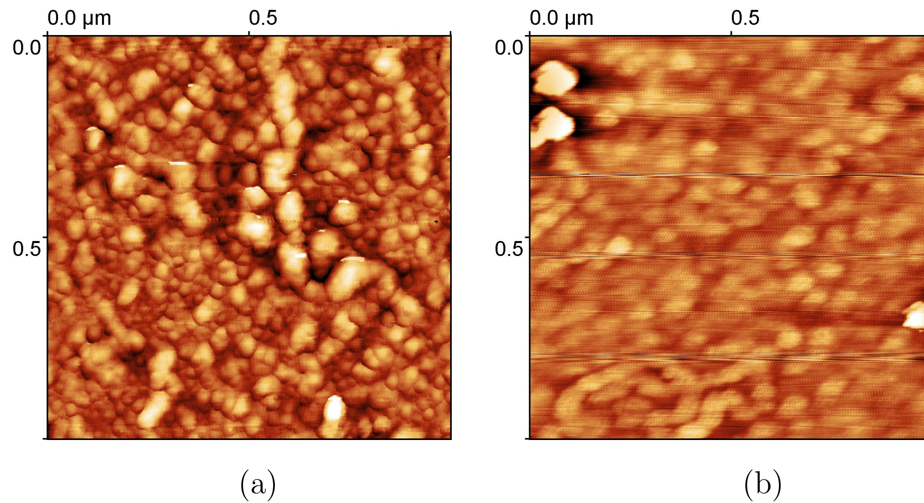

Figure 5.16: AFM images of a-IGZO and SiO_x, where (a) - 10 nm thick top layer of a-IGZO in a-IGZO/SiO_x/a-IGZO film, (b) - 2 nm thick SiO_x on a-IGZO.

Figure 5.16 shows AFM images of both a-IGZO and SiO_x with a continuous surface, where any discontinuous surface and island growth of SiO_x films did not find. This means that in some instances, island-like film deposition takes place at a lower thickness of SiO_2, which acts as electron trap centres and could be the main reason for carrier drop in multi-layers. However, one report confirmed island-like film deposition, but it could be found for oxide thinner than 0.8 nm thick films used here [266].

SEM images of a-IGZO in a-$IGZO_{(20\,nm)}$/$SiO_{x(2\,nm)}$/a-$IGZO_{(20\,nm)}$ film, which in air and in-situ transferred and 2 nm thick SiO_x on a-IGZO films have compared

each other. As shown in Figure 5.17 (a) and (b), there more surface pits were observed on the surface of in-situ transferred samples after the XPS scan. The origin of these pits is unknown. Meantime, the other film's surface shows smooth and continuous properties, as shown in Figure 5.17 (a) and (c).

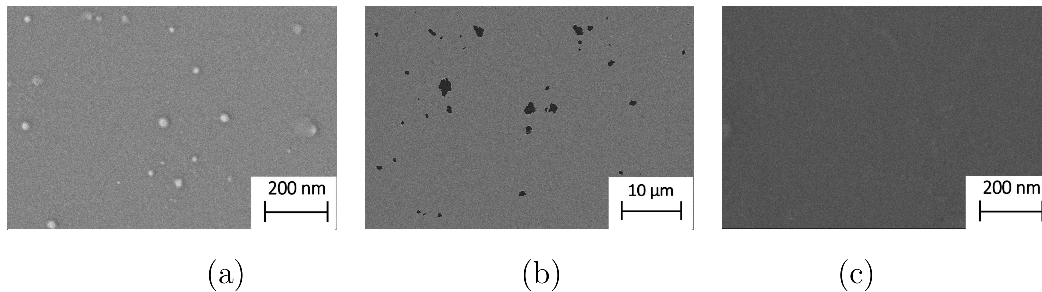

(a) (b) (c)

Figure 5.17: SEM images of a-IGZO and SiO_x, where (a) - a-IGZO in air transferred, (b) - SEM image of top layer of **a-IGZO**$_{20\,nm}$/$SiO_{x(2\,nm)}$/a-IGZO$_{20\,nm}$ that after XPS scan, (c) - 2 nm thick SiO_x on a-IGZO.

At the same time, the XRR system obtained the roughness values of each layer in a-IGZO/SiO_x/a-IGZO multi-layers (more detail here 3.2.2). Through this roughness of layers shown in Table 5.2, There are not many differences between SiO_x and a-IGZO layers in terms of their roughness. This is consistent for all films of SiO_x and a-IGZO. A lower roughness is due to films with a smooth surface by a magnetron sputtering system. The roughness of a-IGZO films in the previous report is around 0.5 nm and is smaller than the roughness of films in this work, which is given in Table 5.2, where the average roughness is 0.7 nm for a-IGZO. A variation in roughness between the previous and this work is due to differences in the kinetic energy of sputtering target atoms with different formation energies by sputtering conditions, such as sputtering temperature and gas pressure. Even if the applied RF power in this work is twice as high as in previous work, there is no substantial change in roughness, and it is independent of this power [267].

SiO_x also showed low surface roughness values as given in Table 5.2. This is in line with the average surface roughness of SiO_x in this report [268]. Generally speaking, the effects of roughness are not considered for a considerable carrier drop in this work. The previous work found that a lower roughness value reduces trap density, where the observed roughness of a-IGZO is 0.53 nm [269]. Also, one study on interfacial roughness between a-IGZO and SiO_2 layers showed that lower

Roughness (nm)	Top layer	SiO_x layer	Bottom layer
a-$IGZO_{20\,nm}/SiO_{x(1\,nm)}$/a-$IGZO_{10\,nm}$	0.57	0.63	0.52
a-$IGZO_{20\,nm}/SiO_{x(2\,nm)}$/a-$IGZO_{10\,nm}$	0.72	0.59	0.82
a-$IGZO_{20\,nm}/SiO_{x(3\,nm)}$/a-$IGZO_{10\,nm}$	0.5	0.66	0.65
a-$IGZO_{20\,nm}/SiO_{x(4\,nm)}$/a-$IGZO_{10\,nm}$	0.6	0.62	0.78
a-$IGZO_{20\,nm}/SiO_{x(5\,nm)}$/a-$IGZO_{10\,nm}$	0.81	0.68	0.6
a-$IGZO_{20\,nm}/SiO_{x(6\,nm)}$/a-$IGZO_{10\,nm}$	0.67	0.8	0.68
a-$IGZO_{20\,nm}/SiO_{x(7\,nm)}$/a-$IGZO_{10\,nm}$	0.48	0.75	0.69

Table 5.2: The roughness values of each layer in a-IGZO/SiO_x/a-IGZO films by XRR measurements.

roughness values correspond to a lower density of interfacial traps [270]. Usually, a-IGZO thin films with <1 nm roughness is usually obtained by magnetron sputtering, which has confirmed that trapping an electron occurs within the insulator layer; it is not between interfacial roughness of layers [271, 272]. Based on these investigations, the roughness studies are not a piece of inconclusive evidence to show the carrier drops in a-IGZO/SiO_x/a-IGZO three-layer.

In summary, AFM and SEM studies on the surface of films revealed no evidence to confirm the charge carrier drop in trilayer structures. Also, roughness studies could not explain a drop in carrier concentration. However, during the studies of these multilayers, a difficulty has arisen with in-situ transferred samples, where all in-situ transferred samples came out (after XPS data was obtained) with better electrical properties than in air transferred a-IGZO/SiO_x/a-IGZO films. In other words, these films had lesser carrier drops. This signals a background gas impact on the electrical properties of materials. Studies continued to try to explain the origin of these issues. The question then arises whether there is any relationship between a variation in electrical properties of in-situ transferred films and charge carrier drop in a-IGZO/SiO_x/a-IGZO films. This will be discussed in the upcoming section.

5.14.3 XRD and XRR data of a-IGZO and Trilayer Films

The thickness of all multi-layers was measured by x-ray Reflectometry (XRR) with an un-monochromated Bruker D8 Discover equipped with a Cu source (more details in Figure 3.8). The XRR pattern of a-IGZO/SiO_x/a-IGZO films showed that each layer was deposited with a minor degree of thickness variation due to a rotating sample stage (Description can be found in the section 3.1.3). As

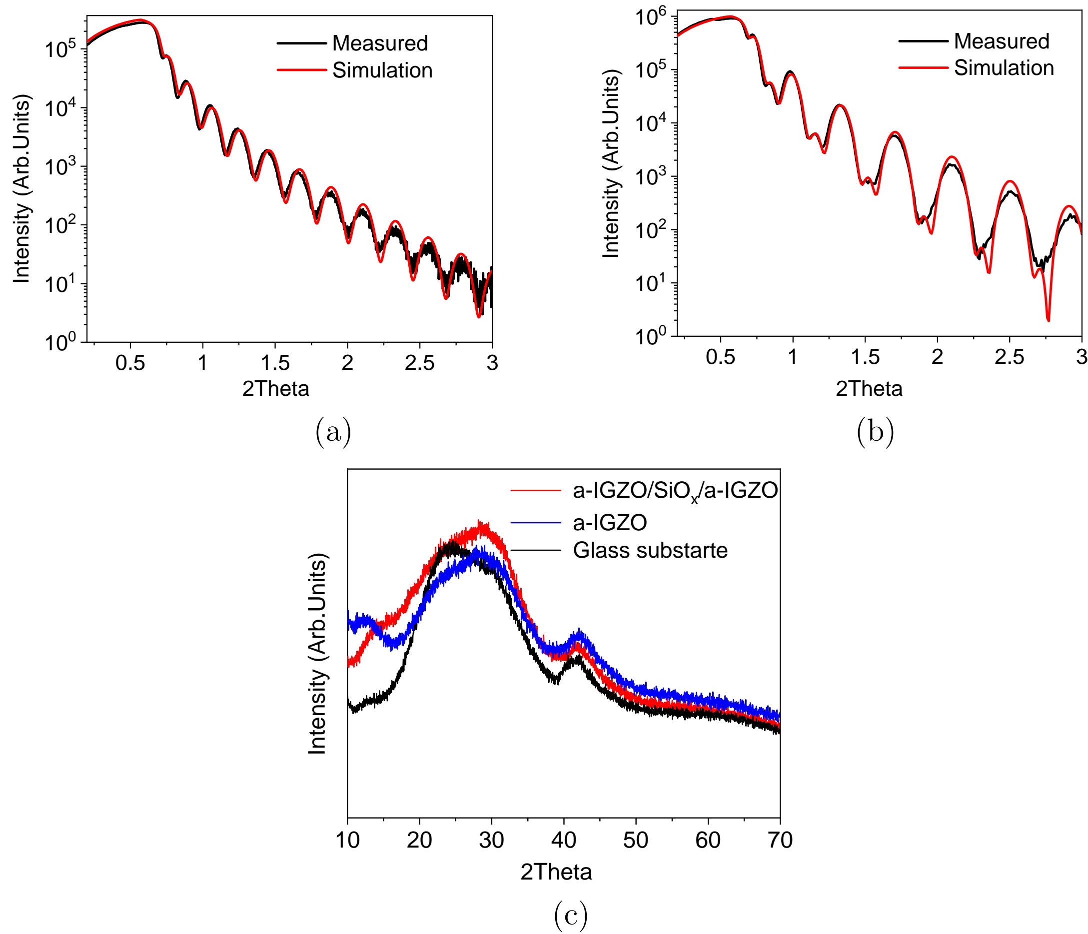

Figure 5.18: XRR and XRD patterns, where (a) - XRR pattern of 30 nm a-IGZO, (b) - XRR pattern of a-IGZO$_{(20.1\,nm)}$/SiO$_{x(2.03\,nm)}$/a-IGZO$_{(10.07\,nm)}$ three layer structure, (c) - XRD data of glass, a-IGZO and a-IGZO/SiO$_x$/a-IGZO multi-layers.

a result, the XRR period of the oscillations remains constant compared with the static sample stage (see XRR curve of samples were deposited by using a static sample stage 3.3) even if at a high angle, as shown in Figure 5.18 (a) and (b). Here, XRR measurement fittings provide the thickness, roughness, and density of deposited a-IGZO. Also, XRR was performed to obtain the average thickness of the three-layer structure, interface roughness and density of each layer. The density of as-deposited a-IGZO was 6.65 g/cm^3, higher than typical values for single crystal InGaZnO$_4$ (6.4 g/cm^3) reported in the previous report. This can be understood by the effects of elemental content change in the elements; it is

due to differences in mass of elements (such as In content in films) [273]. The density of the deposited SiO_x in this work was found at 2.45 g/cm^3, lower than values of crystalline SiO_x that have 2.68 g/cm^3 [274]. This lower density in this binary oxide suggests a porosity of the film and serves as the first indication of a higher than normal level of defects in the thin film. This density value is in line with SiO_x density of 2.46 g/cm^3 in a-ZTO/SiO_x/a-ZTO trilayer films. Average interfaces roughness of a-IGZO and SiO_x is at ≈ 0.55 nm in a-IGZO/SiO_x/a-IGZO film structure, which is a consistent value for interfaces roughness of a-ZTO and SiO_x. This means there is no considerable variation in these films' density and interface roughness.

Figure 5.18 (c) exhibits the XRD pattern of the pure a-IGZO, a-$IGZO_{(20nm)}$/$SiO_{x(2nm)}$/a-$IGZO_{(10nm)}$ three-layer structure film and glass, where any sharp crystalline peaks have not been detected, instead of that, a few halo peaks were observed at around 13°, 24°, and 30°. Peak at 13° might be originated from high variation in the length of amorphous bonds. This halo peak is an indicator of an amorphous nature observed in cited work as well [275]. The peak at 24° corresponds to the glass substrate previously reported [177]. The peaks at 30° and 40-44° are from the XRD sample holder and are observed consistently in three films' XRD data (See sample holder picture in Figure 3.6 (b), 2).

We confirmed the amorphous phase using the XRD system. The thickness and density of a-IGZO/SiO_x/a-IGZO multilayers were obtained by using the XRR data. a-IGZO/SiO_x/a-IGZO films' carrier concentration, electron mobility, and film resistivity were investigated using the Hall system based on the van der Pauw configuration. All results will be outlined in the following sections.

5.14.4 Hall Effect data of a-IGZO/SiO_x/a-IGZO Films

The multilayer investigation was carried out with deposited two three-layer films to obtain their precise carrier concentration and mobility as shown in Table 5.3 and Figure 5.19. A trilayer film was deposited at 180 °C, where high-temperature results in the vanishing of the carrier drop in this film due to in-situ annealing in the sputtering chamber during the growth of the multilayer.

The conductivity of a-$IGZO_{10nm}$/$SiO_{x(2nm)}$/a-$IGZO_{10nm}$ multi-layered film is much lower than a-$IGZO_{20nm}$/$SiO_{x(2nm)}$/a-$IGZO_{10nm}$ multi-layered film because

the carrier concentration drops by a factor of 10 with the insertion of SiO_x film.

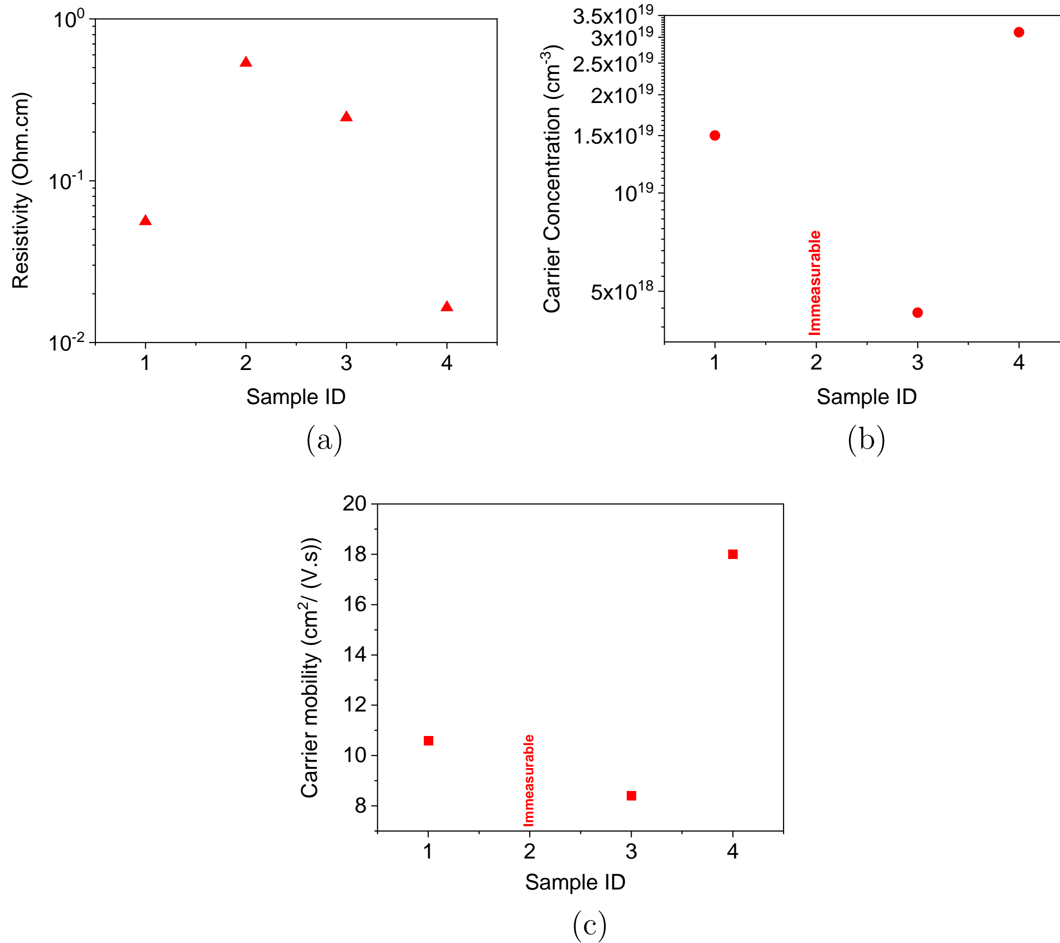

Figure 5.19: Hall measurements of samples for multilayers, where (a) - resistivity, (b) - carrier concentration, (c) - carrier mobility of three-layer samples and sample ID (1) - 30 nm thick bulk a-IGZO, (2) - bottom and top layers are 10 nm thick a-IGZO in three-layered structure, (3) - bottom and top layers are 20 nm and 10 nm thick a-IGZO individually in trilayer film, (4) - bottom and top layers are 20 nm and 10 nm thick three-layer film deposited at 180 °C. (▲) symbol shows resistivity, (●) indicates carrier concentration and (■) symbol for carrier mobility of the films.

Carrier concentration and mobility of a-$IGZO_{10nm}$/$SiO_{x(2nm)}$/a-$IGZO_{10nm}$ multi-layered film are immeasurable with the Hall effect system. As a result, the thickness of the bottom layer of a-IGZO was increased to 20 nm, which gives us the accurate Hall signals (resistivity, carrier concentration and mobility values of these samples) as shown in Table 5.3 and Figure 5.19. Here, we also considered

a-IGZO/SiO_x/a-IGZO	Total thickness (±0.5)	ρ (ohm.cm)	n_c (cm^{-3}) (±0.3)	μ_e (cm^2/Vs) (±1)	Sample ID
Bulk a-IGZO (RT)	30.4 nm	5.59x10^{-2}	1.5x10^{19}	10.6	1
10 nm/2 nm/10 nm (RT)	22.1 nm	5.35x10^{-1}	-	-	2
20 nm/2 nm/10 nm (RT)	32.4 nm	2.46x10^{-1}	4.3x10^{18}	8.4	3
20 nm/2 nm/10 nm (180 °C)	32 nm	1.64x10^{-2}	3.11x10^{19}	18	4

Table 5.3: Hall measurement for certain three-layered samples, where - ρ resistivity, n_c free carrier, μ_e carrier mobility of films. (-) symbol indicates immeasurable carrier concentration and mobility for sample ID (2). RT and 180 °C show room and high temperature grown samples, individually.

the maximum penetration depth (10 nm) of the XPS system, and therefore, the top layer of a-IGZO is kept at 10 nm.

5.14.5 Results and Findings of a-IGZO/SiO_x/a-IGZOs

Figure 5.20 shows that resistivity, carrier concentration and mobility of a-IGZO have been altered by including the ultra-thin SiO_x, where the thickness of the SiO_x varied from 1 nm to 7 nm. The electrical properties of a-IGZO are a function of the SiO_x thickness. In Figure 5.20 (a), the resistivity of the three-layered a-IGZO/SiO_x/a-IGZO films increased rapidly with increasing the thickness of the SiO_x from 1 nm to 3 nm, which recovered to the initial values the thickness of SiO_x of 4 nm and up to 7 nm. The carrier concentration of the three-layered structure a-IGZO/SiO_x/a-IGZO films dropped by a factor of 5 from 1.5×10^{19} cm^{-3} to 3×10^{18} cm^{-3}. These data showed a strong relation between carrier concentration and electron mobility at room temperature. There is an increasing carrier concentration with decreasing carrier mobility due to ionized impurity scattering of charge carriers. This behaviour is in line with previous work [276] and a comparison between previous work as shown in Figure 5.21. As given in a table 5.3, 2 nm thick SiO_x layer induces the most carrier drop behaviour. This thickness has also pointed out the most carrier drop side effect in previous work [39]. The reasons for carrier drop can be discussed in the following paragraphs.

It is clear that a reduction in thickness of SiO_x increases the defectiveness of SiO_x, leading to more sub-oxide phases or other content [277]. Here, an abun-

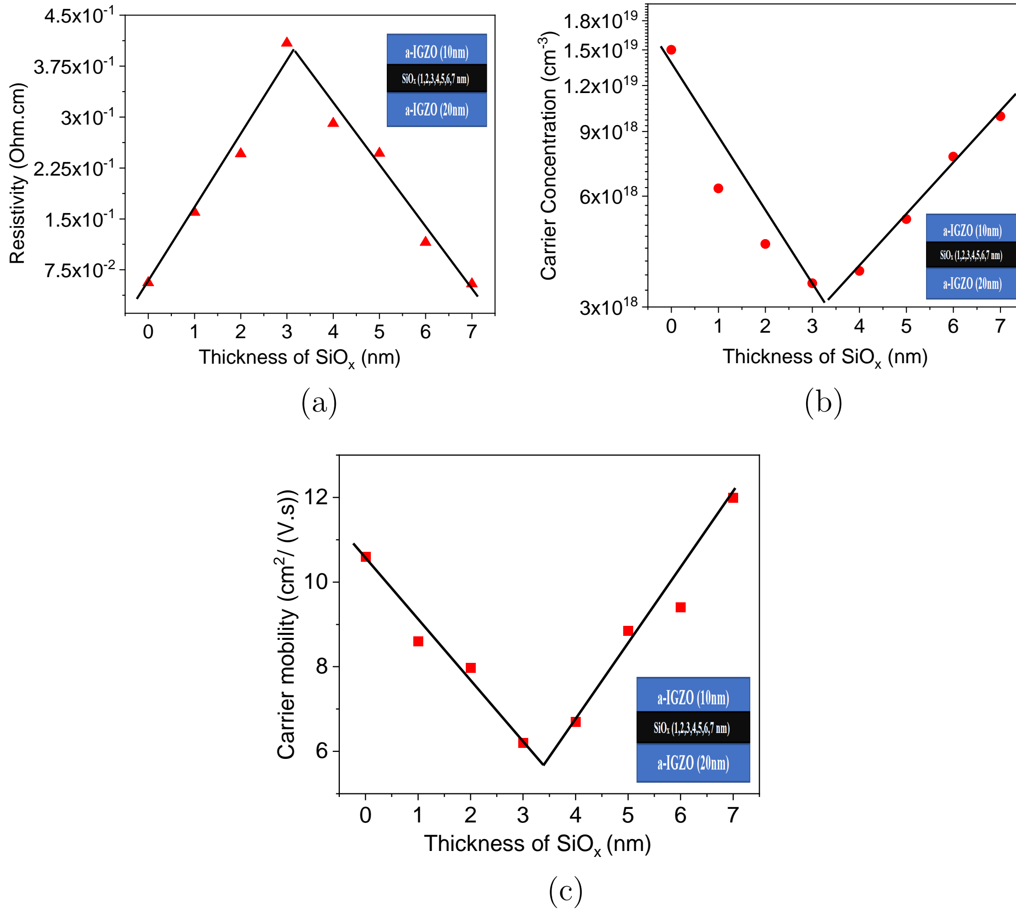

Figure 5.20: a-IGZO/SiO_x/a-IGZO layered structure of the multilayers, where (a) - resistivity, (b) - carrier concentration, (c) - carrier mobility versus thickness of the SiO_x layer's maps. (▲) symbol shows resistivity, (●) indicates carrier concentration and (■) symbol for carrier mobility of the a-IGZO/SiO_x/a-IGZO films.

dance of the interfacial suboxide species is defined by a decrease in the thickness of SiO_x. Increasing the thickness of SiO_x film likely leads to fewer defective films, thus fewer suboxides. This leads to either a reduction in the trapping of the carriers or a reduction in the gettering impact of the layer. This has been observed previously in this report [278]. Two possible preseasons could impact carrier drops in a-IGZO/SiO_x/a-IGZO multilayers.

a-IGZO is highly demanding of oxygen structures, and the electrical properties were controlled by a variation in oxygen partial pressure during the deposition in previous report [30, 87]. In our cases, all films were fabricated in an oxygen-poor

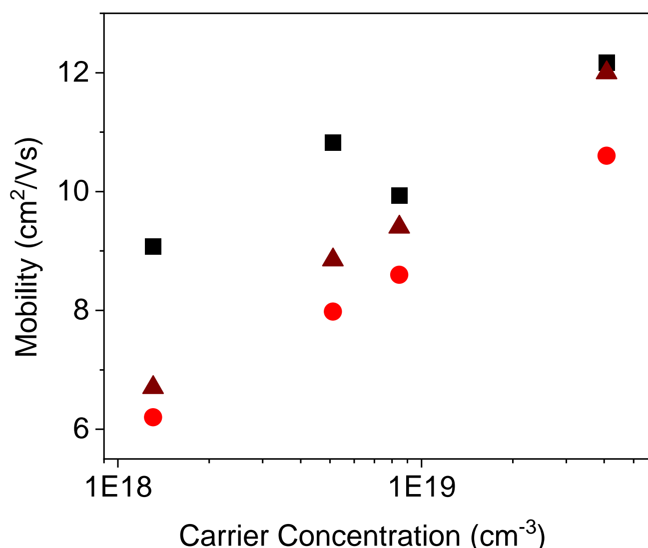

Figure 5.21: Carrier concentration versus carrier mobility of bulk a-IGZO, and a-IGZO/SiO_x/a-IGZO multi-layers in this work, where - (■) values for bulk a-IGZO from cited work [276], (▲) values for a-IGZO/SiO_x/a-IGZO films with thickness of SiO_x veried from 0 nm to 3 nm (in this range carrier concentration drops, see Figure 5.20 (b)), and (●) values for a-IGZO/SiO_x/a-IGZO films with thickness of SiO_x varied from 4 nm to 7 nm (concentration goes up, see Figure 5.20 (b)).

atmosphere (a pure Ar non-reactive sputtering method was used), likely leading to non-stoichiometry of SiO_2 deposition. Also, it is more likely to synthesise oxygen-deficient of a-IGZO films at the same time. This means that non-stoichiometric ultra-thin SiO_x films have more trap states within the bandgap [279], and these trap states can capture electrons. It is possibilities creating Si dangling bonds in SiO_x film, which have a single neutral electron structure with trapping electrons. This report found that a single neutral electron structure acts as an electron trapping side in this report [242]. Several electron trapping centres have been demonstrated due to the changes in Si- O bonding, and oxygen vacancies that result in trapping electrons in the bulk amorphous silicon dioxide [246, 280]. Another possibility is that these suboxide species between interfaces of a-IGZO and SiO_x can facilitate the formation of a new bonding between Si and oxygen atoms because they have different binding energies and electronegativities [132, 133, 135].

We used XPS for studies of oxygen structures in the multilayers. The in-situ

transferring of three multilayer films from the magnetron chamber to the XPS was carried out. Here, the main goal is to prevent oxygen contamination from an atmospheric environment. It is notoriously difficult to prove oxygen structure changes in the sputtering chamber or outside. We discuss the in-situ transfer procedure in the following section.

5.14.6 In-Situ Transfer Process of Multilayers from Magnetron to XPS

X-ray photoelectron spectroscopy (XPS) was employed to study the material composition of thin films. The investigation was carried out of three systems

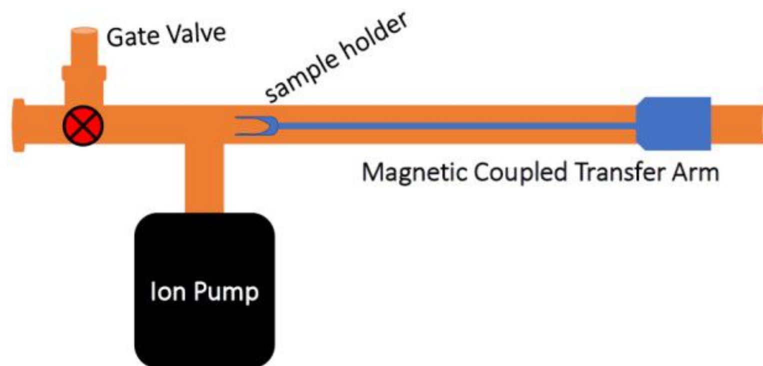

Figure 5.22: An illustration of a transfer arm with an Ultra High Vacuum, (UHV: $\approx 8 \times 10^{-9}$ mbar).

(transfer arm as shown in Figure 5.22) of a-IGZO$_{(20nm)}$/SiO$_{x(2nm)}$/a-IGZO$_{(20nm)}$, a-IGZO$_{(20nm)}$/SiO$_{x(2nm)}$/a-IGZO$_{(7.5nm)}$, and a-IGZO$_{(20nm)}$/SiO$_{x(2nm)}$/a-IGZO$_{(10nm)}$ films that transferred under vacuum using a transfer arm in order to avoid contamination in air.

First multilayer: In the initial stage, the experiment has been done by depositing 20 nm thick a-IGZO thin films on a glass substrate as shown in Figure 5.23 ①, then transported with ultra-high vacuum transfer arm (as referred to UHV transfer arm) to XPS (First layer XPS scan) is shown in Figure 5.23 ②, where XPS scan was done. After the sample was transferred back to the magnetron chamber with the same transfer arm as shown in Figure 5.23 ③ and 2 nm thick SiO$_x$ film was deposited on top of the 20 nm thick a-IGZO (Second layer). This was followed by replicating the process above to obtain an XPS scan of

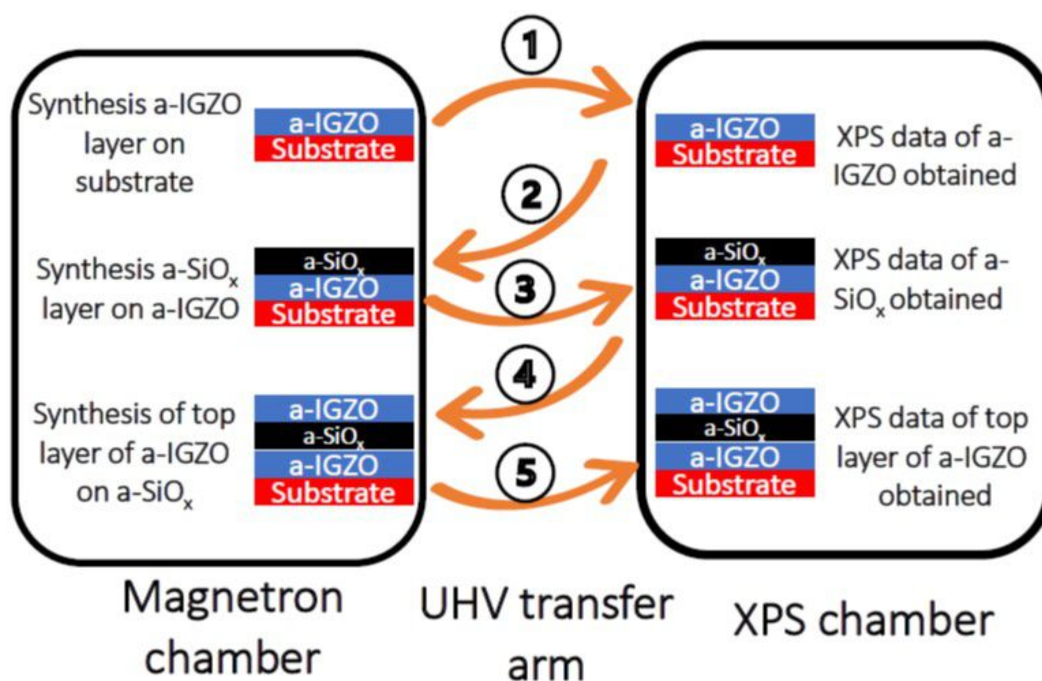

Figure 5.23: The first in-situ transfer of a-IGZO$_{(20nm)}$/SiO$_{x(2nm)}$/a-IGZO$_{(20nm)}$ multilayer from magentron to XPS, where from (1) to (5) indicates as UHV transportation as shown in Figure 5.22.

2 nm thick amorphous SiO$_x$ film (Second layer XPS data) and transferred to the magnetron chamber as shown in Figure 5.23 (4). In the last stage 20 nm thick a-IGZO thin film was synthesised on 2 nm thick SiO$_x$ layer as a top layer(Third layer). This was also transferred under vacuum to XPS (Third layer XPS scan) as shown in Figure 5.23 (5), where obtained the XPS data.

Second attempt: a-IGZO$_{(20\,nm)}$/SiO$_{x(2\,nm)}$/a-IGZO$_{(7.5\,nm)}$ produced in one deposition by Magnetron sputtering, then that has been brought to XPS, where XPS data was collected as shown in Figure 5.24. After obtaining the XPS data for the first multi-layer, there is an assumption to reveal the thickness effects on carrier drop, which could impact surface oxygen structure or elemental changes in a-IGZO/SiO$_x$/a-IGZO film. The thickness of the top a-IGZO layer decreased from 20 nm to 7.5 nm and XPS data was obtained.

The goal of the third attempt was to show consistent data for multilayers with

Figure 5.24: a-IGZO$_{(20\,nm)}$/SiO$_{x(2\,nm)}$/a-IGZO$_{(7.5\,nm)}$ three-layer structure film was transferred with in-situ transfer of from magnetron to XPS under UHV transfer arm as shown in Figure 5.22.

bottom 20 nm thick a-IGZO and top 10 nm thick a-IGZO three-layer, where the thickness of the middle layer of SiO$_x$ was varied to alter electrical properties as shown in Figure 5.20.

Figure 5.25: The third attempt in-situ transfer of a-IGZO$_{(20\,nm)}$/SiO$_{x(2\,nm)}$/a-IGZO$_{(10\,nm)}$ from magentron to XPS via UHV transfer arm as shown in Figure 5.22.

Third attempt: a-IGZO$_{(20\,nm)}$/SiO$_{x(2\,nm)}$/a-IGZO$_{(10\,nm)}$ thin film produced in one deposition by Magnetron sputtering method, which was brought to the XPS, where XPS data obtained is presented in Diagram 5.25.

All results and analysis of in-situ transferred films via XPS will be addressed in the next section.

5.14.7 XPS Studies of a-IGZO/SiO$_x$/a-IGZO Multilayers

XPS data of all three-layer structure films showed consistent elemental ratios as shown in Table 5.4 and Figure 5.26 for all in-situ transferred samples. This

implies that the material ratios do not have any composition alterations because whole films were deposited in the same way.

In-situ transfers	In	Ga	Zn	O	Si/O
First attempt	21%	16%	12%	51%	27% /73%
Second attempt	20.1%	16.5%	12.6%	50.9%	
Third attempt	20.7%	16.3%	12.2%	50.8%	

Table 5.4: The elemental composition of in-situ transferred multilayers.

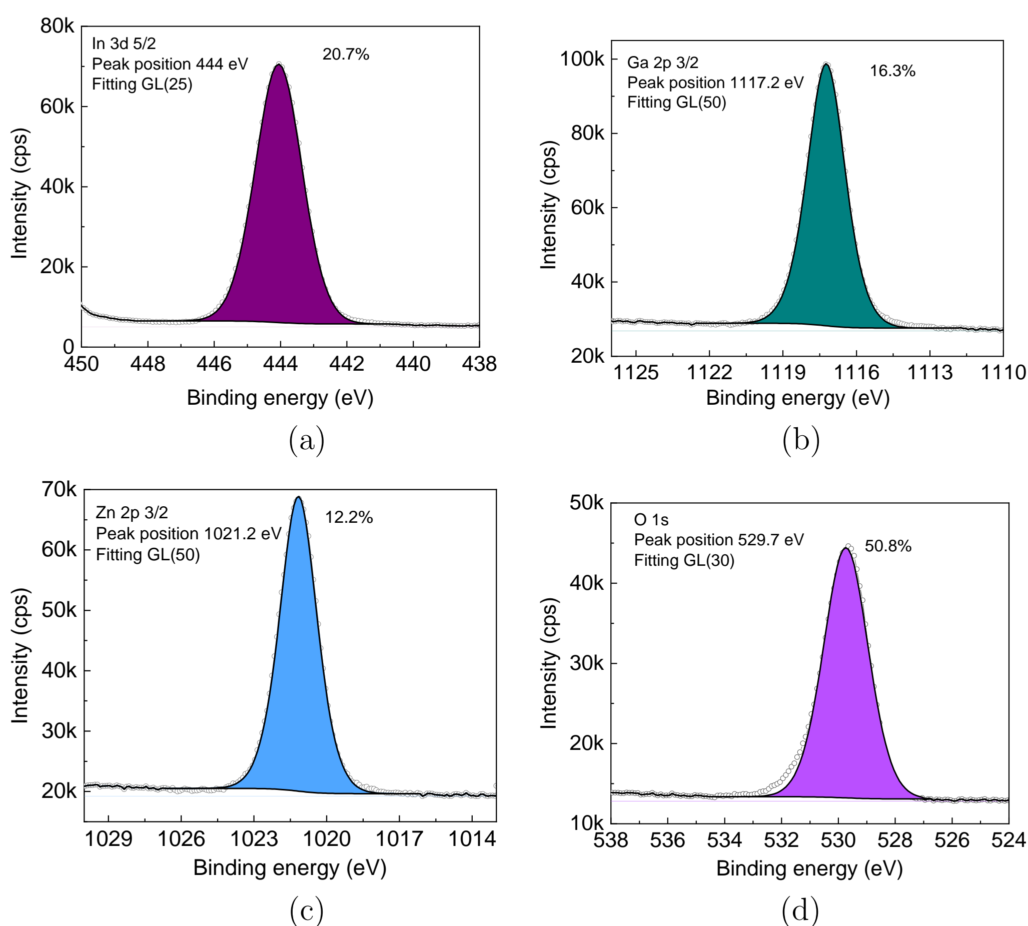

Figure 5.26: An illustration of the elemental ratios of a-IGZO/SiO_x/a-IGZO multilayers, where (a) - Indium, (b) - Gallium, (c) - Zinc, (d) - Oxygen.

However, Figure 5.27 (a) shows XPS data of the bottom layer of a-IGZO, SiO_x layer and top layer of a-IGZO. Furthermore, O 1s peak at around at 532.3 eV corresponds to Si and O bond in SiO_x layer. Splitting of oxygen O 1s peak at $\approx$

530 eV is in line with both the bottom and the top layer of a-IGZO that originated from the metal cations with oxygen bonding in a-IGZO. The O 1s peaks were found in previous work in a-IGZO with different thicknesses on stoichiometric SiO_2 substrates [128]. Unfortunately, Si 2p was not distinguished from Ga 3p XPS peak as they overlap with each other in this work. Furthermore, as compared O 1s peak at around 532.3 eV with different stoichiometry $SiO_{1.8}$ for 534.3 eV and $SiO_{1.6}$ for 533.2 eV peaks in previous study [281, 282], Si and O bond with higher binding energy is related to more stoichiometric silicon oxides.

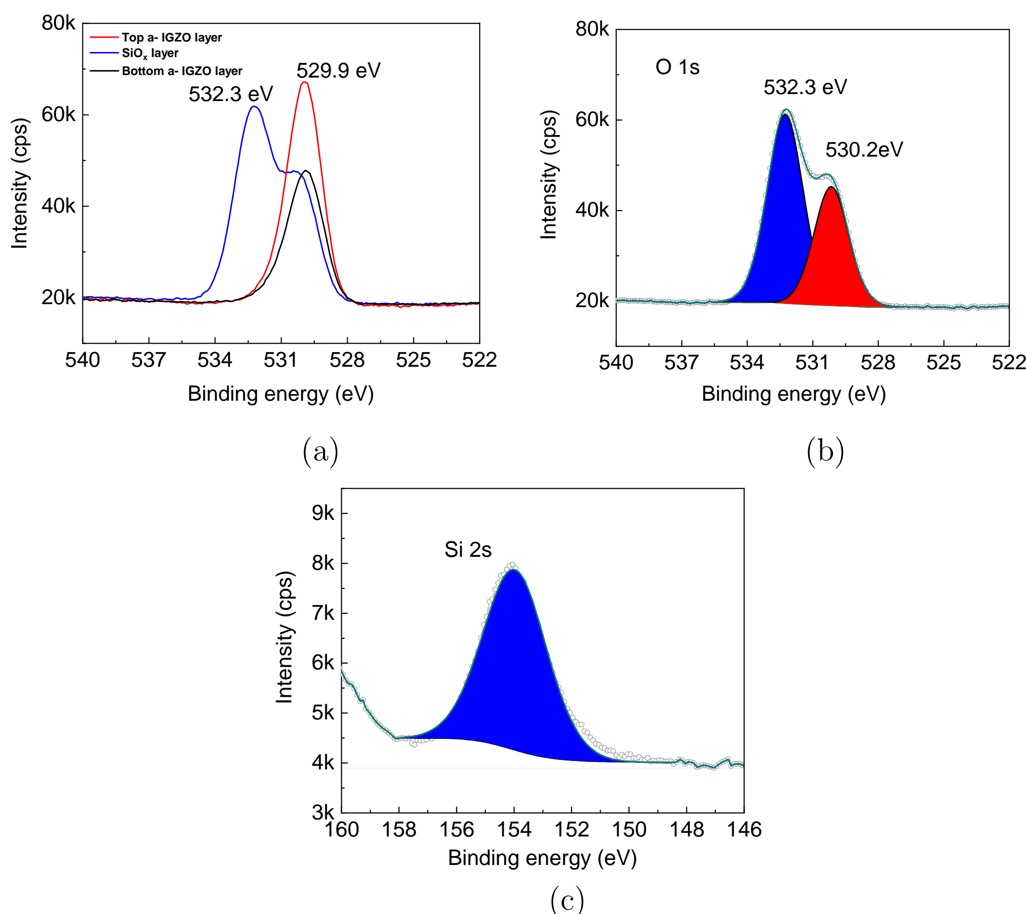

Figure 5.27: XPS scans of oxygen in a-IGZO and SiO_x, where (a) - oxygen XPS peaks from 20 nm thick bottom and top layer of a-IGZO and 2 nm thick SiO_x layer, (b) - O 1s XPS dat obtained from 2 nm thick SiO_x layer, (c) - 2 nm thick Si 2s XPS data.

In this work, we observed lower values of the binding energies O 1s at 532 eV

that is in line with other publications, and it was contributed to the $SiO_{x\sim1.5}$ at 532.0 eV [282, 283]. This implies that the ultra-thin SiO_x layer in this work was deposited with nonstoichiometric arrangements. This is worth mentioning that charge traps were found in the bulk ultra-thin 3 nm thick stoichiometric SiO_2 in this report [284]. This is a proven fact that decreasing the thickness of the SiO_x layer leads to a greater number of defects. The presence of defects in bulk SiO_2 indicated that they originated from the missing atoms without bonding with neighbouring atoms due to oxygen deficiency (usually called dangling bonds) [154, 285]. In the case of the a-IGZO layer, there was a little change in the composition of the films regardless of their thickness as shown in Table 5.4. Also, the XPS data confirmed no change in the oxygen structures in a-IGZO films. All the facts indicate that the a-IGZO films show a little change in their structure, indicating that the a-IGZO itself is not being altered in bulk. This means the change occurs close to the interface between a-IGZO and SiO_x containing a very high density of traps. However, there may be an electron trap in the interface of a-IGZO and SiO_2, but previous work pointed out that the density of this kind of trap is much less than the total density of traps in the oxides [155]. Here, in a-IGZO/SiO_x/a-IGZO multi-layers, electrons might be captured by defect centres in the SiO_x layer. This can cause changes in the properties of the materials. Theoretical work has found that under-coordinated In atoms in a-IGZO play the role of electron traps through electrostatic attraction [123]. This implies that particular undercoordinated In atoms might be created by introducing ultra-thin SiO_x with an absence of the oxygen from Si side. Here, Si may obtain the oxygen atoms from the a-IGZO films due to they possess different electronegativity, namely 1.78 is for In and 1.9 is for Si. The electronegativity could facilitate a significant charge transfer, where the formation of a bond between Si and oxygen. Oxygen is also an element with high electronegativity [135]. This leads to forming more undercoordinated In atom carrier trap centres. This implies that most trap density could be within the bulk of SiO_x layers. Notably, these defect centres serve as trapping free carriers (holes and electrons) [286]. It is difficult to observe these trapping states. However, Electron Paramagnetic Resonance (EPR) has been widely used to understand and investigate precise chemical, and structural details of trapping centres [287]. EPR measurements could be deployed to advance this

research further. One of the standard methods to examine the charge trap is the capacitance-voltage measurement. a-IGZO/SiO$_x$/a-IGZO will be deposited on the FTO substrate; also, gold contacts will be used. In other words, C-V data will be obtained in the future.

In these investigations, the main goal is to observe changes in oxygen structure in a-IGZO and SiO$_x$ layers. However, as shown in Figure 5.27, oxygen structure changes in layered structure films have not been observed. Therefore, more studies were done by other compelling techniques to establish the reasons for carrier concentration drop in a-IGZO/SiO$_x$/a-IGZO three-layer films. In the following section, AFM and SEM methods are involved in identifying carrier drops.

5.14.8 Alteration in Electrical Properties of In-Situ Transferred Trilayers

As mentioned above, Table 5.5 shows three in-situ transferred samples that showed carrier drop reduction in these films was less noticeable.

a-IGZO/SiO$_x$/a-IGZO (±0.5 nm)	Methods	ρ (ohm.cm)	n_c (cm^{-3}) (±0.3)	μ_e (cm^2/Vs) (±1)
20/2/20	normal	1.96x10^{-1}	6.5x10^{18}	12
20/2/20	in-situ	2.22x10^{-2}	2.66x10^{19}	14
20/2/10	normal	2.46x10^{-1}	4.3x10^{18}	8.4
20/2/10	in-situ	8.67x10^{-2}	8x10^{18}	13.7
20/2/7.5	normal	2.96x10^{-1}	3.4x10^{18}	8.27
20/2/7.5	in-situ	5.42x10^{-2}	1.26x10^{19}	9.8
Bulk a-IGZO	normal	5.59x10^{-2}	1.5x10^{19}	10.6

Table 5.5: Comparison of the electrical properties of samples transferred in-situ and under air (referred to as normal in Table) and bulk a-IGZO, where ρ, n_c and μ_e are resistivity, carrier concentration and carrier mobility of the in-situ transferred, in air transferred samples, and bulk a-IGZO.

This is a fact that there are differences in the background pressures between the magnetron chamber and XPS and transfer arm system. To identify the effect of this, trilayer a-IGZO$_{20\,nm}$/SiO$_{x(2\,nm)}$/a-IGZO$_{10\,nm}$ was synthesised in one deposition, and this film was kept for 24 hours in transfer arm system (Figure 5.22). Finally, the electrical properties were compared with in air transferred samples as shown in Table 5.6.

Through this study, the base pressure of the magnetron chamber was 1.6×10^{-5} mbar, and the transfer arm and XPS system were $\approx 1 \times 10^{-10}$ mbar. There

a-IGZO/SiO_x/a-IGZO ($\pm$0.5 nm)	Storage	ρ (ohm.cm)	n_c (cm^{-3}) ($\pm$0.3)	μ_e (cm^2/Vs) ($\pm$1)
20/2/10	air transferred	2.46x10^{-1}	4.3x10^{18}	8.4
20/2/10	transfer arm	1.16x10^{-1}	7.1x10^{18}	7.52
Bulk a-IGZO (30 nm)	air transferred	5.59x10^{-2}	1.5x10^{19}	10.6

Table 5.6: Comparison of the electrical properties of samples were kept in the transfer arm for 24 hours and in air transferred sample, bulk a-IGZO film for comparison, where ρ, n_c and μ_e are resistivity, carrier concentration and carrier mobility of samples kept in transfer arm, in air transferred sample and bulk a-IGZO.

was a considerable difference in the pressure levels at the two chambers that affected the defect passivation in these layers, primarily oxygen gas. Oxygen plays a crucial role in amorphous networks in order to control charge carriers [288]. There could be other gases besides oxygen, such as hydrogen, but it is not easy to detect them. Firstly, a-$IGZO_{20\,nm}$/$SiO_{x(2\,nm)}$/a-$IGZO_{10\,nm}$ film was kept in the transfer arm, and the electrical properties of the samples are shown in Table 5.6. Here, the charge carrier drop effect still exists, but it is small compared with air-transferred samples. This implies that additional passivation or alteration might happen in the XPS chamber. One possible explanation for eliminating the carrier drop insitu transferred sample is that these samples were stored in an XPS chamber or transfer arm for a long time, where a tiny amount of the background gas could alter the electrical properties. This alteration may be part of a reaction between surface and oxygen and oxygen diffusion in film. This implies that there is a relationship between film and background gas [289]. One trilayer film was synthesised by each layer individually, and XPS data of each layer were obtained separately as shown in Figure 5.27 (a). Interestingly, XPS data obtained from trilayer film demonstrated a substantially lower carrier concentration drop than other three-layer films fabricated in one deposition. Note that background oxygen gas has interacted with each layer separately in a-$IGZO_{20\,nm}$/$SiO_{x(2\,nm)}$/a-$IGZO_{20\,nm}$ film. There is a possibility that background oxygen gas altered the electron trap states in SiO_x film. This is because of the sufficient time (around 24 hours) for interaction between each layer and background oxygen gas. It was reported that these sorts of electron trap states had been widely observed and analysed in amorphous SiO_x networks, which can be altered by annealing or oxygen flow during the depo-

sition process [290–292]. In contrast, when a-IGZO$_{20\,nm}$/SiO$_{x(2\,nm)}$/a-IGZO$_{7.5\,nm}$ and a-IGZO$_{20\,nm}$/SiO$_{x(2\,nm)}$/a-IGZO$_{10\,nm}$ films were obtained in one deposition, they have a lower decrease in carrier concentration. This means that it is hard to alter the properties of the most defective SiO$_x$ layer directly, where possible background gas went through the a-IGZO layer, and the defect passivations occurred to a lesser extent in the SiO$_x$ layer.

Furthermore, the alteration in electrical properties of in-situ transferred films has brought attention to oxygen incorporation methods. The investigations were carried out by creating different oxygen atmospheres for trilayers. After the XPS measurements were completed, all samples' electrical properties were immediately measured by the Hall effect system.

To conclude, a partial pressure difference between the two experimental chambers could alter the properties of the samples. Here, the effect of oxygen content in multilayers was studied. The discussion on oxygen content is in the following section.

5.14.9 The Role of Oxygen in a-IGZO/SiO$_x$/a-IGZO and SiO$_x$ Films

To understand the mechanisms that affect the oxygen content in the multilayers, several a-IGZO$_{20\,nm}$/SiO$_{x(2\,nm)}$/a-IGZO$_{10\,nm}$ films were deposited in the same way with other films the only difference being the introduction of oxygen. These investigations are presented in Figure 5.28 and Table 5.7.

Trilayer films were deposited in different oxygen concentrations of atmospheres. The oxygen concentrations could play a key role in a-IGZO/SiO$_x$/a-IGZO films and might be a cause for the identified charge drop in these films. As shown in Figure 5.28 №1 on the x-axis film was fabricated and kept in a magnetron chamber with the base pressure 1.6×10^{-5} mbar for 24 hours (in Table 5.7, №1), and in Figure 5.28 №2 on the x-axis trilayer structure was kept in the sputtering chamber after deposition, then sputtering chamber was filled with pure oxygen gas for 10 minutes, where the pressure of the sputtering chamber was 1 mbar (in Table 5.7, №2). An interaction between the oxygen and film implies that long exposure in the magnetron chamber (amount of background gas) facilitates more oxygen interaction with films, but there is insufficient oxygen for directly passivating

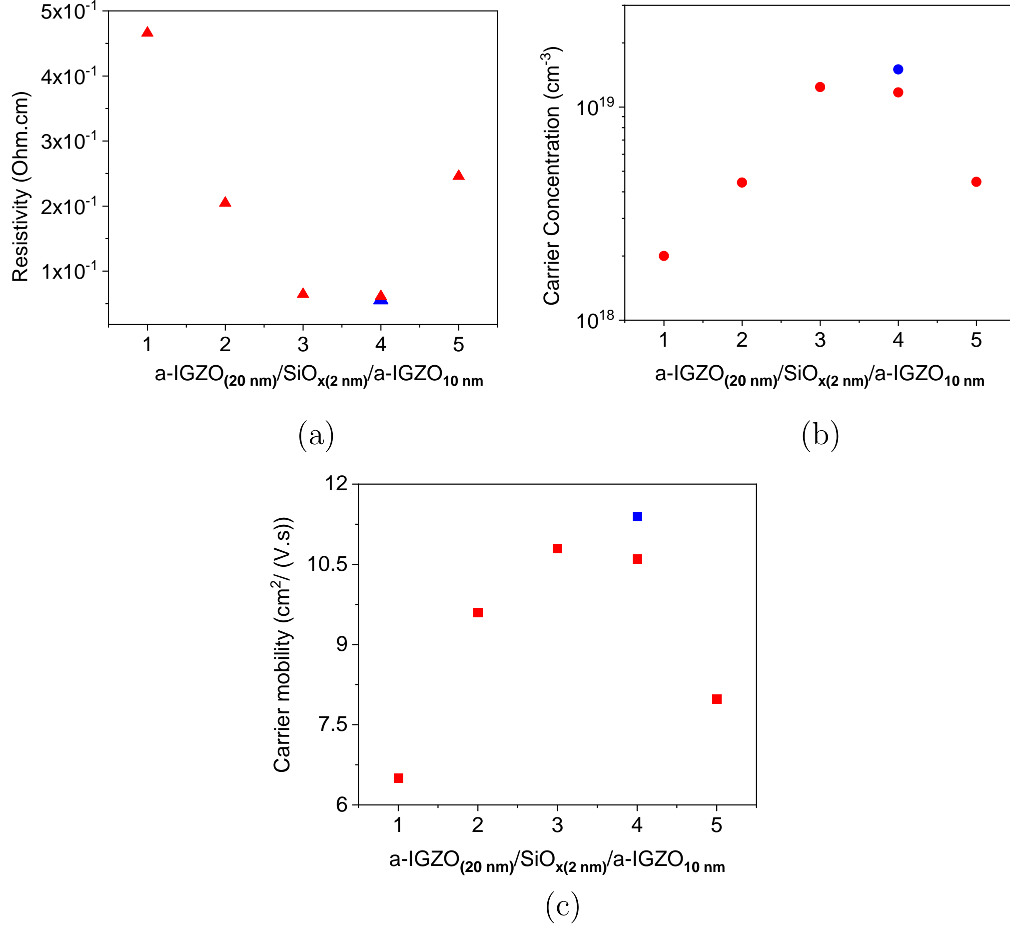

Figure 5.28: The effect of oxygen on a-IGZO$_{20\,nm}$/SiO$_{x(2\,nm)}$/a-IGZO$_{10\,nm}$ films, where (1) - sample deposited, then kept for 24 hours in magnetron chamber, (2) - deposited sample kept in pure oxygen atmosphere 10 minutes in magnetron chamber (1 mbar), (3) - SiO$_x$ layer in a-IGZO$_{20\,nm}$/SiO$_{x(2\,nm)}$/a-IGZO$_{10\,nm}$ was synthesised with 1 sccm oxygen flow, (4) - SiO$_x$ layer in a-IGZO$_{20\,nm}$/SiO$_{x(2\,nm)}$/a-IGZO$_{10\,nm}$ was synthesised with 2 sccm oxygen flow, (5) - a-IGZO$_{20\,nm}$/SiO$_{x(2\,nm)}$/a-IGZO$_{10\,nm}$ film deposited by normal way. (▲) symbol shows resistivity, (●) indicates carrier concentration and (■) symbol for carrier mobility of the a-IGZO$_{20\,nm}$/SiO$_{x(2\,nm)}$/a-IGZO$_{10\,nm}$ films. Second sample in table ★ - 30 nm bulk a-IGZO film and it's resistivity, carrier concentration and carrier mobility for (▲), (●), and (■), respectively.

the defects in SiO$_x$ films. Nevertheless, there is the absorption of oxygen on the surface of the a-IGZO. Here, oxygen might have the least impact on an ultra-thin a-IGZO layer in a-IGZO/SiO$_x$/a-IGZO that film was kept in the sputtering

№	ρ (ohm.cm)	n_c (cm^{-3}) (±0.3)	μ_e (cm^2/Vs) (±1)	Methods
★	5.6x10^{-2}	1.5x10^{19}	10.6	Bulk a-IGZO
1	4.66x10^{-1}	2x10^{18}	6.5	24 hours
2	2.05x10^{-1}	4.42x10^{18}	9.6	pure oxygen
3	6.45x10^{-2}	1.24x10^{19}	10.8	1 sccm
4	6.11x10^{-2}	1.17x10^{19}	11.4	2 sccm
5	2.46x10^{-1}	4.45x10^{18}	7.98	Normal way

Table 5.7: The effect of oxygen on a-$IGZO_{20\,nm}/SiO_{x(2\,nm)}$/a-$IGZO_{10\,nm}$ films, where (★) - 30 nm bulk a-IGZO film for comparison, (1) - sample deposited, then kept 24 hours in magnetron chamber, (2) - deposited sample kept pure oxygen atmosphere for 10 minutes in magnetron chamber (1 mbar), (3) - SiO_x layer synthesised with 1 sccm oxygen in a-$IGZO_{20\,nm}/SiO_{x(2\,nm)}$/a-$IGZO_{10\,nm}$ film deposition, (4) - SiO_x layer synthesised with 2 sccm oxygen in a-$IGZO_{20\,nm}/SiO_{x(2\,nm)}$/a-$IGZO_{10\,nm}$ film growth, (5) - a-$IGZO_{20\,nm}/SiO_{x(2\,nm)}$/a-$IGZO_{10\,nm}$ film deposited by normal way. ρ, n_c and μ_e are resistivity, carrier concentration and carrier mobility of the a-$IGZO_{20\,nm}/SiO_{x(2\,nm)}$/a-$IGZO_{10\,nm}$ films individually.

chamber atmosphere for 24 hours (a tiny amount of oxygen is in the sputtering chamber with 1.6×10^{-5} mbar pressure). That means that electron trap sources in SiO_x film still dominate the carrier concentration drop in trilayers. This can be confirmed by the sample's electrical properties as shown in Figure 5.28, №2 on the x-axis, the sample that was kept in a pure oxygen atmosphere for 10 minutes, there is no substantial variation in final resistivity than film as shown in Figure 5.28 №5 on the x-axis. Here, №5 on the x-axis film was prepared in air transferred sample, which means depositing films and measuring their electrical properties immediately. The concentration of oxygen in 1 mbar pure oxygen atmosphere is much higher than a standard magnetron sputtering chamber (1.6×10^{-5} mbar). As a result of that, oxygen could alter the surface density of the a-IGZO film, but the electrical properties of trilayer film №2 in Table 5.7 is in line with those of multilayer №5 on the x-axis. The changes in the electrical properties of these samples by oxygen content indicated that oxygen has less impact on depositing the samples in one synthesis process. However, this process could be slower and less able to alter the electrical properties of the samples regarding the charge traps in the SiO_x layer so that the oxygen gas flow was introduced to film growth as shown in Figure 5.28. 1 sccm oxygen flow is for 5.28 №3 on the x-axis and 2 sccm oxygen flow is for 5.28 №4 on the x-axis during the growth for SiO_x layer

in a-IGZO$_{20\,nm}$/SiO$_{x(2\,nm)}$/a-IGZO$_{10\,nm}$ films, where aims to obtain close to the stoichiometric SiO$_x$ with less suboxide species. Previous reports suggested that deposition SiO$_x$ films under 2 sccm oxygen flow via magnetron sputtering system produces stoichiometric SiO$_x$ films [293], and this is consistent with our value. However, flow rates are difficult to compare between two different systems due to the two chambers have different geometry and comparison on the basis of the flow rate may not give the correct picture of the conditions. This not only includes the distance from the gas inlet to the target, and substrate surface but also the volume of the chamber etc. While reducing the charge trap states, oxygen deficiency in the SiO$_x$ films changed with oxygen flow as shown in Figure 5.28 №3 on the x-axis and №4 on the x-axis trilayer a-IGZO/SiO$_x$/a-IGZO films. Their electrical properties are in line with a bulk a-IGZO as shown in Table 5.7 (★) symbol and charge carrier drop behaviour in these trilayer structures has been gone away. SiO$_x$ film's electrical properties were defined by oxygen flow in the chamber, which is consistent with previous work. In this work, the electrical properties of SiO$_x$ were altered by oxygen content during the growth of films [281]. Also, theoretical work found that undercoordinated silicon atoms were created due to oxygen deficiency, and they act as trap electrons and holes [245].

5.14.10 Figure of Merit of layered structures

Figure of Merit (FOM) of a-ZTO, a-IGZO and trilayers by TCOs and insulators are shown in Table 5.8, where FoM of these materials was calculated by considering of transmittance (T) and transmittance (T) + reflectance (R). This means that two methods for deriving the FoM are used.

The Figure of Merit of transparent electrode materials is a crucial indicator for some applications and device geometries. This implies that some films with 80% transmission have a similar FOM to those with 30%yet, having higher conductivity values. In some instances, the specific application that requires low transparency or high conductivity might be well accepted. In other words, all transparent electrode films have various uses. Therefore, for materials in this work, it is challenging to compare the Figure of Merits of these materials because they are different materials with various thicknesses. Also, they possess substantially different properties, such as different electrical properties, as shown

Material	R_{sh} $\Omega/\square$	T(%)	R(%)	FoM$_T$ (Ω^{-1}) $\frac{T}{R_{sh}}$	FoM$_{TR}$ (Ω^{-1}) $\frac{1}{R_{sh}ln(T+R)}$
a-ZTO (20 nm)	18349	85.9	13.7	1.2×10^{-5}	2.7×10^{-3}
a-ZTO/SiO$_x$/a-ZTO 10 nm/2 nm/10 nm	69114	84.5	13.1	2.7×10^{-6}	1.2×10^{-3}
a-ZTO/TiO$_x$/a-ZTO 10 nm/2 nm/10 nm	31664	82.4	15.7	4.6×10^{-6}	3.1×10^{-3}
a-IGZO (30 nm)	18652	82	17.09	7.4×10^{-6}	5.3×10^{-3}
a-IGZO/SiO$_x$/a-IGZO 20 nm/2 nm/10 nm	76780	83.6	16.8	2.2×10^{-6}	6.5×10^{-4}

Table 5.8: Comparison of Figure of Merit of trilayers and TCOs, where R(%) and T(%) are the optical reflectance and transmittance of films at 550 nm.

in Table 5.8 and nothing at all to discuss regarding an effective FoM for further use. As shown in Table 5.8 when optical reflectance has been taken into account, this results in considerable differences in interference between the layers. The sheet resistance is a vital factor of the FoM of a single layer of TCOs and layered structures. As discussed above, changes in the FoMs are controlled by the sheet resistance of films, and also it is clearly seen in Table 5.8 the thickness of the films directly affects the FoM of materials. All imply that comparing the FoM of materials must be performed with caution and then assess the FoM of materials for applications.

5.15 Conclusions

I may now put forward a tentative scenario whereby the thickness of the SiO$_x$ alters the electrical properties of the trilayer structure. The thickness of the SiO$_x$ controls the electrical properties of a-ZTO/SiO$_x$/a-ZTO, where the lowest carrier drop in the trilayer was established by 2 nm thick SiO$_x$. Carrier mobility declined under 2 nm thick SiO$_x$ by 40%. The optical properties of trilayers showed no changes in trilayers compared to a single-layer a-ZTO film. For layered a-ZTO/TiO$_x$/a-ZTO films, TiO$_x$ showed less carrier decrease compared to a-ZTO/SiO$_x$/a-ZTO films (80%) in three-layer films, but it maintained the carrier mobility constant. The optical properties showed no changes compared to a single layer a-ZTO. At the same time, a-IGZO/SiO$_x$/a-IGZO films have been

investigated, where the thickness of the SiO_x governs the electrical properties of trilayers. AFM and SEM confirmed no island-like growth and surface damage. The roughness of films does not affect the carrier concentration drop in three layers. In-situ XPS studies observed these films' oxygen structures of multilayers with no changes. Furthermore, changes in in-situ transferred film's electrical properties originated from background gas from the two characterisation techniques: XPS and transfer arm and magnetron. Oxygen gas was involved in altering the electron trap states in the SiO_x layer. The optical properties did not detect/reveal any electron confinement in trilayers. Here, the only feasible explanation of charge carrier drop is by electron trap states of ultra-thin SiO_x.

6 Conclusions

This work has been discussed in three main things: understanding the optimisation of a-ZTO films, altering the defects in a-ZTO thin films by in-situ resistivity monitoring in various annealing environments, and laminating for controlling the electrical properties of amorphous TCOs. Lamination is an approach to insert the ultra-thin (<10 nm) insulator films between two TCO layers. The most common SiO_2 and TiO_2 insulator films were selected as insulator layers. For TCOs, one of the leading performers of a-IGZO and a promising candidate a-ZTO were used in studying multilayers.

The studies of optimisation on a-ZTO films demonstrated that the non-reactive and reactive magnetron sputtering methods generated two distinguishable local bond orders in a-ZTO films. Even though a-ZTO films have two different bonding arrangements, these films showed that the conductivity of a-ZTO thin films is in line with each other. The same conductivity of a-ZTO films results from a variation in material ratios with changing the local bond arrangements of the material. This is attributed to the change in oxygen content in the sputtering process. The difference in the oxygen concentration leads to different local bonding arrangements in films, which was confirmed via Raman spectroscopy. To conclude, the results obtained through two sputtering methods indicated that each fabrication

method needs to be optimised with its own improved optimisation parameters because it is hardly impossible to reuse the same deposited conditions elsewhere.

After optimising a-ZTO films, annealing studies on a-ZTO films were investigated. The analysis of previous reports showed that the annealing study with a fixed annealing time was a lack of in-situ resistivity monitoring in the process of annealing. In this work, annealing studies on a-ZTO thin films with in-situ resistivity monitoring were performed to gain the best electrical properties at a lower temperature. In these annealing studies on a-ZTO films, resistivity, annealing atmospheres and annealing time were controlled precisely with a specific annealing setup as mentioned in the previous chapter. The resistivity improvement curve versus temperature was recorded and investigated. Not all films show degenerately doped semiconductor behaviour before annealing. Also, the activation energies of the reaction were extracted, and the activation energy changed as a function of the temperature. It is important to note that six levels of temperatures were selected for probing the effects of these temperatures respectively. These different levels of temperatures were applied on a-ZTO films to saturate the lowest sheet resistance. The highest conductivity gained at annealing temperature 220 °C is in line with the value at 300 °C. Meanwhile, 38 nm thick a-ZTO was successfully obtained with conductivity of 320 S/cm by annealing at 220 °C instead of 300 °C. This implies that there is a trade-off between annealing temperatures and annealing time.

The demonstration on annealing in an oxygen-rich atmosphere shows that the effects of higher temperatures are replicable at lower values and lower temperatures. However, some annealing parameters can limit the TCO properties. This can include material properties (electrical properties), substrate melting point, and ductility properties. a-ZTO films were annealed in an oxygen-rich atmosphere using the in-situ monitoring of resistivity method, and a-ZTO film's carrier concentration and carrier mobility were enhanced simultaneously. The carrier concentration and mobility improvement can be explained by creating more oxygen vacancy-related defect centres acting as current carrier sources. The enhancement in the carrier mobility is due to reducing the scattering centres in the films, which is originated from undercoordinated metal clusters. These scattering centres were reduced by introducing oxygen into the amorphous networks during

the process of annealing. An in-situ resistivity monitoring method plays a prominent role in enhancing the electrical properties of a-ZTO films and $\approx 300\,\mathrm{S/cm}$ conductivity and average $19\,\mathrm{cm^2/Vs}$ carrier mobility of films were achieved by annealing temperature at $\approx 240\,^{\circ}\mathrm{C}$, which is a much lower temperature than other annealing works at $>350\,^{\circ}\mathrm{C}$. Finally, these annealed samples also indicated degenerately doped semiconductor behaviour after annealing. It implies a highly effective creation of large quantities of charge carriers was found at a lower annealing temperature in an oxygen-rich atmosphere.

This thickness dependency of a-ZTO implies that the reaction during the annealing does not occur at the surface and this hence may be driven by deep changes in bulk. This means that effective post-deposition treatment methods may vary significantly depending on the thickness of the a-ZTO films. We consider that a-ZTO is used in very thin layers for TFTs, and a-ZTO layers up to a micrometre in thickness can be applied in OLED or other devices for front contacts. The variation of film thickness is vital for optimisation conditions and post-deposition treatments. Room temperature deposited a-ZTO films with three different thicknesses, which were involved in this investigation. These films were annealed using an in-situ resistivity monitoring method that showed thicker films take a long time to saturate the lowest resistivity. Carrier concentration in the films annealed in an oxygen-poor atmosphere (nitrogen atmosphere) was enhanced, but electron mobility is still constant. However, films annealed in an oxygen-rich environment showed that carrier concentration and mobility were improved at the same time. The highest conductivity of $\approx 200\,\mathrm{S/cm}$ was obtained for both annealing environments. The carrier mobility of films obtained $12\,\mathrm{cm^2/Vs}$ for a nitrogen atmosphere, but it is $16\,\mathrm{cm^2/V}$ for an oxygen-rich atmosphere.

a-ZTO films were deposited at room temperature and $300\,^{\circ}\mathrm{C}$ that indicated a high temperature plays in-situ annealing in a sputtering chamber during the deposition.

Synthesised a-ZTO films on the bendable substrates showed that substrates did not deteriorate electrical properties; this means that a-ZTO films are highly suitable for mechanical stress by flexible substrates. The importance of these studies is that annealing with in-situ monitoring of resistivity studies is applied on a-ZTO films on Kapton substrates leading to significant improvements in their

electrical properties. Approximately 200 S/cm and 12 cm^2/Vs for conductivity and carrier mobility were obtained, respectively.

TCO-based TFTs are in need of low-carrier concentration TCOs. In this work, both a-IGZO and a-ZTO films' electrical properties (especially carrier concentration) were altered by involving ultra-thin insulator layers, where the primary insulator materials are SiO_2 and TiO_2.

Tuning the electrical properties of a-ZTO films is essential for some optoelectronic devices to satisfy their demand for low-carrier concentration TCOs. One of the best ways is layering (lamination) instead of doping. In this work, a-ZTO films were layered with insulators. a-ZTO films' electrical properties were changed by inserting ultra-thin SiO_x films with thickness variation from 1 nm to 7 nm. The greatest changes in a-ZTO/SiO_x/a-ZTO films were achieved by including 2 nm thick SiO_x, and other SiO_x layers showed the least alterations in the three-layered films. This behaviour is interpreted as the ultra-thin SiO_x layer with some electron trap states within the bandgap, and the electron is captured as tunnelling through these trap centres. Thus, carrier concentration dropped from $2.2\times10^{19}\,cm^{-3}$ to $7.1\times10^{18}\,cm^{-3}$, and carrier mobility dropped by 40% in under 2 nm thick SiO_x. Another possibility of carrier drop in three-layered films is that electronegativity of Si is lower than Sn, and it is higher than the electronegativity of Zn. It is worth noting that the probability of a bond between Si and O (weakly bonding with Z) is high. This bond between Si and O leads to reduced carrier mobility of a-ZTO/SiO_x/a-ZTO films because Zn is the main carrier mobility supporter in a-ZTO films.

In the case of trilayer a-ZTO/TiO_x/a-ZTO films, trilayer films achieved 80% of carrier concentration drop from $3.6\times10^{19}\,cm^{-3}$ to $1.98\times10^{19}\,cm^{-3}$ in three a-$ZTO_{10\,nm}$/$TiO_{x(2\,nm)}$/a-$ZTO_{10\,nm}$ film. However, carrier mobility was maintained at around 6.5 cm^2/Vs which is in line with the a-ZTO film. The mechanism of constant carrier mobility can be interpreted by ultra-thin TiO_x film's trap states. The ultra-thin TiO_x shows a trap and detrapping behaviour that supports smooth carrier movement in films. Apart from trap states, Ti(1.48) has low electronegativity and binding energy values, so fewer changes in the materials' oxidation states directly impact the materials' properties. Also, optical data is being collected by Ellipsometry. The analysis of optical data has been limited

by the low thickness of the films leading to lower Ellipsometry signals. This is attributed to the lack of a rotating compensatory in our ellipsometer, which leads to dramatically lower signals in the Cos (del) than the Tan (PsI).

In a-IGZO/SiO_x/a-IGZO three-layered films, the carrier drop mechanism has been studied by performing a variety of experimental methods. a-$IGZO_{(20nm)}$/$SiO_{x(2nm)}$/a-$IGZO_{(20nm)}$, a-$IGZO_{(20nm)}$/$SiO_{x(2nm)}$/a-$IGZO_{(7.5nm)}$, and a-$IGZO_{(20nm)}$/ $SiO_{x(2nm)}$/a-$IGZO_{(10nm)}$ films were transferred using a high vacuum transfer arm from the magnetron to XPS system to prevent air contamination, and changes in oxygen structure in trilayers were not detected. AFM and SEM confirmed these samples have a smooth surface. The carrier concentration drops in a-IGZO/SiO_x/a-IGZO multilayers, were used in ultra-thin 2 nm thick SiO_x between a-IGZO layers and showed one order of magnitude less than the same thickness of a-IGZO, which is the most effective layer compared with the other six SiO_x layers. The best explanation for this is that changing the film's thickness could impact the film's defect density. Here, the presence of sub-oxide distribution in the ultra-thin SiO_x regarding the thickness is also responsible for free carrier trap centres. There was a small number of interface trap densities, which was not taken into consideration because a significant variation in the roughness of trilayers was not observed. Finally, Si has a high electronegativity to bond with other high electronegativity oxygen elements, which generates undercoordinated In atoms that act as carrier trap centres due to the electrostatic mechanism. The oxygen content was involved in different ways to reduce the trap density of ultra-thin SiO_x films. 2 nm thick layer of SiO_x was fabricated in an oxygen-rich atmosphere in order to passivate the defect levels in SiO_x. As a result of oxygen content during the growth of SiO_x, carrier drop in a-$IGZO_{(20nm)}$/$SiO_{x(2nm)}$/a-$IGZO_{(10nm)}$ film vanished, and charge carrier density of a-$IGZO_{(20nm)}$/$SiO_{x(2nm)}$/a-$IGZO_{(10nm)}$ was in line with the same thickness of a-IGZO film.

References

[1] Lidia Łukasiak and Andrzej Jakubowski, *History of semiconductors*, *Journal of Telecommunications and information technology* , 3 (2010).

[2] Arun Madan Giovanni Bruno, Pio Capezzuto, *Plasma Deposition of Amorphous Silicon-Based Materials*, ACADEMIC PRESS, INC, 1995, ISBN 9780415475976.

[3] Charbel Tannous and R. Lawrence Comstock, *Magnetic Information-Storage Materials*, volume 00, Springer Nature, 2017.

[4] Setiyo Budiyanto, Muhammad Jamil, and Fajar Rahayu, *Feasibility Analysis of the Application of Project Loon as an Equitable Effort for Communication Infrastructure Development in Indonesia*, *Jurnal Telekomunikasi dan Komputer* **9**, 61 (2019).

[5] Rakesh A. Afre, Nallin Sharma, Maheshwar Sharon, and Madhuri Sharon, *Transparent Conducting Oxide Films for Various Applications: A Review*, *REVIEWS ON ADVANCED MATERIALS SCIENCE* **53**, 79 (2018).

[6] Sukanta De and Jonathan N. Coleman, *Are there fundamental limitations on the sheet resistance and transmittance of thin graphene films?*, *ACS Nano* **4**, 2713 (2010).

[7] Kenji Nomura, Hiromichi Ohta, Akihiro Takagi, Toshio Kamiya, Masahiro Hirano, and Hideo Hosono, *Room-temperature fabrication of transparent flexible thin-film transistors using amorphous oxide semiconductors*, *Nature* **432**, 488 (2004).

[8] H. Q. Chiang, J. F. Wager, R. L. Hoffman, J. Jeong, and D. A. Keszler, *High mobility transparent thin-film transistors with amorphous zinc tin oxide channel layer*, *Applied Physics Letters* **86** (2005).

[9] Joe Troughton, Del Atkinson, and Del Atkinson, *Amorphous InGaZnO and metal oxide semiconductor devices : an overview and current status*, *Journal of Materials Chemistry C* (2019).

[10] Toshio Kamiya, Kenji Nomura, and Hideo Hosono, *Subgap states, doping and defect formation energies in amorphous oxide semiconductor a-InGaZnO 4 studied by density functional theory*, *Physica Status Solidi (A) Applications and Materials Science* **207**, 1698 (2010).

[11] Esteban Rucavado, Quentin Jeangros, Daniel F. Urban, Jakub Holovský, Zdenek Remes, Martial Duchamp, Federica Landucci, Rafal E. Dunin-Borkowski, Wolfgang Körner, Christian Elsässer, Aïcha Hessler-Wyser, Monica Morales-Masis, and Christophe Ballif, *Enhancing the optoelectronic properties of amorphous zinc tin oxide by subgap defect*

passivation: A theoretical and experimental demonstration, *Physical Review B* **95**, 1 (2017).

[12] Oliver Lahr, Max Steudel, Holger von Wenckstern, and Marius Grundmann, *Mechanical Stress Stability of Flexible Amorphous Zinc Tin Oxide Thin-Film Transistors*, *Frontiers in Electronics* **2**, 1 (2021).

[13] Yogeenth Kumaresan, Yusin Pak, Namsoo Lim, Yonghun Kim, Min Ji Park, Sung Min Yoon, Hyoc Min Youn, Heon Lee, Byoung Hun Lee, and Gun Young Jung, *Highly Bendable In-Ga-ZnO Thin Film Transistors by Using a Thermally Stable Organic Dielectric Layer*, *Scientific Reports* **6**, 1 (2016).

[14] Cristina Fernandes and et all, *A Sustainable Approach to Flexible Electronics with Zinc-Tin Oxide Thin-Film Transistors*, *Advanced Electronic Materials* **4**, 1 (2018).

[15] H. Kim, C. M. Gilmore, A. Piqué, J. S. Horwitz, H. Mattoussi, H. Murata, Z. H. Kafafi, and D. B. Chrisey, *Electrical, optical, and structural properties of indium-tin-oxide thin films for organic light-emitting devices*, *Journal of Applied Physics* **86**, 6451 (1999).

[16] Matthew J Wahila, Zachary W Lebens-Higgins, Keith T Butler, Daniel Fritsch, Robert E Treharne, Robert G Palgrave, Joseph C Woicik, Benjamin J Morgan, Aron Walsh, and Louis F J Piper, *Accelerated optimization of transparent, amorphous zinc-tin-oxide thin films for optoelectronic applications*, *APL Materials* **7** (2019).

[17] Monica Morales-Masis, Fabien Dauzou, Quentin Jeangros, Ali Dabirian, Herbert Lifka, Rainald Gierth, Manfred Ruske, Date Moet, Aïcha Hessler-Wyser, and Christophe Ballif, *An Indium-Free Anode for Large-Area Flexible OLEDs: Defect-Free Transparent Conductive Zinc Tin Oxide*, *Advanced Functional Materials* **26**, 384 (2016).

[18] Yoon Jang Kim, Seungha Oh, Bong Seob Yang, Sang Jin Han, Hong Woo Lee, Hyuk Jin Kim, Jae Kyeong Jeong, Cheol Seong Hwang, and Hyeong Joon Kim, *Impact of the cation composition on the electrical performance of solution-processed zinc tin oxide thin-film transistors*, *ACS Applied Materials and Interfaces* **6**, 14026 (2014).

[19] Yong Hoon Kim, Min Koo Han, Jeong In Han, and Sung Kyu Park, *Effect of metallic composition on electrical properties of solution-processed indium-gallium-zinc-oxide thin-film transistors*, *IEEE Transactions on Electron Devices* **57**, 1009 (2010).

[20] Jaeyeong Heo, Sang Bok Kim, and Roy G. Gordon, *Atomic layer deposited zinc tin oxide channel for amorphous oxide thin film transistors*, *Applied Physics Letters* **101**, 10 (2012).

[21] Sang Min Lee, Young Hee Joo, and Chang Il Kim, *Influences of film thickness and annealing temperature on properties of sol-gel derived ZnO-SnO 2 nanocomposite thin film*, *Applied Surface Science* **320**, 494 (2014).

[22] Jozeph Park, Keun Tae Oh, Dong Hyun Kim, Hyun Jun Jeong, Yun Chang Park, Hyun Suk Kim, and Jin Seong Park, *High-Performance Zinc Tin Oxide Semiconductor Grown by Atmospheric-Pressure Mist-CVD and the Associated Thin-Film Transistor Properties*, *ACS Applied Materials and Interfaces* **9**, 20656 (2017).

[23] J. H. Ko, I. H. Kim, D. Kim, K. S. Lee, T. S. Lee, B. Cheong, and W. M. Kim, *Transparent and conducting Zn-Sn-O thin films prepared by combinatorial approach*, *Applied Surface Science* **253**, 7398 (2007).

[24] Ainur Zhussupbekova, Aitkazy Kaisha, Rajani K. Vijayaraghavan, Karsten Fleischer, Igor V. Shvets, and David Caffrey, *Importance of Local Bond Order to Conduction in Amorphous, Transparent, Conducting Oxides: The Case of Amorphous ZnSnOy*, *ACS Applied Materials & Interfaces* **11**, 44399 (2019), PMID: 31638369.

[25] Arvind Shah, *THIN-FILM SILICON SOLAR CELLS*, EPFL Press, Lausanne, Switzerland, 2010.

[26] Seok Jun Seo, Young Hwan Hwang, and Byeong Soo Bae, *Postannealing process for low temperature processed sol-gel zinc tin oxide thin film transistors*, *Electrochemical and Solid-State Letters* **13**, 357 (2010).

[27] David Hong and John F. Wager, *Passivation of zinc–tin–oxide thin-film transistors*, *Journal of Vacuum Science & Technology B: Microelectronics and Nanometer Structures* **23**, L25 (2006).

[28] Nitin Kumar, Bhawana Joshi, and K. Asokan, *The effects of thermal annealing on the structural and electrical properties of zinc tin oxide thin films for transparent conducting electrode applications*, *Physica B: Condensed Matter* **558**, 5 (2019).

[29] Vipin Kumar Jain, Praveen Kumar, Mahesh Kumar, Praveen Jain, Deepika Bhandari, and Y. K. Vijay, *Study of post annealing influence on structural, chemical and electrical properties of ZTO thin films*, *Journal of Alloys and Compounds* **509**, 3541 (2011).

[30] Yong Su Lee, Eric Kai Hsiang Yu, Dong Hwan Shim, Hyang Shik Kong, Linsen Bie, and Jerzy Kanicki, *Oxygen flow effects on electrical properties, stability, and density of states of amorphous In-Ga-Zn-O thin-film transistors*, *Japanese Journal of Applied Physics* **53** (2014).

[31] Byung Du Ahn, Dong Won Choi, Changhwan Choi, and Jin Seong Park, *The effect of the annealing temperature on the transition from conductor to semiconductor behavior in zinc tin oxide deposited atomic layer deposition*, *Applied Physics Letters* **105** (2014).

[32] Marius Grundmann, Heiko Frenzel, Alexander Lajn, Michael Lorenz, Friedrich Schein, and Holger Von Wenckstern, *Transparent semiconducting oxides: Materials and devices*, *Physica Status Solidi (A) Applications and Materials Science* **207**, 1437 (2010).

[33] Sebastian C. Dixon, David O. Scanlon, Claire J. Carmalt, and Ivan P. Parkin, *n-Type doped transparent conducting binary oxides: an overview*, *J. Mater. Chem. C* **4**, 6946 (2016).

[34] R. Devi Chandra, Manohar Rao, Keke Zhang, Rajiv Ramanujam Prabhakar, Chen Shi, Jie Zhang, Subodh G. Mhaisalkar, and Nripan Mathews, *Tuning electrical properties in amorphous zinc tin oxide thin films for solution processed electronics*, *ACS Applied Materials and Interfaces* **6**, 773 (2014).

[35] P. F. Ndione, A. Zakutayev, M. Kumar, C. E. Packard, J. J. Berry, J. D. Perkins, and D. S. Ginley, *Tuning the physical properties of amorphous In-Zn-Sn-O thin films using combinatorial sputtering*, *MRS Communications* **6**, 360 (2016).

[36] Ozhet Mauit, David Caffrey, Ardak Ainabayev, Aitkazy Kaisha, Olzat Toktarbaiuly, Yerzhigit Sugurbekov, Gulnar Sugurbekova, Igor V. Shvets, and Karsten Fleischer, *Growth of ZnO:Al by atomic layer deposition: Deconvoluting the contribution of hydrogen interstitials and crystallographic texture on the conductivity*, *Thin Solid Films* **690**, 137533 (2019).

[37] Klaus Ellmer and André Bikowski, *Intrinsic and extrinsic doping of ZnO and ZnO alloys*, *Journal of Physics D: Applied Physics* **49** (2016).

[38] Hideo Hosono Kenji Nomura, Hiromichi Ohta, Kazushige Ueda, Toshio Kamiya, Masahiro Hirano, *Thin-Film Transistor Fabricated in Single-Crystalline Transparent*, *Science* **300**, 1269 (2003).

[39] David Caffrey, Emma Norton, Cormac Coileáin, Christopher M. Smith, Brendan Bulfin, Leo Farrell, Igor V. Shvets, and Karsten Fleischer, *Decoupling the refractive index from the electrical properties of transparent conducting oxides via periodic superlattices*, *Scientific Reports* **6**, 1 (2016).

[40] Pedro Barquinha, Rodrigo Martins, Luis Pereira, and Elvira Fortunato, *Transparent Oxide Electronics From Materials to Devices*, John Wiley & Sons, Ltd, 2012.

[41] D. A. Tashmukhamedova and M. B. Yusupjanova, *Emission and optical properties of SiO2/Si thin films*, *Journal of Surface Investigation. X-ray, Synchrotron and Neutron Techniques* **10**, 1273 (2016).

[42] T. Rangel, D. Kecik, P. E. Trevisanutto, G. M. Rignanese, H. Van Swygenhoven, and V. Olevano, *Band structure of gold from many-body perturbation theory*, *Physical Review B - Condensed Matter and Materials Physics* **86**, 1 (2012).

[43] Y. P. Li and W. Y. Ching, *Band structures of all polycrystalline forms of silicon dioxide*, *Physical Review B* **31**, 2172 (1985).

[44] Marvin Cohen and T.K. Bergstresser, *Band Strucures and Psuedopotential Form Factors*, *Physical Review* **141** (1966).

[45] Juhn Jong Lin and Zhi Qing Li, *Electronic conduction properties of indium tin oxide: Single-particle and many-body transport*, *Journal of Physics Condensed Matter* **26** (2014).

[46] F.J. Hyde, *The Physics of Semiconductors*, volume 16, Springer Berlin Heidelberg New York, 2010, ISBN 9783540253709.

[47] Z. Serbetci, B. Gunduz, A. A. Al-Ghamdi, F. Al-Hazmic, K. Arik, F. El-Tantawy, F. Yakuphanoglu, and W. A. Farooq, *Determination of optical constants of nanocluster CdO thin films deposited by sol-gel technique*, *Acta Physica Polonica A* **126**, 798 (2014).

[48] Sricharani Rao Balmuri, Uthra Selvaraj, Vadivel Vinod Kumar, Savarimuthu Philip Anthony, Aristides Michael Tsatsakis, Kirill Sergeevich Golokhvast, and Thiagarajan Raman, *Effect of surfactant in mitigating cadmium oxide nanoparticle toxicity: Implications for mitigating cadmium toxicity in environment*, *Environmental Research* **152**, 141 (2017).

[49] Clark I. Bright, *Review of Transparent Conductive Oxides (TCO) , 3M Company, Tuscon, Arizona*, *Society of Vacuum Coaters* (2007).

[50] José María Escalante Fernándeza and Alejandro Martínez Abietar, *Theoretical Study of the Emission of Light Stimulated by Phonons in Indirect Bandgap Semiconductor*, *Procedia Computer Science* **7**, 231 (2011).

[51] Iljoon Kang, Chul Hong Park, Eugene Chong, and Sang Yeol Lee, *Role of Si as carrier suppressor in amorphous Zn-Sn-O*, *Current Applied Physics* **12**, S12 (2012).

[52] L. Farrell, K. Fleischer, D. Caffrey, D. Mullarkey, E. Norton, and I. V. Shvets, *Conducting mechanism in the epitaxial p -type transparent conducting oxide C r2 O3:Mg*, *Physical Review B - Condensed Matter and Materials Physics* **91**, 1 (2015).

[53] John Wager and Randy Hoffman, *Thin, fast, and flexible*, *IEEE Spectrum* **48**, 42 (2011).

[54] Klaus Ellmer, *Past achievements and future challenges in the development of optically transparent electrodes*, *Nature Photonics* **6**, 809 (2012).

[55] D. B. Fraser and H. D. Cook, *HIGHLY CONDUCTIVE, TRANSPARENT FILMS OF SPUTTERED In//2// minus //xSn//xO//3// minus //y.*, *Journal of the Electrochemical Society* **119**, 1368 (1972).

[56] G. Haacke, *New figure of merit for transparent conductors*, *Journal of Applied Physics* **47**, 4086 (1976).

[57] Jae Hyun Jeon, Tae Kyung Gong, Young Min Kong, Hak Min Lee, and Daeil Kim, *Effect of post-deposition annealing on the structural, optical and electrical properties of IGZO films*, *Electronic Materials Letters* **11**, 481 (2015).

[58] Karsten Fleischer, Emma Norton, Daragh Mullarkey, David Caffrey, and Igor V. Shvets, *Quantifying the performance of P-type transparent conducting oxides by experimental methods*, *Materials* **10**, 19 (2017).

[59] L. Dong, G. S. Zhu, H. R. Xu, X. P. Jiang, X. Y. Zhang, Y. Y. Zhao, D. L. Yan, L. Yuan, and A. B. Yu, *Preparation of indium tin oxide (ITO) thin film with (400) preferred orientation by sol–gel spin coating method*, *Journal of Materials Science: Materials in Electronics* **30**, 8047 (2019).

[60] Jun Han, Shuai Yuan, Lina Liu, Xiaofeng Qiu, Haibo Gong, Xiaopeng Yang, Cuncheng Li, Yufeng Hao, and Bingqiang Cao, *Fully indium-free flexible Ag nanowires/ZnO:F composite transparent conductive electrodes with high haze*, *Journal of Materials Chemistry A* **3**, 5375 (2015).

[61] Nurul Nazli Rosli, Mohd Adib Ibrahim, Norasikin Ahmad Ludin, Mohd Asri Mat Teridi, and Kamaruzzaman Sopian, *A review of graphene based transparent conducting films for use in solar photovoltaic applications*, *Renewable and Sustainable Energy Reviews* **99**, 83 (2019).

[62] Sophie Sorel, Philip E. Lyons, Sukanta De, Janet C. Dickerson, and Jonathan N. Coleman, *The dependence of the optoelectrical properties of silver nanowire networks on nanowire length and diameter*, *Nanotechnology* **23** (2012).

[63] S. M. Kwok K. Ng Sze and Department, *Physics of Semiconductor Devices*, A JOHN WILEY & SONS, JNC., PUBLICATION, third edit edition, 2007, ISBN 9783540773405.

[64] S.R.Elliot, *Physics of amorphous materials*, 1985, ISSN 0108-7673.

[65] S.L.Kakani; Amit Kakani, *Material science*, New age international limited, first edit edition, 2004.

[66] C. A. Colinge J. P. Colinge, *PHYSICS OF SEMICONDUCTOR DEVICES*, Kluwer Academic Publishers, 2002.

[67] R.B. Dingle, *R . B . Dingle on the Scattering of Electrons and Holes*, *Philosophical Magazine Series 7* **46**, 831 (1955).

[68] Robert Clanget, *Ionized impurity scattering in degenerate In2O3*, *Applied Physics* **2**, 247 (1973).

[69] R. Resta and L. Resca, *Ionized impurity scattering in semiconductors*, *Physical Review B* **20**, 3254 (1979).

[70] B. Sapoval C. Hermann, *Physics of Semiconductors*, volume 1, Springer-Verlag New York Berlin Heidelberg London Paris Tokyo Hong Kong Barcelona Budapest, 1993, ISBN 9788578110796.

[71] Gianfranco Pacchioni And and Sergio Valeri, *Oxide Ultrathin Films Science and Technology*, WILEY-VCH Verlag GmbH & Co. KGaA, 2012, ISBN 978-3-527-33016-4.

[72] J. C. Anderson, *Conduction in thin semiconductor films*, *Advances in Physics* **19**, 311 (1970).

[73] Takeshi Inaoka, Atsushi Nishida, and Masayuki Hasegawa, *Thickness dependence of carrier-electron states in doped semiconductor films*, 1999, ISSN 00319015.

[74] Yongfeng Ju, Tong Chen, Zhiming Wu, and Yadong Jiang, *Electrical properties of amorphous titanium oxide thin films*, *Advances in Condensed Matter Physics* **2013**, 1 (2013).

[75] Tsung-Han Chiang and John F. Wager, *Electronic Conduction Mechanisms in Insulators*, *IEEE Transactions on Electron Devices* **65**, 223 (2018).

[76] Patrick Fiorenza, Marilena Vivona, Ferdinando Iucolano, Andrea Severino, Simona Lorenti, Giuseppe Nicotra, Corrado Bongiorno, Filippo Giannazzo, and Fabrizio Roccaforte, *Temperature-dependent Fowler-Nordheim electron barrier height in SiO2/4H-SiC MOS capacitors*, *Materials Science in Semiconductor Processing* **78**, 38 (2018),

Wide band gap semiconductors technology for next generation of energy efficient power electronics.

[77] Kuan-Chang Chang, Tsung-Ming Tsai, Ting-Chang Chang, Hsing-Hua Wu, Jung-Hui Chen, Yong-En Syu, Geng-Wei Chang, Tian-Jian Chu, Guan-Ru Liu, Yu-Ting Su, Min-Chen Chen, Jhih-Hong Pan, Jian-Yu Chen, Cheng-Wei Tung, Hui-Chun Huang, Ya-Hsiang Tai, Der-Shin Gan, and Simon M. Sze, *Characteristics and Mechanisms of Silicon-Oxide-Based Resistance Random Access Memory*, *IEEE Electron Device Letters* **34**, 399 (2013).

[78] Burt W. Fowler, Yao-Feng Chang, Fei Zhou, Yanzhen Wang, Pai-Yu Chen, Fei Xue, Yen-Ting Chen, Brad Bringhurst, Scott Pozder, and Jack C. Lee, *Electroforming and resistive switching in silicon dioxide resistive memory devices*, *RSC Adv.* **5**, 21215 (2015).

[79] Fu-chien Chiu, *A Review on Conduction Mechanisms in Dielectric Films*, *Advances in Materials Science and Engineering* **2014**, 18 pages (2014).

[80] Kenji Nomura, Hiromichi Ohta, Kazushige Ueda, Toshio Kamiya, Masahiro Hirano, and Hideo Hosono, *Thin-film transistor fabricated in single-crystalline transparent oxide semiconductor*, *Science* **300**, 1269 (2003).

[81] D. J. Rogers, V. E. Sandana, F. Hosseini Teherani, R. McClintock, M. Razeghi, and H.-J. Drouhin, *Amorphous ZnO films grown by room temperature pulsed laser deposition on paper and mylar for transparent electronics applications*, *Oxide-based Materials and Devices II* **7940**, 79401K (2011).

[82] D. B. Buchholz, D. E. Proffit, M. D. Wisser, T. O. Mason, and R. P.H. Chang, *Electrical and band-gap properties of amorphous zinc-indium-tin oxide thin films*, *Progress in Natural Science: Materials International* **22**, 1 (2012).

[83] Seungtae Baek, Jeong Woo Han, Devthade Vidyasagar, Hanbyeol Cho, and Hwi-heon Ha, *Electron Transport Layer for Perovskite Solar Cells*, page 1 (2019).

[84] P. Dutta, Y. Gao, M. Rathi, Y. Yao, Y. Li, M. Iliev, J. Martinez, and V. Selvamanickam, *High mobility single-crystalline-like silicon thin films on inexpensive flexible metal foils by plasma enhanced chemical vapor deposition*, *Acta Materialia* **147**, 51 (2018).

[85] Christos D Dimitrakopoulos and D J Mascaro, *Organic thin film transistors: A review of recent advances*, **45**, 11 (2001).

[86] Ryo Hayashi, Masato Ofuji, Nobuyuki Kaji, Kenji Takahashi, Katsumi Abe, Hisato Yabuta, Masafumi Sano, Hideya Kumomi, Kenji Nomura, Toshio Kamiya, Masahiro Hirano, and Hideo Hosono, *Circuits using uniform TFTs based on amorphous In-Ga-Zn-O*, *Journal of the Society for Information Display* **15**, 915 (2007).

[87] Toshio Kamiya, Kenji Nomura, and Hideo Hosono, *Origins of High Mobility and Low Operation Voltage of Amorphous Oxide TFTs: Electronic Structure, Electron Transport, Defects and Doping**, *Journal of Display Technology* **5**, 468 (2009).

[88] Doo Hee Cho, Shinhyuk Yang, Chunwon Byun, Jaeheon Shin, Min Ki Ryu, Sang Hee Ko Park, Chi Sun Hwang, Sung Mook Chung, Woo Seok Cheong, Sung Min Yoon, and Hye Yong Chu, *Transparent Al-Zn-Sn-O thin film transistors prepared at low temperature*, *Applied Physics Letters* **93**, 2 (2008).

[89] Hiroshi Kawazoe Hideo Hosono, Masahiro Yasakawa, *Novel oxide amorphous semiconductors : transparent conducting amorphous oxides Possible Candidate for HMCs*, *Journal of Non-Crystalline Solids* **203**, 334 (1996).

[90] Sándor Kugler and Koichi Shimakawa, *Dedication*, pages v–vi, Cambridge University Press, 2015.

[91] Dongwoo Kim, Yeong Gyu Kim, Byung Ha Kang, Jin Hyeok Lee, Jusung Chung, and Hyun Jae Kim, *Fabrication of indium gallium zinc oxide phototransistors: Via oxide-mesh insertion for visible light detection*, *Journal of Materials Chemistry C* **8**, 165 (2019).

[92] Doo-Hyoung Lee, Seung-Yeol Han, Gregory S. Herman, and Chih-Hung Chang, *Inkjet Printed High-Mobility Indium Zinc Tin Oxide Thin Film Transistors*, *J. Mater. Chem.* **19**, 3135 (2009).

[93] Xingwei Ding, Jianhua Zhang, Jun Li, Weimin Shi, Hao Zhang, Xueyin Jiang, and Zhilin Zhang, *The Al2O3 gate insulator modified by SiO2 film to improve the performance of IGZO TFTs*, *Superlattices and Microstructures* **69**, 204 (2014).

[94] K. C. Sanal, M. Majeesh, and M. K. Jayaraj, *Growth of IGZO thin films and fabrication of transparent thin film transistor by RF magnetron sputtering*, *Nanostructured Thin Films VI* **8818**, 881814 (2013).

[95] Pradipta K. Nayak, Tito Busani, Elangovan Elamurugu, Pedro Barquinha, Rodrigo Martins, Yongtaek Hong, and Elvira Fortunato, *Zinc concentration dependence study of solution processed amorphous indium gallium zinc oxide thin film transistors using high-k dielectric*, *Applied Physics Letters* **97**, 2 (2010).

[96] Minho Ahn, Venkateswarlu Gaddam, Sungho Park, and Sanghun Jeon, *Effect of Ga composition on mobility in a-InGaZnO thin-film transistors*, *Nanotechnology* **32** (2021).

[97] Un Ki Kim, Sang Ho Rha, Jeong Hwan Kim, Yoon Jang Chung, Jisim Jung, Eun Suk Hwang, Joohwi Lee, Tae Joo Park, Jung Hae Choi, and Cheol Seong Hwang, *Study on the defects in metal-organic chemical vapor deposited zinc tin oxide thin films using negative bias illumination stability analysis*, *Journal of Materials Chemistry C* **1**, 6695 (2013).

[98] F. Ynineb, A. Hafdallah, M. S. Aida, N. Attaf, J. Bougdira, H. Rinnert, and S. Rahmane, *Influence of Sn content on properties of ZnO:SnO2 thin films deposited by ultrasonic spray pyrolysis*, *Materials Science in Semiconductor Processing* **16**, 2021 (2013).

[99] Nark Eon Sung, Han Koo Lee, Keun Hwa Chae, Jitendra Pal Singh, and Ik Jae Lee, *Correlation of oxygen vacancies to various properties of amorphous zinc tin oxide films*, *Journal of Applied Physics* **122**, 0 (2017).

[100] P. Schlupp, H. Von Wenckstern, and M. Grundmann, *Amorphous zinc-tin oxide thin films fabricated by pulsed laser deposition at room temperature*, *Journal of British Studies* **1633**, 101 (2014).

[101] Lucie Prušáková, Pavel Hubík, Asim Aijaz, Tomas Nyberg, and Tomas Kubart, *Room temperature reactive deposition of InGaZnO and ZnSnO amorphous oxide semiconductors for flexible electronics*, *MDPI, Coatings* **10** (2020).

[102] Sung Kyu Park, Yong Hoon Kim, Hyun Soo Kim, and Jeong In Han, *High performance solution-processed and lithographically patterned zinc-tin oxide thin-film transistors with good operational stability*, *Electrochemical and Solid-State Letters* **12**, 256 (2009).

[103] Yong Hoon Kim, Jeong In Han, and Sung Kyu Park, *Effect of Zinc/Tin composition ratio on the operational stability of solution-processed Zinc-Tin-Oxide Thin-Film transistors*, *IEEE Electron Device Letters* **33**, 50 (2012).

[104] Ainur Zhussupbekova, Aitkazy Kaisha, Rajani K. Vijayaraghavan, Karsten Fleischer, Igor V. Shvets, and David Caffrey, *Importance of Local Bond Order to Conduction in Amorphous, Transparent, Conducting Oxides: The Case of Amorphous ZnSnOy*, *ACS Applied Materials and Interfaces* **11**, 44399 (2019).

[105] Po Jui Kuo, Sheng Po Chang, and Shoou Jinn Chang, *Investigation of zinc-tin-oxide thin-film transistors with varying SnO2 contents*, *Electronic Materials Letters* **10**, 89 (2014).

[106] Ainur Zhussupbekova, David Caffrey, Kuanysh Zhussupbekov, Christopher M. Smith, Igor V. Shvets, and Karsten Fleischer, *Low-Cost, High-Performance Spray Pyrolysis-Grown Amorphous Zinc Tin Oxide: The Challenge of a Complex Growth Process*, *ACS applied materials & interfaces* **12**, 46892 (2020).

[107] Kenji Nomura, Toshio Kamiya, Masahiro Hirano, and Hideo Hosono, *Origins of threshold voltage shifts in room-temperature deposited and annealed a-In-Ga-Zn-O thin-film transistors*, *Applied Physics Letters* **95**, 1 (2009).

[108] W. H. Han and K. J. Chang, *Subgap States near the Conduction-Band Edge Due to Undercoordinated Cations in Amorphous In-Ga-Zn-O and Zn-Sn-O Semiconductors*, *Physical Review Applied* **6**, 1 (2016).

[109] Keisuke Ide, Kenji Nomura, Hideo Hosono, and Toshio Kamiya, *Electronic Defects in Amorphous Oxide Semiconductors: A Review*, *Physica Status Solidi (A) Applications and Materials Science* **216**, 1 (2019).

[110] Julia E. Medvedeva, D. Bruce Buchholz, and Robert P.H. Chang, *Recent Advances in Understanding the Structure and Properties of Amorphous Oxide Semiconductors*, *Advanced Electronic Materials* **3** (2017).

[111] PeterCapper(Eds.) Safa Kasap, *Springer Handbook of Electronic and Photonic Materials*, Springer International Publishing AG 2017, 2017, ISBN 9783319489315.

[112] N.F.Mott and E.A. Davis, *Electronics Process in Noncrystalline Materials*, Oxford University Press New York, 1971.

[113] John Robertson, *Disorder and instability processes in amorphous conducting oxides*, *Physica Status Solidi (B) Basic Research* **245**, 1026 (2008).

[114] Wolfgang Körner, Daniel F. Urban, and Christian Elsässer, *Origin of subgap states in amorphous In-Ga-Zn-O*, *Journal of Applied Physics* **114** (2013).

[115] Wolfgang Körner, Peter Gumbsch, and Christian Elsässer, *Analysis of electronic subgap states in amorphous semiconductor oxides based on the example of Zn-Sn-O systems*, *Physical Review B - Condensed Matter and Materials Physics* **86**, 1 (2012).

[116] Shawn Sallis, Nicholas F. Quackenbush, Deborah S. Williams, Mikell Senger, Joseph C. Woicik, Bruce E. White, and Louis F.J. Piper, *Deep subgap feature in amorphous indium gallium zinc oxide: Evidence against reduced indium*, *Physica Status Solidi (A) Applications and Materials Science* **212**, 1471 (2015).

[117] Shunpei Yamazaki, Hideomi Suzawa, Koki Inoue, Kiyoshi Kato, Takuya Hirohashi, Kenichi Okazaki, and Noboru Kimizuka, *Properties of crystalline In-Ga-Zn-oxide semiconductor and its transistor characteristics*, *Japanese Journal of Applied Physics* **53** (2014).

[118] Fuji Funabiki, Toshio Kamiya, and Hideo Hosono, *Doping effects in amorphous oxides*, *Journal of the Ceramic Society of Japan* **120**, 447 (2012).

[119] A. De Jamblinne De Meux, G. Pourtois, J. Genoe, and P. Heremans, *Defects in Amorphous Semiconductors: The Case of Amorphous Indium Gallium Zinc Oxide*, *Physical Review Applied* **9**, 54039 (2018).

[120] Wolfgang Körner and Christian Elsässer, *Density-functional theory study of stability and subgap states of crystalline and amorphous Zn-Sn-O*, *Thin Solid Films* **555**, 81 (2014).

[121] David S. Hideo Hosono Ginley and l David C. Paine, *Handbook of Transparent Conductors*, Springer New York Heidelberg Dordrecht London, 2010, ISBN 978-1-4419-1637-2, URL `http://link.springer.com/10.1007/978-1-4419-1638-9`.

[122] Per Kofstad, *Defect chemistry in metal oxides*, *Phase Transitions: A Multinational Journal* **58**, 75 (1996).

[123] Ho Hyun Nahm and Yong Sung Kim, *Undercoordinated indium as an intrinsic electron-trap center in amorphous InGaZnO4*, *NPG Asia Materials* **6**, 1 (2014).

[124] Hyeon Kyun Noh, K. J. Chang, Byungki Ryu, and Woo Jin Lee, *Electronic structure of oxygen-vacancy defects in amorphous In-Ga-Zn-O semiconductors*, *Physical Review B - Condensed Matter and Materials Physics* **84**, 1 (2011).

[125] Toshio Kamiya, Kenji Nomura, and Hideo Hosono, *Electronic structure of the amorphous oxide semiconductor a-lnGaZnO 4-x: Tauc-Lorentz optical model and origins of subgap states*, *Physica Status Solidi (A) Applications and Materials Science* **206**, 860 (2009).

[126] Sunho Jeong, Young Geun Ha, Jooho Moon, Antonio Facchetti, and Tobin J. Marks, *Role of gallium doping in dramatically lowering amorphous-oxide processing temperatures for solution-derived indium zinc oxide thin-film transistors*, *Advanced Materials* **22**, 1346 (2010).

[127] Yong Su Lee, Eric Kai Hsiang Yu, Dong Hwan Shim, Hyang Shik Kong, Linsen Bie, and Jerzy Kanicki, *Oxygen flow effects on electrical properties, stability, and density of states of amorphous In-Ga-Zn-O thin-film transistors*, *Japanese Journal of Applied Physics* **53** (2014).

[128] Kenji Nomura, Toshio Kamiya, Eiji Ikenaga, Hiroshi Yanagi, Keisuke Kobayashi, and Hideo Hosono, *Depth analysis of subgap electronic states in amorphous oxide semiconductor, a-In-Ga-Zn-O, studied by hard x-ray photoelectron spectroscopy*, *Journal of Applied Physics* **109** (2011).

[129] W. H. Han, Young Jun Oh, K. J. Chang, and Ji Sang Park, *Electronic Structure of Oxygen Interstitial Defects in Amorphous In-Ga-Zn-O Semiconductors and Implications for Device Behavior*, *Physical Review Applied* **3**, 1 (2015).

[130] Peter T. Erslev, Eric S. Sundholm, Rick E. Presley, David Hong, John F. Wager, and J. David Cohen, *Mapping out the distribution of electronic states in the mobility gap of amorphous zinc tin oxide*, *Applied Physics Letters* **95** (2009).

[131] John Wolstenholme John F. Watts, *An Introduction to Surface Analysis by XPS and AES*, John Wiley & Sons Ltd, 2003, ISBN 0470847123.

[132] E. A. Douglas, A. Scheurmann, R. P. Davies, B. P. Gila, Hyun Cho, V. Craciun, E. S. Lambers, S. J. Pearton, and F. Ren, *Measurement of SiO2/InZnGaO4 heterojunction band offsets by x-ray photoelectron spectroscopy*, *Applied Physics Letters* **98**, 2012 (2011).

[133] Dapeng Wang, Dan Li, Wenjing Zhao, and Mamoru Furuta, *Defect gradient control in amorphous InGaZnO for high-performance thin-film transistors*, *Journal of Physics D: Applied Physics* **53**, 1 (2020).

[134] Jaana S. Rajachidambaram, Shail Sanghavi, Ponnusamy Nachimuthu, Vaithiyalingam Shutthanandan, Tamas Varga, Brendan Flynn, Suntharampillai Thevuthasan, and Gregory S. Herman, *Characterization of amorphous zinc tin oxide semiconductors*, *Journal of Materials Research* **27**, 2309 (2012).

[135] Leland C. Allen, *Electronegativity Is the Average One-Electron Energy of the Valence-Shell Electrons in Ground-State Free Atoms*, *Journal of the American Chemical Society* **111**, 9003 (1989).

[136] Elbert J Little and Mark M Jones, *A complete table of electronegativities*, *Journal of Chemical Education* **37**, 231 (1960).

[137] Toshio Kamiya, Kenji Nomura, and Hideo Hosono, *Electronic structures above mobility edges in crystalline and amorphous In-Ga-Zn-O: Percolation conduction examined by analytical model*, *IEEE/OSA Journal of Display Technology* **5**, 462 (2009).

[138] Sándor Kugler Kazuo Morigaki and Koichi Shimakawa., *Amorphous Semiconductors Structural, Optical, and Electronic Properties*, John Wiley & Sons Ltd Registered, 2017, ISBN 9781118757925.

[139] A. V. Nenashev, J. O. Oelerich, S. H.M. Greiner, A. V. Dvurechenskii, F. Gebhard, and S. D. Baranovskii, *Percolation description of charge transport in amorphous oxide semiconductors*, *Physical Review B* **100**, 1 (2019).

[140] DavidAdler Finley R.Shapiro, *Equilibrium transport in amorphous semiconductors*, *Journal of Non-Crystalline Solids* **74**, 189 (1985).

[141] Dou Dou Liang, Binjie Chen, Hai Jun Cho, and Hiromichi Ohta, *Thickness optimization toward high-performance bottom-gated transparent tin dioxide thin-film transistors*, *ACS Applied Electronic Materials* **2**, 3454 (2020).

[142] Dipti Gupta and Yongtaek Hong, *Understanding the effect of semiconductor thickness on device characteristics in organic thin film transistors by way of two-dimensional simulations*, *Organic Electronics* **11**, 127 (2010).

[143] X. D. Li, Siyuan Chen, T. P. Chen, and Y. Liu, *Thickness dependence of optical properties of amorphous indium gallium zinc oxide thin films: Effects of free-electrons and quantum confinement*, *ECS Solid State Letters* **4**, P29 (2015).

[144] Ye Wang, Xiao Wei Sun, Gregory Kia Liang Goh, Hilmi Volkan Demir, and Hong Yu Yu, *Influence of channel layer thickness on the electrical performances of inkjet-printed In-Ga-Zn oxide thin-film transistors*, *IEEE Transactions on Electron Devices* **58**, 480 (2011).

[145] Jaewook Jeong and Yongtaek Hong, *Debye length and active layer thickness-dependent performance variations of amorphous oxide-based TFTs*, *IEEE Transactions on Electron Devices* **59**, 710 (2012).

[146] Jin Seong Park, Jae Kyeong Jeong, Hyun Joong Chung, Yeon Gon Mo, and Hye Dong Kim, *Electronic transport properties of amorphous indium-gallium-zinc oxide semiconductor upon exposure to water*, *Applied Physics Letters* **92**, 34 (2008).

[147] J. S. Kim, J. K. Park, Y. J. Baik, W. M. Kim, J. Jeong, and T. Y. Seong, *Electrical, optical and etching properties of Zn-Sn-O thin films deposited by combinatorial sputtering*, *Journal of the Korean Physical Society* **61**, 1651 (2012).

[148] Li-Chih Liu, Jen-Sue Chen, Jiann-Shing Jeng, and Wei-Yu Chen, *Variation of Oxygen Deficiency in Solution-Processed Ultra-Thin Zinc-Tin Oxide Films to Their Transistor Characteristics*, *ECS Journal of Solid State Science and Technology* **2**, Q59 (2013).

[149] Cheol Gyu Kim, Nam Hyun Lee, Young Kyu Kwon, and Bongkoo Kang, *Effects of film thickness and Sn concentration on electrical properties of solution-processed zinc tin oxide thin film transistors*, *Thin Solid Films* **544**, 129 (2013).

[150] Sunyoung Lee, Sungjoon Kim, Seokhee Shin, Zhenyu Jin, and Yo Sep Min, *Band structure of amorphous zinc tin oxide thin films deposited by atomic layer deposition*, *Journal of Industrial and Engineering Chemistry* **58**, 328 (2018).

[151] S. S. Nekrashevich and V. A. Gritsenko, *Electronic structure of silicon dioxide (a review)*, *Physics of the Solid State* **56**, 207 (2014).

[152] Binay Prasai, Bin Cai, M. Kylee Underwood, James P. Lewis, and D. A. Drabold, *Properties of amorphous and crystalline titanium dioxide from first principles*, *Journal of Materials Science* **47**, 7515 (2012).

[153] D. A. Muller, T. Sorsch, S. Moccio, F. H. Baumann, K. Evans-Lutterodt, and G. Timp, *The electronic structure at the atomic scale of ultrathin gate oxides*, *Nature* **399**, 758 (1999).

[154] Hussein Mohamed Abu El-Oyoun, Takao Inokuma, Yoshihiro Kurata, and Seiichi Hasegawa, *Structural properties of ultrathin amorphous silicon oxynitride layers*, *Japanese Journal of Applied Physics, Part 1: Regular Papers and Short Notes and Review Papers* **42**, 3570 (2003).

[155] M. L. Green, E. P. Gusev, R. Degraeve, and E. L. Garfunkel, *Ultrathin (<4 nm) SiO2 and Si-O-N gate dielectric layers for silicon microelectronics: Understanding the processing, structure, and physical and electrical limits*, *Journal of Applied Physics* **90**, 2057 (2001).

[156] P. V. Sushko, S. Mukhopadhyay, A. M. Stoneham, and A. L. Shluger, *Oxygen vacancies in amorphous silica: Structure and distribution of properties*, *Microelectronic Engineering* **80**, 292 (2005).

[157] Gong-Ru Lin, Chun-Jung Lin, and Chi-Kuan Lin, *Enhanced Fowler-Nordheim tunneling effect in nanocrystallite Si based LED with interfacial Si nano-pyramids*, *Opt. Express* **15**, 2555 (2007).

[158] Zied A. Alothmanc Imran Ali, Mohd Suhail and Abdulrahman Alwarthan, *Recent advances in syntheses , properties and applications of TiO 2 nanostructures*, *RSC Advances* , 30125 (2018).

[159] Zhiwei Zhao, Kang Tay, and Guoqing Yu, *Room-temperature deposition of amorphous titanium dioxide thin film with high refractive index by a filtered cathodic vacuum arc technique*, *APPLIED OPTICS* **43**, 1281 (2004).

[160] A. A. Abd El-Moula, M. Raaif, and F. M. El-Hossary, *Optical properties of nanocrystalline/amorphous TiO2 thin film deposited by rf plasma magnetron sputtering*, *Acta Physica Polonica A* **137**, 1068 (2020).

[161] A. K. Kunti, M. Chowdhury, S. K. Sharma, M. Gupta, and R. J. Chaudhary, *Influence of O2 pressure on structural, morphological and optical properties of TiO2-SiO2 composite thin films prepared by pulsed laser deposition*, *Thin Solid Films* **629**, 79 (2017).

[162] Bandna Bharti, Santosh Kumar, Heung No Lee, and Rajesh Kumar, *Formation of oxygen vacancies and Ti3+ state in TiO2 thin film and enhanced optical properties by air plasma treatment*, *Scientific Reports* **6**, 1 (2016).

[163] M M Abd El-raheem and Ateyyah M Al-baradi, *Optical properties of as-deposited TiO2 thin films prepared by DC sputtering technique*, *International Journal of Physical Sciences* **8**, 1570 (2013).

[164] P. J. Kelly and R. D. Arnell, *Magnetron sputtering: A review of recent developments and applications*, *Vacuum* **56**, 159 (2000).

[165] Ellmer Klaus, *Magnetron sputtering of transparent conductive zinc oxide: relation between the sputtering parameters and the electronic properties*, *Journal of Physics D: Applied Physics* **33**, R17 (2000).

[166] Diederik Depla, Stijn Mahieu, and Joseph Greene, *Sputter deposition processes*, In Peter M Martin, editor, *Handbook of deposition technologies for films and coatings : science, applications and technology*, pages 253–296. William Andrew, 2010, ISBN 9780815520313, URL `http://dx.doi.org/10.1016/B978-0-8155-2031-3.00005-3`.

[167] K. Strijckmans, R. Schelfhout, and D. Depla, *Tutorial: Hysteresis during the reactive magnetron sputtering process*, *Journal of Applied Physics* **124**, 1 (2018).

[168] Kah Yoong Chan and Bee San Teo, *Sputtering power and deposition pressure effects on the electrical and structural properties of copper thin films*, *Journal of Materials Science* **40**, 5971 (2005).

[169] J. Musil, P. Baroch, J. Vlček, K. H. Nam, and J. G. Han, *Reactive magnetron sputtering of thin films: Present status and trends*, *Thin Solid Films* **475**, 208 (2005).

[170] David Caffrey, *TCO / Dielectric Superlattice Structures for the Decoupling of Electrical and Optical Properties*, PhD thesis, Trinity College Dublin, 2016.

[171] N.Archer, *UHV Deposition manipulator instrumental manual*, Technical report, UHV DESIGN LTD, 2020, URL `www.uhvdesign.com`.

[172] S. Berg and T. Nyberg, *Fundamental understanding and modeling of reactive sputtering processes*, *Thin Solid Films* **476**, 215 (2005).

[173] B. Chapman, *Glow Discharge Process-sputtering and plasma etching*, JOHN WILEY & SONS, INC, 1980, ISBN 047107828X.

[174] D. Depla, *On the effective sputter yield during magnetron sputter deposition*, *Nuclear Instruments and Methods in Physics Research, Section B: Beam Interactions with Materials and Atoms* **328**, 65 (2014).

[175] K. Strijckmans and D. Depla, *Modeling target erosion during reactive sputtering*, *Applied Surface Science* **331**, 185 (2015).

[176] Simon Bates, George Zografi, David Engers, Kenneth Morris, Kieran Crowley, and Ann Newman, *Analysis of amorphous and nanocrystalline solids from their X-ray diffraction patterns*, *Pharmaceutical Research* **23**, 2333 (2006).

[177] Q. J. Jiang, C. J. Wu, J. P. Cheng, X. D. Li, B. Lu, Z. Z. Ye, and J. G. Lu, *Solvent sensors based on amorphous ZnSnO thin-film transistors*, *RSC Advances* **5**, 28242 (2015).

[178] Ircttwferenx Von Romtgmstrahten, *D e r physik 5 .*, *ANNALEN DER PHYSIK* (1931).

[179] Brian Cull, Yushan Shi, Satyendra Kumar, Raymond Shih, and J Mann, *X-ray reflectivity study of interface roughness, structure, and morphology of alignment layers and thin liquid crystal films*, *PHYSICAL REVIEW E* **51**, 526 (1995).

[180] Miho Yasaka, *X-ray thin-film measurement techniques V. X-ray reflectivity measurementnt*, *The Rigaku Journal* **26**, 1 (2010).

[181] F Schaefers and R Cimino, *Soft X-ray reflectivity: from quasi-perfect mirrors to accelerator walls*, *ECLOUD'12: Joint INFN-CERN-EuCARD-AccNet Workshop on Electron-Cloud Effects* , 105 (2013).

[182] L. G. Parratt, *Surface studies of solids by total reflection of x-rays*, *Physical Review* **95**, 359 (1954).

[183] A. Ruosi, C. Raisch, A. Verna, R. Werner, B. A. Davidson, J. Fujii, R. Kleiner, and D. Koelle, *Electron sampling depth and saturation effects in perovskite films investigated by soft x-ray absorption spectroscopy*, *Phys. Rev. B* **90**, 125120 (2014).

[184] D. T. Brower, R. E. Revay, and T. C. Huang, *A study of X-ray reflectivity data analysis methods for thin film thickness determination*, *Powder Diffraction* **11**, 114 (1996).

[185] Heinz-Helmut Perkampus, *UV-VIS Spectroscopy and Its Applications*, Springer-Verlag Berlin Heidelberg, 1992, ISBN 9783642774799.

[186] E R Shaaban and I S Yahia, *Validity of Swanepoel ' s Method for Calculating the Optical Constants of Thick Films Optical constants , dispersion and oscillator parameters of di erent thicknesses of amorphous Ge 25 Cd 5 Se 70 have been investigated by optical spectrophotometry measur*, *Acta Physica Polonica a* **121**, 628 (2012).

[187] J. Tauc, R. Grigorovici, and A. Vancu, *Optical Properties and Electronic Structure of Amorphous Germanium*, *physica status solidi (b)* **15**, 627 (1966).

[188] A. Escobedo-Morales, I. I. Ruiz-López, M. de L. Ruiz-Peralta, L. Tepech-Carrillo, M. Sánchez-Cantú, and J. E. Moreno-Orea, *Automated method for the determination of the band gap energy of pure and mixed powder samples using diffuse reflectance spectroscopy*, *Heliyon* **5**, 1 (2019).

[189] Patrycja Makuła, Michał Pacia, and Wojciech Macyk, *How To Correctly Determine the Band Gap Energy of Modified Semiconductor Photocatalysts Based on UV-Vis Spectra*, *Journal of Physical Chemistry Letters* **9**, 6814 (2018).

[190] I. Miccoli, F. Edler, H. Pfnür, and C. Tegenkamp, *The 100th anniversary of the four-point probe technique: The role of probe geometries in isotropic and anisotropic systems*, *Journal of Physics Condensed Matter* **27** (2015).

[191] Ainst.P. J. Jenkins, b.Sc, *Basic Principles of Electronics SEMICONDUCTORS*, volume 2, PERGAMON PRESS, 1966.

[192] Florian Werner, *Hall measurements on low-mobility thin films*, *Journal of Applied Physics* **122** (2017).

[193] R. A. Mereu, A. Le Donne, S. Trabattoni, M. Acciarri, and S. Binetti, *Comparative study on structural, morphological and optical properties of Zn2SnO4 thin films prepared by r.f. sputtering using Zn and Sn metal targets and ZnO-SnO2 ceramic target*, *Journal of Alloys and Compounds* **626**, 112 (2015).

[194] Patrick A. Wäger, Daniel J. Lang, Dominic Wittmer, Raimund Bleischwitz, and Christian Hagelüken, *Towards a more sustainable use of scarce metals. A review of intervention options along the metals life cycle*, *Gaia* **21**, 300 (2012).

[195] Cynthia J. Hines, Jennifer L. Roberts, Ronnee N. Andrews, Matthew V. Jackson, and James A. Deddens, *Use of and occupational exposure to indium in the United States*, *Journal of Occupational and Environmental Hygiene* **10**, 723 (2013).

[196] Kham M. Niang, Junhee Cho, Aditya Sadhanala, William I. Milne, Richard H. Friend, and Andrew J. Flewitt, *Zinc tin oxide thin film transistors produced by a high rate reactive sputtering: Effect of tin composition and annealing temperatures*, *Physica Status Solidi (A) Applications and Materials Science* **214** (2017).

[197] Hye-Ri Kim, Dong-Ho Kim, Eungsun Byon, Goo-Hyun Lee, Gun-Hwan Lee, and Pung-Keun Song, *Effects of Hydrogen Doping on the Electrical Properties of Zinc–Tin–Oxide Thin Films*, *Japanese Journal of Applied Physics* **49**, 121101 (2010).

[198] Pierre Antoine Cormier, Marc Stahl, Anne Lise Thomann, Rémi Dussart, Matthias Wolter, Nadjib Semmar, Jacky Mathias, and Holger Kersten, *On the measurement of energy fluxes in plasmas using a calorimetric probe and a thermopile sensor*, *Journal of Physics D: Applied Physics* **43**, 1 (2010).

[199] Andrew H. Simon, *4 - Sputter Processing*, In Krishna Seshan, editor, *Handbook of Thin Film Deposition (Third Edition)*, pages 55–88. William Andrew Publishing, Oxford, third edition edition, 2012, ISBN 978-1-4377-7873-1, URL `https://www.sciencedirect.com/science/article/pii/B9781437778731000048`.

[200] Xianglin Li, Zhenghua Su, Selvaraj Venkataraj, Sudip Kumar Batabyal, and Lydia Helena Wong, *8.6% Efficiency CZTSSe solar cell with atomic layer deposited Zn-Sn-O buffer layer*, *Solar Energy Materials and Solar Cells* **157**, 101 (2016).

[201] Stefan K. Estreicher David A. Drabold, *Theory of Defects in Semiconductors*, volume 111, Springer-Verlag Berlin Heidelberg, 2007, ISBN 9783540728641, URL `http://www.springer.com/series/560`.

[202] Leo Farrell, Emma Norton, Christopher M. Smith, David Caffrey, Igor V. Shvets, and Karsten Fleischer, *Synthesis of Nanocrystalline Cu Deficient $CuCrO_2$ – A High Figure of Merit p-type Transparent Semiconductor*, *J. Mater. Chem. C* **4**, 126 (2016).

[203] Pranab Biswas, Ardak Ainabayev, Ainur Zhussupbekova, Feljin Jose, Robert O'Connor, Aitkazy Kaisha, Brian Walls, and Igor V. Shvets, *Tuning of oxygen vacancy-induced electrical conductivity in Ti-doped hematite films and its impact on photoelectrochemical water splitting*, *Scientific Reports* **10**, 2 (2020).

[204] D. Ali, M. Z. Butt, C. Coughlan, D. Caffrey, I. V. Shvets, and K. Fleischer, *Nitrogen grain-boundary passivation of In-doped ZnO transparent conducting oxide*, *Physical Review Materials* **2**, 1 (2018).

[205] Yoon Young Choi, Seong Jun Kang, and Han Ki Kim, *Rapid thermal annealing effect on the characteristics of ZnSnO3 films prepared by RF magnetron sputtering*, *Current Applied Physics* **12**, 104 (2012).

[206] Wenbing Hu and Rebecca L. Peterson, *Charge transport in solution-processed zinc tin oxide thin film transistors*, *Journal of Materials Research* **27**, 2286 (2012).

[207] Wendong Yang, Emil J.W. List-Kratochvil, and Changhai Wang, *Metal particle-free inks for printed flexible electronics*, *Journal of Materials Chemistry C* **7**, 15098 (2019).

[208] Valerio Zardetto, Thomas M. Brown, Andrea Reale, and Aldo Di Carlo, *Substrates for flexible electronics: A practical investigation on the electrical, film flexibility, optical, temperature, and solvent resistance properties*, *Journal of Polymer Science, Part B: Polymer Physics* **49**, 638 (2011).

[209] Qian Zhang, Guodong Xia, Lubin Li, Wenwen Xia, Hongyu Gong, and Sumei Wang, *High-performance Zinc-Tin-Oxide thin film transistors based on environment friendly solution process*, *Current Applied Physics* **19**, 174 (2019).

[210] M. A. Islam, K. S. Rahman, H. Misran, N. Asim, M. S. Hossain, M. Akhtaruzzaman, and N. Amin, *High mobility and transparent ZTO ETM prepared by RF reactive co-sputtering for perovskite solar cell application*, *Results in Physics* **14**, 102518 (2019).

[211] M. Anpo, G. Costentin, E. Giamello, H. Lauron-Pernot, and Z. Sojka, *Characterisation and reactivity of oxygen species at the surface of metal oxides*, *Journal of Catalysis* **393**, 259 (2021).

[212] André Schleife, Claudia Rödl, Frank Fuchs, Karsten Hannewald, and Friedhelm Bechstedt, *Optical Absorption in Degenerately Doped Semiconductors: Mott Transition or Mahan Excitons?*, *Phys. Rev. Lett.* **107**, 236405 (2011).

[213] Michael Latzel, Manuela Göbelt, Gerald Brönstrup, Cornel Venzago, Sebastian W. Schmitt, George Sarau, and Silke H. Christiansen, *Modeling the dielectric function of degenerately doped ZnO:Al thin films grown by ALD using physical parameters*, *Opt. Mater. Express* **5**, 1979 (2015).

[214] Y. Z. Chen, M. Döbeli, E. Pomjakushina, Y. L. Gan, N. Pryds, and T. Lippert, *Scavenging of oxygen vacancies at modulation-doped oxide interfaces: Evidence from oxygen isotope tracing*, *Physical Review Materials* **1**, 1 (2017).

[215] Sandeep Kumar Singh, M. Neek-Amal, S. Costamagna, and F. M. Peeters, *Thermomechanical properties of a single hexagonal boron nitride sheet*, *Physical Review B - Condensed Matter and Materials Physics* **87**, 1 (2013).

[216] M. Cavillon, P. D. Dragic, and J. Ballato, *Additivity of the coefficient of thermal expansion in silicate optical fibers*, *Optics Letters* **42**, 3650 (2017).

[217] Xianlei Li, Xiaopeng Hao, Mingwen Zhao, Yongzhong Wu, Jiaxiang Yang, Yupeng Tian, and Guodong Qian, *Exfoliation of Hexagonal Boron Nitride by Molten Hydroxides*, *Advanced Materials* **25**, 2200 (2013).

[218] Uijin Jung, Subin Kim, Dohyun Kim, Dong Su Shin, Zhanpeng Xian, and Jinsub Park, *Metal-Semiconductor-Metal UV Detectors Using Transferrable Amorphous and Crystalline Zinc-Tin-Oxide Microsphere Monolayers*, *ACS Sustainable Chemistry and Engineering* **8**, 60 (2020).

[219] Oliver Lahr, Sofie Vogt, Holger von Wenckstern, and Marius Grundmann, *Low-Voltage Operation of Ring Oscillators Based on Room-Temperature-Deposited Amorphous Zinc-Tin-Oxide Channel MESFETs*, *Advanced Electronic Materials* **5**, 1900548 (2019).

[220] Binghao Wang, Peijun Guo, Li Zeng, Xia Yu, Aritra Sil, Wei Huang, Matthew J. Leonardi, Xinan Zhang, Gang Wang, Shaofeng Lu, Zhihua Chen, Michael J. Bedzyk, Richard D. Schaller, Tobin J. Marks, and Antonio Facchetti, *Expeditious, scalable solution growth of metal oxide films by combustion blade coating for flexible electronics*, *Proceedings of the National Academy of Sciences* **116**, 9230 (2019).

[221] Luc Alaerts, Michael Augustinus, and Karel Van Acker, *Impact of bio-based plastics on current recycling of plastics*, *Sustainability (Switzerland)* **10** (2018).

[222] Dongheon Ha, Zhiqiang Fang, and Nikolai B. Zhitenev, *Paper in Electronic and Optoelectronic Devices*, *Advanced Electronic Materials* **4**, 1700593 (2018).

[223] Wenxi Guo, Zijie Xu, Fayin Zhang, Shuyao Xie, Hongyao Xu, and Xiang Yang Liu, *Recent Development of Transparent Conducting Oxide-Free Flexible Thin-Film Solar Cells*, *Advanced Functional Materials* **26**, 8855 (2016).

[224] P. Barquinha, A. Pimentel, A. Marques, L. Pereira, R. Martins, and E. Fortunato, *Influence of the semiconductor thickness on the electrical properties of transparent TFTs based on indium zinc oxide*, *Journal of Non-Crystalline Solids* **352**, 1749 (2006).

[225] Shin yi Min and Won Ju Cho, *Rare Metal-Free High-Performance Zinc–Tin Oxide Thin Film Transistors Using Efficient Energy Conversion of Microwave Annealing*, *Physica Status Solidi (A) Applications and Materials Science* **217**, 1 (2020).

[226] Kimoon Lee, Yong Hoon Kim, Jiwan Kim, and Min Suk Oh, *Transparent and Flexible Zinc Tin Oxide Thin Film Transistors and Inverters using Low-pressure Oxygen Annealing Process*, *Journal of the Korean Physical Society* **72**, 1073 (2018).

[227] F. Gunkel, D. V. Christensen, Y. Z. Chen, and N. Pryds, *Oxygen vacancies: The (in)visible friend of oxide electronics*, *Applied Physics Letters* **116**, 120505 (2020).

[228] Aleksandar R. Zeradjanin, Justus Masa, Ioannis Spanos, and Robert Schlögl, *Activity and Stability of Oxides During Oxygen Evolution Reaction—From Mechanistic Controversies Toward Relevant Electrocatalytic Descriptors*, *Frontiers in Energy Research* **8**, 1 (2021).

[229] Sungjun Ahn, Tae Geun Kwon, and Sang Yup Lee, *Synthesis of zinc tin oxide (ZTO) nanocrystallites at room temperature through association with peptide-containing bolaamphiphile molecules*, *Journal of Colloid and Interface Science* **362**, 292 (2011).

[230] Derya Baran, Daniel Corzo, and Guillermo Blazquez, *Flexible Electronics: Status, Challenges and Opportunities*, *Frontiers in Electronics* **1** (2020).

[231] F. R. Jeffrey, G. D. Vernstrom, F. E. Aspen, and R. L. Jacobson, *Fabrication of Amorphous Silicon Devices on Plastic Substrates*, *MRS Proceedings* **49**, 41 (1985).

[232] Ke Long, Alexis Kattamis, I.-Chun Cheng, Ying X. Gao, Helena Gleskova, Sigurd Wagner, and James C. Sturm, *P-24: High-Temperature (250°C) Amorphous-Silicon TFT's On Clear Plastic Substrates*, *SID Symposium Digest of Technical Papers* **36**, 313 (2005).

[233] Q. Zhu, Q. Ma, D. B. Buchholz, R. P. H. Chang, M. J. Bedzyk, and T. O. Mason, *Structural and physical properties of transparent conducting, amorphous Zn-doped SnO2 films*, *Journal of Applied Physics* **115**, 033512 (2014).

[234] Byung Du Ahn, Dong-won Choi, Changhwan Choi, and Jin-Seong Park, *The effect of the annealing temperature on the transition from conductor to semiconductor behavior in zinc tin oxide deposited atomic layer deposition*, *Applied Physics Letters* **105**, 092103 (2014).

[235] Shanmugam Parthiban and Jang Yeon Kwon, *Role of dopants as a carrier suppressor and strong oxygen binder in amorphous indium-oxide-based field effect transistor*, *Journal of Materials Research* **29**, 1585 (2014).

[236] Hong Yoon Jung, Youngho Kang, Ah Young Hwang, Chang Kyu Lee, Seungwu Han, Dae Hwan Kim, Jong Uk Bae, Woo Sup Shin, and Jae Kyeong Jeong, *Origin of the improved mobility and photo-bias stability in a double-channel metal oxide transistor*, *Scientific Reports* **4**, 1 (2014).

[237] Sarah Jane O. White and James P. Shine, *Exposure Potential and Health Impacts of Indium and Gallium, Metals Critical to Emerging Electronics and Energy Technologies*, *Current Environmental Health Reports* **3**, 459 (2016).

[238] Esteban Rucavado, Migle Graužinyte, José A. Flores-Livas, Quentin Jeangros, Federica Landucci, Yeonbae Lee, Takashi Koida, Stefan Goedecker, Aïcha Hessler-Wyser, Christophe Ballif, and Monica Morales-Masis, *New Route for "cold-Passivation" of Defects in Tin-Based Oxides*, *Journal of Physical Chemistry C* **122**, 17612 (2018).

[239] Jun Young Choi, Keun Heo, Kyung Sang Cho, Sung Woo Hwang, Sangsig Kim, and Sang Yeol Lee, *Engineering of band gap states of amorphous SiZnSnO semiconductor as a function of Si doping concentration*, *Scientific Reports* **6**, 1 (2016).

[240] Kwok K. Hung, Ping K. Ko, Chenming Hu, and Yiu C. Cheng, *A Unified Model For The Flicker Noise In Metal-Oxide-Semiconductor Field-Effect Transistors*, *IEEE Transactions on Electron Devices* **37**, 654 (1990).

[241] Hisashi Fukuda, Makoto Yasuda, Satoshi Kaneko, Tomo Ueno, and I Introduction, *Process dependence of the Si02 / Si (100) interface trap density*, *Interface* **1906**, 1906 (1992).

[242] Boris Moyzhes, Theodore H. Geballe, Steve Jeong, Daniel Gitlin, and James Karp, *Current through Si O2 gate oxide and its low frequency fluctuations: Trapping on charged dangling bonds with negative Hubbard U*, *Journal of Applied Physics* **97**, 074104 (2005).

[243] J. Bloch, J. G. Mihaychuk, and H. M. Van Driel, *Electron Photoinjection from Silicon to Ultrathin SiO2 Films via Ambient Oxygen*, *Physical Review Letters* **77**, 920 (1996).

[244] M. Nafría, J. Suñé, and X. Aymerich, *Breakdown of thin gate silicon dioxide films - A review*, *Microelectronics Reliability* **36**, 871 (1996).

[245] Nathan L. Anderson, Ravi Pramod Vedula, Peter A. Schultz, R. M.Van Ginhoven, and Alejandro Strachan, *Defect level distributions and atomic relaxations induced by charge trapping in amorphous silica*, *Applied Physics Letters* **100** (2012).

[246] Al Moatasem El-Sayed, Matthew B. Watkins, Alexander L. Shluger, and Valeri V. Afanas'Ev, *Identification of intrinsic electron trapping sites in bulk amorphous silica from ab initio calculations*, *Microelectronic Engineering* **109**, 68 (2013).

[247] S. Sallis, K. T. Butler, N. F. Quackenbush, D. S. Williams, M. Junda, D. A. Fischer, J. C. Woicik, N. J. Podraza, B. E. White, A. Walsh, and L. F.J. Piper, *Origin of deep subgap states in amorphous indium gallium zinc oxide: Chemically disordered coordination of oxygen*, *Applied Physics Letters* **104**, 232108 (2014).

[248] Keisuke Ide, Kenji Nomura, Hidenori Hiramatsu, Toshio Kamiya, and Hideo Hosono, *Structural relaxation in amorphous oxide semiconductor, a-In-Ga-Zn-O*, *Journal of Applied Physics* **111**, 1 (2012).

[249] L. H. AHRENS, *lonization Potentials Implications and Applications*, PERGAMON PRESS, 1983, ISBN 0080252745.

[250] Shaodong Sun, Peng Song, Jie Cui, and Shuhua Liang, *Amorphous TiO2 nanostructures: Synthesis, fundamental properties and photocatalytic applications*, *Catalysis Science and Technology* **9**, 4198 (2019).

[251] Xiaoyang Yang, Yuxin Min, Sibai Li, Dawei Wang, Zongwei Mei, Jun Liang, and Feng Pan, *Conductive Nb-doped TiO2 thin films with whole visible absorption to degrade pollutants*, *Catalysis Science and Technology* **8**, 1357 (2018).

[252] Marius Dobromir, Radu Paul Apetrei, A.V. Rogachev, Dmitry L. Kovalenko, and Dumitru Luca, *Synthesis and Characterization of Nb-Doped TiO2 Thin Films Prepared by RF Magnetron Sputtering*, *Advanced Materials Research* **1117**, 139 (2015).

[253] H.I. Elsaeedy, Ammar Qasem, H.A. Yakout, and Mona Mahmoud, *The pivotal role of TiO2 layer thickness in optimizing the performance of TiO2/P-Si solar cell*, *Journal of Alloys and Compounds* **867**, 159150 (2021).

[254] A. Yildiz, S. B. Lisesivdin, M. Kasap, and D. Mardare, *Electrical properties of TiO2 thin films*, *Journal of Non-Crystalline Solids* **354**, 4944 (2008).

[255] S. K. Mukherjee and D. Mergel, *Thickness dependence of the growth of magnetron-sputtered TiO2 films studied by Raman and optical transmittance spectroscopy*, *Journal of Applied Physics* **114** (2013).

[256] David Mora-Fonz, Moloud Kaviani, and Alexander L. Shluger, *Disorder-induced electron and hole trapping in amorphous TiO2*, *Physical Review B* **102**, 1 (2020).

[257] Hieu H. Pham and Lin Wang Wang, *Oxygen vacancy and hole conduction in amorphous TiO2*, *Physical Chemistry Chemical Physics* **17**, 541 (2015).

[258] Dimitar A. Panayotov, Steven P. Burrows, and John R. Morris, *Infrared Spectroscopic Studies of Conduction Band and Trapped Electrons in UV-Photoexcited, H-Atom n-Doped, and Thermally Reduced TiO2*, *The Journal of Physical Chemistry C* **116**, 4535 (2012).

[259] M. K. Bera, C. Mahata, and C. K. Maiti, *Reliability of ultra-thin titanium dioxide (TiO2) films on strained-Si*, *Thin Solid Films* **517**, 27 (2008).

[260] Xiuli Wang, Zhaochi Feng, Jianying Shi, Guoqing Jia, Shuai Shen, Jun Zhou, and Can Li, *Trap states and carrier dynamics of TiO2 studied by photoluminescence spectroscopy under weak excitation condition*, *Physical Chemistry Chemical Physics* **12**, 7083 (2010).

[261] Peter Deák, Bálint Aradi, and Thomas Frauenheim, *Quantitative theory of the oxygen vacancy and carrier self-trapping in bulk* TiO_2, *Phys. Rev. B* **86**, 195206 (2012).

[262] Liisa J. Antila, Fabio G. Santomauro, Leif Hammarström, Daniel L.A. Fernandes, and Jacinto Sá, *Hunting for the elusive shallow traps in TiO2 anatase*, *Chemical Communications* **51**, 10914 (2015).

[263] Thomas Leichtweiss, Ralph A. Henning, Julius Koettgen, Rüdiger M. Schmidt, Bernd Holländer, Manfred Martin, Matthias Wuttig, and Jürgen Janek, *Amorphous and highly nonstoichiometric titania (TiOx) thin films close to metal-like conductivity*, *Journal of Materials Chemistry A* **2**, 6631 (2014).

[264] Robert Kalescky, Elfi Kraka, and Dieter Cremer, *Identification of the strongest bonds in chemistry*, *Journal of Physical Chemistry A* **117**, 8981 (2013).

[265] Toshio Kamiya, Kenji Nomura, and Hideo Hosono, *Present status of amorphous In-Ga-Zn-O thin-film transistors*, *Science and Technology of Advanced Materials* **11**, 1 (2010).

[266] F. J. Himpsel, F. R. McFeely, A. Taleb-Ibrahimi, J. A. Yarmoff, and G. Hollinger, *Microscopic structure of the SiO2/Si interface*, *Physical Review B* **38**, 6084 (1988).

[267] Junfei Shi, Chengyuan Dong, Wenjun Dai, Jie Wu, Yuting Chen, and Runze Zhan, *The influence of RF power on the electrical properties of sputtered amorphous in - Ga - Zn - O thin films and devices*, *Journal of Semiconductors* **34**, 084003 (2013).

[268] Muhammad Rizwan Amirzada, Andreas Tatzel, Volker Viereck, and Hartmut Hillmer, *Surface roughness analysis of SiO2 for PECVD, PVD and IBD on different substrates*, *Applied Nanoscience (Switzerland)* **6**, 215 (2016).

[269] Nidhi Tiwari, Ram Narayan Chauhan, Po Tsun Liu, and Han Ping D. Shieh, *Electrical characteristics of InGaZnO thin film transistor prepared by co-sputtering dual InGaZnO and ZnO targets*, *RSC Advances* **5**, 51983 (2015).

[270] Min Hoe Cho, Hyunju Seol, Aeran Song, Seonjun Choi, Yunheub Song, Pil Sang Yun, Kwun Bum Chung, Jong Uk Bae, Kwon Shik Park, and Jae Kyeong Jeong, *Comparative Study on Performance of IGZO Transistors With Sputtered and Atomic Layer Deposited Channel Layer*, *IEEE Transactions on Electron Devices* **66**, 1783 (2019).

[271] Yeon Keon Moon, Sih Lee, Do Hyun Kim, Dong Hoon Lee, Chang Oh Jeong, and Jong Wan Park, *Application of DC magnetron sputtering to deposition of InGaZnO films for thin film transistor devices*, *Japanese Journal of Applied Physics* **48**, 031301 (2009).

[272] Wantae Lim, SeonHoo Kim, Yu-Lin Wang, J. W. Lee, D. P. Norton, S. J. Pearton, F. Ren, and I. I. Kravchenko, *High-Performance Indium Gallium Zinc Oxide Transparent Thin-Film Transistors Fabricated by Radio-Frequency Sputtering*, *Journal of The Electrochemical Society* **155**, H383 (2008).

[273] Keisuke Ide, Mitsuho Kikuchi, Masato Sasase, Hidenori Hiramatsu, Hideya Kumomi, Hideo Hosono, and Toshio Kamiya, *Why high-pressure sputtering must be avoided to deposit a-In-Ga-Zn-O films*, In *2016 23rd International Workshop on Active-Matrix Flatpanel Displays and Devices (AM-FPD)*, pages 298–301, 2016.

[274] E. A. Irene, E. Tierney, and J. Angilello, *A Viscous Flow Model to Explain the Appearance of High Density Thermal SiO2 at Low Oxidation Temperatures*, *Journal of The Electrochemical Society* **129**, 2594 (1982).

[275] Hyo-Jun Joo, Min-Gyu Shin, Hwan-Seok Jung, Hyun-Seok Cha, Donguk Nam, and Hyuck-In Kwon, *Oxide Thin-Film Transistor-Based Vertically Stacked Complementary Inverter for Logic and Photo-Sensor Operations*, *Materials* **12** (2019).

[276] Akihiro Takagi, Kenji Nomura, Hiromichi Ohta, Hiroshi Yanagi, Toshio Kamiya, Masahiro Hirano, and Hideo Hosono, *Carrier transport and electronic structure in amorphous oxide semiconductor, a-InGaZnO4*, *Thin Solid Films* **486**, 38 (2005).

[277] A. Hadjadj, O. Simonetti, T. Maurel, G. Salace, and C. Petit, *Si-SiO2 barrier height and its temperature dependence in metal-oxide-semiconductor structures with ultrathin gate oxide*, *Applied Physics Letters* **80**, 3334 (2002).

[278] J. H. Oh, H. W. Yeom, Y. Hagimoto, K. Ono, M. Oshima, N. Hirashita, M. Nywa, A. Toriumi, and A. Kakizaki, *Chemical structure of the ultrathin SiO2/Si(100) interface:An angle-resolved Si 2p photoemission study*, *Physical Review B - Condensed Matter and Materials Physics* **63**, 1 (2001).

[279] David Z. Gao, Jack Strand, Manveer S. Munde, and Alexander L. Shluger, *Mechanisms of oxygen vacancy aggregation in SiO 2 and HfO 2*, *Frontiers in Physics* **7**, 1 (2019).

[280] Anna Kimmel, Peter Sushko, Alexander Shluger, and Gennadi Bersuker, *Positive and Negative Oxygen Vacancies in Amorphous Silica*, *ECS Transactions* **19**, 3 (2009).

[281] Hong Ping Ma, Jia He Yang, Jian Guo Yang, Li Yuan Zhu, Wei Huang, Guang Jie Yuan, Ji Jun Feng, Tien Chien Jen, and Hong Liang Lu, *Systematic study of the SiOx film with different stoichiometry by plasma-enhanced atomic layer deposition and its application in SiOx/SiO2 super-lattice*, *Nanomaterials* **9**, 1 (2019).

[282] Luis G. Gerling, Cristobal Voz, Ramón Alcubilla, and Joaquim Puigdollers, *Origin of passivation in hole-selective transition metal oxides for crystalline silicon heterojunction solar cells*, *Journal of Materials Research* **32**, 260 (2017).

[283] Timothy R. Oldham, *Switching oxide traps*, *International Journal of High Speed Electronics and Systems* **14**, 581 (2004).

[284] Moonkyung Kim, Ravishankar Sundararaman, Sandip Tiwari, and Jo Won Lee, *Charge trapping devices using a bilayer oxide structure*, *Journal of Nanoscience and Nanotechnology* **12**, 423 (2012).

[285] Angelo Bongiorno and Alfredo Pasquarello, *Atomistic structure of the Si(100)-SiO2 interface: A synthesis of experimental data*, *Applied Physics Letters* **83**, 1417 (2003).

[286] F.J. Grunthaner and P.J. Grunthaner, *Chemical and electronic structure of the SiO2/Si interface*, *Materials Science Reports* **1**, 65 (1986).

[287] P. M. Lenahan, *What can electron paramagnetic resonance tell us about the Si/SiO[sub 2] system?*, *Journal of Vacuum Science & Technology B: Microelectronics and Nanometer Structures* **16**, 2134 (1998).

[288] Byungki Ryu, Hyeon Kyun Noh, Eun Ae Choi, and K. J. Chang, *O-vacancy as the origin of negative bias illumination stress instability in amorphous In-Ga-Zn-O thin film transistors*, *Applied Physics Letters* **97**, 2012 (2010).

[289] Shigeto Fukatsu, Tomonori Takahashi, Kohei M. Itoh, Masashi Uematsu, Akira Fujiwara, Hiroyuki Kageshima, Yasuo Takahashi, and Kenji Shiraishi, *The Effect of Partial Pressure of Oxygen on Self-Diffusion of Si in SiO2*, *Japanese Journal of Applied Physics, Part 2: Letters* **42**, 1492 (2003).

[290] L. Do Thanh and P. Balk, *Elimination and Generation of Si - SiO2 Interface Traps by Low Temperature Hydrogen Annealing*, *Journal of The Electrochemical Society* **135**, 1797 (1988).

[291] Bhabani Shankar Sahu, Florian Delachat, Abdelilah Slaoui, Marzia Carrada, Gerald Ferblantier, and Dominique Muller, *Effect of annealing treatments on photoluminescence and charge storage mechanism in Silicon-Rich SiNx: H films*, *Nanoscale Research Letters* **6**, 1 (2011).

[292] J. M. Knaup, P. Deák, Th Frauenheim, A. Gali, Z. Hajnal, and W. J. Choyke, *Defects in SiO2 as the possible origin of near interface traps in the SiC SiO2 system: A systematic theoretical study*, *Physical Review B - Condensed Matter and Materials Physics* **72**, 1 (2005).

[293] Joaquim O. Carneiro, Filipe Machado, Luis Rebouta, Mikhail I. Vasilevskiy, Senen Lanceros-Méndez, Vasco Teixeira, Manuel F. Costa, and Anura P. Samantilleke, *Compositional, optical and electrical characteristics of SiOx thin films deposited by reactive pulsed DC magnetron sputtering*, *Coatings* **9**, 1 (2019).